

Cover Page



Universiteit Leiden



The handle <http://hdl.handle.net/1887/54935> holds various files of this Leiden University dissertation.

Author: Rixel, V.H.S. van

Title: Toward selective anticancer metallodrugs

Issue Date: 2017-10-19

Toward Selective Anticancer Metallodrugs

PROEFSCHRIFT

Ter verkrijging van
de graad van Doctor aan de Universiteit Leiden,
op gezag van Rector Magnificus Prof. mr. C. J. J. M. Stolker,
volgens besluit van het College voor Promoties
te verdedigen op donderdag 19 oktober 2017
klokke 11:15 uur

Vincent Hendrikus Shoichi van Rixel
geboren te Beverwijk, Nederland, 1987

Samenstelling Promotiecommissie

Promotor

Prof. dr. E. Bouwman

Copromotor

Dr. S. Bonnet

Overige Leden

Prof. dr. H.S. Overkleeft

Prof. dr. M. Ubbink

Prof. dr. P.J. Sadler (University of Warwick)

Prof. dr. G.J. Roelfes (Rijksuniversiteit Groningen)

This work has been financially supported by The Netherlands Organization for Scientific Research (NWO).

'Life is what happens to you, while you're busy making other plans.'

John Winston Lennon

'And all the science I don't understand, it's just my job five days a week.'

Sir Elton Hercules John

'Sigh no more.'

Marcus Oliver Johnstone Mumford

'You can check-out any time you like, but you can never leave.'

Donald Hugh Henley

'It's a beautiful day. The sun is shining. I feel good. And no-one's gonna stop me now, oh yeah.'

Freddie Mercury

'Keep building these random memories. Turning our days into melodies. But since I can't stay. I'll just keep playing back. These fragments of time. Everywhere I go. These moments will shine.'

Todd Edwards

Dedicated to those I love and supported me all the way

Table of Contents

Chapter 1	9
Introduction: Transition metal complexes as anticancer drugs	
Chapter 2	33
Preparation, stability, and photoreactivity of thiolato ruthenium polypyridyl complexes: can cysteine derivatives protect ruthenium-based anticancer complexes?	
Chapter 3	53
A microtubule-targeted rigidin analogue caged by a ruthenium polypyridyl complex that can be released with green light	
Chapter 4	67
Green light-induced apoptosis in cancer cells by a tetrapyrindyl ruthenium prodrug offering two <i>trans</i> coordination sites	
Chapter 5	91
Controlling with light the interaction between <i>trans</i> tetrapyrindyl ruthenium complexes and an oligonucleotide	
Chapter 6	111
The metal matters: Tetrapyrindyl nickel, palladium, and platinum anticancer compounds with spectacularly different activity and mechanism of action	

Chapter 7	131
The metal matters II: Protonation and deprotonation of the non-coordinating amines of $[M(H_2bapbpy)]^{2+}$ complexes	
Chapter 8	147
The ligand matters: Pd and Pt anticancer drugs based on a tetrapyridyl ligand containing a single amine bridge	
Chapter 9	163
Summary, Discussion, Conclusion, and Outlook	
Appendix I: General Biochemical methods	179
Appendix II: Supporting Information for Chapter 2	183
Appendix III: Supporting Information for Chapter 3	193
Appendix IV: Supporting Information for Chapter 4	197
Appendix V: Supporting Information for Chapter 5	211
Appendix VI: Supporting Information for Chapter 6	219
Appendix VII: Supporting Information for Chapter 7	225
Appendix VIII: Supporting Information for Chapter 8	231
Appendix IX: Supporting Information for Chapter 9	235
Samenvatting	237
Curriculum Vitae	245
List of Publications	247
Acknowledgements	249

CHAPTER 1

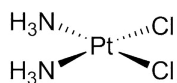
Introduction: Transition metal complexes as anticancer drugs

The discovery of anticancer properties of cisplatin in the 1960s has sparked a wide array of research in the field of transition metal complexes as anticancer drugs. Through key examples of complexes in metal-based chemotherapy, photodynamic therapy, and photoactivated chemotherapy, the state-of-the-art in the field of anticancer metallodrugs is described.

1.1 A new hope: cisplatin

The story of cisplatin (*cis*-[PtCl₂(NH₃)₂], Figure 1.1) is remarkable. For the first time synthesized by Michele Peyrone in 1844,^{1, 2} the actual structure of cisplatin was extensively described 50 years after its discovery by Alfred Werner's 'Beitrag zur Konstitution anorganischer Verbindungen' in 1892.³ Finally, cisplatin played a central role in Werner's theory of coordination chemistry, for which he was later awarded the Nobel Prize in Chemistry 'in recognition of his work on the linkage of atoms in molecules by which he has thrown new light on earlier investigations and opened up new fields of research especially in inorganic chemistry.'⁴

Attention for cisplatin settled until the 1960s, when its anticancer effects were discovered by Barnett Rosenberg. While originally studying the effect of an electric field on mitosis in prokaryotic cells, Rosenberg observed inhibition of cell division of *Escherichia coli* bacteria. After thorough research Rosenberg came to the conclusion that cisplatin was the prime candidate for this effect that in the initial experiments was formed as electrolysis product from a platinum electrode.⁵ After years of research it proved to be a promising anticancer drug candidate in both *in vitro*⁶ and *in vivo* studies.⁷ In these years Rosenberg not only investigated and developed a compound that has become one of the most successful chemotherapeutic agents; he also lay the foundation of a whole new field of research, that of metal-based anticancer drugs. Rosenberg's work in the late 1960s and 1970s comprised platinum anticancer chemistry that included cisplatin analogues, different modes of action of *cis* and *trans* isomers,⁸ and the activation of platinum(IV) complexes by photoreduction,⁹ that all have present-day relevance.



cisplatin

Figure 1.1 Chemical structure of cisplatin.

As a chemotherapeutic agent that is still used in the clinics today, cisplatin is administered intravenously to cancer patients. Due to the high chloride concentration in the bloodstream (> 100 mM), the chloride ligands mostly remain coordinated.¹⁰ Cisplatin can then enter the cell either *via* passive diffusion or *via*

copper(II) transporters.¹¹ In the cell the chloride concentration is much lower (3-20 mM), thus allowing for hydrolysis of cisplatin into $[\text{Pt}(\text{NH}_3)_2(\text{OH}_2)\text{Cl}]^+$.¹² Once inside the nucleus this species can form a coordination bond with thymine, guanine, cytosine, or adenine, the bases of nuclear DNA, of which guanine is the preferred coordination site. Once coordinated, the second chloride ligand is replaced *via* coordination to another DNA base, ultimately forming interstrand or intrastrand crosslinks.¹³ These crosslinks bend and unwind duplex DNA and this distortion attracts high-mobility group proteins.¹⁴ The attachment of these proteins shields the platinated DNA from excision repair and consequently sensitizes the cell for apoptosis.¹⁵ This cisplatin mechanism of action (MoA), as presented here, is the main paradigm in place. However, there is extensive scientific debate if and how interaction with biomolecules, before binding to nuclear DNA, plays a crucial role in the MoA.¹⁶

The development and clinical success of cisplatin have sparked wide interest and allocation of funds to develop new platinum-based anticancer drugs. Cisplatin has a cure rate of over 95% for patients diagnosed with testicular cancer, and is also used in the treatment of bladder and ovarian cancer.¹⁷ However, side effects associated with cisplatin include nephrotoxicity, neurotoxicity, ototoxicity, and nausea. Another drawback is that some cancers have or can acquire cisplatin resistances.¹⁸ Therefore, cisplatin analogues have been developed in the clinic, for example carboplatin or oxaliplatin, that have significantly less side effects (Figure 1.2). Other cisplatin analogues that have been approved in at least one country include nedaplatin, lobaplatin, and heptaplatin (Figure 1.2).¹⁹ All these cisplatin analogues contain two amine ligands coordinated to the platinum center in a *cis* configuration.

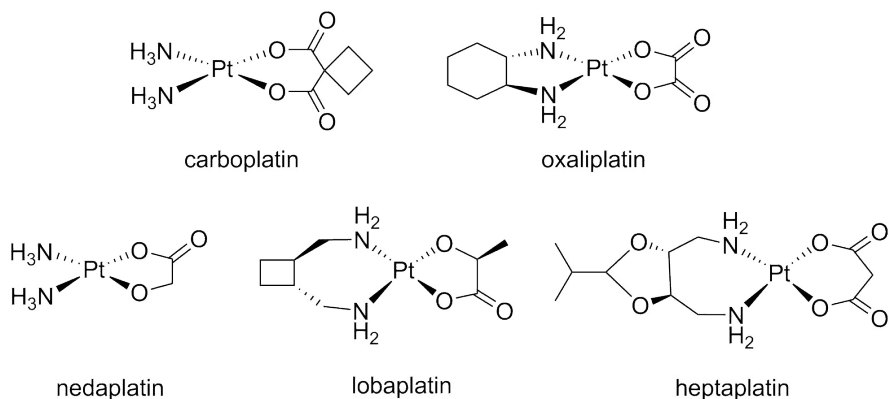


Figure 1.2 Chemical structures of carboplatin, oxaliplatin, nedaplatin, lobaplatin, and heptaplatin.

1.2 Changing metal: the rise of ruthenium

There has been extensive research in metal-based non-platinum anticancer agents, to avoid cisplatin related side effects, to overcome cisplatin resistance, and to improve selectivity. In this context ruthenium complexes have been the most investigated alternative.²⁰ This attention can be explained by the following properties of ruthenium as metal center for building transition metal complexes: a distinct coordination geometry (octahedron vs. square plane), specific binding preferences, access and physiological stability of +II and +III oxidation states, redox activity, and similar ligand exchange kinetics compared to platinum(II).^{21, 22} Moreover, early reports describing promising ruthenium complexes were already published in the eighties and nineties.^{23, 24} This section is not intended to give a complete overview of ruthenium complexes that have been developed, reported, and tested *in vitro* or *in vivo*, but to describe a personal view on key ruthenium complexes that have been critical in the development of ruthenium anticancer chemistry. Ruthenium complexes in combination with phototherapy will be discussed more specifically in section 1.4.

For a long time NAMI-A developed by Sava and Alessio, and KP1019 developed by Keppler et al., have been the ambassadors to the field of ruthenium anticancer chemistry (Figure 1.3). In a Phase I-II study NAMI-A was given to 32 patients with advanced non-small lung cell carcinoma in combination with clinically approved gemcitabine.²⁵ At the highest dose remission was reported for only one patient, and

stable disease was reported for six to eight weeks for ten patients. Patients experienced nausea, vomiting, constipation, diarrhea, fatigue, renal toxicity, and blister formation. These results proved not to be promising enough and NAMI-A was, after many years, qualified as 'insufficiently effective for further use'.²⁵ KP1019 was developed against colon cancer, caused no serious side effects in a Phase I study, and affected stability in five out of six patients up to 10 weeks.²⁶ Due to limited solubility of the compound large infusion volumes were required.²⁷ This low solubility ended the clinical testing of KP1019. However, the legacy of KP1019 lives on in the form of its more water-soluble sodium salt analogue NKP-1339 (Figure 1.3), which, according to its developers, is '*the first ruthenium-based anticancer drug on the edge of clinical application*'.²⁸ In a phase I study NKP-1339 was administered to a total of 34 (heavily pre-treated) patients with various solid tumors. At the highest doses (780 mg.m⁻²), very minor side effects were observed, and a partial response was observed in one patient and disease stabilization in seven patients. These limited effects are a major advantage over current metal-based anticancer drugs, and justify further development of NKP-1339. Despite the fact that NAMI-A and KP1019 did not end up as clinically approved drugs, their development has greatly contributed to ruthenium anticancer chemistry.²⁹

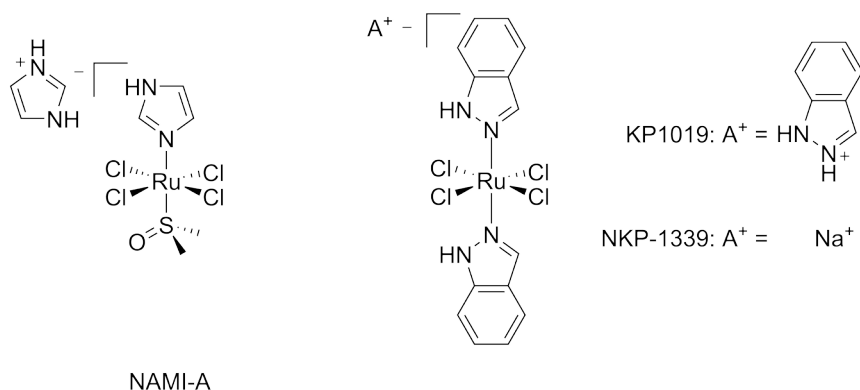


Figure 1.3 Chemical structures of NAMI-A, KP1019, and NKP1339.

It is common to first assess the potential of any new complexes by evaluating their cytotoxicity. Cytotoxicity is commonly reported as the IC₅₀ or EC₅₀ value – the inhibiting or effective concentration at which 50% of the treated cells is dead, compared to untreated control cells. For the sake of clarity and uniformity in this thesis these values will be reported as EC₅₀ values. These values highly depend on

the parameters of the cytotoxicity assay, one of the most important being the drug incubation time, which in the literature typically varies from 1 to 72 hours.

The two main types of compounds in ruthenium anticancer research are categorized as ruthenium arene complexes and ruthenium polypyridyl complexes. The first category of compounds contain a polyhapto-coordinated arene ligand. For example, RAPTA complexes developed by Dyson et al. comprise ruthenium η^6 -arene (RA, the core), the monodentate phosphine ligand 1,3,5-triaza-7-phosphoadamantane (PTA), and two chloride ligands. Dissociation of these chloride ligands is possible, thereby mimicking the first steps of the MoA of cisplatin. The compound RAPTA-C (Figure 1.4) has shown inhibition of tumor growth *in vivo* by approximately 75%, and inhibition of angiogenesis in the chicken chorioallantoic membrane model was demonstrated.³⁰ Similar RAED (ruthenium arene ethylenediamine) complexes reported by Sadler contain a η^6 -arene ligand, a bidentate 1,2-ethylenediamine ligand, and a chloride ligand. From this series the compound RM175 (Figure 1.4) has exhibited growth inhibition against A2780 ovarian cancer cells ($EC_{50} = 9 \mu\text{M}$)³¹ and 46% tumor growth inhibition with two doses of $25 \text{ mg}\cdot\text{kg}^{-1}$ in A2780 xenografts and A2780cis xenografts.³²

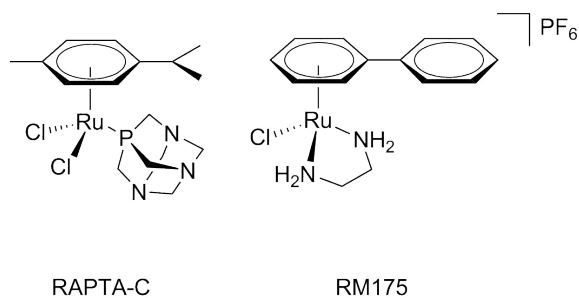


Figure 1.4 Chemical structures of RAPTA-C and RM175.

Ruthenium polypyridyl complexes have been extensively studied as well, not only as anticancer compounds but also as (redox) catalysts or imaging agents.^{33, 34} Due to the wide scope of mono-, bi-, tri-, tetra-, and pentadentate pyridyl ligands, an infinite number of different complexes is possible, and a vast amount of literature has been generated on this family of complexes. In 1995 the simple ruthenium polypyridyl complex $[\text{Ru}(\text{tpy})\text{Cl}_3]$ (tpy = 2,2':6',2''-terpyridine, Figure 1.5) was

reported to have 50% growth inhibition of HeLa cells with 7 μM treatment after 72 hours of exposure *in vitro*, and was claimed to exhibit 'significant antitumor activity' *in vivo*.³⁵ Another example is the cyclometallated ruthenium complex RDC11 (Figure 1.5). *In vivo* it reduced the tumor volume and weight by 40% and performed better than the control compound cisplatin, without causing severe side effects to the liver, kidneys, or the neuronal sensory system.³⁶

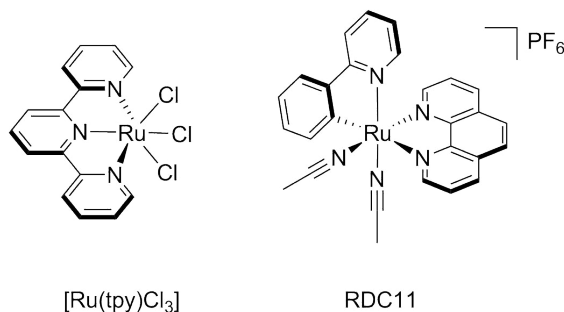


Figure 1.5 Chemical structures of [Ru(tpy)Cl₃] and RDC11.

In conclusion, despite the early development of NAMI-A and KP1019 in the 1980s and clinical testing in the 1990s, the promise of (simple) ruthenium complexes has not been fulfilled yet. To date none of the second generation ruthenium complexes from the arene and polypyridyl groups have ended up in the clinics. The way to the clinic is complicated and lack of success can have many reasons, of which the investment climate is not the least important. Therefore, ruthenium-based anticancer drugs will only become clinically successful when they have superior properties, in terms of key issues such as selectivity, general toxicity, and/or resistance, compared to currently approved drugs and in particular cisplatin analogues.

1.3 No more side effects: in search of selectivity

Side effects caused by chemotherapy are primarily caused by a lack of selectivity. To sustain rapid cell division, cancer cells have a high uptake of molecules of all kinds, which may include anticancer agents. Such high uptake is not limited to cancer cells, but also includes fast-growing healthy cells such as hair cells, or microvilli located in the intestines. As the chemotherapeutic agent is usually distributed across the whole body, only a limited amount ends up in the tumor.

Therefore, improving selectivity would not only reduce side effects stemming from general toxicity, but also allow for more optimal treatment doses.

In inorganic chemistry several approaches have been developed to acquire selectivity in chemotherapeutic compounds. The first one is the prodrug approach, which involves chemical binding of the drug to a moiety that deactivates or cages the active compound. Ideally, the caged or inactive form does not interfere with the cell biochemistry, which prevents non-specific cytotoxicity and undesired side effects. Selectivity can then be induced by local activation, but also by equipping the active compound with targeting moieties. The Keppler group has oxidized oxaliplatin, and introduced axial maleimide ligands to selectively couple the maleimide to the thiol group of cysteine-34 of human serum albumin (HSA) as shown in Figure 1.6.³⁷ HSA is known to accumulate in malignant and inflammatory tissues due to the enhanced permeability and retention effect.³⁸ Mice treated with HSA-functionalized oxaliplatin(IV) exhibited no significant loss of body weight, significant reduction in tumor growth (CT colon xenograft), and disease stabilization.³⁷

The group of Lippard has developed a cisplatin-based platinum(IV) compound containing a (D)-1-methyltryptophan ((D)-1-MT) ligand in one of the axial positions (Figure 1.6). (D)-1-MT inhibits indoleamine-2,3-dioxygenase, an immunosuppressive enzyme in human tumors, leading to immunomodulation and enhanced T-cell proliferation *in vitro*.³⁹ EC₅₀ values of these platinum(IV) complexes ranged from high nanomolar to micromolar concentrations against a panel of human ovarian cancer cell lines. In summary, square-planar cisplatin analogues can be oxidized into an octahedral platinum(IV) compound. After uptake of this prodrug, the platinum(IV) compound is subsequently reduced to the original cisplatin analogue, and then acts similar to the platinum(II)-based drugs. The two extra coordination sites can be used to couple the prodrug to ligands that have high target affinity. In the process alternative cell uptake mechanisms may be operative, overcoming acquired drug resistance that stem from lowered uptake.

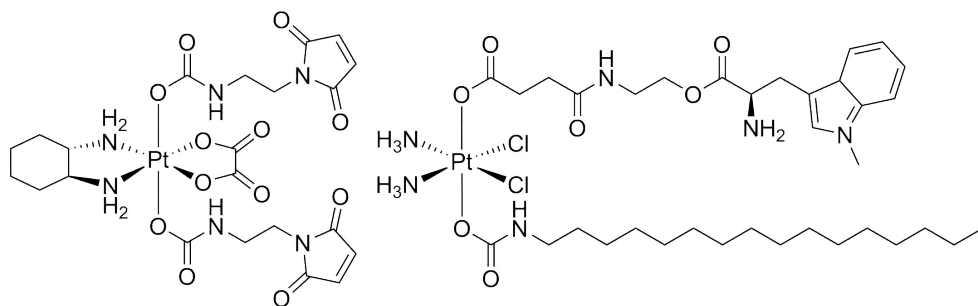


Figure 1.6 Chemical structures of maleimide functionalized oxaliplatin (left) and (D)1-methyl tryptophan functionalized cisplatin (right).^{37, 39}

An alternative strategy in targeting cancer cells is to disturb their distinct and delicate redox balance. Healthy cells commonly have tight regulation of reactive oxygen species (ROS) and metal homeostasis to maintain this intracellular redox balance.⁴⁰ Enzymatic reactions performed by reductases, oxidases, and peroxidases, and non-enzymatic reactions involving glutathione (GSH) and thioredoxin, are employed by cells to preserve this redox balance.⁴¹ For example, the disturbance of homeostasis caused by cisplatin increases the intracellular ROS levels, and is associated with cisplatin-induced side effects ototoxicity and nephrotoxicity.^{42, 43} Cancer cells are characterized by an imbalance in redox homeostasis that leads to enhanced intracellular ROS presence, and subsequently higher levels of oxidative stress.^{44, 45} The higher concentrations of ROS are not only caused by a high metabolic activity to sustain rapid cell division, but are also caused by lower levels of antioxidants. Cancer cells, thus, have a lower ROS-buffering capacity and can deal less efficiently with extracellular stress compared to healthy cells. Anticancer compounds that are designed to induce ROS may thus be more cytotoxic toward cancer cells than toward healthy cells.

Drawing inspiration from transfer hydrogenation catalysis by ruthenium-arene complexes, Sadler et al. have developed complexes capable of pushing the coenzyme $\text{NAD}^+ + \text{H}^- \rightleftharpoons \text{NADH}$ equilibrium towards NADH in the presence of an excess sodium formate acting as the hydride donor.⁴⁶ Excess NADH results in reductive stress causing the cells to die. Treatment of A2780 cancer cells with $[\text{Ru}(p\text{-cym})(\text{MsEn})\text{Cl}]$ ($\text{MsEn} = N\text{-}(2\text{-aminoethyl})\text{methanesulfonamide}$, Figure 1.7, left) without formate resulted in EC_{50} values of 11.9 μM . When co-treated with formate, an enhanced antiproliferative activity, characterized by an EC_{50} lower

than 1.0 μM , was measured. In contrast, $[(\eta^5\text{-Cp}^{\text{xbiph}})\text{Ir}(\text{phpy})\text{py}]\text{PF}_6$ (Cp^{xbiph} = biphenyltetramethyl-cyclopentadienyl, Hphpy = phenylpyridine, py = pyridine, Figure 1.7, right) *in vitro* acts as an oxidation catalyst and pushes the $\text{NAD}^+ + \text{H} \rightleftharpoons \text{NADH}$ equilibrium towards NAD^+ , resulting in higher levels of H_2O_2 .⁴⁷ Co-treatment with L-buthionine sulfoximine (BSO), an inhibitor of γ -glutamylcysteine synthetase, results in a two-fold increase of the activity of this compound, to EC_{50} values of 60 nM. As BSO lowers the ability of cells to scavenge ROS, the enhanced cytotoxicity of the iridium complex is explained by its capacity to interfere with the redox balance of the cancer cell.

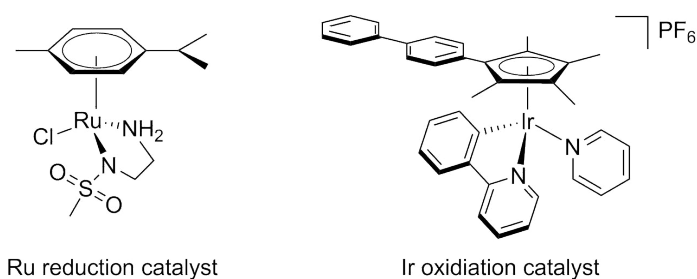


Figure 1.7 Chemical structures of ruthenium reduction catalyst and iridium oxidation catalyst developed by Sadler.

1.4 Phototherapy in anticancer treatment

Phototherapy is a rapidly developing method in cancer research to increase the selectivity of chemotherapeutic drugs. It relies on the local activation of a prodrug by *in vivo* light irradiation of the tumor. Ideally, the prodrug is non-toxic and becomes highly toxic after activation in the irradiated tumor tissue. Phototoxicity is quantified as the ratio of the EC_{50} value obtained in a dark control and that obtained after light irradiation. This factor is commonly defined as the Photo Index (PI), and it should ideally be as large as possible. In phototherapy, light activation by lower-energy light (red light) is preferred over activation by high-energy light (UV- and blue light), because low-energy light is less scattered, less damaging to cells, and less absorbed *in vivo*, meaning that it can penetrate further in biological tissues.⁴⁸ In contrast, UV light is carcinogenic in itself,⁴⁹ and does not penetrate deeply in tissues, which limits *in vivo* applications. Several features determine the potential efficiency of phototherapy agents: (i) water solubility, (ii) stability in the

dark in aqueous media and serum, (iii) uptake by cells, (iv) PI, and (v) wavelength at which the compound can be activated.²²

Photodynamic therapy (PDT) relies on absorbance of light by a photosensitizer, and transfer of this energy to ground state triplet oxygen ($^3\text{O}_2$) to form highly reactive excited state singlet oxygen ($^1\text{O}_2$). The photogenerated $^1\text{O}_2$ can induce damages to biomolecules, or react with biomolecules to form other ROS species such as H_2O_2 . This type of PDT is commonly referred to as PDT type 2. PDT type 1 involves the direct reaction between a photosensitizer and biomolecules without the direct involvement of dioxygen, but it is much less common than PDT type 2. To date, PDT photosensitizers approved in the clinic are the organic molecules Photofrin, Foscan, Levulan, and Metvixia cream. Among inorganic PDT photosensitizers the water-soluble palladium porphyrin complex, Padeliporfin (WST11), developed by Scherz and Salomon, is the only compound clinically tested and even approved in some countries (Figure 1.8, left).⁵⁰ Phase II clinical trials demonstrated that 4 mg/kg WST11, and light doses of $200 \text{ J}\cdot\text{cm}^{-1}$ ($\lambda_{\text{irr}} = 753 \text{ nm}$), are the optimal treatment conditions for patients with localized low-risk prostate cancer. Evaluation six months after treatment demonstrated that > 80% of patients were tested negatively for prostate cancer. WST11 has passed Latin America Phase III clinical trials, and is currently clinically available in Mexico. Results of a European Phase III clinical trial have been submitted to the European Medicine Agency in January 2016 and approval of WST11 is pending. In the field of ruthenium chemistry a highly promising PDT photosensitizer, TLD1433, has been developed by McFarland et al. (Figure 1.8, right). *In vitro* this compound has an EC_{50} value after light activation by red light ($\lambda_{\text{irr}} = 625 \text{ nm}$) of $19 \mu\text{M}$, while in the dark it remains higher than $300 \mu\text{M}$ in HL-60 cells.⁵¹ In 2016 TLD1433 finished Phase I-II clinical trials with promising outcomes as treatment for bladder cancer, and it is currently lining up for Phase III clinical trials.⁵²

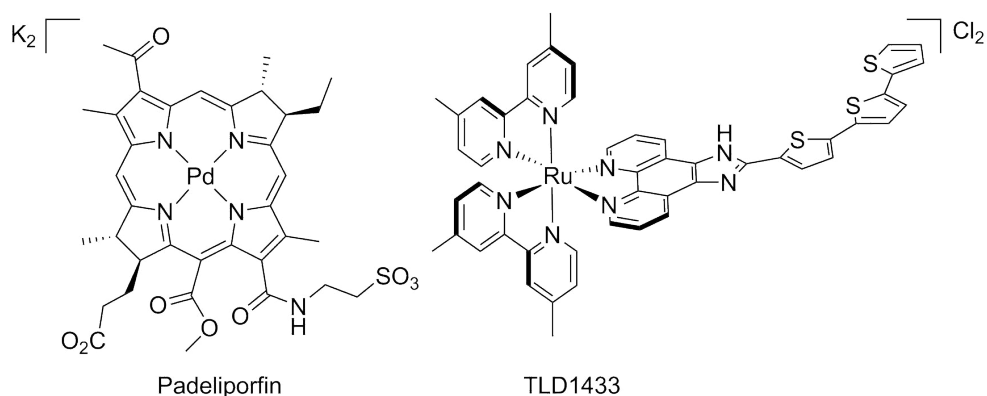


Figure 1.8 Chemical structure of Padeliporfin (WST11) and TLD1433.

1.5 Photoactivated chemotherapy

1.5.1 Introduction photoactivated chemotherapy

Many sections of tumors are poorly oxygenated (hypoxic), while PDT type 2 relies on the presence and activation of dioxygen.⁵³ PhotoActivated ChemoTherapy (PACT) is an alternative phototherapy that takes advantage of local photochemical activation of a prodrug to acquire high specificity. The concept of PACT relies on a (non-toxic) prodrug that upon light activation undergoes photolysis or photosubstitution.²² Whereas the prodrug has no biological activity, at least one of its photoproducts is a biologically active molecule. Typically in anticancer treatment this is a prodrug that after light activation becomes cytotoxic.

One of the key research areas in the field of PACT focuses on ruthenium polypyridyl complexes. Upon irradiation, this type of metal complexes first is excited to a singlet metal-to-ligand charge transfer (¹MLCT) state, from which very fast (femtosecond time scale) intersystem crossing populates the corresponding triplet MLCT state (³MLCT). From this long-lived ³MLCT state the system can then either relax to the ground state by emission of a photon (phosphorescence) or thermally populate triplet metal-centered states (³MC) if these states are low enough in energy. ³MC states have a dissociative character because an antibonding $d\sigma^*$ orbital of the metal center is occupied by one electron.⁵⁴ ³MC population hence leads to increased lability of at least one of the ligands that subsequently may be photosubstituted. In other words, such light-activatable ruthenium complexes can undergo ligand photosubstitution.⁵⁵⁻⁵⁷ Ligands that can be photosubstituted are

typically bound to a ruthenium(II) center *via* nitrile, amine, pyridine, sulfoxide, or thioether functional groups.⁵⁸⁻⁶⁰ In the following sections several examples of ruthenium complexes will be described that have been reported as light-activatable anticancer drugs *in vitro*.

1.5.2 PACT based on *cis* Ru complexes

The complex $[\text{Ru}(\text{bpy})_2(\text{dmbpy})]\text{Cl}_2$ (bpy = 2,2'-bipyridine, dmbpy = 6,6'-dimethyl-2,2'-bipyridine) developed by Glazer et al. was the first reported ruthenium-based PACT complex (Figure 1.9).⁶¹ Upon visible light irradiation ($\lambda_{\text{irr}} > 450 \text{ nm}$) $[\text{Ru}(\text{bpy})_2(\text{dmbpy})]\text{Cl}_2$ releases its sterically demanding dmbpy ligand. *In vitro* this light activation increases cytotoxicity of the compound from an EC_{50} of over 150 μM in the dark to an EC_{50} of 1.1 μM after light activation, which represents a 136-fold increase in cytotoxicity. Similarly, $[\text{Ru}(\text{biq})(\text{phen})_2]\text{Cl}_2$ (biq = 2,2'-biquinoline, phen = 1,10-phenanthroline), displayed in Figure 1.9, was also shown by Glazer et al. to be a potential PACT compound. Photoejection of the biq ligand *in vitro* is accompanied by lowering of the EC_{50} from 52.5 μM in the dark to 1.2 μM after light activation with white light ($\lambda_{\text{irr}} > 400 \text{ nm}$).⁶² Glazer attributed the enhanced toxicity of the compound to the two available *cis* coordination positions that become available upon photosubstitution of biq by two labile aqua ligands. Binding of the light activated ruthenium complex to DNA similar to cisplatin-DNA binding was suggested as a possible cause for light-enhanced cytotoxicity.

The cyclometallated compound RDC11 – described in section 1.2 – also exhibited a 14-fold increase in cytotoxicity after red-light activation ($\lambda_{\text{irr}} = 690 \text{ nm}$), from an EC_{50} in the dark of 1.0 μM to an EC_{50} after light irradiation of 70 nM.⁶³ The Turro lab has also developed PACT compounds such as $[\text{Ru}(\text{bpy})(\text{dppn})(\text{CH}_3\text{CN})_2](\text{PF}_6)_2$ (dppn = benzo[*i*]dipyrido[3,2-*a*;2',3'-*c*]phenazine, Figure 1.9) that photosubstitutes both CH_3CN ligands in H_2O . *In vitro* on HeLa cells the toxicity of the complex increases from an EC_{50} of 331 μM in the dark to an EC_{50} of 0.47 μM after blue-light ($\lambda_{\text{irr}} = 466 \text{ nm}$) activation. According to Turro the enhanced cytotoxicity is induced for this compound both by the generation of $^1\text{O}_2$ (PDT type 2) and by photosubstitution of the CH_3CN ligands (PACT). A double mechanism of action is always possible. The examples discussed in this section are all ruthenium(II) compounds with bidentate ligands similar to bpy. Photosubstitution of one of the bpy ligands offers available coordination sites in the *cis* configuration that are able to bind to DNA in a similar mode as cisplatin. These complexes also have in

common that from the two photoproducts that are produced by photosubstitution reactions, i.e., the ruthenium bis-aqua complex and the free photosubstituted ligand, the metal fragment is usually believed to act as the active species, i.e., the metal-based drug is caged by an organic ligand that can be photosubstituted.

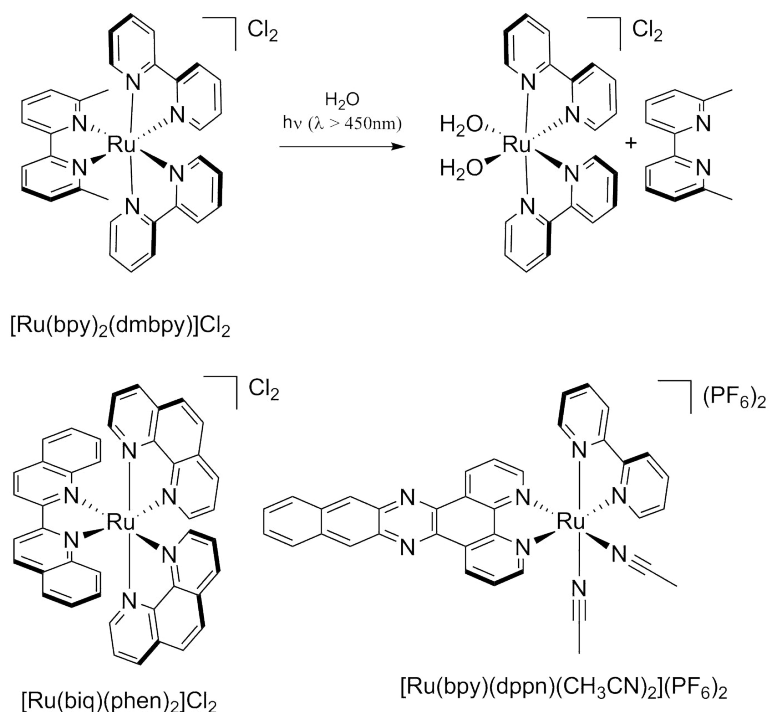
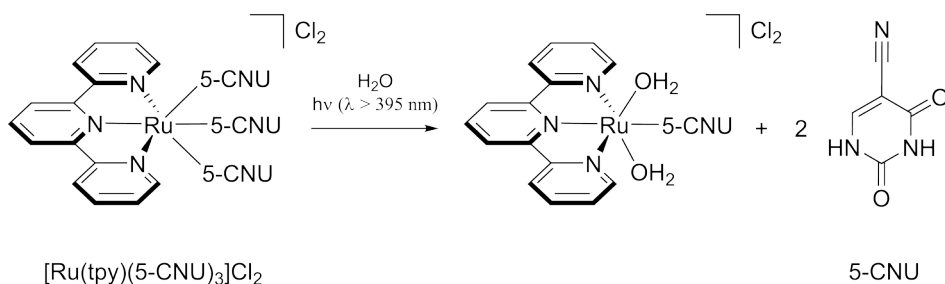


Figure 1.9 Chemical structures of $[\text{Ru}(\text{bpy})_2(\text{dmbpy})]\text{Cl}_2$, $[\text{Ru}(\text{biq})(\text{phen})_2]\text{Cl}_2$, and $[\text{Ru}(\text{bpy})(\text{dppn})(\text{CH}_3\text{CN})_2](\text{PF}_6)_2$, and photosubstitution reaction with $[\text{Ru}(\text{bpy})_2(\text{dmbpy})]\text{Cl}_2$.

1.5.3 Photocaging

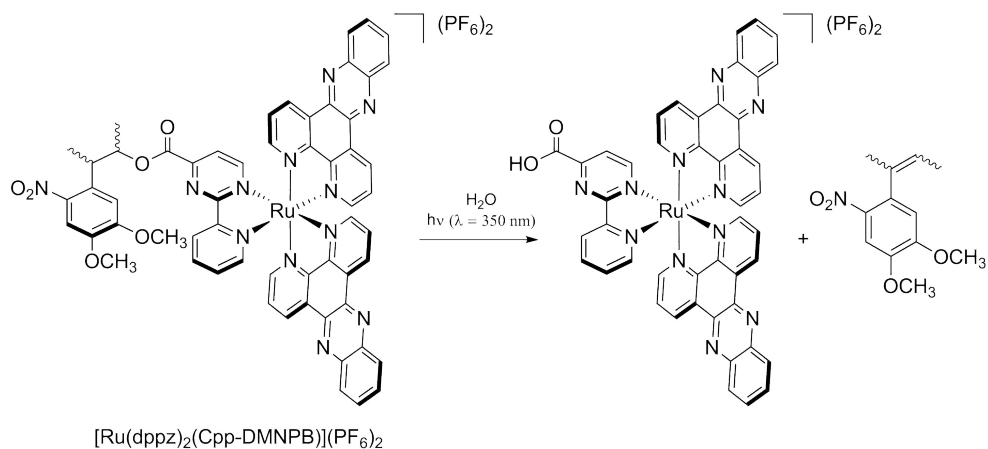
The concept of PACT relies on light activation of a prodrug resulting in photosubstitution. In case of a mononuclear complex for example photosubstitution will lead to a metal-based and an organic fragment. In previous sections a PACT strategy was described wherein the metal fragment acts as the cytotoxic drug. An alternative PACT approach is a strategy wherein the photosubstituted organic part acts as the drug and the metal fragment as the caging agent. In light of this strategy Turro has coordinated 5-cyanouracil (5-CNU), the nitrile analogue of the clinically approved anticancer drug fluorouracil, to $[\text{Ru}(\text{bpy})_2(\text{OH}_2)_2](\text{PF}_6)_2$. Binding of $[\text{Ru}(\text{bpy})_2(5\text{-CNU})_2](\text{PF}_6)_2$ to DNA in gel

electrophoresis experiments could be photocontrolled ($\lambda_{\text{irr}} > 395 \text{ nm}$), but no phototoxicity data was reported.⁶⁴ In another example reported by Turro $[\text{Ru}(\text{tpy})(\text{OH}_2)_3]^{2+}$ was utilized as cage, to form $[\text{Ru}(\text{tpy})(5\text{-CNU})_3]\text{Cl}_2$.⁶⁵ Activation using visible light ($\lambda_{\text{irr}} > 395 \text{ nm}$) in water showed the formation of the bis-aqua species $[\text{Ru}(\text{tpy})(5\text{-CNU})(\text{OH}_2)_2]\text{Cl}_2$ *via* the mono-aqua species $[\text{Ru}(\text{tpy})(5\text{-CNU})_2(\text{OH}_2)]\text{Cl}_2$ (Scheme 1.1). When HeLa cells were treated with $[\text{Ru}(\text{tpy})(5\text{-CNU})_3]\text{Cl}_2$ a qualitative fluorescence (SYTOX) assay confirmed that cells were dying to a higher degree upon light activation ($\lambda_{\text{irr}} > 400 \text{ nm}$), compared to a dark control. When in a control experiment cells were treated with 1 molar equivalent of free 5-CNU, the same cytotoxic activity was observed as with the photoactivated compound $[\text{Ru}(\text{tpy})(5\text{-CNU})_3]\text{Cl}_2$. Caging of existing drugs to improve selectivity could be a viable path to the development for new therapies, as pharmacological data on the existing drugs is present. Apart from chemotherapy this could also include other medication where selectivity and dosage are crucial such as antibiotics.



Scheme 1.1 Photochemical reaction of the PACT compound $[\text{Ru}(\text{tpy})(5\text{-CNU})_3]\text{Cl}_2$.

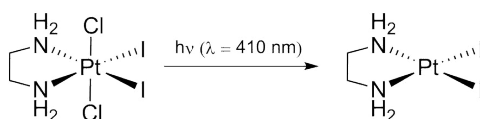
Photocaging is not limited to breaking coordination bonds between a metal and a ligand, but may also occur within one of the ligands. For example, Gasser has developed the compound $[\text{Ru}(\text{dppz})_2(\text{Cpp-DMNPB})](\text{PF}_6)_2$ (dppz = dipyrido[3,2-a:2',3'-c]phenazine, Cpp = 2-(2-pyridyl)pyrimidine-4-carboxylate, DMNPB = 2-(4,5-dimethoxy-2-nitrophenyl)butene, Scheme 1.2) in which the DMNPB moiety can be cleaved off upon UV irradiation ($\lambda_{\text{irr}} = 350 \text{ nm}$), to result in the cytotoxic carboxylate ruthenium complex and a non-toxic organic fragment.⁶⁶ *In vitro* this reaction results in a 5-fold enhancement of cytotoxicity ($\text{EC}_{50,\text{dark}} > 100 \mu\text{M}$, $\text{EC}_{50,\text{light}} = 17 \mu\text{M}$). This enhancement in cytotoxicity was attributed to the released metal fragment, as cytotoxicity studies of only the metal fragment resulted in an $\text{EC}_{50,\text{dark}}$ of $16 \mu\text{M}$.



Scheme 1.2 Photochemical reaction of the PACT compound [Ru(dppz)₂(Cpp-DMNPB)](PF₆)₂.

1.5.4 PACT based on platinum complexes

PACT is not limited to ruthenium complexes. In fact, many transition metal complexes based on rhodium, iridium, or platinum have been developed as PACT agents.⁶⁷ For platinum(IV) complexes photoreduction to a platinum(II) species may occur upon irradiation with UV light or high-energy visible light. Apart from photolysis, this photoreaction typically results in a change from an octahedral platinum(IV) complex to a square-planar platinum(II) complex. This concept was first reported by Nagle.⁶⁸ Photoactivation of *trans,cis*-[Pt(Cl₂)(I₂)(en)] ($\lambda_{\text{irr}} = 410$ nm, en = 1,2,-diaminoethane) resulted in [Pt(I₂)(en)] (Scheme 1.3). However, when SK-MEL-24 (melanoma cancer) or TCCSUP (bladder cancer) cells were treated with the platinum(IV) complex no significant enhanced cytotoxicity was observed when *trans,cis*-Pt(Cl₂I₂(en)] was light activated *in vitro* compared to the dark control.



Scheme 1.3 Photochemical reaction of the PACT compound *trans,cis*-[Pt(Cl₂)(I₂)(en)].

Coordination of azides to a platinum(IV) metal center enables the photoactivation of platinum(IV) complexes. Irradiation of these Pt^{IV}-azide compounds may lead to reduction to a Pt^{II} complex and the release of nitrogen.^{69, 70} This concept was introduced by Sadler with *cis,trans*-[Pt^{IV}(en)(N₃)₂(OH)₂] shown in Figure 1.10.⁷¹

Treatment of 5637-bladder cancer cells with *cis,trans*-[Pt^{IV}(en)(N₃)₂(OH)₂] resulted in a 7-fold higher cytotoxicity (EC_{50, dark} = 357 μM, EC_{50, light} = 49 μM) and a more than 3-fold increase for the 5637-cisplatin resistant cell line (EC_{50, dark} > 200 μM, EC_{50, light} = 67 μM) after activation at λ_{irr} = 366 nm.⁷² In this assay the cytotoxicity of the [Pt^{II}(en)Cl₂] was found to be much lower (EC₅₀ = 2.3-14 μM) for both cell lines without change in activity after light activation. Further development by Sadler of this type of complexes resulted in *trans,trans,trans*-[Pt^{IV}(N₃)₂(OH)₂(NH₃)(py)] shown in Figure 1.10,⁷³ that after photoactivation (λ_{irr} = 365 nm) showed EC₅₀ values of 1.9 μM compared to 244 μM in the dark on A2780 cancer cells, which corresponds to a 129-fold increase in cytotoxicity. This work has recently led to the development of *trans,trans,trans*-[Pt^{IV}(N₃)₂(OH)₂(py)₂] (Figure 1.10) that after photoactivation (λ_{irr} = 365 nm) showed an EC₅₀ value of 1.4 μM compared to > 212 μM in the dark on A2780 cancer cell lines.⁷⁴ Although these platinum(IV) complexes have poor absorbance in the visible spectrum, activation with blue light (λ_{irr} = 420-450 nm) was also possible in cell tests.

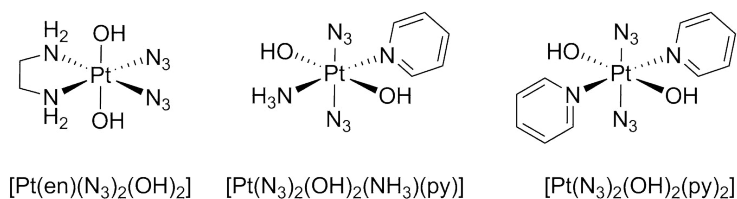


Figure 1.10 Chemical structures of *cis,trans*-[Pt^{IV}(en)(N₃)₂(OH)₂], *trans,trans,trans*-[Pt^{IV}(N₃)₂(OH)₂(NH₃)(py)], and *trans,trans,trans*-[Pt^{IV}(N₃)₂(OH)₂(py)₂].

1.6 Conclusion

Ruthenium complexes have gained increasing attention as metal-based anticancer drug candidates, especially in the field of PACT. However, to date ruthenium complexes have never been more than drug candidates, as only four ruthenium complexes have entered clinical trials. NAMI-A and KP1019 were not further investigated after Phase II clinical trials, NKP-1339 successfully completed Phase I trials, and initiation of Phase III clinical trials for TLD1433 is pending. These investigations are to a certain extent eclipsed by the number of platinum-based compounds (at least 24) that have entered clinical trials which resulted in seven platinum-based chemotherapeutic treatments approved for clinical use.¹⁹ None of these approved platinum drugs involve light activation or a PACT strategy. To be

noted, pharmacological and chemical properties are not the only drivers when it comes to successful development of a drug.

The MoA of platinum(IV) compounds commonly relies on the reduction of a platinum complex to a (known) cisplatin analogue. Functionalization with ligands containing aromatic functional groups instead of the chloride or ammonia ligands or extension of aromaticity can increase the absorbance properties in the visible (and phototherapy relevant) domain, but would strongly alter the biochemical properties, potentially preventing a similar MoA as cisplatin.⁷⁵ In addition, it is difficult to reach the red region of the spectrum using this strategy. The limited light absorption properties of platinum compounds in the phototherapeutic window strongly hampers development of this type of platinum(IV) compounds as PACT agents. Ruthenium(II) anticancer complexes on the other hand almost exclusively contain aromatic arene or polypyridyl ligands. Absorbance in the far red of the spectrum is feasible with these kind of ruthenium complexes, and as powerful lasers have become cheap, low absorbance is in principle sufficient to obtain photoactivation. Overall, the potential of ruthenium complexes as photosensitizers in PDT, and their robust photochemistry in PACT, make ruthenium polypyridyl complexes more promising compared to the known light-activatable platinum systems. Furthermore, development of ruthenium complexes is not constrained by a powerful paradigm like the DNA targeting MoA of cisplatin is for research into new platinum based chemotherapy.

1.7 Aim and outline of this thesis

The aim of the research described in this thesis is to develop transition metal-based anticancer drugs. In Chapter 2, the potential of thiols and thioethers as photosubstitutionally labile ligands using $[\text{Ru}(\text{tpy})(\text{bpy})(\text{OH}_2)]^{2+}$ as model complex are compared. Thiols have been often overlooked as photosubstitutable ligands, although they are omnipresent in biotechnology.⁷⁶ This omission is all the more remarkable as GSH is abundant *in vitro* and *in vivo* and known to interact with anticancer metallodrugs. It is shown in Chapter 2 that once coordinated to ruthenium, thiols are very sensitive to oxidation, leading to dissociation even in the dark. This specific reactivity makes them unsuitable as protective group for metal-based PACT compounds. In Chapter 3, the use of the poorly toxic $[\text{Ru}(\text{tpy})(\text{bpy})(\text{OH}_2)]^{2+}$ fragment to cage an organic thioether-containing anticancer

compound is described. This cytotoxic thioether ligand is a microtubule-targeting rigidin moiety that can coordinate to ruthenium(II) and be released upon light irradiation. Upon green-light irradiation the rigidin drug is indeed shown to be released, which results *in vitro* in a 20-fold increase in cytotoxicity compared to the dark control. Further studies are also included that demonstrate that the photoreleased rigidin interferes with the polymerization of microtubule.

In Chapter 4, two ruthenium complexes with photosubstitutionally labile sulfoxide or thioether ligands in *trans* positions are presented that are based on the tetrapyrrolyl ligand H₂biqbpy (6,6'-bis[N-(isoquinolyl)-1-amino]-2,2'-bipyridine). This tetrapyrrolyl ligand was developed for iron(II)-based spin-crossover materials, but it is new in the context of ruthenium photochemistry. Upon coordination to a metal center in an octahedral geometry it leaves two *trans* coordination positions for the binding of (non-toxic) sulfur-based ligands. Upon green light irradiation a 20-fold increase in cytotoxicity is demonstrated *in vitro* compared to the dark control. Green light activation of these compounds induces cell death *via* apoptosis, unlike PDT compounds that commonly induce necrosis. We also demonstrate that light-induced cell death is obtained even with insignificant ¹O₂ generation quantum yields. In Chapter 5, the synthesis of a series of three new ruthenium polypyridyl complexes based on the H₂biqbpy ligand and the analogous H₂bapbpy (6,6'-bis[N-(pyridyl)-1-amino]-2,2'-bipyridine) is described. The interaction of these complexes with a 12-mer oligonucleotide is demonstrated to be controlled by light. For the first time, the ruthenium-oligonucleotide adducts formed under light irradiation are analyzed by high-resolution mass spectrometry and gel electrophoresis.

Investigations regarding tetrapyrrolyl ligands, already discussed in Chapter 4 and 5, are extended in Chapters 6, 7, and 8, to 'regular', i.e. non light-activatable, chemotherapeutic metallodrugs based on column 10 transition metals. In Chapter 6, the synthesis and anticancer properties of a series of three new complexes based on the H₂bapbpy ligand coordinated to nickel(II), palladium(II), and platinum(II) are presented. The *in vitro* cytotoxic activity of these complexes ranges from EC₅₀ values in a mild micromolar range for the nickel complex, to sub-micromolar concentrations for the platinum analogue, and even spectacular nanomolar EC₅₀ values for the palladium complex. We further show that the activity of the palladium complex is based on the generation of ROS. On the other hand, the

activity of the structurally similar platinum complex seems to depend on DNA interaction. A physicochemical study of the $[\text{Pd}(\text{H}_2\text{bapbpy})]^{2+}$ and $[\text{Pt}(\text{H}_2\text{bapbpy})]^{2+}$ complexes is presented in Chapter 7. In particular, deprotonation of the H_2bapbpy ligand leads to a dramatic increase of the absorbance of these complexes in the visible domain; TD-DFT calculations confirm that Intra-Ligand-Charge-Transfer excited states responsible for the absorption changes are far less present in $[\text{Pd}(\text{H}_2\text{bapbpy})]^{2+}$ than in $[\text{Pd}(\text{bapbpy})]$. Crystal structures of each protonation state of the palladium(II) complex ($[\text{Pd}(\text{H}_2\text{bapbpy})]^{2+}$, $[\text{Pd}(\text{Hbapbpy})]^+$, and $[\text{Pd}(\text{bapbpy})]$) were obtained and described. In Chapter 8, the synthesis and characterization of $[\text{Pd}(\text{Hbbpya})]^{2+}$ and $[\text{Pt}(\text{Hbbpya})]^{2+}$ are described ($\text{Hbbpya} = \text{N,N-bis}(2,2'\text{-bipyrid-6-yl})\text{amine}$). Compared to H_2bapbpy , the Hbbpya ligand is much more coordinated in a single plane to the metal center, and contains not two, but only one secondary amine. This difference causes marked changes in cytotoxicity, pK_a , and uptake of $[\text{Pd}(\text{Hbbpya})]^{2+}$ and $[\text{Pt}(\text{Hbbpya})]^{2+}$ compared to the H_2bapbpy analogues. In Chapter 9, a summary, general conclusion, and outlook are presented.

1.8 References

1. M. Peyrone, *Liebigs Ann.*, 1844, **51**, 1-29.
2. G. B. Kauffman, R. Pentimalli, S. Doldi and M. D. Hall, *Platin. Met. Rev.*, 2010, **54**, 250-256.
3. A. Werner, *Z. Anorg. Allg. Chem.*, 1893, **3**, 267-330.
4. Nobelprize.org, *Nobel Lectures, Chemistry*, 1913.
5. B. Rosenberg, L. Van Camp and T. Krigas, *Nature*, 1965, **205**, 698-699.
6. J. H. Burchenal, K. Kalaher, K. Dew, L. Lokys and G. Gale, *Biochimie*, 1978, **60**, 961-965.
7. B. Rosenberg, L. Vancamp, J. E. Trosko and V. H. Mansour, *Nature*, 1969, **222**, 385-386.
8. M. J. Cleare and J. D. Hoeschele, *Bioinorg. Chem.*, 1973, **2**, 187-210.
9. B. Rosenberg, L. Van Camp, E. B. Grimley and A. J. Thomson, *J. Biol. Chem.*, 1967, **242**, 1347-1352.
10. L. Kelland, *Nat. Rev. Cancer*, 2007, **7**, 573-584.
11. S. Ishida, J. Lee, D. J. Thiele and I. Herskowitz, *Proc. Natl. Acad. Sci. USA*, 2002, **99**, 14298-14302.
12. M. S. Davies, S. J. Berners-Price and T. W. Hambley, *Inorg. Chem.*, 2000, **39**, 5603-5613.
13. S. E. Sherman and S. J. Lippard, *Chem. Rev.*, 1987, **87**, 1153-1181.
14. U.-M. Ohndorf, M. A. Rould, Q. He, C. O. Pabo and S. J. Lippard, *Nature*, 1999, **399**, 708-712.
15. D. B. Zamble, D. Mu, J. T. Reardon, A. Sancar and S. J. Lippard, *Biochemistry*, 1996, **35**, 10004-10013.
16. A. Casini and J. Reedijk, *Chem. Sci.*, 2012, **3**, 3135-3144.
17. E. H. Einhorn, *Clin. Canc. Res.*, 1997, **3**, 2630-2632.
18. A.-M. Florea and D. Büsselberg, *Cancers*, 2011, **3**, 1351.
19. N. J. Wheate, S. Walker, G. E. Craig and R. Oun, *Dalton Trans.*, 2010, **39**, 8113-8127.
20. G. Sava and A. Bergamo, in *Platinum and Other Heavy Metal Compounds in Cancer Chemotherapy: Molecular Mechanisms and Clinical Applications*, eds. A. Bonetti, R. Leone, F. M. Muggia and S. B. Howell, Humana Press, Totowa, NJ, 2009, pp. 57-66.
21. M. A. Jakupec, M. Galanski, V. B. Arion, C. G. Hartinger and B. K. Keppler, *Dalton Trans.*, 2008, **2**, 183-194.
22. N. J. Farrer, L. Salassa and P. J. Sadler, *Dalton Trans.*, 2009, **48**, 10690-10701.
23. G. Sava, S. Pacor, G. Mestroni and E. Alessio, *Clin. Exp. Metastasis*, 1992, **10**, 273-280.
24. B. K. Keppler, M. Henn, U. M. Juhl, M. R. Berger, R. Niebl and F. E. Wagner, in *Ruthenium and Other Non-Platinum Metal Complexes in Cancer Chemotherapy*, eds. E. Baulieu, D. T. Forman, M. Ingelman-Sundberg, L. Jaenicke, J. A. Kellen, Y. Nagai, G. F. Springer, L. Träger, L. Will-Shahab and J. L. Wittliff, Springer Berlin Heidelberg, Berlin, Heidelberg, 1989, pp. 41-69.
25. S. Leijen, S. A. Burgers, P. Baas, D. Pluim, M. Tibben, E. van Werkhoven, E. Alessio, G. Sava, J. H. Beijnen and J. H. M. Schellens, *Invest. New Drugs*, 2015, **33**, 201-214.
26. C. G. Hartinger, M. A. Jakupec, S. Zorbas-Seifried, M. Groessl, A. Egger, W. Berger, H. Zorbas, P. J. Dyson and B. K. Keppler, *Chem. Biodiversity*, 2008, **5**, 2140-2155.
27. F. Lentz, A. Drescher, A. Lindauer, M. Henke, R. A. Hilger, C. G. Hartinger, M. E. Scheulen, C. Dittrich, B. K. Keppler, U. Jaehde and i. c. w. C. E. S. f. A. D. Research-EWIV, *Anti Canc. Drugs*, 2009, **20**, 97-103.
28. R. Trondl, P. Heffeter, C. R. Kowol, M. A. Jakupec, W. Berger and B. K. Keppler, *Chem. Sci.*, 2014, **5**, 2925-2932.
29. E. Alessio, *Eur. J. Inorg. Chem.*, 2017, **2017**, 1549-1560.
30. A. Weiss, R. H. Berndsen, M. Dubois, C. Muller, R. Schibli, A. W. Griffioen, P. J. Dyson and P. Nowak-Sliwinska, *Chem. Sci.*, 2014, **5**, 4742-4748.
31. R. E. Morris, R. E. Aird, P. del Socorro Murdoch, H. Chen, J. Cummings, N. D. Hughes, S. Parsons, A. Parkin, G. Boyd, D. I. Jodrell and P. J. Sadler, *J. Med. Chem.*, 2001, **44**, 3616-3621.
32. R. E. Aird, J. Cummings, A. A. Ritchie, M. Muir, R. E. Morris, H. Chen, P. J. Sadler and D. I. Jodrell, *Br. J. Cancer*, 2002, **86**, 1652-1657.
33. J. J. Concepcion, J. W. Jurs, M. K. Brennaman, P. G. Hoertz, A. O. T. Patrocínio, N. Y. M. Iha, J. L. Templeton and T. J. Meyer, *Acc. Chem. Res.*, 2009, **42**, 1954-1965.
34. S. Campagna, F. Puntoriero, F. Nastasi, G. Bergamini and V. Balzani, in *Photochemistry and Photophysics of Coordination Compounds I*, eds. V. Balzani and S. Campagna, 2007, vol. 280, pp. 117-214.
35. O. Novakova, J. Kasparkova, O. Vrana, P. M. van Vliet, J. Reedijk and V. Brabec, *Biochemistry*, 1995, **34**, 12369-12378.

36. X. Meng, M. L. Leyva, M. Jenny, I. Gross, S. Benosman, B. Fricker, S. Harlepp, P. Hébraud, A. Boos, P. Wlosik, P. Bischoff, C. Sirlin, M. Pfeffer, J.-P. Loeffler and C. Gaiddon, *Cancer Res.*, 2009, **69**, 5458-5466.
37. V. Pichler, J. Mayr, P. Heffeter, O. Domotor, E. A. Enyedy, G. Hermann, D. Groza, G. Kollensperger, M. Galanksi, W. Berger, B. K. Keppler and C. R. Kowol, *Chem. Commun.*, 2013, **49**, 2249-2251.
38. F. Kratz, *J. Controlled Release*, 2008, **132**, 171-183.
39. S. G. Awuah, Y.-R. Zheng, P. M. Bruno, M. T. Hemann and S. J. Lippard, *J. Am. Chem. Soc.*, 2015, **137**, 14854-14857.
40. U. Jungwirth, C. R. Kowol, B. K. Keppler, C. G. Hartinger, W. Berger and P. Heffeter, *Antioxid. Redox Signaling*, 2011, **15**, 1085-1127.
41. I. Romero-Canelón and P. J. Sadler, *Inorg. Chem.*, 2013, **52**, 12276-12291.
42. Y. Kawai, T. Nakao, N. Kunimura, Y. Kohda and M. Gemba, *J. Pharmacol. Sci.*, 2006, **100**, 65-72.
43. L. P. Rybak, C. A. Whitworth, D. Mukherjea and V. Ramkumar, *Hear. Res.*, 2007, **226**, 157-167.
44. A. Gupte and R. J. Mumper, *Canc. Treat. Rev.*, 2009, **35**, 32-46.
45. C. Gorrini, I. S. Harris and T. W. Mak, *Nat. Rev. Drug Discov.*, 2013, **12**, 931-947.
46. J. J. Soldevila-Barreda, I. Romero-Canelón, A. Habtemariam and P. J. Sadler, *Nat. Comm.*, 2015, **6**, 6582.
47. Z. Liu, I. Romero-Canelón, B. Qamar, J. M. Hearn, A. Habtemariam, N. P. E. Barry, A. M. Pizarro, G. J. Clarkson and P. J. Sadler, *Angew. Chem., Int. Ed.*, 2014, **53**, 3941-3946.
48. A. Vogel and V. Venugopalan, *Chem. Rev.*, 2003, **103**, 577-644.
49. D. E. Brash, J. A. Rudolph, J. A. Simon, A. Lin, G. J. McKenna, H. P. Baden, A. J. Halperin and J. Pontén, *Proc. Natl. Acad. Sci. USA*, 1991, **88**, 10124-10128.
50. A.-R. Azzouzi, E. Barret, C. M. Moore, A. Villers, C. Allen, A. Scherz, G. Muir, M. de Wildt, N. J. Barber, S. Lebdai and M. Emberton, *BJU Int.*, 2013, **112**, 766-774.
51. G. Shi, S. Monro, R. Hennigar, J. Colpitts, J. Fong, K. Kasimova, H. Yin, R. DeCoste, C. Spencer, L. Chamberlain, A. Mandel, L. Lilge and S. A. McFarland, *Coord. Chem. Rev.*, 2015, **282-283**, 127-138.
52. Y. Arenas, S. Monro, G. Shi, A. Mandel, S. McFarland and L. Lilge, *Photodiagnosis Photodyn. Ther.*, 2013, **10**, 615-625.
53. P. Vaupel, F. Kallinowski and P. Okunieff, *Cancer Res.*, 1989, **49**, 6449-6465.
54. A. J. Göttle, F. Alary, M. Boggio-Pasqua, I. M. Dixon, J.-L. Heully, A. Bahreman, S. H. C. Askes and S. Bonnet, *Inorg. Chem.*, 2016, **55**, 4448-4456.
55. P. C. Ford, *Coord. Chem. Rev.*, 1982, **44**, 61-82.
56. S. Campagna, F. Puntoriero, F. Nastasi, G. Bergamini and V. Balzani, in *Photochemistry and Photophysics of Coordination Compounds I*, eds. V. Balzani and S. Campagna, Springer Berlin Heidelberg, Berlin, Heidelberg, 2007, pp. 117-214.
57. A. C. Laemmel, J. P. Collin and J. P. Sauvage, *Eur. J. Inorg. Chem.*, 1999, **1999**, 383-386.
58. A. Juris, V. Balzani, F. Barigelletti, S. Campagna, P. Belser and A. von Zelewsky, *Coord. Chem. Rev.*, 1988, **84**, 85-277.
59. M. Frascioni, Z. Liu, J. Lei, Y. Wu, E. Strelakova, D. Malin, M. W. Ambrogio, X. Chen, Y. Y. Botros, V. L. Cryns, J.-P. Sauvage and J. F. Stoddart, *J. Am. Chem. Soc.*, 2013, **135**, 11603-11613.
60. C. Jean-Paul and S. Jean-Pierre, *Chem. Lett.*, 2005, **34**, 742-747.
61. B. S. Howerton, D. K. Heidary and E. C. Glazer, *J. Am. Chem. Soc.*, 2012, **134**, 8324-8327.
62. E. Wachter, D. K. Heidary, B. S. Howerton, S. Parkin and E. C. Glazer, *Chem. Commun.*, 2012, **48**, 9649-9651.
63. A. M. Palmer, B. Peña, R. B. Sears, O. Chen, M. El Ojaimi, R. P. Thummel, K. R. Dunbar and C. Turro, *Phil. Trans. R. Soc. A*, 2013, **371**, 20120135.
64. R. N. Garner, J. C. Gallucci, K. R. Dunbar and C. Turro, *Inorg. Chem.*, 2011, **50**, 9213-9215.
65. M. A. Sgambellone, A. David, R. N. Garner, K. R. Dunbar and C. Turro, *J. Am. Chem. Soc.*, 2013, **135**, 11274-11282.
66. T. Joshi, V. Pierroz, C. Mari, L. Gemperle, S. Ferrari and G. Gasser, *Angew. Chem., Int. Ed.*, 2014, **53**, 2960-2963.
67. K. L. Ciesieski and K. J. Franz, *Angew. Chem.*, 2011, **50**, 814-824.
68. N. Kratochwil, P. Bednarski, H. Mrozek, A. Vogler and J. Nagle, *Anti-cancer Drug Des.*, 1996, **11**, 155-171.
69. A. Vogler and J. Hlavatsch, *Angew. Chem.*, 1983, **95**, 153-153.
70. A. Vogler, A. Kern, B. Füsseder and J. Huttermann, *Z. Naturforsch. B Chem. Sci.*, 1978, **33**, 1352-1356.

71. P. Müller, B. Schröder, J. A. Parkinson, N. A. Kratochwil, R. A. Coxall, A. Parkin, S. Parsons and P. J. Sadler, *Angew. Chem., Int. Ed.*, 2003, **42**, 335-339.
72. P. J. Bednarski, R. Grünert, M. Zielzki, A. Wellner, F. S. Mackay and P. J. Sadler, *Chem. Biol.*, 2006, **13**, 61-67.
73. F. S. Mackay, J. A. Woods, P. Heringová, J. Kašpárková, A. M. Pizarro, S. A. Moggach, S. Parsons, V. Brabec and P. J. Sadler, *Proc. Natl. Acad. Sci. USA*, 2007, **104**, 20743-20748.
74. N. J. Farrer, J. A. Woods, L. Salassa, Y. Zhao, K. S. Robinson, G. Clarkson, F. S. Mackay and P. J. Sadler, *Angew. Chem., Int. Ed.*, 2010, **49**, 8905-8908.
75. S. Bonnet, *Comments Inorg. Chem.*, 2015, **35**, 179-213.
76. H. S. Jung, X. Chen, J. S. Kim and J. Yoon, *Chem. Soc. Rev.*, 2013, **42**, 6019-6031.

CHAPTER 2

Preparation, stability, and photoreactivity of
thiolato ruthenium polypyridyl complexes:
can cysteine derivatives protect
ruthenium-based anticancer complexes?

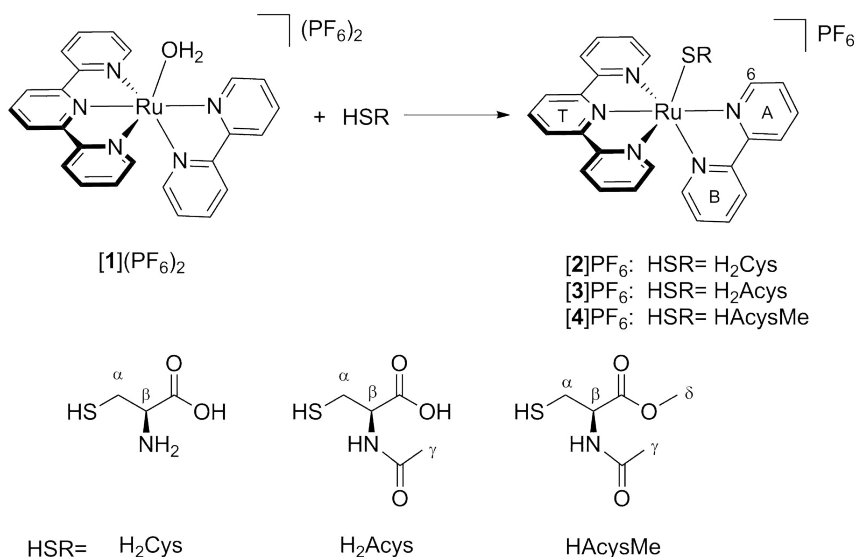
This chapter was published as an Original Research paper: Vincent H.S. van Rixel, Anja Busemann, Adrien J. Göttle, Sylvestre Bonnet, *J. Inorg. Biochem.* **2015**, 150, 174-181.

2.1 Introduction

The success of cisplatin and its second-generation derivatives (carboplatin and oxaliplatin) have inspired chemists to develop new metal-based anticancer agents.^{1, 2} Although ruthenium-based frontrunners, NAMI-A and KP1019, have both failed to end up in the clinics, ruthenium-based compounds are still subject of intense research.³⁻⁵ A specific research area is the development of light-activatable ruthenium polypyridyl complexes. These complexes have been proposed as prodrugs that, upon light irradiation, can be locally activated to kill tumor cells resulting in fewer side effects for patients.⁶⁻¹⁰ Upon photochemical generation of a metal-to-ligand charge transfer (MLCT) excited state, such light-activatable complexes are capable of substituting one or two ligand(s) by water molecule(s). Ligands that can be photosubstituted are typically bound to ruthenium(II) *via* nitrile, amine, pyridine, or thioether functional groups, and up to now thiols have not been thoroughly investigated as photocleavable protecting groups. Naturally-occurring thiols such as glutathione (GSH) are known to interact with many anticancer metallodrugs in cells. This interaction can be responsible for both detoxification and enhanced cytotoxicity.¹¹⁻¹³ Therefore, the interaction of GSH, and of its simpler version cysteine, has been investigated with anticancer ruthenium-based drug candidates by a few groups.^{6, 14-17} For instance, the Sadler group has found evidence for the oxidation of ruthenium-thiol arene compounds, wherein the metal-coordinated thiol ligand oxidizes with O₂ to form sulfenato and sulfinato complexes.^{18, 19}

Our group started investigating the use of thioether-based protecting ligands for light-activatable anticancer ruthenium polypyridyl complexes.^{20, 21} The non-basic properties and soft nature of a thioether ligand allows for the formation of Ru-S coordination bonds that are much stronger in water and in the dark than, for example, Ru-Cl bonds. Thus, the aqua complex [Ru(tpy)(bpy)(OH₂)]²⁺ ([1]²⁺) can be protected by coordination of N-acetyl-L-methionine (HAMet) to ruthenium, while deprotection is obtained using blue light irradiation.^{20, 21} Thioethers and methionine residues, however, are not as ubiquitous in biotechnologies as thiols and cysteine residues, and binding of ruthenium complexes to targeting peptides and proteins *via* coordination to thiols would open many doors in targeted photochemotherapy, provided that the Ru-S bond with thiol ligands is strong enough in the dark, and photocleavable. The photochemistry of thiolato-ruthenium complexes remains

largely unknown, however. In this chapter, we report hence the coordination studies between $[1]^{2+}$ and the three thiol ligands L-cysteine (H_2Cys), N-acetyl-L-cysteine (H_2Acys), and N-acetyl-L-cysteine methyl ester ($HAcysMe$); the isolation of two ruthenium thiolato complexes $[Ru(tpy)(bpy)(HCys)]PF_6$ ($[2]PF_6$), and $[Ru(tpy)(bpy)(HAcys)]PF_6$ ($[3]PF_6$, see Scheme 2.1); and their thermal and photochemical reactivity in aqueous solution.



Scheme 2.1 Reaction between complex $[1](PF_6)_2$ and thiol ligands H_2Cys , H_2Acys , or $HAcysMe$.

2.2 Results

2.2.1 Coordination chemistry of thiols and $[Ru(tpy)(bpy)(OH_2)](PF_6)_2$ ($[1](PF_6)_2$)

The reaction between $[1](PF_6)_2$ and H_2Cys , H_2Acys , or $HAcysMe$ in aqueous solution was first studied under an argon atmosphere using 1H NMR spectroscopy. H_2Cys can coordinate to ruthenium via the S, N, or O atoms, whereas for H_2Acys N-coordination is impossible, and for $HAcysMe$ only S-coordination is feasible. In all 1H NMR spectra the A6 proton of the bpy ligand was monitored as it appears at very low fields (9.0 to 11.0 ppm), and is very sensitive to the nature of the monodentate ligand coordinated to ruthenium. In the dark, in phosphate buffer (pD = 7.8) and at 298 K H_2Cys hardly reacted with $[1]^{2+}$ (●), and after 15 days unassigned signals at 10.15 and 9.69 ppm arose (Figure SII.1). When heated to 353

K, however (Figure 2.1), a new peak appeared at 10.08 ppm (\diamond) after one day, together with a minor peak at 9.73 ppm that disappeared upon prolonged heating. 3 days were required to almost completely convert $[1]^{2+}$. Coordination of H_2Cys to the complex is thus a thermally activated process, as has been observed for thioethers.^{20, 21} Although S-coordination is expected because of the softness of ruthenium(II), the possibility of N- or O-coordination cannot be excluded at this stage.

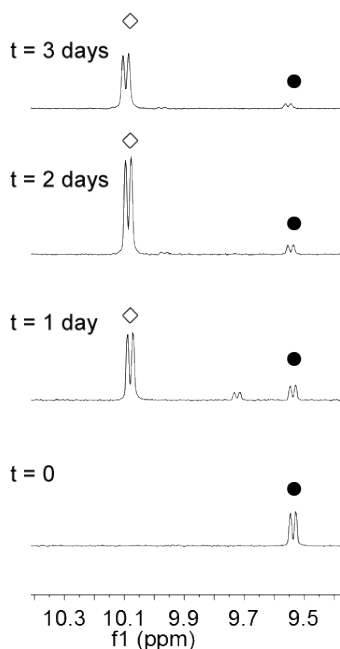


Figure 2.1 Evolution of the A6 proton of coordinated bpy (see Scheme 2.1) followed by 1H NMR spectroscopy of a mixture of $[1](PF_6)_2$ and 1 equivalent of thiol ligand H_2Cys at different time intervals at 353 K under argon in phosphate buffer (pD = 7.8) in the dark (10.4-9.4 ppm). Conditions: $[Ru]_0 = 5.0$ mM. Notations: $\bullet = [1]^{2+}$; $\diamond = [2]^{2+}$.

A similar reaction was performed in the dark using 1.2 equivalents of H_2Acys , a ligand in which the amine can neither be protonated nor coordinate to the metal. At 298 K in phosphate buffer (pD = 7.8) a new peak (\blacklozenge) at 10.00 ppm was observed after 24 h (Figure 2.2A), and the red solution turned purple brown. At 353 K the same peak at 10.00 ppm (\blacklozenge) and a color change appeared within 1.5 h (Figure 2.2B). Mass spectrometry at this point showed peaks at $m/z = 508.0$ and 653.1 corresponding to the hydroxo complex $[1 - H]^+$ (calc. $m/z = 508.1$) and to the

expected thiolato complex $[\text{Ru}(\text{tpy})(\text{bpy})(\text{HAcys})]^+$ (calc. $m/z = 653.0$). After 24 h at 353 K a second peak at 10.12 ppm appeared (■) and after 72 h the former signal (◆) was not present anymore. As shown by the evolution of the composition of the solution as a function of reaction time (Figure SII.2), $[\text{Ru}(\text{tpy})(\text{bpy})(\text{HAcys})]^+$ is a kinetic product, thus it is unstable under such conditions.

An alternative way to produce $[\text{Ru}(\text{tpy})(\text{bpy})(\text{HAcys})]^+$ was to irradiate white light at 298 K on a D_2O mixture of $[\mathbf{1}]^{2+}$ and H_2Acys (Figure 2.2C); after 1.5 hour the peak at 10.00 ppm was clearly visible, and a similar color change as under thermal activation was observed. Mass spectrometry after 1.5 h irradiation showed two peaks at $m/z = 254.6$ and 653.1 , confirming the presence of $[\mathbf{1}]^{2+}$ and of $[\text{Ru}(\text{tpy})(\text{bpy})(\text{HAcys})]^+$. Further irradiation, however, did not result in full conversion to the pure HAcys^- adduct. After 3.5 h of irradiation the species at 10.12 ppm (■) observed upon heating in the dark arose as well, and had become the major product after 10 h irradiation. Thus, coordination of H_2Acys to ruthenium only occurs upon thermal or photochemical activation, and the adduct $[\text{Ru}(\text{tpy})(\text{bpy})(\text{HAcys})]^+$ is unstable.

To exclude O-coordination the reaction between $[\mathbf{1}]^{2+}$ and HAcysMe was studied as well; CD_3OD was chosen as solvent due to the poor solubility of the HAcysMe ligand in water, and to avoid ester hydrolysis during coordination. In presence of 7.5 equivalents of HAcysMe , $[\mathbf{1}]^{2+}$ reacted in the dark and after 20 min at 353 K, to form two new species characterized by A6 doublets at 10.44 and 10.20 ppm (Figure SII.3); $[\mathbf{1}]^{2+}$ can still be observed by its A6 doublet at 9.55 ppm (●). According to mass spectrometry the new signals correspond to the $[\text{Ru}(\text{tpy})(\text{bpy})(\text{AcysMe})]^+$ complex $[\mathbf{4}]^+$ ($m/z = 667.1$, calc $m/z = 667.1$) and $[\text{Ru}(\text{tpy})(\text{bpy})\text{Cl}]^+$ ($m/z = 525.9$, calc $m/z = 526.0$), respectively. The chloride complex originated from chloride salts found in the commercial ligand HAcysMe . From this reaction and from TLC analysis of the reaction mixture it was concluded that the S-bound complex $[\mathbf{4}]^+$ is purple, and that the purple color observed in the reaction of $[\mathbf{1}]^{2+}$ with H_2Cys or H_2Acys is due to the formation of the κS complexes $[\mathbf{2}]^+$ and $[\mathbf{3}]^+$, respectively. Overall, the three different reactions with the three thiol ligands indicate a similar binding mode *via* the soft sulfur atom, i.e., the preferential formation of thiolato complexes $[\mathbf{2}]^+$, $[\mathbf{3}]^+$, and $[\mathbf{4}]^+$.

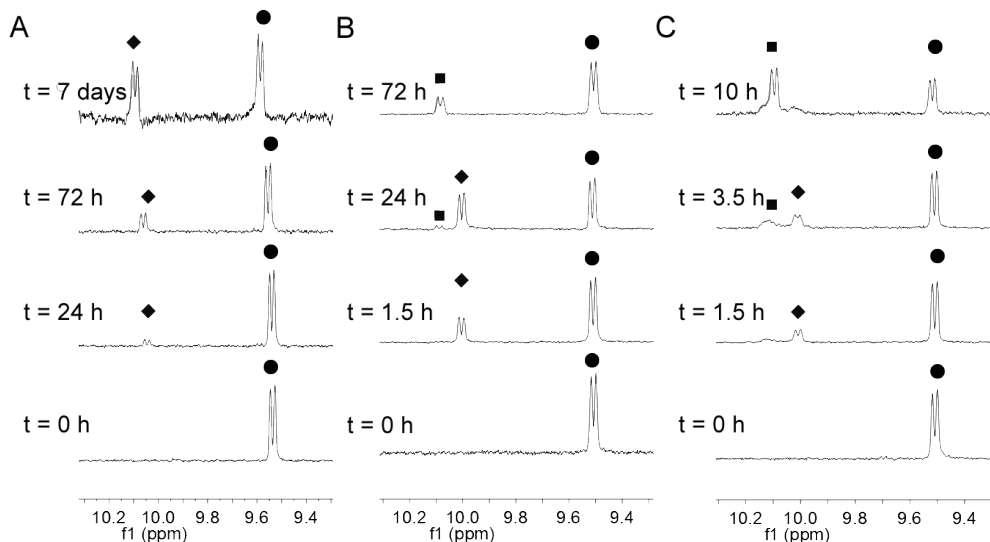


Figure 2.2 Evolution of the A6 proton in the reaction between $[1](PF_6)_2$ and H_2Acys at different time intervals under argon monitored by 1H NMR spectroscopy (region 10.3-9.3 ppm). The 1H NMR peaks in this region correspond to the A6 proton for each complex. a) In phosphate buffer (pD = 7.8) at 298 K in the dark, $[H_2Acys] = 6.0$ mM. b) in D_2O at 353 K in the dark, $[H_2Acys] = 4.0$ mM. c) in phosphate buffer (pD = 7.8) under white light irradiation at 298 K, $[H_2Acys] = 10.1$ mM. $[Ru]_0 = 5.0$ mM. Notations: ● = $[1]^{2+}$; ◆ = $[3]$; ■ = $[Ru(tpy)(bpy)(HAcysO_2)]^+$ (see text).

DFT calculations were performed, first in vacuum and then in water using the COSMO model (see Experimental for details), to quantify the relative stability of S-, N-, and O-coordination of cysteine in $[2]^+$. For each binding mode (S, N, and O) two different minima were found. The optimized structures, their energies in vacuum and in water, are given in Figure SII.4 and Table SII.1, respectively. For the S- and O-bound isomers, the two different minima arise from different arrangements of the hydrogen atoms in the carboxylate and amine groups and for the N-bound isomer they come from the migration of a proton between the thiol and carboxylate groups. The S-bound isomer $[\kappa S-2]^+$ is the most stable, with the N-bonded and the O-bonded isomers being, respectively, 15.7 kcal.mol⁻¹ and 13.2 kcal.mol⁻¹ higher in energy in vacuum (relative stabilities: S > O > N) and 6.5 kcal.mol⁻¹ and 12.9 kcal.mol⁻¹ higher in water (relative stabilities: S > N > O). It is noteworthy that the relative stabilities of the O-bound and N-bound isomers are different in vacuum and in water, which is probably due to the stabilization of the carboxylate group in water due to the polar environment. Overall, the energies in

water of the most stable conformers $[\kappa S-2]^+$, $[\kappa N-2]^+$, and $[\kappa O-2]^+$, confirmed that in $[2]^+$ the κS binding mode of the H_2Cys^- ligand is preferred, and that the peak at 10.08 ppm (■) observed in Figure 2.2 is that of $[\kappa S-2]^+$. Everything considered, DFT results confirm that H_2Cys , and therefore probably H_2Acys , coordinates to the ruthenium center *via* the sulfur atom in aqueous solution.

2.2.2 Synthesis and characterization of two thiolato complexes $[2]PF_6$ and $[3]PF_6$

As it was obvious that the thiolato complexes $[2]^+$ and $[3]^+$ are unstable even in presence of the trace amounts of oxygen present when working with Schlenk techniques, new conditions were investigated that would allow for isolating pure samples of the complexes. Full conversion into $[2]PF_6$ and $[3]PF_6$ without formation of oxidized side products was achieved by adding a large excess of the thiol ligand H_2Cys or H_2Acys to $[1](PF_6)_2$ in deionized water upon heating. As shown in Figure 2.3, 50 equivalents of H_2Cys , and 100 equivalents of H_2Acys were required to quantitatively convert $[1]^{2+}$ into $[2]^+$ and $[3]^+$ after 1.5 h at 353 K under argon.

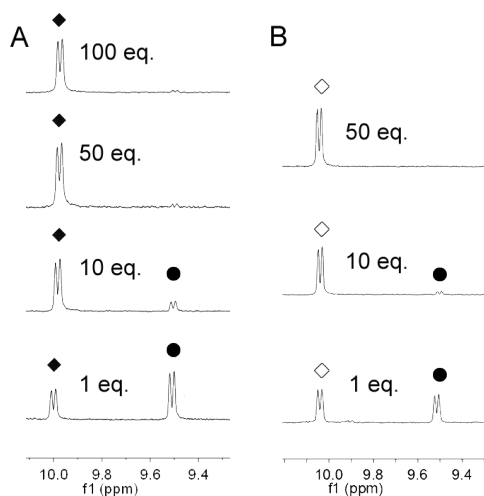


Figure 2.3 1H NMR spectra of the A6 proton of mixtures of $[1](PF_6)_2$ (●) with different equivalents of H_2Acys (a) or H_2Cys (b) after 1.5 hour at 353 K under argon in D_2O (A6 region, 10.2-9.3 ppm) forming $[3]^+$ (◆) or $[2]^+$ (◇). Conditions: $[Ru]_0 = 5.0$ mM, in the dark.

The compounds were synthesized on a larger scale and purified from the excess ligand using size exclusion chromatography (see Experimental Part). $[2]PF_6$ and $[3]PF_6$ appeared to be too sensitive to oxidation to give correct elemental analysis data or to allow purification by HPLC. However, all spectroscopic data concluded to NMR-pure samples (> 95%) of the κS isomers as shown in Scheme 2.1. In mass

spectrometry peaks at $m/z = 611.0$ and $m/z = 653.0$ were observed, corresponding to $[2]^+$ (calc. $m/z = 611.1$) and $[3]^+$ (calc. $m/z = 653.0$), respectively. According to ^1H NMR in CD_3OD , the aliphatic protons of the S-coordinated ligands (2.86 (β) and 1.75 ppm (α) for HCys^- in $[2]^+$; 3.77 (β), 1.85 (γ), and 1.71 ppm (α) for HAcys^- in $[3]^+$, see Figure SII.5 and Figure SII.6) are shielded in the ruthenium complexes, compared to the free thiol ligands (3.72 (β) and 3.00 ppm (α) for H_2Cys and 4.60 (β), 2.91 (α), and 2.02 ppm (γ) for H_2Acys).

According to NOESY analysis of $[3]^+$ the α protons of the thiol ligand are closer from the aromatic A6 and T6 protons than the β proton (Figure SII.7), as expected for sulfur coordination. The characteristic aromatic A6 protons of the two compounds are both observed at 10.49 ppm in CD_3OD , suggesting that both $[2]^+$ and $[3]^+$ have the same κS binding mode. UV-vis absorption spectra of $[3]\text{PF}_6$ in water showed a maximum at 492 nm (Figure SII.8), which is 40 nm bathochromically shifted compared to its thioether analogue $[\text{Ru}(\text{tpy})(\text{bpy})(\text{HAMet})]\text{Cl}_2$ ($[\mathbf{5}]\text{Cl}_2$, $\text{HAMet} = \text{N-acetyl-L-methionine}$). Such redshift of the MLCT band can be explained by the anionic nature of the thiolate ligand, which increases the σ -donating properties of the sulfur atom of thiolates compared to thioethers, and thus increases the energy level of the t_{2g} orbitals on the metal with respect to the π^* orbitals of the polypyridyl ligands. This electronic effect is responsible for the different colors (purple *vs.* red) of aqueous solution of the N-acetyl-L-cysteine and N-acetyl-L-methionine ruthenium complexes $[3]^+$ and $[\mathbf{5}]^{2+}$, respectively.

2.2.3 Thermal stability of the isolated thiolato ruthenium complex $[3]\text{PF}_6$

The thermal stability of complex $[3]\text{PF}_6$ in the dark was studied by ^1H NMR in D_2O at 298 K under air and under an argon atmosphere (Figure 2.4A-B). The composition of the mixture was determined by relative integration of the ^1H NMR signals in the A6 region (10.3-9.3 ppm, for overview see Table SII.2). When the NMR sample was prepared under air the signal initially present at 10.12 ppm (\blacksquare) indicated that the starting compound $[3]^+$ (\blacklozenge) decomposed even in the solid state. After 1 day the signal of $[3]^+$ had decreased in intensity and the aqua complex $[\mathbf{1}]^{2+}$ had appeared (\bullet). After 3 weeks, $[3]^+$ was fully decomposed; the final reaction mixture consisted of 26% of an oxidized side product (\blacksquare), of a major fraction (55%) of $[\mathbf{1}]^{2+}$, and of a second side product (19%) characterized by an A6 doublet at 9.71 ppm. Mass spectrometry analysis after 3 weeks revealed, next to the expected

peaks at $m/z = 507.9$ and 653.0 , new peaks at $m/z = 684.9$, 706.9 , and 814.0 which correspond to the sulfinato complexes $[3 + 2 \times O]^+$ (calc. $m/z = 685.1$) and $[3 - H + Na + 2 \times O]^+$ (calc. $m/z = 707.1$), and the disulfide complex $[Ru(tpy)(bpy)(HAcys_2)]^+$ (calc. $m/z = 814.1$), respectively. Interestingly, the reaction between the free disulfide ligand **6** (Figure 2.5) and $[1]^{2+}$ in D_2O at 353 K did not lead to any coordination (Figure SII.9). Preparing the NMR tube under argon allowed for slowing down decomposition of $[3]^+$, as after 3 weeks at 298 K an 85:15 mixture of $[3]^+:[1]^{2+}$ was established. In this case mass spectrometry analysis also showed the presence of the aqua, thiolato, and sulfinato complexes.

The thermal instability of $[3]^+$ was also monitored by UV-vis spectroscopy in a phosphate buffer ($pH = 7.4$). Under argon a slow change of the UV-vis spectrum is observed, and under air the blue shift of the MLCT band of the ruthenium complex takes place significantly faster (Figure 2.4C). After 16.7 h at 298 K , mass spectrometry analysis resulted in peaks at $m/z = 507.9$, 653.0 , 669.0 , 691.0 , and 723.0 , corresponding to $[1]^+$, $[3]^+$, to the sulfenato $[3 + O]^+$ (calc. $m/z = 669.1$), to the $[3 - H + Na + O]^+$ or $[3 - H + K]^+$ cation (both calc. $m/z = 691.1$), and to the sulfinato species $[3 - H + K + 2 \times O]^+$ (calc. $m/z = 723.0$). Overall, combined NMR, MS, and UV-vis data indicate that decomposition of $[3]^+$ occurs *via* oxidation into the sulfenato, sulfinato, and disulfide complexes (an overview of the various oxidation states of N-acetyl-L-cysteine is given in Figure 2.5). Thermal decomposition of $[3]^+$ can be slowed down significantly by preparing samples under argon using Schlenk techniques, but it was impossible to prevent decomposition.

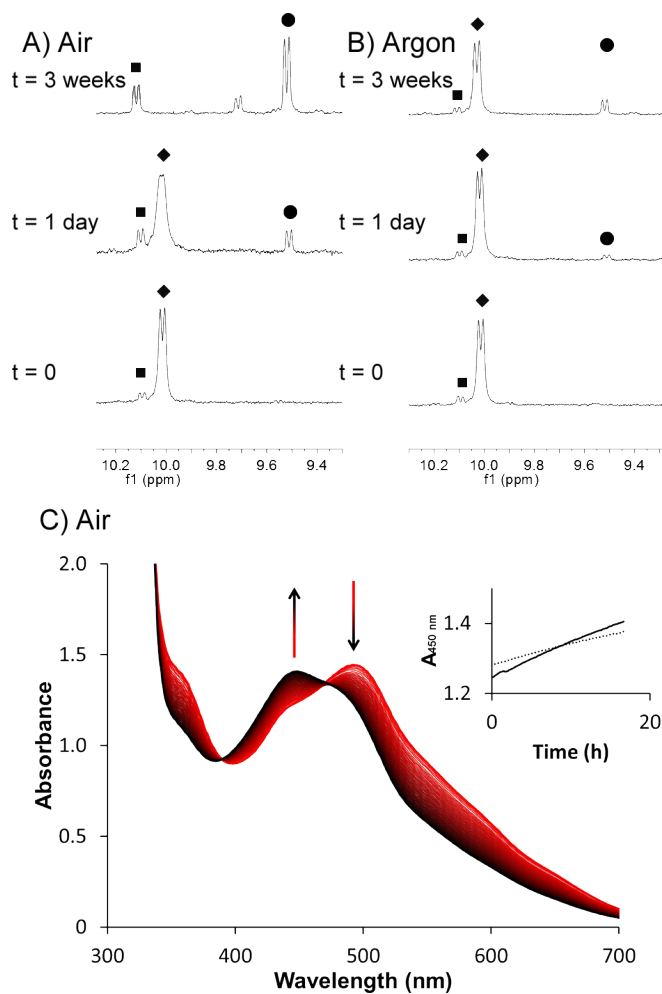


Figure 2.4 ^1H NMR spectra (10.2-9.4 ppm) of $[3]\text{PF}_6$ in the dark at different time intervals under air (A) and under argon (B) at 298 K in D_2O . Notations: ■ = sulfinato complex $[\text{Ru}(\text{tpy})(\text{bpy})(\text{HAcysO}_2)]^+$; ◆ = $[3]$; ● = $[1]^{2+}$. ^1H NMR peaks in this region correspond to the A6 proton of the bipyridine ligand of each ruthenium complex. Conditions: $[\text{Ru}]_0 = 6.4$ mM. C) Evolution of the absorbance of a solution of $[3]\text{PF}_6$ in the dark under air. Time: 0 hour (red curve), 16.7 h (black curve). Conditions: $[\text{Ru}]_0 = 0.20$ mM, pH = 7.4 in 3.00 mL phosphate buffer, $T = 298$ K. Inset: Plot of the absorbance at 450 nm as a function of time under air (continuous line) and argon (dashed line) atmosphere.

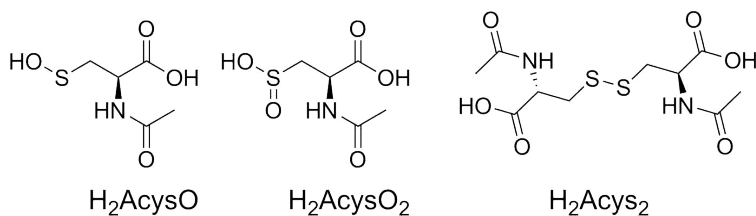


Figure 2.5 Formula of the oxidized sulfenate (H₂AcysO), sulfinate (H₂AcysO₂), and disulfide (H₂Acys₂) forms of N-acetyl-L-cysteine.

2.2.4 Photoreactivity

To investigate the stability of [3]PF₆ under light irradiation, a solution of the complex in a phosphate buffer at pH = 7.4 was irradiated with blue light ($\lambda_{\text{irr}} = 465$ nm) for 1000 min at 298 K. The evolution of the solution was monitored under argon and under air by UV-vis spectroscopy and mass spectrometry, and compared to a control reaction in the dark. The absorbance of the solutions changed over time following different patterns under irradiation in air and under argon, indicating that a different decomposition mechanism may be involved when oxygen is present. The mass spectrum of the sample irradiated under argon showed peaks next to the $m/z = 653.1$ and 691.1 peaks of [3]⁺ and [3 - H + K]⁺ (calc. $m/z = 690.7$), respectively, a weak signal at $m/z = 522.9$ matching with [1 - H₂O + MeOH]⁺ (calc. $m/z = 523.1$), i.e., with a photosubstituted product. Under air additional peaks at $m/z = 669.0$ and 685.0 were clearly observed that can be attributed to the sulfenato ([3 + O]⁺, calc. $m/z = 669.1$) and sulfinato complexes ([3 + 2×O]⁺, $m/z =$ calc. 685.1). Full conversion to [1]²⁺ (Figure 2.6, dashed line) was not achieved under argon (Figure 2.6a) or under air (Figure 2.6B) after 1000 min. This was confirmed by mass spectrometry as the $m/z = 653.0$ peak for [3]⁺ was still present in both irradiated solutions.

These UV-vis results were confirmed by ¹H NMR spectroscopy (Figure 2.7). When a D₂O solution of [3]PF₆ in an NMR tube was irradiated under argon and at room temperature using white light, the peak of the aqua complex (●) appeared first, followed by smaller amounts of the signal at 10.12 ppm (■), which is interpreted as the sulfinato species [Ru(tpy)(bpy)(HAcysO₂)]⁺. Thus, photoproduction of the aqua complex [1]²⁺ can occur either without oxidation of the thiolate ligand, i.e., *via* a photosubstitution process releasing the free thiol ligand similar to that observed for thioether ruthenium complexes, or *via* photooxidation to the sulfinato species,

followed by thermal substitution of the HAcysO_2^- ligand by H_2O . Overall the photoreactivity of $[\mathbf{3}]^+$ is much slower than that of the thioether analogue complex $[\mathbf{5}]^{2+}$: indeed, less than 30% conversion was obtained after 4.5 h irradiation of $[\mathbf{3}]^+$ (Figure 2.7), whereas full conversion of $[\mathbf{5}]^{2+}$ into $[\mathbf{1}]^{2+}$ was obtained after only 65 min irradiation under similar conditions.²⁰ The slower photosubstitution for $[\mathbf{3}]^+$, compared to $[\mathbf{5}]^{2+}$, can also be linked to the difference in color between the two ruthenium complexes: if the thiolate cysteine ligand is more electron-donating than the thioether methionine, then the dissociative ^3MC states are expected to be higher in energy in $[\mathbf{3}]^+$ than in $[\mathbf{5}]^{2+}$ compared to the $^3\text{MLCT}$ states, which leads to a lower photosubstitution quantum yield for $[\mathbf{3}]^+$.

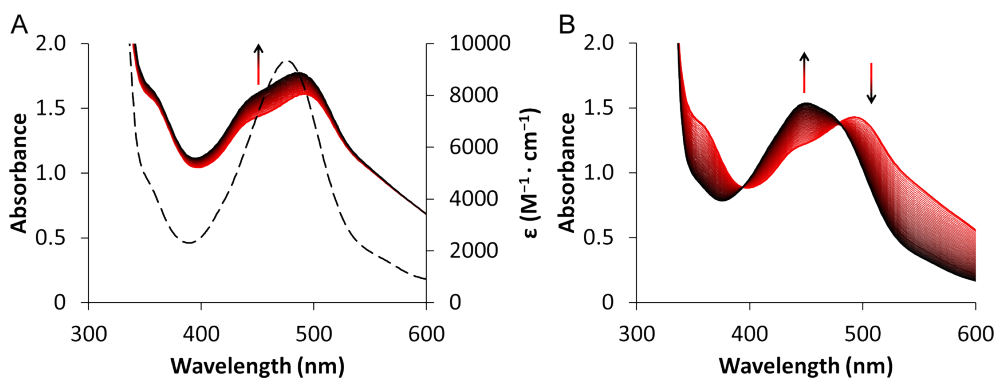


Figure 2.6 Evolution of the absorbance (left axis) of a solution of $[\mathbf{3}]^+$ under argon (A) and under air atmosphere (B) upon blue-light irradiation ($\lambda = 465 \text{ nm}$, $\Delta\lambda_{1/2} = 25 \text{ nm}$, $3.8 \times 10^{-8} \text{ mol}\cdot\text{s}^{-1}$). As an indication the molar extinction coefficient of $[\mathbf{1}](\text{PF}_6)_2$ (dashed curve, right axis) is also shown. Time: 0 min (red curve), 1000 min (black curve). Conditions: $[\text{Ru}]_0 = 0.20 \text{ mM}$, phosphate buffer $\text{pH} = 7.4$, irradiated volume 3.00 mL , $T = 298 \text{ K}$.

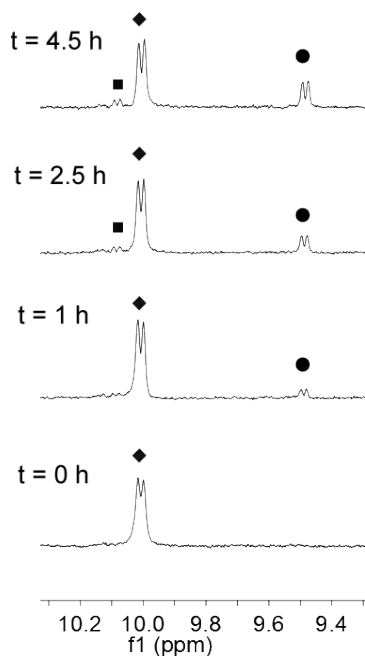


Figure 2.7 Evolution of the ^1H NMR spectra (10.3–9.3 ppm) of the A6 proton of solution of $[\mathbf{3}]\text{PF}_6$ in D_2O under white light irradiation at 298 K. Notations: ■ = $[\text{Ru}(\text{tpy})(\text{bpy})(\text{HAcysO}_2)]^+$; ◆ = $[\mathbf{3}]^+$, ● = $[\mathbf{1}]^{2+}$.

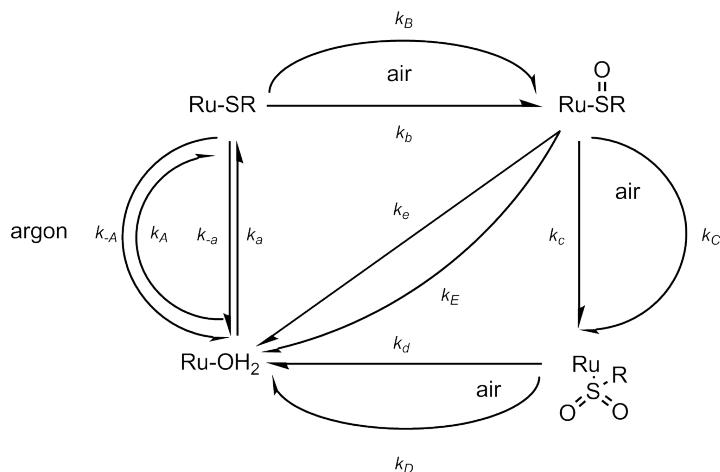
2.3 Discussion

The formation of $[\mathbf{2}]^+$ from $[\mathbf{1}]^{2+}$ and L-cysteine was previously studied by ^1H NMR by Mijatović et al. However, in our hands these results were impossible to reproduce (Figure SII.10).¹⁴ Instead, $[\mathbf{2}]^+$ and $[\mathbf{3}]^+$ do not form at room temperature but need thermal or photochemical activation to appear in solution. In addition, these thiolato complexes are unstable even when working with Schlenk techniques, where minute traces of oxygen result in (slow) decomposition into several oxidation products. However, using a large excess of the thiol ligand, i.e., 50 equivalents of H_2Cys or 100 equivalents of H_2Acys , allowed for isolating the thiolato compounds $[\mathbf{2}]\text{PF}_6$ and $[\mathbf{3}]\text{PF}_6$ without the formation of any sulfenato or sulfinato ruthenium complexes. Under such conditions, traces of oxygen in the reaction mixture are probably quenched by the excess of thiol, and as the disulfide ligand does not coordinate to the ruthenium center (Figure SII.9) an analytically pure sample of the thiolato complex is finally obtained.

Possible binding and decomposition pathways of thiolato ruthenium complex $[3]^+$ are summarized in Scheme 2.2. The results of spectroscopic and mass spectrometry investigations in aqueous solution suggest that in the strict absence of oxygen and in the dark the S-bound thiolato ruthenium complex $[3]^+$ (hereafter Ru-SR) may directly decompose, either thermally (-a) or photolytically (-A), into $[1]^{2+}$. The decomposition consists of a ligand substitution reaction, and is also accompanied by the release of non-oxidized thiol ligand. Photosubstitution of the thiolate ligand by water is significantly slower than for thioether complexes because of the higher electron density of the alkyl thiolate ligand. Back-binding of the thiolate ligand to the aqua ruthenium complex $[1]^{2+}$ to produce the thiolato adduct $[3]^+$ occurs *via* thermal (a) or photochemical (A) activation. While photochemical substitution of a sulfur-based ligand by an aqua ligand is a well-known phenomenon in ruthenium chemistry,^{20, 22-24} photochemical binding of a sulfur-based ligand to ruthenium is a much less common phenomenon, but should not be ignored.

In the presence of even traces of oxygen irreversible decomposition of the thiolato complex takes place through the formation of a ruthenium sulfenato complex. Either thermal (b) or photochemical oxidation (B) may take place. Subsequently, the unstable sulfenato complex can be thermally hydrolyzed into $[1]^{2+}$ and release the free sulfenate ligand HAcysO^- , but the reverse reaction does not occur as $[1]^{2+}$ is the final product of all stability experiments performed under air (e or E). The sulfenato complex can also be further oxidized to the slightly more stable sulfinato complex (c or C), which can be observed by ^1H NMR but will subsequently be hydrolyzed to the aqua complex $[1]^{2+}$ (d or D). Decomposition of $[3]^+$ into the aqua complex may also occur *via* a disulfide complex $[\text{Ru}(\text{tpy})(\text{bpy})(\text{HAcys}_2)]^+$ observed by mass spectrometry, but this disulfide complex must be transient as it does not form by mixing the disulfide ligand and $[1]^{2+}$. In all these pathways the ruthenium thiolato complex Ru-SR may be oxidized either *via* reaction of its ground state with molecular oxygen, or *via* excitation of Ru-SR to its singlet state, followed by intersystem crossing to the triplet excited state and reaction with dioxygen ($^3\text{O}_2$) to produce singlet oxygen ($^1\text{O}_2$). $^1\text{O}_2$ has a higher reactivity than $^3\text{O}_2$, which would explain the higher rate of formation of the oxidized complexes under visible light irradiation, compared to dark conditions. Finally, because of the low efficiency of the oxygen-independent thiol photosubstitution reaction, photosubstitution rates become negligible as soon as the oxygen concentration is non-zero, and release of the aqua complex $[1]^{2+}$ occurs mostly *via* irreversible ligand (photo)oxidation

followed by thermal substitution by water of the sulfenate, sulfinate, or disulfide ligand. Basically, the electron-richness of alkyl thiolates is too high for the complex to resist oxygen. Using less basic thiols such as thiophenol might lower the propensity of thiolato ruthenium complexes to be thermally oxidized.



Scheme 2.2 Proposed mechanism of the different reactions of [3]⁺ in the dark and under blue light irradiation, in the presence of either an argon or an air atmosphere. Lower case annotation represents a thermal reaction, and upper case represents a photoreaction.

2.4 Conclusion

Unlike their methionine analogues, cysteine derivatives cannot be used for the protection of ruthenium polypyridyl complexes such as [1]²⁺. First, a large excess of thiol is required to achieve full conversion of the aqua complex to the thiolato compound without formation of oxidized side products. Such preparation conditions seem poorly compatible with the preparation of cancer-targeted ruthenium compounds using cysteine-terminated peptides that directly coordinate to the metal center. Second, the isolated thiolato metal compound is unstable in the dark: it reacts with trace amounts of oxygen to form the sulfenato, sulfinato, or disulfide complexes, which eventually decompose in aqueous solution to release the aqua complex [1]²⁺. In this case, visible light irradiation in presence of trace amounts of oxygen acts as an accelerator of the oxidative decomposition of the complex, instead of a trigger inducing selective delivery of an active metallodrug at the place and time of irradiation. In contrast, the methionine complex [5]²⁺ shows no trace of decomposition in D₂O after 3 weeks in the dark at human body

temperature,²⁰ and blue light irradiation efficiently converts the Ru-S complex [5]²⁺ into the aqua complex [1]²⁺ by simple ligand substitution. Overall, light irradiation of thiolato ruthenium complexes such as [3]⁺ results in an intricate combination of reversible, oxygen-independent ligand exchange processes and irreversible, oxygen-dependent ligand oxidation processes, ultimately leading to the formation of oxidized thiol ligands and the aqua complex [1]²⁺. In contrast to thioethers, cysteine derivatives produce thermally unstable ruthenium complexes, i.e., they do not act as a protecting group for ruthenium complexes such as [1]²⁺. In turn, the ability of [1]²⁺ to oxidize cysteine derivatives upon light irradiation, possibly in the cell to induce oxidative stress, could be a cytotoxic concept worth pursuing. It would require the development of compounds that have much higher oxidation rates than achieved in this chapter to be considered as potential selective anticancer drugs.

2.5 Experimental

2.5.1 Materials and Methods

The ligands 2,2';6',2''-terpyridine (tpy), N-acetyl-L-cysteine (H₂Acys), and N-acetyl-L-cysteine methyl ester (HAcysMe), as well as lithium chloride (LiCl), and triethylamine (NEt₃) were purchased from Sigma-Aldrich; silver hexafluorophosphate (AgPF₆) and L-cystine (6) from Acros Organics; L-cysteine (H₂Cys) from Merck; N-acetyl-L-cystine (H₂Acys₂) from Bachem; and 2,2'-bipyridine (bpy) from Brunschwig Chemie. All reactants and solvents were used without further purification. The synthesis of complex [1](PF₆)₂ was carried out according to a modified literature procedure.²⁵ [Ru(tpy)(bpy)Cl]Cl (200 mg, 0.356 mmol) and AgPF₆ (180 mg, 0.712 mmol) were dissolved in a 3:1 acetone/H₂O mixture (20 mL). The resulting mixture was stirred and heated to reflux under argon at 353 K overnight. The suspension was filtered hot over Celite, and acetone was removed by rotary evaporation. The mixture was stored in the refrigerator for 4 days resulting in the formation of a precipitate that was filtered and dried under vacuum. Yield: 160 mg (57%). ¹H NMR data were in good agreement with literature references.²⁶ All other metal complexes were synthesized in dim light and stored in darkness.

NMR spectra were recorded on a Bruker DPX-300 spectrometer. Chemical shifts are indicated in ppm. For NMR experiments under argon, NMR tubes with PTFE stopper were used. For some NMR reactions phosphate buffers in D₂O were used (0.01 M phosphate, pD = 7.8, equivalent to pH = 7.4). The preparation was carried out according to the literature procedure for H₂O buffers and the pH was measured with a pH meter, taking into account that the measured pD = pH* + 0.4, where pH* is the meter reading in D₂O solutions.^{27, 28}

Mass spectra were recorded by using a Thermoquest Finnagen AQA Spectrometer and a MSQ Plus Spectrometer. For the irradiation experiments of NMR tubes, the light of a LOT 1000 W Xenon Arc lamp filtered with an infrared filter was used. UV-vis experiments were performed on a Cary Varian spectrometer. When following photoreactions by UV-vis, a LED light source ($\lambda_{\text{irr}} = 465 \text{ nm}$) with a light intensity of 2.78 mW was used.

2.5.2 Reaction of [1](PF₆)₂ with thiols

The synthesis procedure was adapted from the synthesis reported for [Ru(tpy)(bpy)(HAMet)]Cl₂ ([5]Cl₂).²⁰ 2.0 mg of compound [1](PF₆)₂ (2.5 μmol) and the desired number of equivalents of HSR (H₂Cys, H₂Acys, or HAcysMe) or RSSR (H₂Acys₂) were weighed in a NMR tube. When necessary, the further preparation of the NMR tube was done under argon. 0.5 mL of the (degassed) solvent (D₂O, D₂O-based phosphate buffer, or CD₃OD) was added. The tube was kept in the dark either at 298 K or was heated at 353 K until the maximum conversion took place. ¹H NMR spectra of the reaction were recorded for each sample at different time intervals.

2.5.3 Photoreaction of [1](PF₆)₂ with H₂Acys

Compound [1](PF₆)₂ (2.7 mg, 3.4 μmol) and H₂Acys (1.4 mg, 8.6 μmol) were weighed into a NMR tube and 0.5 mL of degassed D₂O was added. The tube was prepared under argon and irradiated at 298 K by the white light of a Xenon 1000 W lamp with a thermostat. In addition, a control experiment without white light irradiation was performed. The reactions were monitored by ¹H NMR at various time intervals.

2.5.4 Synthesis of [Ru(tpy)(bpy)(HCys)]PF₆ ([2]PF₆) and [Ru(tpy)(bpy)(HAcys)]PF₆ ([3]PF₆)

[1](PF₆)₂ (60 mg, 0.075 mmol) and H₂Cys or H₂Acys (7.5 mmol) were dissolved in degassed H₂O (15 mL). The resultant mixture was stirred and heated to reflux under argon for 1.5 h at 353 K. H₂O was removed by freeze-drying. For purification, size exclusion column chromatography (Sephadex LH-20, MeOH) was performed for both complexes. Finally, methanol was removed by rotary evaporation to yield dark brown powders. Yield: [2]PF₆ 12 mg (63%) and [3]PF₆ 36 mg (60%).

[2]PF₆: ¹H NMR (300 MHz, CD₃OD, 298 K, in ppm): $\delta = 10.48$ (d, $J = 5.6 \text{ Hz}$, 1H, A6), 8.75 (d, $J = 8.0 \text{ Hz}$, 1H, A3), 8.64 (d, $J = 8.1 \text{ Hz}$, 2H, T3'), 8.55 – 8.48 (m, 3H, T3 + B3), 8.29 (td, $J = 7.9, 1.5 \text{ Hz}$, 1H, A4), 8.10 (t, $J = 8.1 \text{ Hz}$, 1H, T4'), 8.01 (ddd, $J = 7.2, 5.7, 1.2 \text{ Hz}$, 1H, A5), 7.91 (tdd, $J = 8.0, 2.8, 1.5 \text{ Hz}$, 2H, T4), 7.80 (td, $J = 8.1, 1.5 \text{ Hz}$, 1H, B4), 7.68 (d, $J = 5.5 \text{ Hz}$, 2H, T6), 7.35 – 7.27 (m, 2H, T5), 7.26 – 7.21 (m, 1H, B6), 7.09 (ddd, $J = 7.0, 5.7, 1.2 \text{ Hz}$, 1H, B5), 2.87 (dd, $J = 9.4, 3.7 \text{ Hz}$, 1H, β), 1.88 – 1.60 (m, 2H, α). ES MS m/z (calc): 610.9 (611.1, [M – H – 2×PF₆]⁺)

[3]PF₆: ¹H NMR (300 MHz, CD₃OD, 298 K, in ppm): $\delta = 10.48$ (d, $J = 4.8 \text{ Hz}$, 1H, A6), 8.75 (d, $J = 8.0 \text{ Hz}$, 1H, A3), 8.63 (dd, $J = 8.2, 0.9 \text{ Hz}$, 2H, T3'), 8.56 – 8.46 (m, 3H, T3 + B3), 8.29 (td, $J = 7.7, 1.5 \text{ Hz}$, 1H, A4), 8.10 (t, $J = 8.1 \text{ Hz}$, 1H, T4'), 8.02 – 7.86 (m, 3H, A5 + T4), 7.86 – 7.75 (m, 1H,

B4), 7.73 – 7.61 (m, 2H, T6), 7.30 (ddd, $J = 7.0, 5.5, 1.3$ Hz, 2H, T5), 7.23 (ddd, $J = 5.5, 1.5, 0.7$ Hz, 1H, B6), 7.09 (ddd, $J = 7.1, 5.5, 1.3$ Hz, 1H, B5), 3.75 (dd, $J = 7.2, 5.1$ Hz, 1H, β), 1.86 (s, 3H, γ), 1.79 – 1.60 (m, 2H, α). ^{13}C NMR (75 MHz, CD_3OD , 298 K, in ppm): $\delta = 174.78$ (C=O acid), 172.57 (C=O N-acetyl), 159.59, 159.54, 158.45, 158.39, 157.66 (T2 + T'2 + A2), 154.68 (A6), 152.84 + 152.76 (T6), 150.97 (B6), 137.82 + 137.69 + 137.65 + 137.60 (A4 + B4 + T4), 133.28 (T4'), 128.37 + 127.98 + 127.54 (A5 + B5 + T5), 124.73 + 124.60 + 124.38 (A3 + B3 + T3), 123.69 (T3'), 56.50 (β), 28.13 (α), 22.49 (γ). UV-vis: λ_{max} (ϵ in $\text{M}^{-1}\cdot\text{cm}^{-1}$) in H_2O : 492 nm (7300). High resolution ES MS m/z (calc): 653.0901 (653.0911, $[\text{M} - \text{H} - 2\times\text{PF}_6]^+$), 669.08500 (669.08599, $[\text{M} + \text{O} - \text{H} - 2\times\text{PF}_6]^+$), 685.0805 (685.0809, $[\text{M} + 2\times\text{O} - \text{H} - 2\times\text{PF}_6]^+$).

2.5.5 Stability measurements at room temperature of [3]PF₆

To measure the stability of compound [3]PF₆ under argon or in the presence of air, [3]PF₆ (2.6 mg, 0.003 mmol) was weighed into a standard NMR tube and a NMR tube with PTFE stopper, respectively. 0.5 mL of (degassed) D₂O was added to each tube and both tubes stored at 298 K in the dark. ^1H NMR spectra of each sample were recorded after preparation and after 4 h, 1 day, 4 days, and 3 weeks.

2.5.6 Photochemistry of [3]PF₆

UV-vis spectroscopy was performed using a UV-vis spectrometer equipped with temperature control set to 298 K and a magnetic stirrer. The measurements were performed in a quartz cuvette, containing 3 mL of solution. A stock solution of complex [3]PF₆ (4.0 mg in 10 mL buffer, 5.01×10^{-4} M) was prepared. The buffer used was a phosphate buffer (pH 7.4, I = 50 mM). 1 mL of the stock solution was added to a UV-vis cell and was completed to 3 mL with pH 7.4 buffer ($c = 1.67 \times 10^{-4}$ M). After degassing the sample for 30 min, a UV-vis spectrum was measured under argon every 10 min for a total of 1000 min while a LED lamp was irradiating the sample at 465 nm. The experiment was repeated without argon. For both experiments, a control measurement under the same conditions but without visible light irradiation was performed.

2.5.7 DFT

Electronic structure calculations were performed using DFT to quantify the relative stability of the S-, N-, and O-bound isomers of complex [2]⁺. ORCA 3.0.2 code²⁹ was used for all calculations. All structures were optimized in vacuum and their energies in water were obtained by performing single point energy calculations with the conductor-like screening model³⁰ (COSMO) as implemented in ORCA.³¹ The PBE0³² functional was used in combination with the last Grimme's empirical method^{33, 34} to take dispersion interactions into account (DFT-D3 method). The Ahlrichs triple- ξ quality basis set plus one polarization function (VTZP)³⁵ was used for all atoms except the ruthenium. For this last, the quasi-relativistic Stuttgart-Dresden SD (28,MWB) effective core potential³⁶ was used together with the high quality Ahlrichs def2-TZVP³⁷ valence basis set.

2.6 References

1. P. C. A. Bruijninx and P. J. Sadler, *Curr. Opin. Chem. Biol.*, 2008, **12**, 197-206.
2. S. Ray, R. Mohan, J. K. Singh, M. K. Samantaray, M. M. Shaikh, D. Panda and P. Ghosh, *J. Am. Chem. Soc.*, 2007, **129**, 15042-15053.
3. R. Trondl, P. Heffeter, C. R. Kowol, M. A. Jakupec, W. Berger and B. K. Keppler, *Chem. Sci.*, 2014, **5**, 2925-2932.
4. J. B. Aitken, S. Antony, C. M. Weekley, B. Lai, L. Spiccia and H. H. Harris, *Metallomics*, 2012, **4**, 1051-1056.
5. A. Levina, A. Mitra and P. A. Lay, *Metallomics*, 2009, **1**, 458-470.
6. B. S. Howerton, D. K. Heidary and E. C. Glazer, *J. Am. Chem. Soc.*, 2012, **134**, 8324-8327.
7. M. A. Sgambellone, A. David, R. N. Garner, K. R. Dunbar and C. Turro, *J. Am. Chem. Soc.*, 2013, **135**, 11274-11282.
8. T. Joshi, V. Pierroz, C. Mari, L. Gemperle, S. Ferrari and G. Gasser, *Angew. Chem., Int. Ed.*, 2014, **53**, 2960-2963.
9. S. Bonnet, B. Limburg, J. D. Meeldijk, R. J. M. K. Gebbink and J. A. Killian, *J. Am. Chem. Soc.*, 2010, **133**, 252-261.
10. A.-C. Laemmel, J.-P. Collin and J.-P. Sauvage, *Eur. J. Inorg. Chem.*, 1999, **1999**, 383-386.
11. Y. Kasherman, S. Sturup and D. Gibson, *J. Med. Chem.*, 2009, **52**, 4319-4328.
12. X. Wang and Z. Guo, *Anti-Cancer Agents Med. Chem.*, 2007, **7**, 19-34.
13. J. D. Aguirre, A. M. Angeles-Boza, A. Chouai, J.-P. Pellois, C. Turro and K. R. Dunbar, *J. Am. Chem. Soc.*, 2009, **131**, 11353-11360.
14. A. Mijatović, B. Šmit, A. Rilak, B. Petrović, D. Čanović and Ž. D. Bugarčić, *Inorg. Chim. Acta*, 2013, **394**, 552-557.
15. F. Wang, J. Xu, K. Wu, S. K. Weidt, C. L. Mackay, P. R. R. Langridge-Smith and P. J. Sadler, *Dalton Trans.*, 2013, **42**, 3188-3195.
16. F. Wang, J. Xu, A. Habtemariam, J. Bella and P. J. Sadler, *J. Am. Chem. Soc.*, 2005, **127**, 17734-17743.
17. D. R. Frasca and M. J. Clarke, *J. Am. Chem. Soc.*, 1999, **121**, 8523-8532.
18. H. Petzold, J. Xu and P. J. Sadler, *Angew. Chem., Int. Ed.*, 2008, **47**, 3008-3011.
19. T. Sriskandakumar, H. Petzold, P. C. A. Bruijninx, A. Habtemariam, P. J. Sadler and P. Kennepohl, *J. Am. Chem. Soc.*, 2009, **131**, 13355-13361.
20. R. E. Goldbach, I. Rodriguez-Garcia, J. H. van Lenthe, M. A. Siegler and S. Bonnet, *Chem. Eur. J.*, 2011, **17**, 9924-9929.
21. A. Bahreman, B. Limburg, M. A. Siegler, E. Bouwman and S. Bonnet, *Inorg. Chem.*, 2013, **52**, 9456-9469.
22. S. Bonnet, J.-P. Collin, N. Gruber, J.-P. Sauvage and E. R. Schofield, *Dalton Trans.*, 2003, -, 4654-4662.
23. J.-P. Collin, D. Jouvenot, M. Koizumi and J.-P. Sauvage, *Inorg. Chim. Acta*, 2007, **360**, 923-930.
24. R. N. Garner, L. E. Joyce and C. Turro, *Inorg. Chem.*, 2011, **50**, 4384-4391.
25. K. J. Takeuchi, M. S. Thompson, D. W. Pipes and T. J. Meyer, *Inorg. Chem.*, 1984, **23**, 1845-1851.
26. D. J. Wasylenko, C. Ganesamoorthy, B. D. Koivisto, M. A. Henderson and C. P. Berlinguette, *Inorg. Chem.*, 2010, **49**, 2202-2209.
27. R. Dawson, D. Elliott, W. Elliott and K. Jones, *Data For Biochemical Research*, Oxford Science Publication, 1985.
28. P. K. Glasoe and F. A. Long, *J. Phys. Chem.*, 1960, **64**, 188-190.
29. F. Neese, *WIREs Comput. Mol. Sci.*, 2012, **2**, 73-78.
30. A. Klamt, *J. Phys. Chem.*, 1995, **99**, 2224-2235.
31. S. Sinnecker, A. Rajendran, A. Klamt, M. Diedenhofen and F. Neese, *J. Phys. Chem. A*, 2006, **110**, 2235-2245.
32. C. Adamo and V. Barone, *J. Chem. Phys.*, 1999, **110**, 6158-6170.
33. S. Grimme, J. Antony, S. Ehrlich and H. Krieg, *J. Chem. Phys.*, 2010, **132**, 154104.
34. S. Grimme, S. Ehrlich and L. Goerigk, *J. Comput. Chem.*, 2011, **32**, 1456-1465.
35. A. Schaefer, H. Horn and R. Ahlrichs, *J. Chem. Phys.*, 1992, **97**, 2571.
36. D. Andrae, U. Häußermann, M. Dolg, H. Stoll and H. Preuß, *Theor. Chim. Acta*, 1990, **77**, 123-141.
37. F. Weigend and R. Ahlrichs, *Phys. Chem. Chem. Phys.*, 2005, **7**, 3297-3305.

CHAPTER 3

A microtubule-targeted rigidin analogue
caged by a ruthenium polypyridyl complex
that can be released with green light

This chapter is to be submitted as a full paper: Vincent H.S. van Rixel, Tugba Ozel, Tania Betancourt, Lucien N. Lameijer, Alexander Kornienko, Sylvestre Bonnet, *manuscript in preparation*.

3.1 Introduction

Microtubules play an essential role in mitosis, specifically in the separation of duplicated chromosomes before the cell divides.¹ This feature makes them a potential target for novel chemotherapeutic agents. Paclitaxel, a taxane drug used in clinics to treat various forms of breast, ovarian, and non-small cell lung cancer, promotes polymerization of stable and dysfunctional microtubules that in the end causes cell death.² However, side effects associated with the use of paclitaxel are not uncommon, and include neutropenia, neurotoxicity, and disturbances in cardiac rhythm.^{3, 4} Additionally, cancer cell resistance to paclitaxel therapy limits its clinical efficacy making the development of alternative microtubule-targeting agents an important area of research.

One family of alternative compounds are analogues derived from marine alkaloid rigidins.^{5, 6} These rigidins have shown cytotoxic activity in the low-nanomolar range, trigger complete collapse of mitotic microtubule organization *in vitro*, and result in significant tumor growth reduction *in vivo*. However, drug uptake by healthy tissues causing side effects can always jeopardize the success of a drug. In this work we investigated the functionalization of the original 7-deaxahypoxanthines with a thioether group at the C2-position, and coordination of this thioether to a light-activatable ruthenium complex, a strategy called 'photocaging'.⁷⁻¹⁵ Upon light irradiation, the metal complex undergoes a photosubstitution reaction in which the ligand is released and can interact with its biological target. Photocaging is part of the phototherapeutic approach of photoactivated chemotherapy (PACT), a concept in which a metal complex is prevented from interaction with biological molecules in the dark.¹³ After light activation the metal complex is structurally modified, commonly through the release of a ligand, and then either the free ligand or complex (or both) may bind to their targets. Overall, the photochemical local activation of anticancer prodrugs in cancerous tissue should limit the toxicity of the treatment to the irradiated tumor, thus lowering side effects that stem from the general toxicity of biologically active compounds.

Ruthenium(II) polypyridyl complexes belong to the most widely investigated PACT compounds due to their well-known and tunable light absorption properties. For example, irradiation of RuBiGABA-2 (see Figure 3.1) developed by

Etchenique releases γ -aminobutyric acid, which was shown to induce a motoneural response in leech ganglions.¹⁶ In another example from Turro the nitrile analogue 5CNU of clinically approved anticancer compound 5-fluorouracil was caged with ruthenium, triggering to form $[\text{Ru}(\text{tpy})(5\text{-CNU})_3]\text{Cl}_2$ (Figure 3.1) phototoxicity in HeLa cells as demonstrated by a qualitative SYTOX assay.⁷ Recently, our group reported toxic ruthenium polypyridyl complexes that photosubstitute sulfoxide or thioether ligands upon blue or green light activation, and induce a phototoxic response in human cancer cell lines.¹⁷⁻¹⁹ In this chapter the successful caging of the thioether-containing rigidin 7-deazahypoxanthines **1** (provided by Dr. Alexander Kornienko) by a $[\text{Ru}(\text{tpy})(\text{bpy})]^{2+}$ moiety that can be released upon green light irradiation is reported. To the best of our knowledge, this is the first example of an anticancer drug with a well-defined target, which is caged by a ruthenium complex. Quantitative *in vitro* data on cancer cell cytotoxicity in the dark and after light irradiation is provided, including strong evidence that confirms the light-controllable the interaction of our drug with the microtubules.

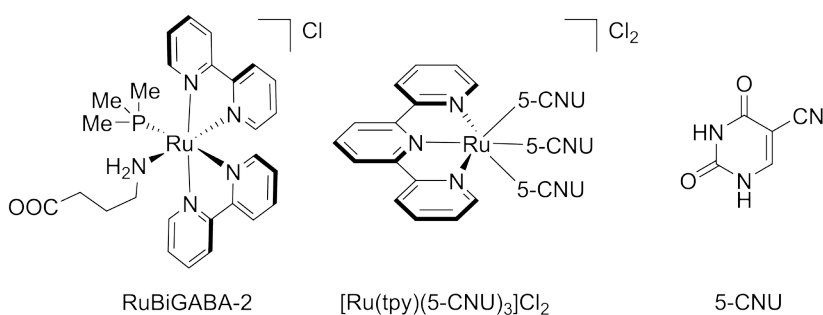


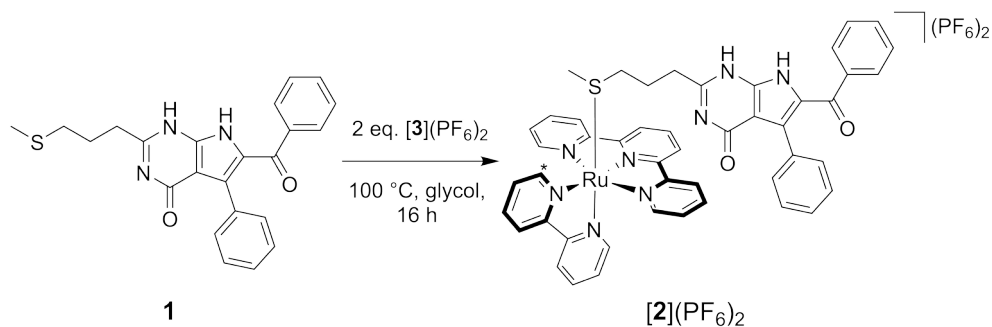
Figure 3.1 Chemical structures of RuBiGABA-2, $[\text{Ru}(\text{tpy})(5\text{-CNU})_3]\text{Cl}_2$, and 5-CNU.

3.2 Results

3.2.1 Synthesis

Complex $[\text{Ru}(\text{tpy})(\text{bpy})(\mathbf{1})](\text{PF}_6)_2$ (**[2]**(PF₆)₂) was synthesized by reacting **1** with 2 equivalents of $[\text{Ru}(\text{tpy})(\text{bpy})(\text{OH}_2)](\text{PF}_6)_2$ (**[3]**(PF₆)₂) as shown in Scheme 3.1. ¹H NMR spectroscopy showed the characteristic upfield shift at 1.47 ppm of the coordinated SMe group, that is normally found around > 2.0 ppm in protic solvents

for these type of complexes. Comparison with the free ligand is lacking due to its poor solubility in protic solvents.²⁰ Further NMR spectroscopy and elemental analysis showed that the compound was pure, and high resolution mass spectrometry confirmed the successful synthesis of $[2](PF_6)_2$.



Scheme 3.1 Synthesis scheme of $[2](PF_6)_2$. * indicates the A6 proton of the bpy ligand.

3.2.2 Photochemistry

Under green light irradiation ($\lambda_{irr} = 530\text{ nm}$) of a solution of $[2](PF_6)_2$ in acetonitrile in a nitrogen atmosphere, a significant increase of the absorbance at 452 nm and a slight shift of the maximum of the 1MLCT band from 452 nm to 454 nm were observed (Figure 3.2). Under these conditions a steady state was obtained after 30 minutes (inset in Figure 3.2). Mass spectrometry (MS) of the solution after light irradiation showed peaks at $m/z = 266.4$ corresponding to $[Ru(tpy)(bpy)(CH_3CN)]^{2+}$ (calc. $m/z = 266.1$, Figure SIII.1), whereas MS of the dark control showed a major signal at $m/z = 447.0$ corresponding to $[2]^{2+}$ (calc. $m/z = 447.1$, Figure SIII.1). Thus, under irradiation ligand **1** was photosubstituted by a solvent molecule. Similar evolutions were observed under blue light irradiation (450 nm, Figure SIII.2) and under such conditions a photosubstitution quantum yield Φ_{Ps} of 0.0060 was obtained. The photoreaction was also monitored by 1H NMR. After 5 minutes irradiation by white light the characteristic A6 proton (Scheme 3.1) at 9.66 ppm from the bpy ligand was fully replaced by a peak at 9.59 ppm characteristic for $[Ru(tpy)(bpy)(CH_3CN)]^{2+}$, indicating full conversion of the photoreaction of $[2]^{2+}$ (Figure SIII.3).²¹ Also, the initial singlet peak at 1.32 ppm indicating coordinated SME is fully replaced by a singlet peak at 2.54 ppm for non-coordinated **1**. When the same light irradiation reaction was performed in demineralized water and followed by UV-vis spectroscopy, Rayleigh scattering occurred quickly due to

precipitation of the free ligand **1**, which is poorly soluble in water with a maximum solubility of 10 μM in demineralized water (Figure SIII.4). Thus, it can be concluded that the Ru-S bond of $[\mathbf{2}]^{2+}$ is photoactivatable in CH_3CN and aqueous solution using either blue, green, or white light.

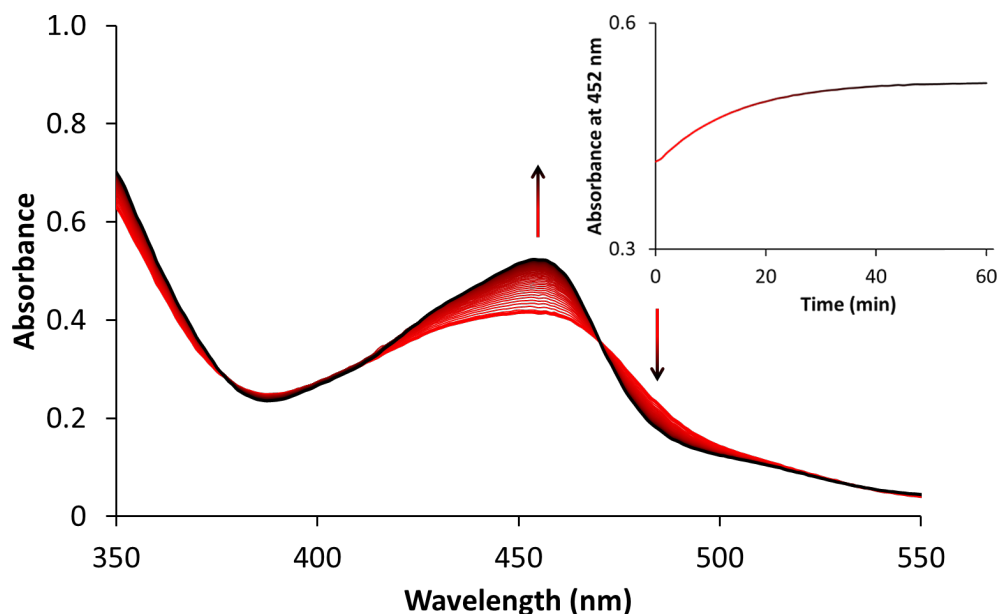


Figure 3.2 Evolution of the electronic absorption spectra of a solution of $[\mathbf{2}](\text{PF}_6)_2$ in acetonitrile upon green light irradiation under nitrogen ($\lambda = 530 \text{ nm}$, $\Delta\lambda_{1/2} = 17 \text{ nm}$, 6.0 mW , photon flux $4.1 \times 10^{-8} \text{ mol}\cdot\text{s}^{-1}$). Time: 0 min (red curve) to 30 min (black curve) Conditions: $[\text{Ru}]_0 = 50 \mu\text{M}$, $V = 3.00 \text{ mL}$, $T = 293 \text{ K}$. Inset: Plot of the absorbance at 452 nm as a function of irradiation time.

3.2.3 (Photo)toxicity studies

To demonstrate whether cytotoxicity of $[\mathbf{2}](\text{PF}_6)_2$ could be controlled by light activation, an *in vitro* photocytotoxicity assay was performed. The cytotoxicity of **1**, $[\mathbf{2}](\text{PF}_6)_2$, and $[\mathbf{3}](\text{PF}_6)_2$ was investigated against cancerous A375, A431, and A549 cells, and non-cancerous MRC-5 cells. $[\mathbf{3}](\text{PF}_6)_2$ was included in the assay to ensure that cytotoxicity does not originate from the metal cage, while cisplatin was included as positive control. Cell growth inhibition effective concentrations (EC_{50}), defined as the compound concentration that reduces cell viability by 50% compared to untreated cells, were measured in the dark and after light activation

following a protocol adapted from Hopkins et al.²² and the results are reported in Table 3.1. In the dark EC₅₀ values between 0.16 μM and 0.23 μM were found for **1** in A375, A431, and MRC-5 cells, and a higher value of 6.5 μM was found for A549 cells. Compound [**3**](PF₆)₂ showed no activity across all tested cell lines, which is in agreement with previous findings,¹⁹ while treatment with cisplatin resulted in EC₅₀ values in the expected micromolar range, i.e. between 0.85-3.1 μM. For the caged compound [**2**](PF₆)₂ in the dark, EC₅₀ values of 7-14 μM in A375, A431, and MRC-5 cells were observed, while for A549 cells an EC₅₀ value of 35 μM was measured. Thus, caging of **1** to the [Ru(tpy)(bpy)]²⁺ moiety strongly inhibited, up to 83 times for MRC-5 cells, the cytotoxicity of the microtubule inhibitor in the dark.

Table 3.1 Cell growing inhibition effective concentrations (EC₅₀ values with 95% confidence interval in μM) of **1, [**2**](PF₆)₂, [**3**](PF₆)₂, and cisplatin on skin (A375, A431) and lung (A549) cancer cell lines. The photo index (PI), defined as EC_{50,dark}/EC_{50,light}, are also indicated. Toxicity of the compounds in non-cancerous lung cell line (MRC-5) were also tested for comparison.**

Cell Line	Light dose (J.cm ⁻²)	1		[2](PF ₆) ₂		P.I	[3](PF ₆) ₂		cisplatin	
		EC ₅₀ (μM)	±CI	EC ₅₀ (μM)	±CI		EC ₅₀ (μM)	EC ₅₀ (μM)	±CI	
A375	0	0.16	-0.053 +0.079	6.8	-1.4 +1.7	21	> 100	0.85	-0.079 +0.087	
	38	0.20	-0.069 +0.11	0.33	-0.11 +0.16		> 100	0.87	-0.062 +0.067	
A431	0	0.23	-0.028 +0.032	14	-3.0 +3.9	28	> 100	2.8	-0.28 +0.31	
	38	0.24	-0.038 +0.045	0.49	-0.059 +0.067		> 100	3.1	-0.37 +0.43	
A549	0	6.5	-1.5 +2.0	35	-8.7 +12	4	> 100	1.3	-0.41 +0.62	
	38	3.4	-0.47 +0.54	9.2	-4.0 +7.1		> 100	2.0	-0.30 +0.36	
MRC-5	0	0.17	-0.07 +0.13	8.1	-1.4 +1.7	9	> 100	1.5	-0.20 +0.23	
	38	0.34	-0.15 +0.27	0.67	-0.28 +0.49		> 100	2.2	-0.23 +0.26	

Green light (520 nm) was chosen for photochemical activation since *in vitro* and *in vivo* it is much less toxic to living cells than blue or UV-light.²²⁻²⁴ Preliminary studies in a 96-well plate (Figure SIII.5) demonstrated that under the conditions of our cell-irradiation setup (21 mW.cm⁻²) a 30 minutes irradiation time, corresponding to a dose of 38 J.cm⁻², was necessary to completely activate [2](PF₆)₂ (60 μM). Although a 38 J.cm⁻² dose of green light barely induced photocytotoxicity by itself, nor changed the cytotoxicity of the uncaged inhibitor **1**, the caging complex [3](PF₆)₂, or cisplatin (Table 3.1), the effect observed when the caged inhibitor [2](PF₆)₂ was irradiated was remarkable for all cell lines tested. EC₅₀ values for A375, A431, A549, and MRC-5 cells were 0.33, 0.49, 9.2, and 0.67 μM, leading to phototoxic indices of 21, 28, 4, and 12, respectively. Figure 3.3 shows, as an example, the dose-response curves for A431 cells treated with **1** (brown curve), [2](PF₆)₂ in the dark (black curve), [2](PF₆)₂ irradiated with green light (green curve), and [3](PF₆)₂ in the dark (grey curve). The data suggests that [Ru(tpy)(bpy)]²⁺ is an excellent photocaging agent for **1** as Ru-coordination strongly reduces the cytotoxicity of **1**, while photosubstitution performed in living cells restores a high toxicity typical for ligand **1**.

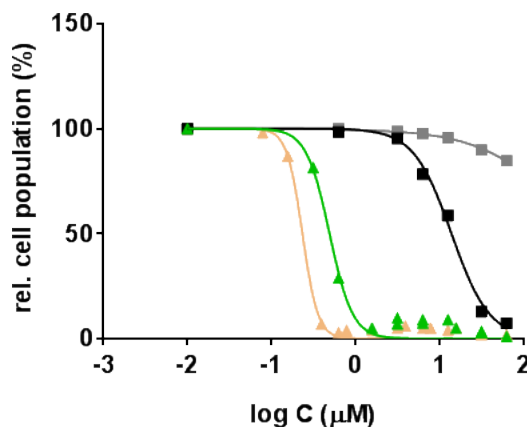


Figure 3.3 Dose response curves for A431 cells incubated with **1** in the dark (light brown), [2](PF₆)₂ in the dark (black), [2](PF₆)₂ with green light irradiation (green), and [3](PF₆)₂ in the dark (grey). Phototoxicity assay: cells seeded at 8×10^3 cells/well at $t = 0$ h, treated at $t = 24$ h, irradiated at $t = 30$ h, and SRB assay performed at $t = 96$ h. Conditions: $T = 37$ °C, $v/v\%$ CO₂ = 7%, $\lambda_{irr} = 520$ nm, light dose = 38 J.cm⁻².

3.2.4 Tubulin polymerization assay

In order to investigate how caging and photoactivation influences the ability of compound [2](PF₆)₂ to interact with its biological microtubule target, a fluorescence-based tubulin polymerization assay was performed by Dr. Tania Betancourt to compare the tubulin polymerization properties of [2](PF₆)₂ in the dark and under light irradiation. In this assay tubulin polymerization leads to a marked increase of the fluorescence intensity. The control compound paclitaxel, which strongly stabilizes the polymerized microtubule, showed as expected a rapid rise in fluorescence that stabilized after 30 minutes, indicating nucleation, growth, and a steady state equilibrium, of the microtubule formulation as shown in Figure 3.4.⁵ Fluorescence of an untreated sample initially shows a slight reduction in intensity and then stabilizes around its original value as shown by the dashed curve in Figure 3.4. Treatment of the tubulin mixture with the caged inhibitor [2](PF₆)₂ (25 μM, black curve) showed, in the dark, an overall increase in fluorescence after 60 minutes which was slower and less prominent than that measured for paclitaxel. Treatment with the caged inhibitor [2](PF₆)₂ (25 μM) activated by green light irradiation (30 min, 21 mW.cm⁻²) showed no increase in fluorescence at all. These results demonstrate that indeed upon treatment with non-activated [2](PF₆)₂ tubulin polymerization is possible, i.e., the caged inhibitor does not inhibit polymerization, whereas after green light activation of [2](PF₆)₂ tubulin polymerization is inhibited. In other words, green light irradiation uncages the inhibitor **1** efficiently. To conclude, microtubule polymerization is controlled by light. Green light activation of [2](PF₆)₂ inhibits microtubule polymerization by release of **1**.

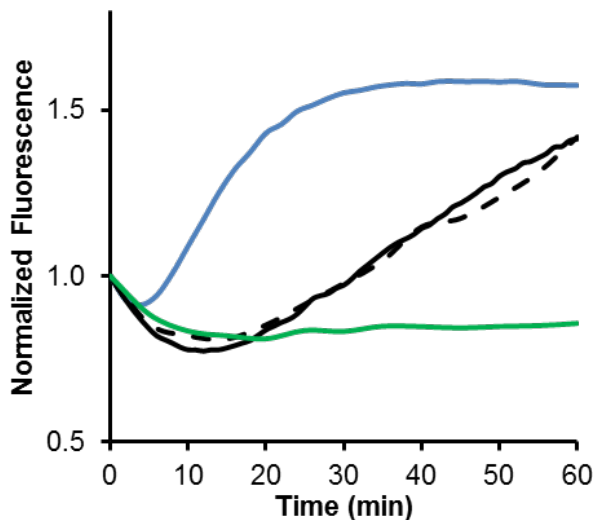


Figure 3.4 Evolution of tubulin polymerization $[2](PF_6)_2$ in the dark (25 μM , black curve), green light-activated $[2](PF_6)_2$ (25 μM , green curve), Paclitaxel (3 μM , blue curve), and untreated sample (black dashed curve).

3.3 Discussion & Conclusion

In this chapter we have demonstrated that the microtubulin-targeted rigidin thioether conjugate **1** can be caged by $[Ru(tpy)(bpy)]^{2+}$. *In vitro* green light photosubstitution of the ruthenium-caged rigidin in $[2](PF_6)_2$ induces an up to 28-fold increase in cytotoxicity with values that are similar to that of the uncaged compound **1**. As many microtubule-targeting compounds are used in the clinic as anticancer compounds,^{1, 25, 26} the herein presented strategy of ruthenium caging and green light photorelease provides a basis for a new cancer-targeted photoactivated chemotherapy. This strategy is clearly distinct from the approach of organic chemists in photopharmacology, where azobenzene-functionalized protein inhibitors are switched ‘on’ and ‘off’ via *cis-trans* photoisomerization.²⁷⁻³⁰ Coordination of an inhibitor to a light-sensitive metal complex, as proposed in this work, can overcome several issues associated with the azobenzene isomerization approach. First, in photopharmacology the light activation wavelength is crucial. Low-energy green or red light can penetrate into tissues much deeper, and is less harmful, than high-energy UV or blue light. Although recently some azobenzenes have been developed that can be activated by visible or even red light,³¹⁻³³ ruthenium polypyridyl chemistry provides a solid, tunable, and predictive fundament for making photopharmacological agents that can be activated by

visible light.^{13, 34-37} Second, as azobenzenes have a low or no dipole moment, especially in their *trans* form, they are highly lipophilic and poorly water-soluble. Ruthenium complexes on the other hand are typically positively charged molecules, which can enhance water solubility. Next, contrary to azobenzenes the modification of the cage does not alter too much the photoactivation kinetics. Last but not least, light activation of metal-based PACT compounds usually entails an irreversible process, whereas *cis-trans* photoisomerization of azobenzenes is notoriously reversible. Permanent activation of azobenzene-functionalized compounds would require permanent irradiation to maintain activity. On the other hand, it may provide opportunities for limiting systemic toxicity to the activated area, as when not irradiated the compound turns back into a non-toxic form. With metal caging, irreversible activation at the place of irradiation may be followed by diffusion of the activated drugs in other places, which for *in vivo* applications, would need to be controlled.

In the development of anticancer drugs both organic and inorganic chemists cope with similar problems, i.e. drug resistance, dose-limiting side effects, and poor water solubility. In this chapter the use of combining organic chemistry, which offers stable compounds and well-defined targets, with inorganic caging compounds, which can reduce dark toxicity, increase water solubility, and allow for irreversible uncaging using visible light, demonstrates how both fields are complementary. By crossing research borders, innovative solutions can be found that can contribute to ground-breaking developments in photopharmacology and science.

3.4 Experimental

3.4.1 Materials and methods

All NMR spectra were recorded on a Bruker AV-500 spectrometer. Chemical shifts are indicated in ppm relative to tetramethylsilane. Mass spectra were recorded by using a MSQ Plus Spectrometer positive ionization mode. UV-vis experiments were performed on a Cary 50 Varian spectrometer equipped with a Cary Single Cell Peltier for temperature control.

3.4.2 Synthesis of [Ru(tpy)(bpy)(1)](PF₆)₂ ([2](PF₆)₂)

First, **1** and [3](PF₆)₂ were synthesized according to literature procedures.^{5, 21} Then, in a 2-necked round-bottom flask [3](PF₆)₂ (75 mg, 0.48 mmol) and **1** (22 mg, 0.25 mmol) were added in ethylene glycol (10 mL) under argon. The solution was stirred overnight at 100 °C

under argon resulting in a red solution. The reaction mixture was added to a CH₂Cl₂ and KPF₆ saturated water mixture. After full extraction to the CH₂Cl₂ layer, the combined CH₂Cl₂ layers were washed with KPF₆ saturated water to remove ethylene glycol. After evaporation *in vacuo*, the crude was dissolved in acetone and purified by size exclusion chromatography (Sephadex LH-20, acetone). After evaporation *in vacuo*, the product was reprecipitated from acetone by the addition of diethyl ether, filtered, and obtained as a red powder. Yield: 13 mg (20%). ¹H NMR (500 MHz, CD₃OD, 293 K, in ppm): δ = 9.74 (d, J = 5.5 Hz, 1H, A6), 8.82 (d, J = 8.0 Hz, 1H, A3), 8.72 (d, J = 8.0 Hz, 2H, D3 + D3'), 8.69 (d, J = 8.0 Hz, 1H, B3), 8.51 (t, J = 8.0 Hz, 2H, C3 + C3'), 8.39 (dd, J = 8.0, 1.2 Hz, 1H, A4), 8.37 (dd, J = 8.4, 1H, D4), 8.03 (ddd, J = 7.8 Hz, 5.5 Hz, 1.5 Hz, 1H, A5), 7.95 (dd, J = 8.0 Hz, 2H, C4 + C4'), 7.92 (dd, J = 7.5 Hz, 1.5 Hz, 1H, B4), 7.73 (d, J = 5.5 Hz, 2H, C6), 7.52 (dd, J = 8.5, 1.0 Hz, 2H, Ph), 7.35 (ddd, J = 0.5, 6.0, 6.0 Hz, 2H, C5), 7.32-7.18 (m, 5H, Ph + B5), 7.14-7.05 (m, 5H, Ph + B6), 2.63 (t, J = 6 Hz, 2H, CH₂), 1.91 (p, J = 7.0 Hz, 2H, CH₂), 1.91 (t, J = 7.5 Hz, 2H, CH₂), 1.47 (s, 3H, CH₃). ¹³C NMR (125 MHz, CD₃OD, 293 K, in ppm): δ = 190.4 (C=O), 161.7 (pp), 159.2 (pp), 158.8 (pp), 158.7 (pp), 158.1 (pp), 158.1 (pp), 154.2 (Ph), 153.0 (Ph), 151.2 (Ph), 150.8 (Ph), 140.1 (Ph), 139.6 (C4), 138.6 (py-q), 138.3 (D4), 133.7 (py-q), 133.3 (A6), 132.6 (Ar), 130.6 (Ar), 129.7 (Ar-q), 129.4 (Ar-q), 129.2 (A5), 129.1 (C5), 128.9 (Ar), 126.1 (C3'), 126.0 (C3), 125.4 (A3), 125.2 (D3), 32.8 (CH₂₊), 32.80 (CH₂₋), 23.7 (CH₂), 14.6 (CH₃). *Elem. Anal. Calcd. for C₄₈H₄₀F₁₂N₈O₂P₂RuS*: C, 48.69; H, 3.41; N, 9.46. Found: C, 49.35; H, 3.53; N, 9.32. *High resolution ES MS m/z (calc): 447.10198 (447.1019, [M - 2×PF₆]²⁺)*.

3.4.3 Photochemistry

The UV-vis spectroscopy study shown in Figure 3.2 was performed using a UV-vis spectrometer equipped with temperature control set to 298 K. The measurements were performed in a quartz cuvette, containing 3 mL of solution in CH₃CN or water. The stirred sample was degassed by nitrogen, irradiated perpendicularly to the axis of the spectrometer by the beam of a green (λ = 530 nm, Δλ_{1/2} = 25 nm, 3.02 mW, photon flux 2.1 × 10⁻⁸ mol.s⁻¹) or blue (λ = 445 nm, Δλ_{1/2} = 11 nm, 10.5 mW, photon flux 1.27 × 10⁻⁷ mol.s⁻¹) LED fitted to the top of the cuvette, and an absorption spectrum was measured at regular time intervals and analyzed using Microsoft Excel. Mass spectrometry was performed at the beginning and at the end of the irradiation to confirm the nature of the reagent and products. The ¹H NMR spectroscopy study of Figure SIII.3 was performed using the white light of a LOT 1000 W Xenon Arc lamp mounted with an infrared and a long pass filter.

3.4.4 Green light irradiation in the cell irradiation set-up

The photochemical reactivity of [2](PF₆)₂ was measured in 96-well plates by dissolving it in cell culturing medium (Opti-MEM complete, 31 μM), followed by irradiation using the green light of the irradiation setup used for cell irradiation (520 nm, 38 J.cm⁻²) to mimic the conditions of the photocytotoxicity assay. Figure SIII.5 shows that the absorbance change at

300 nm for [2](PF₆)₂ after 30 minutes irradiation is leveling off as in no further activation occurs after 30 minutes.

3.4.5 Phototoxicity assay

See Appendix I for comprehensive description of the assay.

3.4.6 Tubulin polymerization assay

For investigation of the ability of the drug to inhibit the polymerization of tubulin in its caged ([2](PF₆)₂) and uncaged form (1), the fluorescence-based Tubulin Polymerization Assay (Cat. # BK011P) from Cytoskeleton, Inc. Prior was used to conduct the assay, a 2 mM stock solutions of paclitaxel and 16.7 mM solutions of the caged drug and the uncaged drug were prepared in DMSO. These drug stock solutions were then diluted to 250 μM with water to provide aqueous solutions of each drug with a constant DMSO content of 1.5% v/v. At this point, 40 μL samples of the caged drug were pipetted into separate black 96-well plates for irradiation with blue or green light independently. The solutions of the caged drug were then irradiated with either a blue LED (LED Engin LZ1-00B200, 450 nm) or a green LED (LED Engin LZ1-10G102-0000, 523 nm) driven with a BK Precision DC power supply 1630. Light power was measured with a Thorlabs PM50 photometer. Specifically, the appropriate power (W) of light were detected through a 0.6 cm-diameter circular well from a 96-well plate. The green light was used at a power density of 21 mW.cm⁻² (6 mW, 0.28 cm² well). The samples were irradiated for a total of 30 minutes in 10-minute intervals for a total laser exposure of 38 J.cm⁻². The absorption spectrum of the drug solutions were collected before and after each 10 minutes of irradiation.

For the assay, the following reagents were used. Buffer A contained 80 mM piperazine-N,N'-bis[2-ethanesulfonic acid] sequisodium salt, 2 mM MgCl₂, 0.5 mM ethylene glycol-bis(B-amino-ethyl ether)-N,N,N',N'-tetraacetic acid pH 6.9, and 10 μM fluorescent reporter. Tubulin glycerol buffer contains 80 mM piperazine-N,N'-bis[2-ethanesulfonic acid] sequisodium salt, 2 mM MgCl₂, 0.5 mM ethylene glycol-bis(B-amino-ethyl ether)-N,N,N',N'-tetraacetic acid pH 6.9, and 60% v/v glycerol. Guanosine triphosphate (GTP) stock contains 100 mM. Finally, a tubulin protein stock solution at 10 mg/mL was prepared in a 0.001% v/v solution of GTP in buffer A.

The tubulin reaction mixture used in the assay was prepared by combining 243 μL of buffer A, 112 tubulin glycerol buffer, 4.4 μL of GTP stock, and 85 μL of tubulin stock. This reaction mixture was kept on ice until used within 30 minutes of preparation. A Biotek Synergy H4 hybrid multi-mode plate reader was pre-heated to 37 °C. Prior to starting the assay, a half-area black 96-well plate was preheated within the plate reader. A volume of 5 μL of each of the samples was pipetted into separate wells of the plate and incubated in the warm plate reader for 1 minute. A volume of 45 μL of the tubulin reaction mixture was then mixed into

each of the wells, thereby diluting the drug solutions to the final concentration of 25 μM (total DMSO content of 0.15%). The fluorescence of the samples ($\lambda_{\text{irr}} = 360/20 \text{ nm}$, $\lambda_{\text{em}} = 485/20 \text{ nm}$) was then recorded every minute for 60 minutes. Paclitaxel at a final concentration of 3 μM was used as a tubulin polymerization inducing control.

3.5 References

1. M. A. Jordan and L. Wilson, *Nat. Rev. Cancer*, 2004, **4**, 253-265.
2. E. K. Rowinsky and R. C. Donehower, *N. Engl. J. Med.*, 1995, **332**, 1004-1014.
3. A.-L. Salmela and M. J. Kallio, *Chromosoma*, 2013, **122**, 431-449.
4. M. Markman, *Supp. Care Cancer*, 2003, **11**, 144-147.
5. D. C. Medellin, Q. Zhou, R. Scott, R. M. Hill, S. K. Frail, R. Dasari, S. J. Ontiveros, S. C. Pelly, W. A. L. van Otterlo, T. Betancourt, C. B. Shuster, E. Hamel, R. Bai, D. V. LaBarbera, S. Rogelj, L. V. Frolova and A. Kornienko, *J. Med. Chem.*, 2016, **59**, 480-485.
6. L. V. Frolova, I. V. Magedov, A. E. Romero, M. Karki, I. Otero, K. Hayden, N. M. Evdokimov, L. M. Y. Banuls, S. K. Rastogi, W. R. Smith, S.-L. Lu, R. Kiss, C. B. Shuster, E. Hamel, T. Betancourt, S. Rogelj and A. Kornienko, *J. Med. Chem.*, 2013, **56**, 6886-6900.
7. M. A. Sgambellone, A. David, R. N. Garner, K. R. Dunbar and C. Turro, *J. Am. Chem. Soc.*, 2013, **135**, 11274-11282.
8. R. N. Garner, J. C. Gallucci, K. R. Dunbar and C. Turro, *Inorg. Chem.*, 2011, **50**, 9213-9215.
9. H. Chan, J. B. Ghayche, J. Wei and A. K. Renfrew, *Eur. J. Inorg. Chem.*, 2017, **2017**, 1679-1686.
10. N. Karaoun and A. K. Renfrew, *Chem. Commun.*, 2015, **51**, 14038-14041.
11. L. Zayat, C. Calero, P. Albores, L. Baraldo and R. Etchenique, *J. Am. Chem. Soc.*, 2003, **125**, 882-883.
12. Z. Chen, Y. Xiong, R. Etchenique and S. Wu, *Chem. Commun.*, 2016, **52**, 13959-13962.
13. C. Mari, V. Pierroz, S. Ferrari and G. Gasser, *Chem. Sci.*, 2015, **6**, 2660-2686.
14. M. Huisman, J. K. White, V. G. Lewalski, I. Podgorski, C. Turro and J. J. Kodanko, *Chem. Commun.*, 2016, **52**, 12590-12593.
15. K. Arora, J. K. White, R. Sharma, S. Mazumder, P. D. Martin, H. B. Schlegel, C. Turro and J. J. Kodanko, *Inorg. Chem.*, 2016, **55**, 6968-6979.
16. O. Filevich and R. Etchenique, *Photochem. Photobiol. Sci.*, 2013, **12**, 1565-1570.
17. V. H. S. van Rixel, B. Siewert, S. L. Hopkins, S. H. C. Askes, A. Busemann, M. A. Siegler and S. Bonnet, *Chem. Sci.*, 2016, **7**, 4922-4929.
18. L. N. Lameijer, S. L. Hopkins, T. G. Brevé, S. H. C. Askes and S. Bonnet, *Chem. Eur. J.*, 2016, **22**, 18484-18491.
19. B. Siewert, V. H. S. van Rixel, E. J. van Rooden, S. L. Hopkins, M. J. B. Moester, F. Ariese, M. A. Siegler and S. Bonnet, *Chem. Eur. J.*, 2016, **22**, 10960-10968.
20. R. E. Goldbach, I. Rodriguez-Garcia, J. H. van Lenthe, M. A. Siegler and S. Bonnet, *Chem. Eur. J.*, 2011, **17**, 9924-9929.
21. V. H. S. van Rixel, A. Busemann, A. J. Göttle and S. Bonnet, *J. Inorg. Biochem.*, 2015, **150**, 174-181.
22. S. L. Hopkins, B. Siewert, S. H. C. Askes, P. Veldhuizen, R. Zwier, M. Heger and S. Bonnet, *Photochem. Photobiol. Sci.*, 2016, **15**, 644-653.
23. T. J. McMillan, E. Leatherman, A. Ridley, J. Shorrocks, S. E. Tobi and J. R. Whiteside, *J. Pharm. Pharmacol.*, 2008, **60**, 969-976.
24. S. Wäldchen, J. Lehmann, T. Klein, S. van de Linde and M. Sauer, *Sci. Rep.*, 2015, **5**, 15348.
25. S. Prasad, S. C. Gupta and B. B. Aggarwal, *Trends Pharmacol. Sci.*, 2016, **37**, 435-450.
26. K. S. Chan, C. G. Koh and H. Y. Li, *Cell Death and Dis.*, 2012, **3**, e411.
27. J. Broichhagen, J. A. Frank and D. Trauner, *Acc. Chem. Res.*, 2015, **48**, 1947-1960.
28. W. A. Velema, W. Szymanski and B. L. Feringa, *J. Am. Chem. Soc.*, 2014, **136**, 2178-2191.
29. M. Dong, A. Babalhavaeji, S. Samanta, A. A. Beharry and G. A. Woolley, *Acc. Chem. Res.*, 2015, **48**, 2662-2670.
30. M. Schönberger and D. Trauner, *Angew. Chem., Int. Ed.*, 2014, **53**, 3264-3267.
31. S. Samanta, C. Qin, A. J. Lough and G. A. Woolley, *Angew. Chem., Int. Ed.*, 2012, **51**, 6452-6455.
32. S. Samanta, T. M. McCormick, S. K. Schmidt, D. S. Seferos and G. A. Woolley, *Chem. Commun.*, 2013, **49**, 10314-10316.
33. M. M. Lerch, M. J. Hansen, W. A. Velema, W. Szymanski and B. L. Feringa, *Nat. Comm.*, 2016, **7**, 12054.

34. S. Bonnet, *Comments Inorg. Chem.*, 2015, **35**, 179-213.
35. D. Crespy, K. Landfester, U. S. Schubert and A. Schiller, *Chem. Commun.*, 2010, **46**, 6651-6662.
36. J. D. Knoll, B. A. Albani and C. Turro, *Acc. Chem. Res.*, 2015, **48**, 2280-2287.
37. N. J. Farrer, L. Salassa and P. J. Sadler, *Dalton Trans.*, 2009, **48**, 10690-10701.

CHAPTER 4

Green light-induced apoptosis in cancer cells by a
tetrapyridyl ruthenium prodrug offering
two *trans* coordination sites

This chapter was published as an Edge Article: Vincent H.S. van Rixel, Bianka Siewert, Samantha L. Hopkins, Sven H.C. Askes, Anja Busemann, Maxime A. Siegler, Sylvestre Bonnet, *Chem. Sci.*, **2016**, *7*, 4922-4929.

4.1 Introduction

In classical chemotherapy side effects are a burden for patients, limit treatment doses, and thus lower chances on a successful outcome. Light-activated anticancer prodrugs have appeared as an alternative strategy to increase the selectivity of chemotherapeutic agents.¹⁻⁶ Ideally, their inactive form should interact minimally with biological molecules to limit the toxicity of the prodrug to non-irradiated tissues. Upon *in vivo* light irradiation these prodrugs are locally activated to selectively kill tumor cells. Light-activated ruthenium(II)-based compounds have been extensively studied due to their superior light absorption properties and rich photoreactivity. The majority of light-activated ruthenium-based anticancer compounds described to date belong to the class of photodynamic therapeutic agents (PDT agents) that generate singlet oxygen ($^1\text{O}_2$) as a means to locally kill cancer cells.⁷⁻¹⁵ For example, phase II clinical trials were recently completed with ruthenium-oligothiophene dyads TLD1411 and TLD1433, which are red-light-activated, water-soluble, and resistant to photobleaching.⁹ A less common family of ruthenium compounds consists of photoactivated chemotherapy agents (PACT agents), where visible light excitation (350-800 nm) leads to the cleavage of a protecting group. This irreversible photoreaction releases a toxic ligand,^{16, 17} modifies part of this ligand,^{18, 19} or generates open coordination sites on the metal center, which enables biological ligands to bind.^{20, 21} In PACT a light-induced modification of the interaction between the metal compound and biological molecules triggers cell death.^{17, 18, 20, 22-25} The major advantage of this mechanism of activation, compared to PDT, is that it does not depend on the presence of molecular oxygen, and hence may be applied to treat hypoxic tumors, a type of tumor characterized by low response to standard chemotherapy and fast cancer progression.²⁶

Many ruthenium PACT agents known to date contain two bidentate ligands based on the 2,2'-bipyridine scaffold.^{20, 27-30} After irradiation, bis-aqua photoproducts are formed with a *cis* configuration to mimic the binding pattern of cisplatin to DNA.^{31, 32} Transplatin on the other hand, is not active *in vivo* and less cytotoxic than cisplatin *in vitro*. Therefore, anticancer metallodrugs with a *trans* geometry, usually based on platinum(II), have not been considered until recently.³³⁻³⁶ New *trans* platinum(IV) compounds have also been prepared as PACT agents that can be activated with UV A (320-400 nm) or high-energy visible light (400-450 nm).^{21, 37}

This type of light is, however, harmful to cells³⁸⁻⁴⁰ and penetrates biological tissues sub-optimally.⁴¹ We embarked on developing ruthenium-based PACT agents with a *trans* geometry that can be activated at higher wavelengths, i.e., closer to the photodynamic window.⁴²

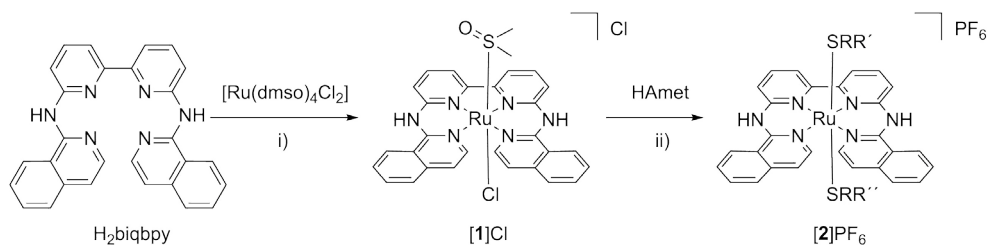
In this chapter we report on two *trans* ruthenium-based PACT compounds that can be activated using green light. The two ruthenium complexes, [Ru(H₂biqbpy)(dmsO)Cl]Cl (**[1]Cl**, H₂biqbpy = 6,6'-bis[N-(isoquinolyl)1-amino]-2,2'-bipyridine) and [Ru(H₂biqbpy)(Amet)(HAmet)]PF₆ (**[2]PF₆**, HAmet = N-acetyl-L-methionine, see Scheme 4.1), are based on a tetrapyridyl ligand (H₂biqbpy) specifically developed to coordinate in the basal plane of octahedral metal complexes and to leave two *trans* positions for the coordination of monodentate ligands.⁴³ In order to minimize interactions of the metal center with biomolecules in the dark, sulfur-based monodentate ligands were selected, i.e., one dmsO in **[1]Cl**, and a HAmet and Amet⁻ ligand in **[2]PF₆**, that can be removed by visible light irradiation.^{44, 45} The synthesis, photochemistry, and biological properties of these compounds are reported demonstrating that they can trigger apoptosis in human cancer cell lines upon green light irradiation.

4.2 Results and Discussion

4.2.1 Synthesis and characterization

Complex **[1]Cl** was synthesized by reacting H₂biqbpy with 1.1 equivalents of [Ru(dmsO)₄Cl₂] in ethanol overnight at 80 °C (Scheme 4.1). After filtration **[1]Cl** was obtained as a red-brown powder. Slow vapor diffusion of a methanol solution containing **[1]Cl** into ethyl acetate gave ruby-colored crystals suited for X-ray diffraction (Figure 4.1). In the structure of **[1]Cl** the ligand H₂biqbpy is coordinated to ruthenium(II) in a highly distorted fashion with an N1-N3-N4-N6 torsion angle of 12.78(9)°. The difference between the bond angle N1-Ru1-N6 = 97.90(8)° at the open-ended site of the complex and the angle N4-Ru1-N3 = 80.78(8)° at the bpy site demonstrates the distortion of the coordination octahedron. Strain is caused by the repulsion between the hydrogen atoms bound to C1 and C28, and forces **[1]⁺** to assume a helical, thus chiral configuration. The crystal structure of **[1]Cl**·MeOH is a racemate containing both the right-handed (*P*) and left-handed (*M*) helices.

Reacting [1]Cl with 20 equivalents of HAmet in water overnight at 80 °C was required to substitute both apical ligands by the monodentate thioethers (Scheme 4.1). Anion exchange to the PF₆ salt increased the lipophilicity of [2]⁺ allowing extraction of the compound using ethyl acetate. Purification using size exclusion chromatography resulted in analytically pure [2]PF₆. Coordination of two N-acetyl-L-methionine ligands was confirmed using high-resolution mass spectrometry (HRMS), NMR, and elemental analysis.



Scheme 4.1 Synthesis of [1]Cl and [2]PF₆. Conditions: i) 1.1 eq. [Ru(dmsO)₄Cl₂], 80 °C, in EtOH under argon, 16 h, yield 43%; ii) 20 eq. HAmet, 80 °C, in water under argon, 16 h, yield, 43%.

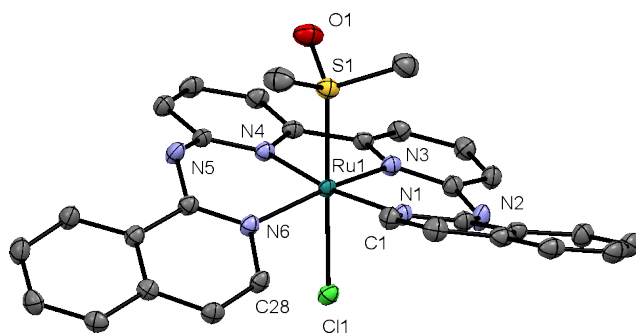
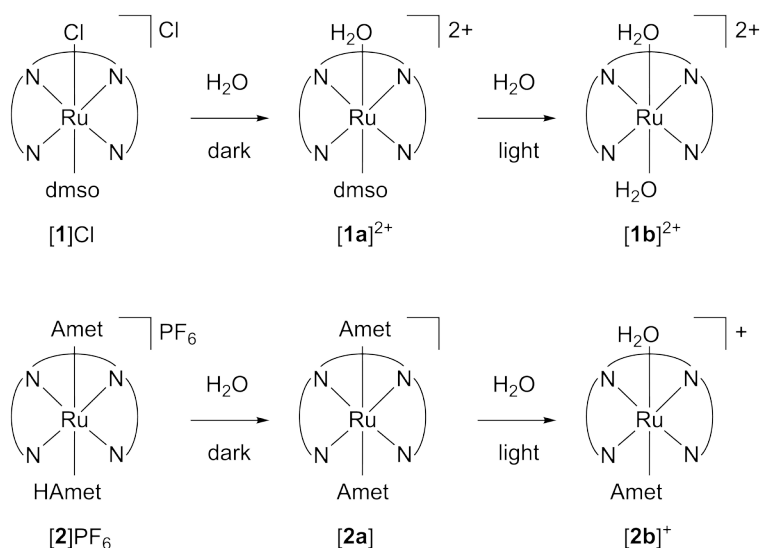


Figure 4.1 Displacement ellipsoid of cationic *M*-[1]⁺ (50% probability level) as observed in the crystal structure of ([1]Cl·CH₃OH). Chloride counter-anions, H atoms, lattice CH₃OH, and disorder, have been omitted for clarity.

4.2.2 Dark Stability

Testing the dark stability of anticancer metallodrugs under conditions relevant for biological testing is critical for interpreting uptake and cytotoxicity data. Stability assays were thus performed in the dark in aqueous and DMSO solutions. Like for cisplatin the dark stability of [1]Cl in aqueous solution depends on chloride concentration. According to ¹H NMR (Figure SIV.1) and mass spectrometry upon dissolution in deionized water or D₂O the chloride ligand of [1]⁺ immediately

dissociated to afford $[\text{Ru}(\text{H}_2\text{biqbp})\text{(dms)}(\text{H}_2\text{O})]^{2+}$ (**[1a]**²⁺, see Scheme 4.2). Upon adding NaCl the concentration of **[1]**⁺ increased, to reach a ratio **[1]**⁺:**[1a]**²⁺ in solution of 1:3 at 0.15 M of NaCl. The dark behavior of **[2]**PF₆ was quite different. Although the protonation of one HAmet ligand in the solid state is corroborated by elemental analysis, in aqueous solution at neutral pH the complex is deprotonated into the neutral species **[2a]** (Scheme 4.2). In D₂O, this species remained stable in the dark (Figure SIV.2). Overall, in aqueous solution **[2]**PF₆ appears as a ‘protected’ version of **[1]**Cl, as the hydrolysable Ru-Cl bond of **[1]**Cl has been replaced by a thermally stable Ru-S bond.



Scheme 4.2 Ligand exchange processes upon dilution of **[1]**Cl and **[2]**PF₆ in aqueous solutions, and upon green light irradiation.

4.2.3 Photoreactivity of **[1]**Cl and **[2]**PF₆

Green light irradiation ($\lambda_{\text{irr}} = 520 \text{ nm}$) under argon of a solution of **[1]**Cl in water resulted in a shift of the absorption maximum from 305 nm to 320 nm, and a slight increase of the absorbance in the visible region (Figure 4.2A). Mass spectrometry after light irradiation showed new peaks at $m/z = 288.7$ corresponding to $[\text{Ru}(\text{H}_2\text{biqbp})\text{(H}_2\text{O})_2]^{2+}$ (**[1b]**²⁺ in Scheme 4.2, calc. $m/z = 288.8$). Thus, the dms ligand was photosubstituted by water. This reactivity is typical for geometrically distorted ruthenium(II) compounds that possess low-lying triplet metal-centered (³MC) excited states with a strongly dissociative character.⁴⁶ ¹H NMR confirmed this analysis, as a new resonance at 2.72 ppm, characteristic of free dms, appeared

after green light irradiation, but not in the dark (Figure SIV.3). Similar evolutions were observed upon blue light irradiation (450 nm, Figure SIV.5), which also allowed to determine a photosubstitution quantum yield (Φ_{PS}) of 0.3%. Overall, cleavage of the Ru-S bond of **[1]**⁺ is a photochemical process, and compound **[1]Cl** can be seen as a semi-protected light-activated prodrug. One of the two apical ligands is thermally labile in water, while the other is only labile under visible light irradiation.

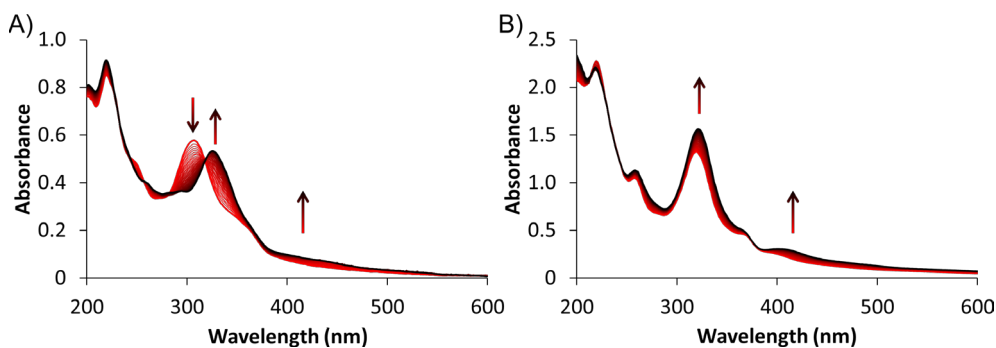


Figure 4.2 Evolution of the electronic absorption spectra of a solution of **[1]Cl** (a) and **[2]PF₆** (b) in demineralized water upon green light irradiation under argon ($\lambda = 530$ nm, $\Delta\lambda_{1/2} = 25$ nm, 3.02 mW, 2.1×10^{-8} mol.s⁻¹). Time: 0 min (red curve) to 120 min (black curve, a) or 160 min (black curve, b). Conditions $[Ru]_0 = 0.025$ mM (a), 0.078 mM (b), irradiated volume was 3.00 mL at 298 K.

For **[2]PF₆**, green light irradiation in aqueous solution under argon (Figure 4.2B) was accompanied by a higher intensity of the metal-to-ligand charge transfer (MLCT) absorption band near 400 nm and of the transition near 325 nm, and several isosbestic points. Mass spectrometry gave a clearer indication about the photoreaction occurring under these conditions. The initial peak at $m/z = 923.4$ characteristic for **[2]**⁺ (calc. $m/z = 923.2$) was gradually replaced by a signal at $m/z = 732.4$, characteristic for **[Ru(H₂biqbpy)(Amet)]⁺** (calc. $m/z = 732.1$), indicating the formation of **[Ru(H₂biqbpy)(Amet)(H₂)⁺**, **[2b]**⁺. A signal at $m/z = 605.1$ for **[Ru(H₂biqbpy)(MeOH)(OMe)]⁺** (calc. $m/z = 605.1$) or $m/z = 386.6$ for **[Ru(H₂biqbpy)(CH₃CN)₂]²⁺** (calc. $m/z = 387.1$) could only be obtained under extensive blue light irradiation (450 nm, see Figure SIV.6; MeOH and CH₃CN were solvents used for MS, respectively). Irradiation with high-energy visible light was hence necessary to form the bis-aqua complex **[1b]**²⁺ from **[2b]**⁺ (Scheme 4.2). Under

our conditions the formation of $[1b]^{2+}$ under green light irradiation was too slow to be observed. This result was confirmed by 1H NMR (Figure SIV.4), as only one ligand was photosubstituted by water under green light irradiation at a dose of $75 J.cm^{-2}$. In conclusion, complex $[2]PF_6$ is a water-soluble, fully protected complex: both *trans* N-acetyl-L-methionine ligands remain coordinated to the metal in the dark, while one of them is cleaved off by green light irradiation, and the second one is removed by high doses of blue light.

4.2.4 (Photo)cytotoxicity Studies

The cytotoxicity of compounds $[1]Cl$ and $[2]PF_6$ was investigated against three cell lines, i.e., A549 (human adenocarcinoma alveolar basal epithelial cells), A431 (human epidermoid carcinoma cells), and MRC-5 (noncancerous human foetal lung fibroblasts). The effective concentrations (EC_{50}), defined as the compound concentration that reduces cell viability by 50% compared to untreated wells, were measured, in the dark and after light activation, following a protocol described in details by Hopkins et al.³⁸ These studies aimed at establishing whether the photosubstitution reactions observed in a chemical environment may translate into *in vitro* light activation. Although both blue and green light resulted in photosubstitution, green light (520 nm) was chosen for the photocytotoxicity tests because it is much less toxic to human cell lines than blue light³⁸ and it penetrates further into biological tissues. Preliminary studies in a 96-well plate (Figure SIV.7, Figure SIV.8) demonstrated that under the conditions of the cell-irradiation setup ($21 mW.cm^{-2}$) a 60 min irradiation time, corresponding to a dose of $75 J.cm^{-2}$, was necessary to activate 0.8-1.6 nmol of the compounds (the maximum amount present in each well for concentrations of 40-80 μM). The EC_{50} of complexes $[1]Cl$, $[2]PF_6$, and cisplatin, against A431, A549, and MRC-5 cell lines, measured in the dark and after green light irradiation, are reported in Table 4.1.

In the dark, the EC_{50} values of ~ 10 and $\sim 35 \mu M$ were observed for $[1]Cl$ and $[2]PF_6$, respectively in A431 cells (Table 4.1). For the A549 cell line similar trends were observed with EC_{50} values of 6-9 μM for $[1]Cl$ and 11-20 μM for $[2]PF_6$. Thus, $[1]Cl$ has similar cytotoxicity in the dark as cisplatin, whereas the two thioether ligands in $[2]PF_6$ decreased the cytotoxicity by a factor of two to four compared to $[1]Cl$. This result suggested that coordination of the sulfur ligands slows down or diminishes the cellular response to these ruthenium compounds.

Whereas identical doses of green light did not induce photocytotoxicity by themselves (Figure SIV.9), nor modify the cytotoxicity of cisplatin (Table 4.1), a dramatically decreased cell population was observed when the cells were incubated with compound [1]Cl or [2]PF₆ for 6 h or 24 h, and then irradiated with 75 J.cm⁻² of green light (Table 4.1, Figure 4.4). For complex [1]Cl, EC₅₀ values close to 1 μM or lower were observed for all cell lines independently of when irradiation was performed. For A549 cells treated with complex [2]PF₆, the EC₅₀ decreased from 20 μM to 3.6 μM when irradiation occurred 6 h after treatment, and from 11 μM to 5 μM when it was done 24 h after treatment. Similar trends were observed for A431 cells.

After green light irradiation, complex [2]PF₆ showed cytotoxicity comparable to the dark toxicity of [1]Cl, although compound [2]PF₆ was less toxic in the dark than [1]Cl. For both compounds, the photo index (PI) was higher when irradiation occurred 6 h after treatment, compared to 24 h. This effect was mostly a consequence of lower EC₅₀ values in the dark after 24 h incubation, which suggested a higher degree of thermal activation with longer dark incubation times. Overall, these results suggest that the sulfur ligands of [1]Cl (dmsO) and of [2]PF₆ (HAMet) partially inhibit the cytotoxicity of the ruthenium center in the dark, and that ligand photosubstitution is accompanied by an increase of the cytotoxicity of the compound. In other words, selectivity is realized by light activation.

Table 4.1 Cytotoxicity (EC₅₀ with confidence interval (CI, 95%) in μM) of [1]Cl, [2]PF₆, and cisplatin on skin (A431) and lung (A549) cancer cell lines given with photo index (PI). In addition, the complexes were tested against a non-cancerous lung cell line (MRC-5) for comparison.

Cell line	t _{inc} (h)	Light dose (J.cm ⁻²)	[1]Cl			[2]PF ₆			cisplatin		
			EC ₅₀ (μM)	\pm CI (95%)	PI	EC ₅₀ (μM)	\pm CI (95%)	PI	EC ₅₀ (μM)	\pm CI (95%)	
A431	6	0	13	-1.2 +1.3	22	38	-7.2 +8.8	4.9	4.3	-1.1 +1.5	
		75	0.60	-0.04 +0.04		7.8	-0.90 +1.0		4.6	-1.2 +1.6	
	24	0	11	-0.56 +0.59	12	30	-3.8 +4.3	2.2	4.8	-1.2 +1.6	
		75	0.88	-0.19 +0.24		14	-1.0 +1.1		4.9	-1.2 +1.6	
	A549	6	0	9.3	-1.8 +2.3	16	20	-4.7 +6.1	5.5	3.1	-0.47 +0.55
			75	0.58	-0.07 +0.08		3.6	-0.75 +0.95		3.6	-0.64 +0.77
24		0	6.2	-0.76 +0.86	10	12	-1.0 +1.12	2.3	3.3	-0.47 +0.55	
		75	0.65	-0.06 +0.07		5.0	-0.41 +0.44		3.3	-0.46 +0.54	
MRC-5		6	0	8.5	-1.1 +0.98	5.3	8.5	-2.5 +3.5	> 8.5	3.8	-1.1 +1.5
			75	1.6	-2.4 +0.97		< 1	-		n.d.	-
	24	0	8.3	-0.90 +1.0	4.8	18	-1.3 +1.4	> 18	6.9	-1.0 +1.2	
		75	1.7	-0.99 +2.3		< 1	-		n.d.	-	

4.2.5 Singlet Oxygen Production

Due to the long-lived triplet excited states of many photostable ruthenium polypyridyl complexes, singlet oxygen ($^1\text{O}_2$) generation is often a dominant pathway leading to cytotoxicity upon light irradiation.^{5, 9, 47-50} However, photosubstitution reactions observed with distorted octahedral ruthenium(II) complexes often lead to quenching of their long-lived $^3\text{MLCT}$ states by nearby ^3MC excited states, which lowers the quantum yields of phosphorescence and $^1\text{O}_2$ generation. These trends present a unique opportunity for PACT, as the hypoxic conditions in many tumor tissues requires new oxygen-independent photoactivation strategies. In order to test whether compounds [1]Cl and [2]PF₆ would qualify better as PDT or as PACT agents their quantum yields of $^1\text{O}_2$ generation ($\Phi_{1\text{O}_2}$) were measured by Sven Askes under 450 nm excitation by direct detection of the 1274 nm infrared emission of $^1\text{O}_2$ in CD₃OD. The prototypical [Ru(bpy)₃]Cl₂ complex was used as a reference ($\Phi_{1\text{O}_2} = 73\%$).⁵¹ $\Phi_{1\text{O}_2}$ values of 1.3% and 2.3% were found for [1]Cl and [2]PF₆, respectively (Table SIV.1 and Figure SIV.11). According to these results, both [1]Cl and [2]PF₆ are extremely poor $^1\text{O}_2$ generators, and the photoactivation observed *in vitro* is not a PDT effect.

4.2.6 Light-induced Apoptosis

To investigate which type of cell death occurred, the morphology of A549 cells were inspected by Dr. Bianka Siewert in the dark and after green light irradiation using bright field microscopy (Figure 4.3 and Figure SIV.13). Directly after irradiation (520 nm, 75 J.cm⁻²), cells treated with [1]Cl (1.5 μM) displayed cell shrinkage, loss of cell-cell contact, and membrane blebbing as depicted in Figure 4.3B. An enhanced effect was detected when the cells were incubated for an additional 24 h after light irradiation (Figure 4.3D). The changes in cell morphology are characteristic for apoptotic cell death.^{52, 53}

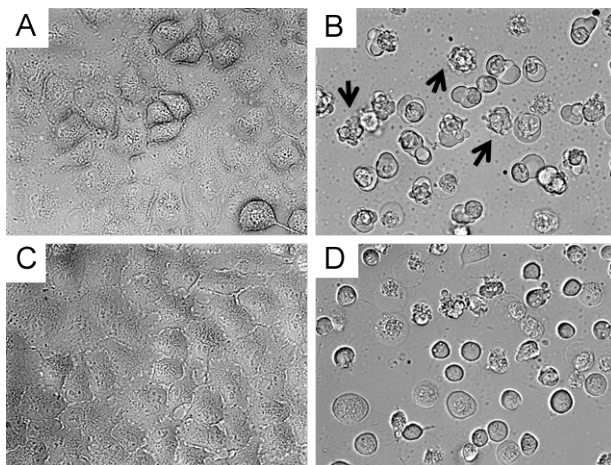


Figure 4.3 Bright field microscopy images (40 \times magnification) of A549 cells treated with [1]Cl (1.5 μ M) for 6 + 1 h in the dark (A) and 6 h in the dark followed by 1 h green light irradiation (B, 520 nm, 75 J.cm⁻²). Images (C) and (D) show sample A) and B) after an additional 24 h incubation in the dark. Arrows in (B) show examples of membrane-blebbing, which is characteristic for early apoptosis.

To confirm that a majority of the A549 cells treated with [1]Cl or [2]PF₆ and irradiated with green light died by apoptosis, their fate was investigated by Dr. Bianka Siewert using the Annexin V–propidium iodide assay and analyzed using flow cytometry (FC).⁵⁴ Figure 4.4 shows representative density plots of non-irradiated A549 cells treated with [1]Cl (1.5 μ M, Figure 4.4A) or [2]PF₆ (10 μ M, Figure 4.4C). The majority of the cells are in the lower left quadrant, i.e., alive. However, upon green light irradiation (1 h, 75 J.cm⁻²) a clear shift of the cell population to the bottom right quadrant indicates Annexin V binding for both [1]Cl and [2]PF₆ treated cells, thus apoptotic cells. The lack of cells in the top left quadrant indicates the absence of purely necrotic cells. Cells in the top right are commonly referred to as ‘secondary necrotic’, and are a known artefact in *in vitro* assays.

According to the FC data, the photocytotoxicity of [1]Cl and [2]PF₆ occurs *via* apoptosis without any sign of necrosis. In addition, confocal microscopy of A549 cells stained with tetramethylrhodamine ethyl ester (mitochondria) and DRAQ5 (nuclear DNA) showed that light irradiation diminished the mitochondrial membrane potential and induced chromosomal condensation, especially for [1]Cl (Figure SIV.14). All of the tested cellular responses clearly demonstrate that

compounds [1]Cl and [2]PF₆ belong to a rare sub-family of metallodrugs that can trigger apoptosis with green light.^{55, 56}

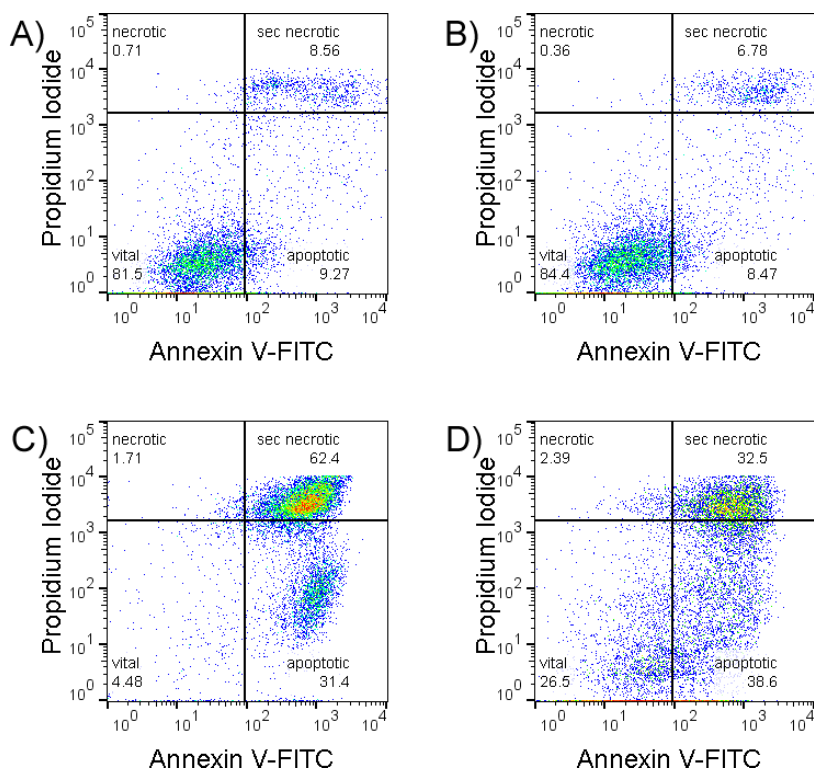


Figure 4.4 Representative flow cytometry density plots (Annexin V-FITC (525 nm)/Propidium iodide (670 nm) of A549 cells incubated with [1]Cl (1.5 μM) in the dark for 6 + 1 + 24 h (a), or in the dark for 6 h, followed by irradiation with green light for 1 h, followed by 24 h incubation (b) or treated with [2]PF₆ (10 μM) and left in the dark for 31 h (c) or irradiated 1 h with green light 6 h after treatment and further incubated for 24 h in the dark (d). Irradiation conditions: 520 nm, 60 min, 75 J.cm⁻². Quantification: see Figure SIV.12.

4.2.7 Intracellular Distribution and Uptake

In order to gather information on the intracellular localization of [1]Cl and [2]PF₆, and to investigate whether the difference in cytotoxicity between [1]Cl and [2]PF₆ in the dark was due to differences in cell-uptake and/or of intracellular distribution, cell fractionation was performed. For this experiment, A549 cells were incubated with [1]Cl or [2]PF₆ for 6 h in the dark at concentrations corresponding

to the EC₅₀ value. The cells were then harvested, the cytosol, membrane, nuclei, and cytoskeleton fractions were separated by Anja Busemann (see Experimental section), and the ruthenium concentration in each fraction was measured by ICP-MS (Figure SIV.15). The observed total uptake of [2]PF₆ (7.5 ng/10⁶ cells) was significantly lower compared to that of [1]Cl (16 ng/10⁶ cells). As the effect of both treatments was identical (i.e., reducing the cell population by 50%), [2]PF₆ seems to be more potent than [1]Cl, although larger EC₅₀ values were found for [2]PF₆. This result suggests that the dark cytotoxicity of [2]PF₆ might be limited by a lower uptake. In terms of intracellular distribution both complexes were found in all fractions, with a slight ([2]PF₆) to strong ([1]Cl) preference for the membrane fraction, and to a lesser extent in the nuclear fractions. The membrane fraction does not only contain the cell membrane but also mitochondria, endosomes, and lysosomes. These results are in agreement with contemporary literature suggesting an endocytosis-dependent uptake mechanism for polypyridyl metal complexes (thus high Ru content in endosomes and lysosomes), and accumulation of lipophilic cationic species in the mitochondrial membranes.^{57, 58}

4.2.8 Cell-free DNA Binding Studies

Thermal and photoinduced DNA binding studies were performed by Dr. Samantha L. Hopkins to establish whether the photolabile sulfur ligands in [1]Cl and [2]PF₆ were protecting the compounds from interaction with biomolecules. The pUC19 plasmid used for this study (2686 bp) exists in three forms: supercoiled (SC, most condensed form, migrates the fastest), single-nicked open circular (OC, relaxed form of the SC, migrates in between the SC and LD) and linear dimer (LD, largest form at 5372 bp, migrates the slowest). For both the thermal and photoinduced DNA binding studies, phosphate buffer was used to model a pseudo intracellular environment. For the dark thermal binding experiments, [1]Cl and [2]PF₆ were incubated at varied DNA base pair (BP) to metal complex (MC) ratios for 24 h (Figure SIV.16). Both [1]Cl and [2]PF₆ showed negligible binding (minimal change in migration of the OC or SC forms), even at the largest concentration of metal complex (5:1 BP:MC ratio). Cisplatin was included as a positive control (5:1 BP:MC ratio) and displayed typical DNA binding results as those observed in literature.⁵⁹ In the dark, [1]Cl and [2]PF₆ have a low affinity and negligible association with any of the forms of the plasmid DNA.

In a second experiment, the ruthenium complexes and cisplatin were photolysed ($\lambda_{\text{irr}} = 520 \text{ nm}$) for different amounts of time (0-60 min) in the presence of pUC19 plasmid (Figure 4.5). For these experiments, a 50:1 BP:MC ratio was used, which displayed insignificant dark thermal binding. However, following green light irradiation complex [1]Cl showed significant retardation of the SC form (Figure 4.5A, lanes 5-9) compared to [2]PF₆ (Figure 4.5B, lanes 5-9), which itself showed slight changes in the OC and SC forms compared to the control. Additionally, a change in the intensity of the staining indicates that increased photoinduced binding of the metal complexes interferes with the intercalation of ethidium bromide. These studies clearly show that after light activation, [1]Cl interacts strongly with the pUC19 plasmid, whereas [2]PF₆ interacts less but still significantly more than in the dark. Clearly, ¹O₂-based DNA cleavage was not observed under irradiation in presence of either ruthenium compound. Although these simple results neither allow to specify in details the binding mode of [1]Cl and [2]PF₆ to DNA, nor to say whether this interaction is relevant for cell death, they clearly demonstrate that the photosubstitution reactions occurring under green light irradiation induces critical changes the two ruthenium compounds and the way they interact with biomolecules.⁶⁰

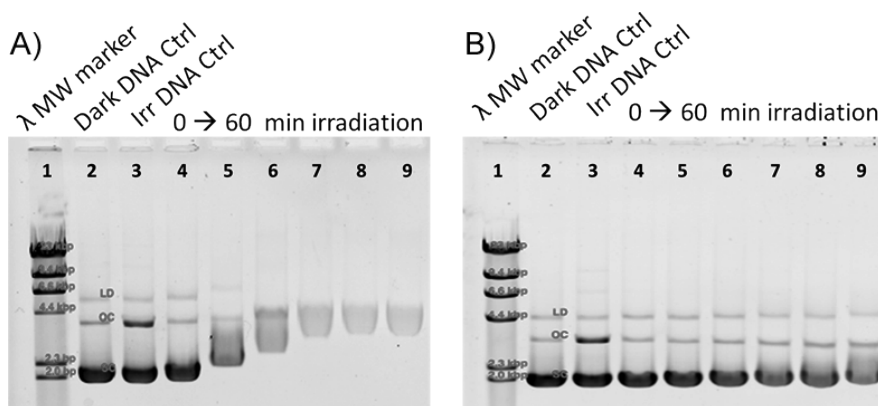


Figure 4.5 Agarose gel of photoinduced binding of [1]Cl (a) and [2]PF₆ (b) to pUC19 plasmid DNA. The lanes correspond to (1) λ DNA MW marker, (2) dark DNA only control, (3) irradiated DNA only control, (4) dark 50:1 BP:MC control, (5-9) 5, 15, 30, 45, and 60 min irradiated 50:1 BP:MC samples, respectively. The bands of the λ MW marker correlate to 23, 9.4, 6.6, 4.4, 2.3, and 2.0 kbp. The dark DNA control bands are labelled according to the form, linear dimer (LD), open circular (OC), and supercoiled (SC).

4.3 Conclusion

Complexes [1]Cl and [2]PF₆ are the first light-activated *trans* ruthenium-based anticancer prodrugs. In the dark these water-soluble complexes are well taken up and display mild cytotoxicity to A431 and A549 cancer cells. However, upon green light irradiation, [1]Cl and [2]PF₆ are activated resulting in highly cytotoxic compounds, with EC₅₀ values below 1 μM and PIs of up to 22. Clearly the combination of these compounds and green light irradiation induces apoptosis, and the low ¹O₂ generation efficiency and the absence of DNA photocleavage make us conclude that cell death is not due to a photodynamic effect. The dose of light necessary to activate [1]Cl and [2]PF₆ *in vitro* (75 J.cm⁻²) is somewhat higher compared to values published for other photoactivated ruthenium or *trans*-platinum complexes (typically 10 J.cm⁻²). However, the green light used in this work (520 nm) is much less harmful to cells than the shorter wavelength (UV or blue light) reported previously,^{18, 21, 38, 40, 49, 61-65} so that high doses do not necessarily represent a problem. Green light also penetrates deeper into the skin tissue,⁴¹ which makes it more relevant for phototherapy.

Overall, the data presented in this chapter suggests that the activation mechanism for this new type of *trans* ruthenium polypyridyl complexes relies on ligand photosubstitution reactions. The ruthenium species [2a] bound to two sulfur protecting ligands is the least cytotoxic, followed by the two mono-protected species [1a]²⁺ and [2b]⁺ bound to a single sulfur ligand, while the bis-aqua, fully deprotected species [1b]²⁺ shows the highest cytotoxicity. Although cell-free DNA studies showed clear photoinduced DNA-binding by [1]Cl and, to a lesser extent, by [2]PF₆, DNA only represents one of the possible biological target(s) of these compounds, as they distribute in the whole cell. It will be necessary to follow for example chemical biological methods described by Hartinger et al.,⁵⁹ to determine which interaction with which biomolecule is actually responsible for the green light-induced apoptosis observed with [1]Cl and [2]PF₆.

4.4 Experimental

4.4.1 Materials and methods

All NMR spectra were recorded on a Bruker DMX-400 or a Bruker AV-600 spectrometer. Chemical shifts are indicated in ppm relative to tetramethylsilane. Mass spectra were recorded by using a Thermoquest Finnagen AQA Spectrometer and a MSQ Plus

Spectrometer positive ionization mode. See Figure S1 for the specific NMR-assignments of [1a]²⁺ and [2]⁺. For NMR experiments under argon, J. Young NMR tubes with PTFE stopper were used. UV-vis experiments were performed on a Cary 50 Varian spectrometer equipped with a Cary Single Cell Peltier for temperature control. The elemental ultra-trace analyses were performed with an FAST (Elemental Scientific, Omaha, Nebraska, USA), i-CAP-Q ICP-MS (Thermo Scientific, Waltham, Massachusetts, USA) MP2 peristaltic pump controlled flow 110 µl/min standardized setup.

The ligand 6,6'-bis[N-(isoquinolyl)-1-amino]-2,2'-bipyridine (H₂biqbpy), [Ru(dmsO)₄Cl₂], and [Ru(bpy)₃]Cl₂ were synthesized according to literature procedures.^{43, 66} N-acetyl-L-methionine (HAMet) was purchased from Alfa Aesar. The complexes were synthesized in dim light and stored in the dark in the freezer.

4.4.2 Synthesis of [Ru(H₂biqbpy)(dmsO)Cl]Cl ([1]Cl)

In a 2-necked round-bottom flask [Ru(dmsO)₄Cl₂] (86 mg, 0.34 mmol) and H₂biqbpy (71 mg, 0.34 mmol) were added in degassed ethanol (10 mL). The solution was stirred overnight at 80 °C under argon resulting in a dark red suspension. Then, the flask was cooled in an ice bath and the red suspension was filtered over a membrane filter, washed with cold ethanol (3 × 10 mL), diethylether (3 × 10 mL), and hexanes (3 × 10 mL). The complex was obtained as a red brown powder. Yield: 48 mg (43%). ¹H NMR (600 MHz, D₂O, 293 K, in ppm): δ = 8.66 (dd, J = 8.6, 0.9 Hz, 2H, qi-4), 8.37 (d, J = 7.9 Hz, 1.0 Hz, 2H, H³), 8.36 (d, J = 7.3 Hz, 2H, qi-10), 8.25 (dd, J = 8.4, 7.7 Hz, 2H, H⁴), 8.05 (d, J = 8.0 Hz, 2H, qi-7), 7.96 (ddd, J = 8.1, 7.0, 1.0 Hz, 2H, qi-6), 7.89 (ddd, J = 8.4, 7.0, 1.3 Hz, 2H, qi-5), 7.86 (dd, J = 8.4, 0.9 Hz, 2H, H⁵), 7.60 (d, J = 6.7 Hz, 2H, qi-9), 2.41 (s, 6H, H^α) ppm; ¹³C NMR (150 MHz, D₂O, 293K, in ppm): δ = 156.3 (C₂), 151.9 (qi-2), 151.7 (C₆), 144.3 (qi-10), 140.0 (C₄), 137.0 (qi-3), 133.4 (qi-6), 129.8 (qi-5), 128.3 (qi-7), 123.3 (qi-4), 120.6 (qi-8), 119.5 (C₃), 118.0 (qi-9), 117.2 (C₅), 44.6 (C^α) ppm; UV-vis: λ_{max} (ε in M⁻¹.cm⁻¹) in H₂O: 308 nm (2.3 × 10⁴); High resolution ES MS m/z (calc): 310.0465 (310.0464, [M - 2×Cl]²⁺). Elem. Anal. Calcd. for C₃₀H₂₆Cl₂N₆O₂RuS,H₂O: C, 50.85; H, 3.98; N, 11.86. Found: C, 50.85; H, 4.23; N, 11.76.

4.4.3 Synthesis of [Ru(H₂biqbpy)(HAMet)(Amet)]PF₆ ([2]PF₆)

In a 2-necked round-bottom flask [1]Cl (30 mg, 0.043 mmol) and N-acetyl-L-methionine (160 mg, 0.87 mmol) were added in degassed demineralized water (15 mL). The solution was stirred overnight at 80 °C under argon resulting in a red solution. Solid KPF₆ (2.0 g) was added and the complex was extracted using ethyl acetate. After rotary evaporation at 30 °C the compound was purified using size exclusion chromatography (Sephadex, LH-20 in MeOH). After rotary evaporation at 30 °C the compound was obtained as a red powder. Yield: 20 mg (43%). ¹H NMR (400 MHz, CD₃OD, 293 K, in ppm): δ = 8.75 (d, J = 8.4 Hz, 2H, qi-4), 8.53 (d, J = 8.4 Hz, 2H, qi-7), 8.47 (d, J = 8.4 Hz, 2H, qi-9), 8.28 (t, J = 7.8 Hz, 2H, qi-6), 8.07 (d, J = 7.8 Hz, 2H, H^{3/5}), 8.00-7.88 (m, 6H, qi-5-H⁴-H^{3/5}), 7.67 (d, J = 6.6 Hz, 2H, qi-10), 3.99 (dd,

$J = 7.8, 3.0$ Hz, 2H, H^β), 1.58 (s, 6H, H^γ), 1.76-1.22 (m, 4H, H^γ), 1.42 (t, $J = 6.9$ Hz, 4H, H^β), 1.40 (s, 6H, H^α). ¹³C NMR (100 MHz, CD₃OD, 293 K, in ppm): $\delta = 173.8$ (COOH), 173.0 (CON), 156.9 (C²), 152.8 (C⁶), 152.0 (qi-2), 146.1 (qi-9), 139.4 (qi-6), 137.7 (qi-8), 133.7 (*), 130.5 (*), 129.0 (C^{3/5}), 124.1 (qi-4), 121.3 (qi-3), 120.6 (qi-7), 118.8 (qi-10), 117.8 (*), 51.7 (C⁶), 33.2 (C^β), 31.2 (C^γ), 22.2 (C^α), 16.1 (C^γ). UV-vis: λ_{max} (ϵ in M⁻¹.cm⁻¹) in H₂O: 363 nm (8.9×10^3). High resolution ES MS m/z (calc): 923.1954 (923.1951, [M - PF₆]⁺), 462.1008 (462.1012, [M - PF₆ + H]²⁺). Elem. Anal. Calcd. for C₄₂H₄₅F₆N₈O₆PRuS₂ + 3×MeOH: C, 46.43; H, 4.94; N, 9.63 Found: C, 46.20; H, 5.05; N, 9.30.

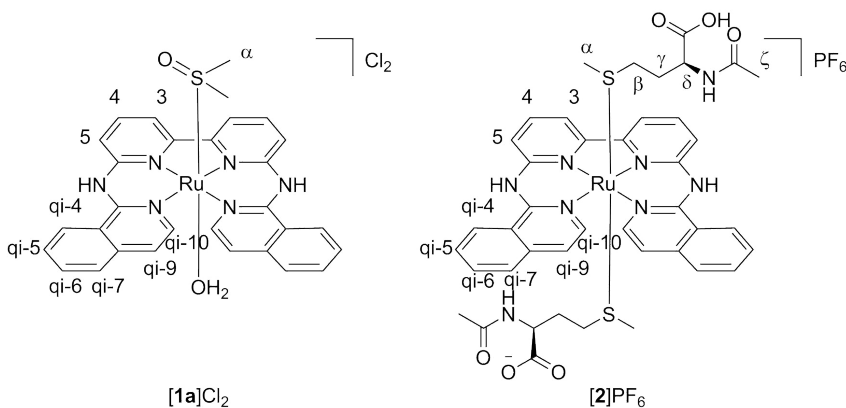


Figure 4.6 Schematic representation of [Ru(Hzbiqbpy)(dmsodmsobpy)(H₂O)]Cl₂ and of [Ru(Hzbiqbpy)(HAmet)(Amet)]PF₆ with atom numbering used in NMR attribution.

4.4.4 Crystal structure determination

For X-ray diffraction all reflection intensities were measured at 110(2) K using a SuperNova diffractometer (equipped with Atlas detector) with Cu K α radiation ($\lambda = 1.54178$ Å) under the program CrysAlisPro. The program CrysAlisPro was used to refine the cell dimensions. Data reduction was done using the program CrysAlisPro (Version 1.171.36.32 Agilent Technologies, 2013). The structure was solved with the program SHELXS-2014/7 and was refined on F^2 with SHELXL-2014/7.⁶⁷ Analytical numeric absorption corrections based on a multifaceted crystal model were applied using CrysAlisPro. The temperature of the data collection was controlled using the system Cryojet (manufactured by Oxford Instruments). The H atoms were placed at calculated positions using the instructions AFIX 43 or AFIX 137 with isotropic displacement parameters having values 1.2 or 1.5 times U_{eq} of the attached C atoms. The H atoms attached to N2, N5 and O1S were found from difference Fourier maps, and their coordinates and isotropic temperature factors were refined freely.

4.4.5 Details of crystal structure

The X-ray crystal structure is ordered. [1]Cl: Fw = 722.64, orange plate, $0.23 \times 0.15 \times 0.04$ mm³, triclinic, $P-1$ (no. 2), $a = 9.5443(3)$, $b = 12.2675(3)$, $c = 13.2983(4)$ Å, $\alpha = 68.395(3)$, $\beta =$

89.878(2), $\gamma = 84.475(2)^\circ$, $V = 1439.98(8) \text{ \AA}^3$, $Z = 2$, $D_x = 1.667 \text{ g cm}^{-3}$, $\mu = 7.139 \text{ mm}^{-1}$, abs. corr. Range: 0.309–0.765. 22804 Reflections were measured up to a resolution of $(\sin \theta/\lambda)_{\text{max}} = 0.62 \text{ \AA}^{-1}$. 5599 Reflections were unique ($R_{\text{int}} = 0.0365$), of which 5286 were observed [$I > 2\sigma(I)$]. 403 Parameters were refined using 3 restraints. $R1/wR2$ [$I > 2\sigma(I)$]: 0.0283/0.0743. $R1/wR2$ [all refl.]: 0.0301/0.0760. $S = 1.043$. Residual electron density found between -0.60 and 0.98 e \AA^{-3} .

4.4.6 Photochemistry monitored by UV-vis spectroscopy

The UV-vis spectroscopy study of Figure 4.2 was performed using a UV-vis spectrometer equipped with temperature control set to 298 K and a magnetic stirrer. The measurements were performed in a quartz cuvette, containing 3 mL of solution (10^{-5} M). The stirred sample was degassed by argon, irradiated perpendicularly to the axis of the spectrometer with the beam of a green ($\lambda = 530 \text{ nm}$, $\Delta\lambda_{1/2} = 25 \text{ nm}$, 3.02 mW , $2.1 \times 10^{-8} \text{ mol.s}^{-1}$) or blue LED (450 nm , $\Delta\lambda_{1/2} = 25 \text{ nm}$, 0.65 mW , $8.53 \times 10^{-9} \text{ mol.s}^{-1}$) fitted to the top of the cuvette, and an absorption spectrum was measured at regular time intervals and analyzed using Microsoft Excel. Mass spectrometry was performed at the beginning and at the end of the irradiation to confirm the nature of the reagent and products.

4.4.7 Green light irradiation in the wells of a 96-well plate, followed by ^1H NMR

Green light irradiation experiments in D_2O were performed in a 96-well plate with the LED source described in details by Hopkins et al.³⁸ for the photocytotoxicity assay. Three adjacent wells per compound were loaded with $200 \mu\text{L}$ of a $38 \mu\text{M}$ solution of [1]Cl or [2]PF₆, and irradiated for 60 min ($520 \pm 20 \text{ nm}$, 75 J.cm^{-2}) at 37°C , while control wells were kept in the dark at the same temperature. For each condition the content of the 3 wells was mixed, and ^1H NMR spectroscopy was performed on the 4 samples (2 compounds, dark or light). As shown in Figure SIV.3, for [1]Cl clear release of free dmsO is observed (new peak at 2.71 ppm) and a complete reorganization of the aromatic peaks indicate that full conversion to [1b]²⁺ is achieved under these conditions. For [2]PF₆ (Figure SIV.4) the photosubstitution is demonstrated by the formation of the characteristic peak of the proton on the chiral carbon of free HAmet at 4.5 ppm (square). The remaining peak at 3.7 ppm indicated by a circle represents the chiral proton of the coordinated HAmet. Photosubstitution under the irradiation conditions used for cell testing (1 h green light) does not lead to photosubstitution of the second Amet⁻ ligand, i.e., the photoproduct is [2b]⁺ (Scheme 2), which is in line with our other photochemical experimental data under green light (only ~1 eq. HAmet is photosubstituted).

4.4.8 Green light activation under biological conditions

The photochemical reactivity of [1]Cl ($38 \mu\text{M}$) and [2]PF₆ ($88 \mu\text{M}$) was measured in 96-well plates by dissolving each compound in Opti-MEM complete and by irradiating with green light (520 nm , 75 J.cm^{-2}) to mimic the conditions of the photocytotoxicity assay. Figure SIV.7 and Figure SIV.8 show that the absorbance change at 315 nm for [1]Cl and 320 nm for [2]PF₆

after 60 min irradiation with green light are levelling off for [1]Cl, i.e., that no further activation occurs after 1 h irradiation, and is significantly activated for [2]PF₆. Since further activation for [2]PF₆ would become experimentally impractical, 60 minutes was chosen as the green light irradiation time in the photocytotoxicity assay.

4.4.9 Cell culturing and EC₅₀ (photo)cytotoxicity assay

See Appendix I for extensive description of the assay.

4.4.10 Singlet oxygen quantum yield measurements

The quantum yield of singlet oxygen generation was determined in a custom-built setup (Figure SIV.10), in which both UV-vis absorption and UV-vis and NIR emission spectroscopy could be performed. All optical parts were connected with optical fibers from Avantes (Apeldoorn, The Netherlands), with a diameter of 200-600 μm. 2 mL of sample, consisting of the compound in CD₃OD, was placed in a stirred 111-OS macro fluorescence cuvette from Hellma in a CUV-UV/VIS-TC temperature-controlled cuvette holder from Avantes. The sample was allowed to equilibrate for 5 minutes. Emission spectroscopy was performed with a 450 nm fiber-coupled laser (Laser system LRD-0450 from Laserglow, Toronto, Canada), which was set to 101 mW at the cuvette (4 mm beam diameter; 0.4 W.cm⁻²) at a 90° angle with respect to the spectrometers. The excitation power was measured using a S310C thermal sensor connected to a PM100USB power meter (Thorlabs). Two spectrometers that were coupled to the cuvette holder with a bifurcated optical fiber, visualized the emission spectrum from 300 nm to 900 nm (Avantes 2048L StarLine spectrometer) and from 1000 nm to 1700 nm (Avantes NIR256-1.7TEC spectrometer). The infrared emission spectrum was acquired in ≤ 50 seconds, after which the laser was turned off directly. UV-vis absorption spectra before and after emission spectroscopy were measured using an Avalight-DHc halogen-deuterium lamp (Avantes) as light source (turned off during emission spectroscopy) and the Avantes UV-vis spectrometer (2048L StarLine spectrometer) as detector, both connected to the cuvette holder at a 180° angle. All spectra were recorded with Avasoft software from Avantes and further processed with Microsoft Office Excel 2010 and Origin Pro software.

4.4.11 Annexin V-FITC/PI assay

200 × 10³ A549 cells were seeded in 35 mm petri dishes in Opti-MEM complete media (2 mL). After 24 h, the media was replaced with drug loaded media (2 ml) using the following concentrations: Rose Bengal 10 μM, Staurosporine 0.3 μM, [1]Cl 1.5 μM, [2]PF₆ 10 μM. The non-light sensitive protein kinase inhibitor Staurosporine, and Rose Bengal, a green light absorbing PDT reagent, were used as positive controls.^{68, 69} As control also compound-free Opti-MEM complete was added to one dish. Cells were irradiated (520 nm, 75 J.cm⁻²) using the same irradiation setup as for the EC₅₀ determination, leading to a set of light irradiated cells and a set of dark controls. 24 h after irradiation, all cells were collected, washed twice

with PBS, and suspended in Annexin V binding buffer (1×10^6 cells/mL). The cell suspension (100 μ L) was stained with propidium iodide (5 μ L, 10 μ g/ml) and the Annexin V-FITC conjugate (3 μ L, Bio connect) in the dark for 15 minutes. After addition of Annexin V binding buffer (200 μ L) the cells were submitted to FACS measurement.⁷⁰ Quantification of the induced cell death was performed with FlowJo, using a standard protocol.⁷¹

4.4.12 Investigation of the mitochondrial membrane potential

A549 cells were seeded at 10,000 cell/well in a eight chamber (ibidi, μ -Slide 8 well). After 24 h, the media was replaced with drug loaded media (300 μ L, OMEM complete) using the following concentrations: Rose Bengal 10 μ M, Staurosporine 0.3 μ M, cisplatin 5 μ M, [1]Cl 1.5 μ M, [2]PF₆ 10 μ M. The non-light sensitive protein kinase inhibitor Staurosporine, and the green light absorbing PDT agent Rose Bengal were used as positive controls. Further, compound-free Opti-MEM complete was added to one chamber as control. Cells were irradiated (520 nm, 75 J.cm⁻²) using the same irradiation setup as for the EC₅₀ determination, leading to a set of light irradiated cells and a set of dark controls. Directly after irradiation the media was replaced by fluorescence-dyes loaded media. Tetramethylrhodamine ethyl (600 μ M), a mitochondrial sensitive dye, and Draq5 (1 μ M), a DNA-staining fluorophore were used. After 30 min of incubation the media was removed and replaced with TMRE loaded media (150 μ M). Subsequently, the microscope slides were transferred to a Leica SPE confocal microscope.

4.4.13 Cell fractionation

Cell fractionation for intracellular distribution studies for complexes [1]Cl and [2]PF₆ were conducted on A549 lung cancer cells. 3×10^6 cells were seeded at $t = 0$ h in Opti-MEM complete in 175 cm² flasks. At $t = 24$ h cells were treated with complexes to give a final concentration corresponding to the EC₅₀ values in the dark after 6 h in a total volume of 24 mL. After 6 h of drug incubation at 37 °C, the medium was aspirated, the cells were washed with PBS-buffer, trypsinized, counted and pelleted by centrifugation $700 \times g$ for 5 min. Then, the pellets were fractionated using to FractionPREP cell fractionation kit from BioVision according to the suppliers's instructions. Samples were digested overnight in concentrated HNO₃ (> 65%) and diluted with MilliQ water to obtain a final concentration of 5% HNO₃. For ICP-MS measurements, the system was optimized with a ruthenium-platinum solution. The calibration range was from 0 to 25 μ g/l, and the obtained detection limit for all isotopes ensued 0.01 μ g/l. Silver and Indium were used for internal standard, to correct for the sample dependent matrix effects. No reference sample was available; therefore several samples were spiked with a standard concentration. The recoveries of the spiked accustomed concentrations were all within a 10% deviation. The data from three independent biological replications was used to obtain the uptake bars shown in Figure SIV.15.

4.4.14 DNA (photo)binding studies

The pUC19 plasmid used for this study (2686 bp) exists in three forms: supercoiled (SC), single-nicked open circular (OC) and linear dimer (LD). Of particular interest are the SC and OC forms. Although these two forms have the same number of BP, the SC form migrates faster through the agarose gel compared to the OC form due to the condensed SC form. However, when the positively charged metal complexes associates with the SC form, the shape may become larger and it will be less negatively charged, ultimately resulting in slower migration. Alternatively, if metal complexes coordinatively modify the OC form, it may induce coiling or a condensed structure causing an increase in migration and thus coalescence of the SC and OC form on increasing metal complex concentration. However, if there is no condensation of the OC plasmid structure, but the positively charged metal complexes associate with the OC form then the observed migration would be retarded. Finally, if the metal complexes generate enough singlet oxygen, then upon irradiation the SC form is converted via a nick in one of the DNA strands to the relaxed OC form. However, due to the low Φ_{1O_2} , DNA photocleavage was unexpected.

Agarose gel electrophoresis was used to assay the thermal and photoinduced binding of [1]Cl and [2]PF₆ to pUC19 plasmid DNA. Two buffers were used for the experiments: 5X tris-boric acid buffer (TBA) and phosphate buffer (PB). The TBA buffer (45 mM tris(hydroxymethyl)amino methane and 45 mM boric acid, pH = 7.4) was used in the gel and running buffer. PB (100 mM NaH₂PO₄, pH = 7.0) was used for DNA-MC interactions. The agarose gels were 0.8% w/w agarose gel (0.24 g agarose, 24 g DI H₂O, and 6 mL TBA) and were cast in the OWL B1A Easycast system.

The molar concentration of the pUC19 plasmid DNA base pairs (BP) was determined using the extinction coefficient ($\epsilon_{260\text{ nm}} = 13,200\text{ M}^{-1}\text{cm}^{-1}$).⁵⁸ All aliquots were prepared with a final volume of 20 μL and prior to loading 4 μL of 6X loading dye was added. The λ DNA-*Hind*III digest molecular weight (MW) marker was prepared by adding 2 μL (1 μg) of the DNA MW marker, 18 μL PB, and 4 μL 6X loading dye. The MW marker was heated for 3 min at 60 °C prior to loading. In each well, 12 μL (1 μg of pUC19 DNA or 0.5 μg of MW marker) of each sample was loaded.

For each gel, the electrophoresis chamber was filled with 50 mL TBA and 210 mL deionized water. Each gel was run at a constant voltage of 105 V for 90 min. All gels were stained using 10 μL (10 mg/mL) ethidium bromide in 200 mL deionized water for 30 min with slight shaking and then destained in 200 mL deionized water for 20 min. Immediately following destaining, the gel was imaged using a BioRad ChemiDoc imaging system (ethidium bromide setting). Image Lab software was used to process the images.

The samples for thermal binding were prepared under ambient light in amber centrifuge tubes. For each sample 2 μL of pUC19 plasmid (2 μg , $[\text{BP}]_i = 1.95 \times 10^{-3} \text{ M}$) was used and the amount of metal complex and PB were adjusted to a final volume of 20 μL . Several ratios of base pairs of the plasmid (BP) to metal complex (MC) (100:1, 50:1, 25:1, 15:1, 10:1, and 5:1 BP:MC) and incubated at 37 $^\circ\text{C}$ for 24 h. Additionally, the negative control (DNA without metal complex) and a positive control (cisplatin, 5:1 BP:MC ratio) were incubated under the same conditions. Lanes were loaded as follows: **(1)** λ MW marker, **(2)** DNA only control, **(3)** cisplatin (5:1 BP:MC, $[\text{cisplatin}]_i = 390 \mu\text{M}$) control, **(4)** Ru complex (100:1 BP:MC, $[\text{Ru}]_i = 20 \mu\text{M}$), **(5)** Ru complex (50:1 BP:MC, $[\text{Ru}]_i = 40 \mu\text{M}$), **(6)** Ru complex (25:1 BP:MC, $[\text{Ru}]_i = 80 \mu\text{M}$), **(7)** Ru complex (15:1 BP:MC, $[\text{Ru}]_i = 130 \mu\text{M}$), **(8)** Ru complex (10:1 BP:MC, $[\text{Ru}]_i = 195 \mu\text{M}$), **(9)** Ru complex (5:1 BP:MC, $[\text{Ru}]_i = 390 \mu\text{M}$), and **(10)** DNA only control. The gels were run, stained, and processed as described above (Figure SIV.16).

The samples for photoinduced binding were prepared under ambient light and then irradiated in a well of a 96-well plate using the LED array system described for cell culturing ($\lambda_{\text{irr}} = 520 \text{ nm}$). A 50:1 BP:MC ratio ($[\text{BP}]_i = 1.95 \times 10^{-3} \text{ M}$ and $[\text{Metal complex}]_i = 40 \mu\text{M}$) was used for all metal complexes. For each gel, a dark DNA only control, irradiated DNA only control, dark 50:1 BP:MC control ($[\text{Metal complex}]_i = 40 \mu\text{M}$), and irradiated 50:1 BP:MC sample were prepared. The DNA only controls consisted of 8 μL pUC19 plasmid DNA and 72 μL PB. The dark 50:1 BP:MC controls were composed of 4 μL pUC19 plasmid DNA, 33 μL PB, and 3 μL of the metal complex in PB (0.5 mM). A total volume of 200 μL (20 μL pUC19 plasmid DNA, 164 μL PB, and 16 μL metal complex in PB (0.5 mM) was prepared for the irradiated 50:1 BP:MC samples and 20 μL aliquots were removed for each time point. The time points were 5, 15, 30, 45, and 60 min correlating to light doses of 6.3, 18.8, 37.6, 56.4, and 75.2 Jcm^{-2} , respectively. At the end of the experiment, 20 μL of the dark DNA control, irradiated DNA control, and dark DNA-metal complex control ($t = 0 \text{ min irr}$) were removed. Loading dye was added to each of the aliquots and the gel was loaded. The lanes were as follows: **(1)** λ MW marker, **(2)** dark DNA control, **(3)** irradiated DNA control (75.2 Jcm^{-2}), **(4)** dark 50:1 BP:MC control, **(5)** irradiated 50:1 BP:MC (5 min, 6.3 Jcm^{-2}), **(6)** irradiated 50:1 BP:MC (15 min, 18.8 Jcm^{-2}), **(7)** irradiated 50:1 BP:MC (30 min, 37.6 Jcm^{-2}), **(8)** irradiated 50:1 BP:MC (45 min, 56.4 Jcm^{-2}), and **(9)** irradiated 50:1 BP:MC (60 min, 75.2 Jcm^{-2}). The gels were run, stained and processed as specified above.

4.5 References

- N. J. Farrer, L. Salassa and P. J. Sadler, *Dalton Trans.*, 2009, **48**, 10690-10701.
- J. D. Knoll and C. Turro, *Coord. Chem. Rev.*, 2015, **282-283**, 110-126.
- S. Yano, S. Hirohara, M. Obata, Y. Hagiya, S.-i. Ogura, A. Ikeda, H. Kataoka, M. Tanaka and T. Joh, *J. Photochem. Photobiol. C*, 2011, **12**, 46-67.
- D. Crespy, K. Landfester, U. S. Schubert and A. Schiller, *Chem. Commun.*, 2010, **46**, 6651-6662.
- U. Schatzschneider, *Eur. J. Inorg. Chem.*, 2010, **2010**, 1451-1467.
- W. A. Velema, W. Szymanski and B. L. Feringa, *J. Am. Chem. Soc.*, 2014, **136**, 2178-2191.
- H.-J. Yu, S.-M. Huang, L.-Y. Li, H.-N. Jia, H. Chao, Z.-W. Mao, J.-Z. Liu and L.-N. Ji, *J. Inorg. Biochem.*, 2009, **103**, 881-890.
- H. Huang, P. Zhang, B. Yu, C. Jin, L. Ji and H. Chao, *Dalton Trans.*, 2015, **44**, 17335-17345.
- G. Shi, S. Monro, R. Hennigar, J. Colpitts, J. Fong, K. Kasimova, H. Yin, R. DeCoste, C. Spencer, L. Chamberlain, A. Mandel, L. Lilge and S. A. McFarland, *Coord. Chem. Rev.*, 2015, **282-283**, 127-138.
- J. Fong, K. Kasimova, Y. Arenas, P. Kaspler, S. Lazic, A. Mandel and L. Lilge, *Photochem. Photobiol. Sci.*, 2015, **14**, 2014-2023.
- S. P. Foxon, M. A. H. Alamiry, M. G. Walker, A. J. H. M. Meijer, I. V. Sazanovich, J. A. Weinstein and J. A. Thomas, *J. Phys. Chem. A*, 2009, **113**, 12754-12762.
- H. Huang, B. Yu, P. Zhang, J. Huang, Y. Chen, G. Gasser, L. Ji and H. Chao, *Angew. Chem., Int. Ed.*, 2015, **54**, 14049-14052.
- M. R. Gill and J. A. Thomas, *Chem. Soc. Rev.*, 2012, **41**, 3179-3192.
- P. Agostinis, K. Berg, K. A. Cengel, T. H. Foster, A. W. Girotti, S. O. Gollnick, S. M. Hahn, M. R. Hamblin, A. Juzeniene, D. Kessel, M. Korbelik, J. Moan, P. Mroz, D. Nowis, J. Piette, B. C. Wilson and J. Golab, *CA Cancer J. Clin.*, 2011, **61**, 250-281.
- C. Mari, V. Pierroz, R. Rubbiani, M. Patra, J. Hess, B. Spingler, L. Oehninger, J. Schur, I. Ott, L. Salassa, S. Ferrari and G. Gasser, *Chem. Eur. J.*, 2014, **20**, 14421-14436.
- R. Sharma, J. D. Knoll, P. D. Martin, I. Podgorski, C. Turro and J. J. Kodanko, *Inorg. Chem.*, 2014, **53**, 3272-3274.
- M. A. Sgambellone, A. David, R. N. Garner, K. R. Dunbar and C. Turro, *J. Am. Chem. Soc.*, 2013, **135**, 11274-11282.
- T. Joshi, V. Pierroz, C. Mari, L. Gemperle, S. Ferrari and G. Gasser, *Angew. Chem., Int. Ed.*, 2014, **53**, 2960-2963.
- A. Presa, R. F. Brissos, A. B. Caballero, I. Borilovic, L. Korrodi-Gregório, R. Pérez-Tomás, O. Roubeau and P. Gamez, *Angew. Chem.*, 2015, **127**, 4644-4648.
- B. S. Howerton, D. K. Heidary and E. C. Glazer, *J. Am. Chem. Soc.*, 2012, **134**, 8324-8327.
- N. J. Farrer, J. A. Woods, L. Salassa, Y. Zhao, K. S. Robinson, G. Clarkson, F. S. Mackay and P. J. Sadler, *Angew. Chem., Int. Ed.*, 2010, **49**, 8905-8908.
- S. Bonnet, B. Limburg, J. D. Meeldijk, R. J. M. K. Gebbink and J. A. Killian, *J. Am. Chem. Soc.*, 2010, **133**, 252-261.
- A.-C. Laemmel, J.-P. Collin and J.-P. Sauvage, *Eur. J. Inorg. Chem.*, 1999, **1999**, 383-386.
- G. Ragazzon, I. Bratsos, E. Alessio, L. Salassa, A. Habtemariam, R. J. McQuitty, G. J. Clarkson and P. J. Sadler, *Inorg. Chim. Acta*, 2012, **393**, 230-238.
- F. Barragan, P. Lopez-Senin, L. Salassa, S. Betanzos-Lara, A. Habtemariam, V. Moreno, P. J. Sadler and V. Marchan, *J. Am. Chem. Soc.*, 2011, **133**, 14098-14108.
- J.-P. Cosse and C. Michiels, *Anti-Cancer Agents Med. Chem.*, 2008, **8**, 790-797.
- A. N. Hidayatullah, E. Wachter, D. K. Heidary, S. Parkin and E. C. Glazer, *Inorg. Chem.*, 2014, **53**, 10030-10032.
- R. N. Garner, J. C. Gallucci, K. R. Dunbar and C. Turro, *Inorg. Chem.*, 2011, **50**, 9213-9215.
- O. Filevich and R. Etchenique, *Photochem. Photobiol. Sci.*, 2013, **12**, 1565-1570.
- L. Salassa, C. Garino, G. Salassa, R. Gobetto and C. Nervi, *J. Am. Chem. Soc.*, 2008, **130**, 9590-9597.
- F. Arnesano, M. Losacco and G. Natile, *Eur. J. Inorg. Chem.*, 2013, **2013**, 2701-2711.
- P. M. Takahara, A. C. Rosenzweig, C. A. Frederick and S. J. Lippard, *Nature*, 1995, **377**, 649-652.
- U. Kalinowska-Lis, J. Ochocki and K. Matlowska-Wasowska, *Coord. Chem. Rev.*, 2008, **252**, 1328-1345.
- A. G. Quiroga, *J. Inorg. Biochem.*, 2012, **114**, 106-112.
- S. M. Aris and N. P. Farrell, *Eur. J. Inorg. Chem.*, 2009, **2009**, 1293-1302.

36. Y. Zhao, J. A. Woods, N. J. Farrer, K. S. Robinson, J. Pracharova, J. Kasparkova, O. Novakova, H. Li, L. Salassa, A. M. Pizarro, G. J. Clarkson, L. Song, V. Brabec and P. J. Sadler, *Chem. Eur. J.*, 2013, **19**, 9578-9591.
37. F. S. Mackay, J. A. Woods, P. Heringová, J. Kašpárková, A. M. Pizarro, S. A. Moggach, S. Parsons, V. Brabec and P. J. Sadler, *Proc. Natl. Acad. Sci. USA*, 2007, **104**, 20743-20748.
38. S. L. Hopkins, B. Siewert, S. H. C. Askes, P. Veldhuizen, R. Zwier, M. Heger and S. Bonnet, *Photochem. Photobiol. Sci.*, 2016, **15**, 644-653.
39. T. J. McMillan, E. Leatherman, A. Ridley, J. Shorrocks, S. E. Tobi and J. R. Whiteside, *J. Pharm. Pharmacol.*, 2008, **60**, 969-976.
40. S. Wäldchen, J. Lehmann, T. Klein, S. van de Linde and M. Sauer, *Sci. Rep.*, 2015, **5**, 15348.
41. S. L. Jacques, *Phys. Med. Biol.*, 2013, **58**, R37.
42. S. Bonnet, *Comments Inorg. Chem.*, 2015, **35**, 179-213.
43. Z. Arcis-Castillo, S. Zheng, M. A. Siegler, O. Roubeau, S. Bedoui and S. Bonnet, *Chem. Eur. J.*, 2011, **17**, 14826-14836.
44. A. Bahreman, B. Limburg, M. A. Siegler, E. Bouwman and S. Bonnet, *Inorg. Chem.*, 2013, **52** 9456-9469.
45. R. E. Goldbach, I. Rodriguez-Garcia, J. H. van Lenthe, M. A. Siegler and S. Bonnet, *Chem. Eur. J.*, 2011, **17**, 9924-9929.
46. P. C. Ford, *Coord. Chem. Rev.*, 1982, **44**, 61-82.
47. O. J. Stacey and S. J. A. Pope, *RSC Adv.*, 2013, **3**, 25550-25564.
48. A. Ruggi, F. W. B. van Leeuwen and A. H. Velders, *Coord. Chem. Rev.*, 2011, **255**, 2542-2554.
49. C. Mari, V. Pierroz, S. Ferrari and G. Gasser, *Chem. Sci.*, 2015, **6**, 2660-2686.
50. R. Lincoln, L. Kohler, S. Monro, H. Yin, M. Stephenson, R. Zong, A. Chouai, C. Dorsey, R. Hennigar, R. P. Thummel and S. A. McFarland, *J. Am. Chem. Soc.*, 2013, **135**, 17161-17175.
51. M. C. DeRosa and R. J. Crutchley, *Coord. Chem. Rev.*, 2002, **233-234**, 351-371.
52. Z. Darzynkiewicz, G. Juan, X. Li, W. Gorczyca, T. Murakami and F. Traganos, *Cytometry*, 1997, **27**, 1-20.
53. G. Melino and D. Vaux, *Cell Death*, Wiley, 2010.
54. M. van Engeland, L. J. W. Nieland, F. C. S. Ramaekers, B. Schutte and C. P. M. Reutelingsperger, *Cytometry*, 1998, **31**, 1-9.
55. M. Dickerson, Y. Sun, B. Howerton and E. C. Glazer, *Inorg. Chem.*, 2014, **53**, 10370-10377.
56. L. He, Y. Huang, H. Zhu, G. Pang, W. Zheng, Y.-S. Wong and T. Chen, *Adv. Funct. Mater.*, 2014, **24**, 2754-2763.
57. M. Groessl, O. Zava and P. J. Dyson, *Metallomics*, 2011, **3**, 591-599.
58. S. M. Zeman and D. M. Crothers, *Methods Enzymol.*, 2001, **340**, 51-68.
59. M. V. Babak, S. M. Meier, K. V. M. Huber, J. Reynisson, A. A. Legin, M. A. Jakupec, A. Roller, A. Stukalov, M. Gridling, K. L. Bennett, J. Colinge, W. Berger, P. J. Dyson, G. Superti-Furga, B. K. Keppler and C. G. Hartinger, *Chem. Sci.*, 2015, **6**, 2449-2456.
60. B. Zhang, S. Seki, K. Akiyama, K. Tsutsui, T. Li and K. Nagao, *Acta Med. Okayama*, 1992, **46**, 427-434.
61. G. M. Findlay, *Lancet*, 1928, **212**, 1070-1073.
62. C. Kielbassa, L. Roza and B. Epe, *Carcinogenesis*, 1997, **18**, 811-816.
63. B. H. Mahmoud, C. L. Hexsel, I. H. Hamzavi and H. W. Lim, *Photochem. Photobiol.*, 2008, **84**, 450-462.
64. C. Opländer, S. Hidding, F. B. Werners, M. Born, N. Pallua and C. V. Suschek, *J. Photochem. Photobiol. B*, 2011, **103**, 118-125.
65. M. Frascioni, Z. Liu, J. Lei, Y. Wu, E. Strekalova, D. Malin, M. W. Ambrogio, X. Chen, Y. Y. Botros, V. L. Cryns, J.-P. Sauvage and J. F. Stoddart, *J. Am. Chem. Soc.*, 2013, **135**, 11603-11613.
66. E. Dulière, M. Devillers and J. Marchand-Brynaert, *Organometallics*, 2003, **22**, 804-811.
67. G. Sheldrick, *Acta Crystallogr. Sect. C*, 2015, **71**, 3-8.
68. R. Bertrand, E. Solary, P. O'Connor, K. W. Kohn and Y. Pommier, *Exp. Cell Res.*, 1994, **211**, 314-321.
69. E. Panzarini, V. Inguscio and L. Dini, *Int. J. Photoenergy*, 2011, **2011**.
70. G. Koopman, C. P. Reutelingsperger, G. A. Kuijten, R. M. Keehnen, S. T. Pals and M. H. van Oers, *Blood*, 1994, **84**, 1415-1420.
71. O. Williams, in *Apoptosis Methods and Protocols*, ed. H. M. Brady, Humana Press, 2004, vol. 282, ch. 3, pp. 31-42.

CHAPTER 5

Controlling with light the interaction between *trans* tetrapyridyl ruthenium complexes and an oligonucleotide

This chapter is to be published as a full paper: Vincent H.S. van Rixel, Geri F. Moolenaar, Maxime A. Siegler, Luigi Messori, Sylvestre Bonnet, *manuscript submitted*.

5.1 Introduction

The leading anticancer drug cisplatin is one of the landmarks in modern inorganic chemistry.¹ In the body cisplatin enters cells, hydrolyzes, and forms irreversible adducts with DNA, ultimately triggering cell death via apoptosis.²⁻⁴ However, because of their lack of selectivity, severe side effects are commonly associated with the use of cisplatin, including nephrotoxicity, neurotoxicity, ototoxicity, and nausea.⁵ Furthermore, cancer cells can acquire increasing levels of cisplatin-resistance.⁶ Alternatively, as transplatin is not active *in vivo* and less cytotoxic than cisplatin *in vitro*, anticancer metallodrugs with a *trans* configuration have not been seriously considered until recently.⁷⁻¹⁰

Photodynamic therapy (PDT) is used in the clinics to locally activate anticancer prodrugs, improve their selectivity, and reduce their side effects. PDT relies on the local activation of ground state triplet oxygen to highly reactive excited state singlet oxygen, and thus critically depends on the presence of dioxygen. In anticancer therapy photoactivated chemotherapy (PACT) is an emerging alternative strategy based on compounds that are chemically modified upon light irradiation without depending on the presence of dioxygen.¹¹⁻¹⁹ Platinum-based PACT compounds have been described and often rely on the photoreduction of an octahedral platinum(IV) center to a square-planar platinum(II) complex.^{12, 20-23} However, they usually lack strong absorption in the visible region; thus ruthenium polypyridyl compounds have emerged as a promising alternative due to their excellent visible light absorption properties.^{24, 25} Most of the ruthenium-based PACT agents known to date contain two bidentate ligands based on the 2,2'-bipyridine scaffold.^{11, 26-29} After light activation a *cis* bis-aqua complex is obtained that can bind to DNA in a fashion similar to cisplatin.³⁰

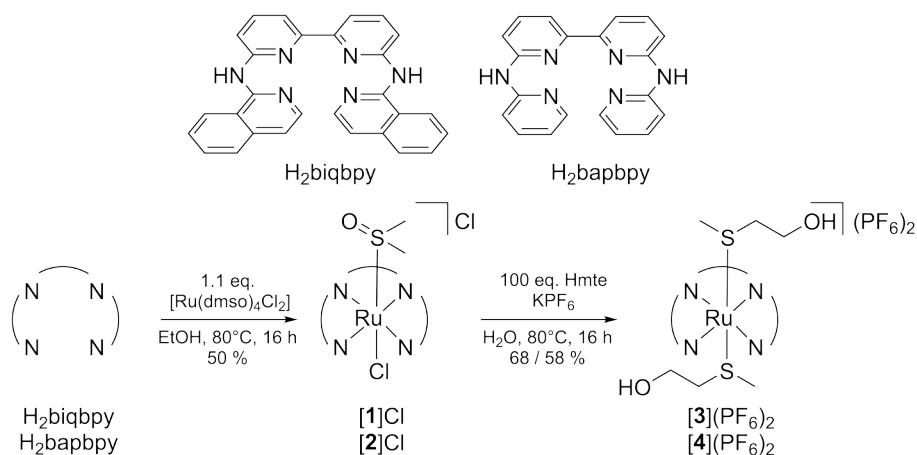
The compound $[\text{Ru}(\text{H}_2\text{biqbpy})(\text{dmsO})\text{Cl}]\text{Cl}$ (**[1]Cl**) (H_2biqbpy = 6,6'-bis[N-(isoquinolyl)-1-amino]-2,2'-bipyridine) has recently been reported as a phototoxic PACT agent that induces apoptosis upon green light activation.³¹ This type of *trans* octahedral ruthenium complex contains a tetrapyrindyl H_2biqbpy ligand that coordinates in one plane of the octahedron, allowing coordination of two axial monodentate ligands that can be photochemically or thermally substituted. In an initial study we reported that a significant amount of the ruthenium complex ends up in the nucleus of the cell, which justified DNA-binding studies using gel electrophoresis and circular pUC19 plasmid DNA. These studies clearly showed that interaction with DNA was switched on by light irradiation. However, the nature of the metal-DNA adducts was unclear. In this work three new derivatives of **[1]Cl** are reported: $[\text{Ru}(\text{H}_2\text{biqbpy})(\text{Hmte})_2](\text{PF}_6)_2$ (**[3](PF₆)₂**, Hmte = 2-methylthioethanol), and their two H_2bapbpy analogues

[Ru(H₂bapbpy)(dmsO)Cl]Cl ([2]Cl) and [Ru(H₂bapbpy)(Hmte)₂](PF₆)₂ ([4](PF₆)₂ (H₂bapbpy = 6,6'-bis[N-(pyridyl)-1-amino]-2,2'-bipyridine), and the study of their interactions, in the dark and after light activation, with the oligodeoxyribonucleotide (ODN) s(⁵CTACGGTTTCAC³) (ODN1). Oligonucleotides have been widely used as models for DNA, to study its interaction with potential anticancer compounds.³²⁻³⁶ A combined approach of gel electrophoresis and high resolution electrospray injection mass spectrometry is introduced to study the binding of a light-activated drug to oligonucleotides.

5.2 Results

5.2.1 Synthesis

[2]Cl was synthesized by reacting H₂bapbpy with 1.1 equivalents of [Ru(dmsO)₄Cl₂] in ethanol overnight at 80 °C (Scheme 5.1) following the synthetic method of [1]Cl.³¹ Reacting [1]Cl or [2]Cl with an excess of Hmte overnight at 80 °C in water, followed by anion exchange using KPF₆, and size exclusion chromatography, afforded [3](PF₆)₂ and [4](PF₆)₂, respectively (Scheme 5.1). In this reaction the chloride ligand instantly dissociates, but an excess of thioether and heat are required to also substitute thermally the dmsO ligand. In [3](PF₆)₂ and [4](PF₆)₂ an upfield shift of the ¹H NMR signals corresponding to the methyl group of Hmte is observed (1.53 and 1.56 ppm in acetone-d₆), compared to free Hmte (2.11 ppm). This upfield shift is characteristic for the shielding cone of polypyridyl ligands coordinated to the metal center, and indicates that Hmte is coordinated to ruthenium.^{31, 37}



Scheme 5.1 Synthesis of tetrapyrindyl ruthenium complexes [1]Cl, [2]Cl, and their *trans* Hmte analogues [3](PF₆)₂ and [4](PF₆)₂. Conditions adapted from Van Rixel et al.³¹

5.2.2 Crystal structures

Slow vapor diffusion of ethyl acetate into a methanol solution containing [2]Cl, and vapor diffusion of diethyl ether into an acetone solution of [3](PF₆)₂ or [4](PF₆)₂ yielded ruby-colored crystals suitable for X-ray structure determination. In the structure of [2]Cl, [3](PF₆)₂, and [4](PF₆)₂ the dmsu or Hmte ligands were found to bind *via* their sulfur atom to ruthenium, as expected from the softness of the sulfur and ruthenium(II) atoms (Figure 5.1). In the structure of [2]Cl, two independent molecules with slightly different geometries were found in the asymmetric unit. Selected bond distances, angles, torsion angles, and dihedral angles, are summarized in Table 5.1 and Table 5.2. The bond distances Ru-N1 and Ru-N6 fall between 2.09-2.11 Å, compared to 2.02-2.04 Å for Ru-N3 and Ru-N4. For [2]Cl like for [1]Cl (Van Rixel et al.³¹) the Ru-S1 bond is 2.2266(13) Å, whereas the Ru-S1 bonds for [3](PF₆)₂ and [4](PF₆)₂ are 2.3661(7) and 2.3822(8) Å, respectively. This difference in bond length can be explained by the more electron-accepting character of the sulfoxide ligand, and the better electron donating character of the chloride ligand *trans* to dmsu, compared to Hmte.

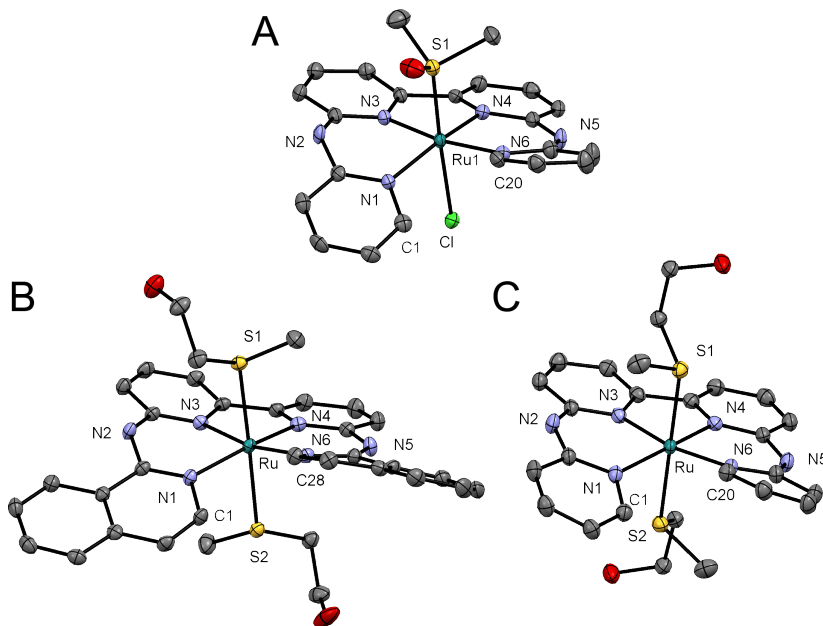


Figure 5.1 Displacement ellipsoid plots (50% probability level) of the cationic part, as observed in [2]Cl (A), [3](PF₆)₂ (B), and [4](PF₆)₂ (C). Counter anions and H atoms have been omitted for clarity.

Table 5.1 Selected bond lengths (Å) for [1]Cl, [2]Cl, [3](PF₆)₂, and [4](PF₆)₂. See Figure 5.1 for atom labeling.

Bond	[1]Cl ^a	[2]Cl	[3](PF ₆) ₂	[4](PF ₆) ₂
Ru-N1	2.1018(19)	2.102(4)	2.109(3)	2.101(3)
Ru-N3	2.020(2)	2.027(4)	2.036(2)	2.029(3)
Ru-N4	2.0220(19)	2.031(4)	2.025(3)	2.029(3)
Ru-N6	2.087(2)	2.098(4)	2.098(2)	2.101(3)
Ru-Cl	2.4363(5)	2.4513(13)	-	-
Ru-S1	2.2262(6)	2.2266(13)	2.3661(7)	2.3822(8)
Ru-S2	-	-	2.3847(7)	2.3847(7)

^a Values taken from Van Rixel et al.³¹

Table 5.2 Selected angles (°) and torsion angles (°) for [1]Cl, [2]Cl, [3](PF₆)₂, and [4](PF₆)₂. See Figure 5.1 for atom labeling.

Angle	[1]Cl ^a	[2]Cl	[3](PF ₆) ₂	[4](PF ₆) ₂
N1-Ru-N3	91.77(8)	89.89(14)	90.13(9)	91.56(11)
N1-Ru-N4	170.80(8)	165.10(15)	166.35(10)	169.80(10)
N1-Ru-N6	97.90(8)	97.98(15)	99.08(9)	96.68(14)
N3-Ru-N4	80.78(8)	80.63(14)	80.77(10)	80.94(15)
N3-Ru-N6	164.83(8)	170.92(14)	168.14(9)	169.80(10)
N4-Ru-N6	90.51(8)	92.51(14)	91.38(10)	91.56(11)
N1-N3-N4-N6	12.78(9)	12.5(2)	13.7(1)	9.9(1)
α - β ^b	45.38	42.89	44.50	30.43

^a Values taken from Van Rixel et al.³¹

^b Dihedral angle α - β is formed by the planes between the terminal pyridyls (N1-C1-C2-C3-C4-C5 and N6-C16-C17-C18-C19-C20) or quinolyls (N1-C1-C2-C3-C4-C5-C6-C7-C8-C9 and N6-C20-C21-C22-C23-C24-C25-C26-C27-C28).

The torsion angle N1-N3-N4-N6 in all four complexes varied between 9.88-13.72°. The dihedral angle between the average planes of the terminal pyridyl or quinolyl moiety of the ligand labelled as α - β (Table 5.2) is also a measure for the flatness of the tetrapyridyl ligand. For [1]Cl, [2]Cl, [3](PF₆)₂, and [4](PF₆)₂ these angles are 45.38, 42.89, 44.50, and 30.40°, respectively. These values for [4](PF₆)₂ strongly deviate due to crystal lattice effects (polar π and hydrogen bonding interactions). Nonetheless, the data demonstrates that the ruthenium complexes are distorted, due to the steric hindrance between the two hydrogen atoms bound to the C1 and C20 or C28 ortho-carbon atoms that constrain the ligand conformation to wrap in a

helical fashion around the metal center.^{38,39} Neither the nature of the apical ligands (Hmte *vs.* dmsO) nor the replacement of the terminal pyridyl moiety (in H₂bapbpy) by an isoquinolyl moiety (in H₂biqbpy) has a strong effect on the bond angles and coordination bond distances of the tetrapyridyl ligand.

5.2.3 Photoreactivity of [2]Cl, [3](PF₆)₂, and [4](PF₆)₂

The photoreactivity of [2]Cl, [3](PF₆)₂, and [4](PF₆)₂ was tested under blue light irradiation ($\lambda_{\text{irr}} = 445 \text{ nm}$) in aqueous solution and monitored by mass spectrometry and UV-vis spectroscopy. For [2]Cl, initially dissolved in CD₃OD, mass spectrometry before irradiation and for dark control samples (Figure 5.2A) showed peaks at $m/z = 280.3$ corresponding to [Ru(H₂bapbpy)(dmsO) + CD₃OD]²⁺ (calc. $m/z = 280.1$), indicating that the chloride ligand dissociates quickly and spontaneously upon dissolution in water, but that the dmsO ligand remains coordinated. After light irradiation, however, a new set of peaks is observed at $m/z = 249.7$ corresponding to [Ru(H₂bapbpy)(H₂O) + CD₃OD]²⁺ (calc. $m/z = 250.0$). This indicates that the dmsO ligand in [2]Cl (similar to [1]Cl) is quantitatively photosubstituted by a solvent molecule upon irradiation. When the photoreaction was monitored by UV-vis spectroscopy, irradiation of [2]Cl was characterized by isosbestic points at 281 and 302 nm, and resulted in a final spectrum characterized by absorption maxima at 306, 335, 404, and 495 nm. The quantum yield for the photosubstitution of dmsO by water was found to be 0.004, and comparable to that for [1]Cl.³¹

For [3](PF₆)₂ and [4](PF₆)₂ blue light irradiation in aqueous solution analyzed afterwards by mass spectrometry showed peaks at $m/z = 317.2$ and $m/z = 266.9$ corresponding to [3 - Hmte]²⁺ and [4 - Hmte]²⁺, respectively (calc. $m/z = 317.1$ and 267.0, respectively). Dark control samples also contained these peaks, but in addition peaks at $m/z = 363.0$ and $m/z = 313.1$ corresponding to [3]²⁺ and [4]²⁺ (calc. $m/z = 363.1$ and 313.1) were detected. This data indicates that blue light irradiation of complexes [3](PF₆)₂ and [4](PF₆)₂ results in the photosubstitution of one Hmte ligand for a solvent molecule. When the irradiation reaction of [3](PF₆)₂ was monitored by UV-vis spectroscopy the spectrum evolved over time showed an overall increase in intensity and a slight red-shift of the metal-to-ligand-charge transfer (MLCT) from 451 nm to 465 nm (Figure 5.2B). Upon irradiation of a solution of [4](PF₆)₂ a general increase in the visible domain through an isosbestic point at 398 nm was observed (Figure SV.2). Overall, the three new complexes show and confirm that coordination of H₂bapbpy or H₂biqbpy to ruthenium enables photosubstitution of the axial ligands.

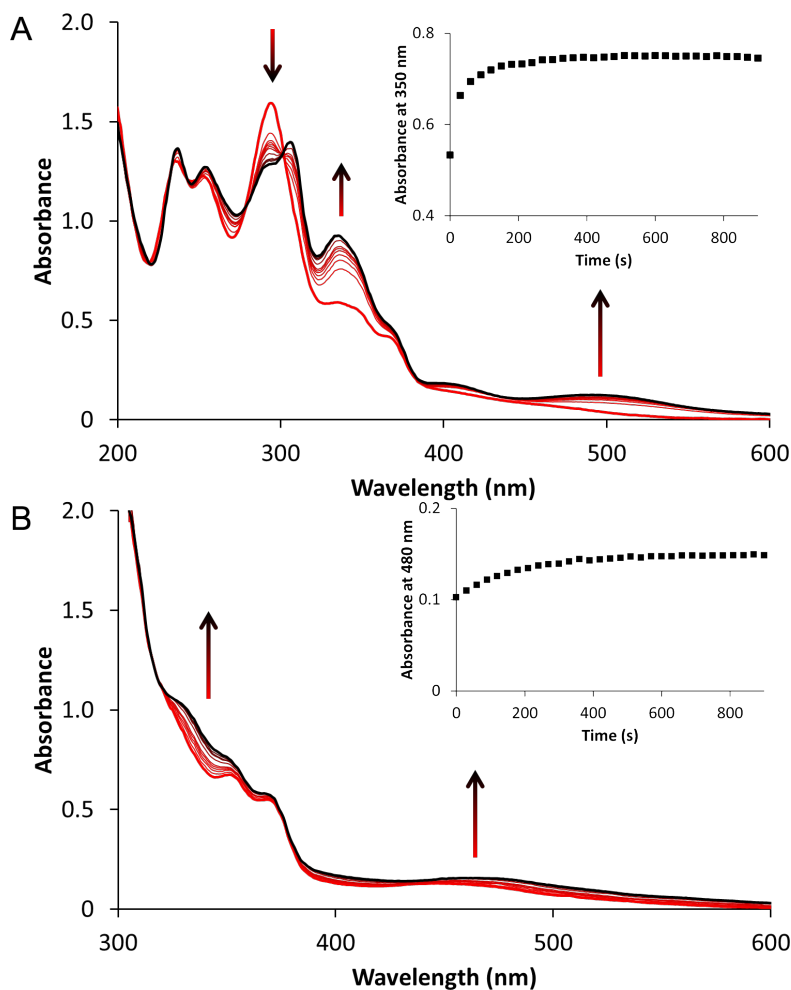


Figure 5.2 Evolution of the electronic absorption spectra of a solution of [2]Cl (A) in demineralized water (5% v/v CD₃OD) and of [3](PF₆)₂ (B) in demineralized water upon (5% v/v acetone-d₆) upon blue light irradiation ($\lambda_{\text{irr}} = 445 \text{ nm}$, $\Delta\lambda_{1/2} = 22 \text{ nm}$, photon flux $\Phi = 1.81 \times 10^{-7} \text{ mol}\cdot\text{s}^{-1}$, $t_{\text{irr}} = 15 \text{ min}$). Time: 0 min (red curve) to 15 min (black curve). Conditions $[\text{Ru}]_0 = 0.05 \text{ mM}$, irradiated volume was 3.0 mL at 298 K. Inset: Plot of the absorbance at 350 nm (A) or 480 nm (B) as a function of irradiation time.

5.2.4 Gel electrophoresis with ODN1

ODNs have proven to be valuable model targets for anticancer compounds because they can be specifically designed, and easily studied by for instance mass spectrometry.^{40, 41} As [1]Cl is phototoxic, cytotoxic, and enters the nucleus, we aimed to study our small library of tetrapyridyl ruthenium complexes in their reactions with a standard ODN. Thus, ODN1 (s(⁵CTACGGTTTCAC^{3'})) was reacted

with [1]Cl, [2]Cl, [3](PF₆)₂, and [4](PF₆)₂ to start building a structure-activity relationship. Like in previous studies ODN1 contains a GG-box, an important binding motif for cisplatin.⁴⁰

The outcomes of the dark and photochemical reactions were analyzed using gel electrophoresis to study the influence of light on the interaction of the ruthenium complexes with ODN1 and were performed by Geri F. Moolenaar. The binding of a ruthenium complex to ODN1 significantly adds to the molecular weight of the oligonucleotide, and can add up to two positive charges per ruthenium complex to an otherwise negatively charged oligonucleotide. Both factors contribute to retardation of migration of ODN1 on the gel. In these experiments three equivalents of [1]Cl, [2]Cl, [3](PF₆)₂, or [4](PF₆)₂ were added to ODN1, light-activated, and incubated for 6 hours with ODN1 ([ODN] = 0.25 mM, [Ru] = 0.75 mM). The mixtures were then pipetted on to a gel, the gel was run, and the adducts were visualized using toluidine blue (Figure 5.3).⁴² Without light activation all complexes (Figure 5.3, lane 1, 3, 5, and 7) showed band migration identical to the untreated ODN1 (lane 9), indicating that under such conditions no ruthenium-ODN1 adducts formed, irrespective of the structure of the complex. When the compounds were light-activated in the presence of ODN1, all free ODN1 bands decreased in intensity, and two extra bands appeared above the original ODN1 band (Figure 5.3, lane 2, 4, 6, and 8). This strongly indicates that each light-activated ruthenium complex forms two distinct adducts with ODN1.

Another gel electrophoresis measurement was performed including 19-, 23-, 24-, and 31-mer oligonucleotides, together with an irradiated but untreated ODN1 (12-mer) control sample (Figure SV.7). The first ruthenium-ODN1 adduct band ended up between the bands of the 24-mer and 31-mer control ODNs. The second ruthenium-ODN1 adduct band ended up between the 19-mer control and the untreated ODN1 control. As coordination of ruthenium complexes to ODN1 would add the molecular weight equivalent of 1-2 base pairs, the band of such an adduct would be at the level of a 13- or 14-mer in the case of a monoruthenium adduct, and at the level of a 15- or 16-mer for a bisruthenium adduct. As migration of the adduct bands did not correspond to these levels, the (di)cationic charge of the ruthenium must have an extra lagging effect of the adduct band in gel migration. Lastly, the irradiated ODN1 control band runs at the same level as the dark ODN1 control band, indicating that irradiation does not have any effect on the ODN1 itself. Overall, whereas no reaction occurred in the dark, light activation of all four ruthenium complexes induced strong interactions with ODN1. However, it is impossible at this stage to characterize these adducts.

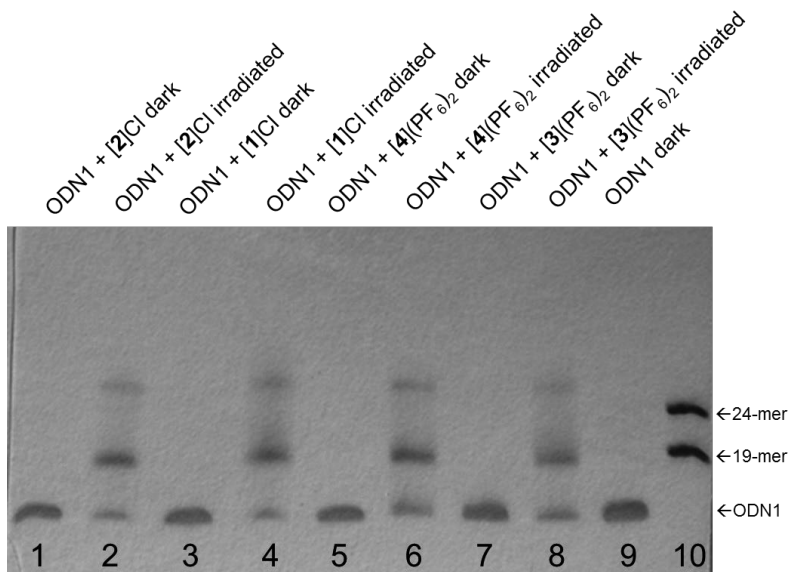


Figure 5.3 Polyacrylamide gel of mixtures of ODN1 ($5'$ CTACGGTTTCAC $3'$) and [2]Cl, [1]Cl, [4](PF₆)₂, or [3](PF₆)₂. Lane 1, 3, 5, and 7 correspond to dark reaction between ODN1 and [2]Cl, [1]Cl, [4](PF₆)₂, or [3](PF₆)₂, respectively. Lane 2, 4, 6, and 8 have the same composition but were irradiated. Lane 9 and 10 correspond to ODN1 and 19-24 mer controls, respectively (in the dark). Conditions: T = 25 °C, [Ru] = 0.75 mM, [ODN] = 0.25 mM, Staining agent: Toluidine blue. Conditions: irradiation $\lambda_{\text{irr}} = 445$ nm, $\Delta\lambda_{1/2} = 22$ nm, photon flux $\Phi = 2.2 \times 10^{-7}$ mol.s⁻¹, $t_{\text{irr}} = 10$ min, $t_{\text{inc}} = 6$ h.

5.2.5 High resolution mass spectrometry

In order to identify the ruthenium-ODN1 adducts similar experiments were run but samples were investigated using high resolution mass spectrometry (HRMS). For dark reaction ODN1 was incubated in LC-MS grade water at 25 °C for 6 hours – while shielded from light – in the presence of three equivalents of one of the four ruthenium complexes. Then, mass spectra in negative mode were recorded, and deconvoluted for clarity.⁴³⁻⁴⁵ Incubation of ODN1 with [1]Cl or [2]Cl without light activation resulted in major signals at $m = 3595.7$ corresponding to free ODN (calc. $m = 3594.6$). Minor signals at $m = 4213.6$ corresponding to [ODN1 + Ru(biqbpy)(dmsO)] (calc. $m = 4212.7$, see Figure 5.4A and Figure SV.10A), or at $m = 4113.1$ corresponding to [ODN1 + Ru(bapbpy)(dmsO)] (calc. $m = 4112.7$, see Figure SV.11A), respectively, indicated that limited adduct formation in the dark was possible, but that the dmsO stayed bound to ruthenium. When comparing [1]Cl and [2]Cl the ratio between the adduct signals and that of the free ODN1 was found to be lower for [1]Cl than for [2]Cl, indicating that under such conditions [2]Cl was more susceptible for adduct formation with ODN1 than [1]Cl. When ODN1 was incubated with [3](PF₆)₂ or [4](PF₆)₂ major peaks were found at $m =$

3595.7 corresponding to the free ODN1 (calc. $m = 3594.6$, Figure SV.12A and Figure SV.13A, respectively). Whereas incubation with [3](PF₆)₂ resulted in virtually no ruthenium adduct signals, with [4](PF₆)₂ a minor signal at $m = 4034.7$ corresponding to ruthenium adducts [ODN1 + Ru(bapbpy)] (calc. $m = 4034.7$) was found. It appears that Hmte ligands do not stay coordinated to the ruthenium center in such adducts; but these signals were of lower intensity compared to that of the ruthenium adducts found with [2]Cl (Figure SV.11A). Overall, for both the H₂bapbpy and H₂biqbpy complexes coordination of two *trans* thioethers strongly inhibits the formation of ODN1-ruthenium adducts, compared to the coordination of dmsO and a *trans* chloride ligand that is hydrolyzed thermally in water.

Adduct-formation was also measured by HRMS after mixing ODN1 and ruthenium complex, after visible light activation ($\lambda_{\text{irr}} = 445 \text{ nm}$) and 6 hours incubation. With [1]Cl the signals for free ODN1 were still dominant but a new set of peaks was present at $m = 4136.3$ that corresponded to the adduct [ODN1 + Ru(biqbpy)] (calc. $m = 4136.7$, see Figure 5.4B and Figure SV.10B). This peak is different from the peak observed in the dark, since the dmsO ligand appeared to be removed. With [2]Cl the strongest signals were observed at $m = 4035.6$ corresponding to a similar adduct [ODN1 + Ru(bapbpy)] (calc. $m = 4034.7$), while a minor set of peaks at $m = 4475.0$ corresponds to the dinuclear adduct [ODN1 + 2(Ru(bapbpy))] (calc. $m = 4474.7$, Figure 5.4C and Figure SV.11B). Noteworthy, the signals at $m = 3617.0$ corresponding to [ODN1 + Na] (calc. $m = 3617.6$) remained, but it was significantly less intense compared to the dark control. These results show that the ligand dmsO in these tetrapyrrolyl ruthenium complexes has an inhibiting effect on adduct-formation with ODN1.

With [3](PF₆)₂ upon light irradiation new signals were observed at $m = 4135.3$ corresponding to the adduct [ODN1 + Ru(biqbpy)] (calc. $m = 4134.7$, see Figure SV.12). However, the signals at $m = 3617.4$ correspond to [ODN1 + Na] are still dominant. This behavior was similar to that found for [1]Cl in presence of light, which confirmed the observations using gel electrophoresis that [1]Cl and [3](PF₆)₂ are, after light irradiation, similar. With [4](PF₆)₂ like with [2]Cl dominant signals were observed, after light activation, at $m = 4034.8$ corresponding to the adduct [ODN1 + Ru(bapbpy)] (calc. $m = 4034.7$, see Figure SV.13). Here as well, both thioether ligands had been photosubstituted and traces of a dinuclear-ODN1 adduct were observed. This result confirmed that [4](PF₆)₂ and [2]Cl interact in a similar fashion with ODN1 after light irradiation, and that the H₂bapbpy-based complexes interact better with ODN1 than the H₂biqbpy-based analogues.

Overall, from these HRMS experiments three well-defined trends can be delineated. First, light activation of the complex strongly enhances adduct

formation between tetrapyrridyl ruthenium complexes and ODN1, which depends on whether none, one, or two axial protecting ligands are coordinated. Second, the nature of the tetrapyrridyl ligand, H₂bapbpy vs. H₂biqbpy, influences significantly the degree of adduct formation after light activation: H₂bapbpy complexes are more prone to interact with ODN1 than H₂biqbpy complexes. Third, light activation of [2]Cl and [4](PF₆)₂ leads to the formation of adducts with ODN1 that can have either one or two bound ruthenium complexes.

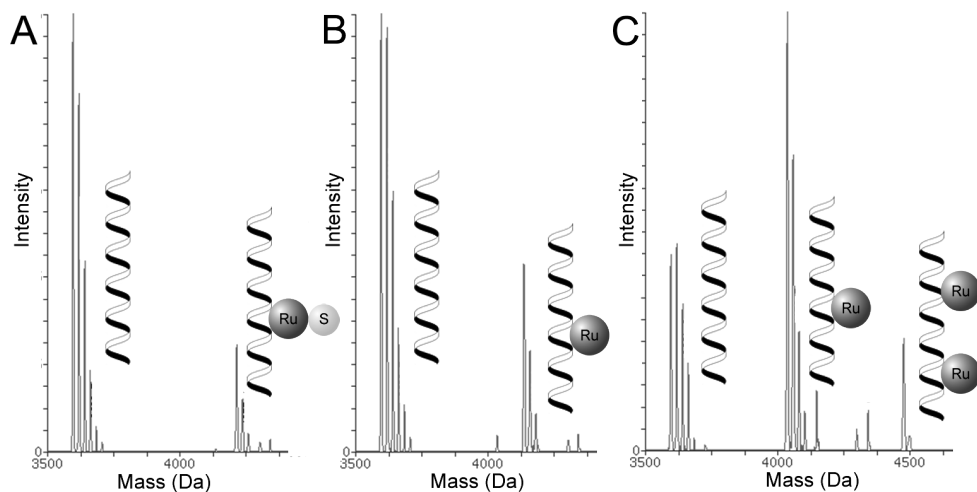


Figure 5.4 Representative scheme of the deconvoluted mass spectrometry data of ODN1 incubated with [1]Cl (A), incubated with light-activated [1]Cl (B), and incubated with light-activated [2]Cl. Full data set and interpretation can be found in the Supplementary Information. Conditions: [ODN] = 0.03 mM, [Ru] = 0.09 mM, $t_{\text{irr}} = 10$ min, $t_{\text{inc}} = 6$ h, $T = 298$ K, $\lambda_{\text{irr}} = 445$ nm ($\Delta\lambda_{1/2} = 22$ nm), photon flux $\Phi = 2.2 \times 10^{-7}$ mol.s⁻¹

5.3 Discussion & Conclusion

In this work it has been demonstrated that light can be used to control the interaction between ruthenium complexes with a H₂bapbpy or H₂biqbpy ligand and an oligonucleotide. The absence of adduct formation in the dark demonstrates that a single dmsoligand, or two *trans* thioether ligands, strongly inhibit the interaction of the metal complex with nucleotides. Meanwhile, by combining gel electrophoresis and mass spectrometry results, we observed that the adducts formed upon light activation consist of a single strand containing one or two complexes. No traces of adducts containing one ruthenium center and two oligonucleotides were found, indicating that no inter-strand crosslinking occurs.

Trans ruthenium complexes cannot mimic the cisplatin binding mode, which implies a different type of DNA binding. While the HRMS data in our study

suggests that after light activation the complexes have two coordination sites available for DNA interaction, it is hard to imagine both being employed by coordination to adjacent DNA bases like cisplatin. Transplatin, on the other hand, is known to form crosslinks between different strands, but we found no indication that the *trans* ruthenium complexes [1]⁺-[4]²⁺ form adducts with more than one strand. Another interaction responsible for DNA binding of metallodrugs is their ability to form hydrogen bonds with especially the phosphate backbone of DNA.²
^{46, 47} All four compounds are similar in having non-coordinated amines that may engage into H-bonding. Thus, the differences observed between the H₂biqbpy and H₂bapbpy complexes can probably not be explained by differences in H-bonding; it is unclear whether such H-bonding is taking place for this series of complexes. On the other hand, the *trans* tetrapyrindyl complexes, and in particular the ones based on H₂biqbpy, have a strong lipophilic character due to their tetrapyrindyl ligands, that are often involved in stacking or intercalation interactions.⁴⁸⁻⁵⁰ Despite the lack of stacking surface and flatness, the complexes do interact differently with oligonucleotides when either a H₂bapbpy or H₂biqbpy tetrapyrindyl ligand is employed under the same conditions. As other compound parameters, such as bond distances and bond angles, are similar for all investigated ruthenium complexes, it follows that non-coordinating interactions may play an important role in DNA interaction and could explain the essential differences observed between H₂bapbpy and H₂biqbpy complexes.⁵¹ Further studies are currently ongoing investigate this question.

5.4 Experimental

5.4.1 Synthesis of [Ru(H₂bapbpy)(dmsO)Cl]Cl ([2]Cl)

In a 2-necked round-bottom flask [Ru(dmsO)₄Cl₂] (200 mg, 0.413 mmol) and H₂bapbpy (144 mg, 0.413 mmol) were added in degassed ethanol (30 mL). The solution was stirred overnight at 80 °C, upon which a dark red suspension was formed. After filtration and drying a red powder was obtained. Yield: 121 mg (50%). ¹H NMR (300 MHz, D₂O, 293 K, in ppm): δ = 8.54 (dd, 2H J = 6.1, 1.1 Hz, H^{py-6}), 8.24 (dd, 2H, J = 7.8, 0.9 Hz, H⁵), 8.15 (t, 2H, J = 8.1 Hz, H⁴), 8.05 (m, 2H, H^{py-5}), 7.51 (dd, 2H, J = 8.3, 0.8 Hz, H³), 7.45 (dd, 2H, J = 8.4, 0.8 Hz, H^{py-3}), 7.28 – 7.18 (m, 2H, H^{py-4}), 2.43 (s, 6H, H^α). ¹³C NMR (100 MHz, 300 K, D₂O, in ppm): δ = 152.69 (C^{py-3}), 140.16 (C^{py-5}), 139.85 (C⁴), 119.46 (C^{py-4}), 118.33 (C⁵), 116.17 (C^{py-6}), 115.79 (C³), 44.44 (C^α). High resolution ES MS m/z (calc): 555.0304 (555.0308 for [M – Cl – H]⁺), 519.053 (519.054 for [M – 2Cl – H]⁺). Elem. anal. calcd. for C₂₂H₂₂Cl₂N₆ORuS: C, 44.75; H, 3.76; N, 14.23. Found: C, 44.71; H, 3.76; N, 14.17.

Single crystals of [2]Cl were obtained by crystallization via liquid-vapor diffusion using MeOH as solvent and EtOAc as counter-solvent. In short, 1.0 mg of [2]Cl was dissolved in 1

mL of MeOH and placed in a small GC vial. This vial was placed in a larger vial containing 2.8 mL EtOAc. The large vial was closed and vapor diffusion occurred within a few days to afford X-ray quality crystals.

5.4.2 Synthesis of [Ru(H₂biqbpy)(Hmte)₂](PF₆)₂ ([3](PF₆)₂)

In a 2-necked round-bottom flask [1]Cl (19 mg, 0.028 mmol) and Hmte (0.24 mL, 2.7 mmol) were added in degassed demineralized water (10 mL). The reaction mixture was stirred overnight at 80 °C, resulting in a red solution. After full conversion was checked by TLC (eluent: acetone/water/aqueous KPF₆ (sat.), 5:2:2), the reaction was cooled down to room temperature and KPF₆ (0.4 g, 2.2 mmol) was added. Then, the aqueous layer was extracted with dichloromethane (3 × 15 mL), and the organic layer was evaporated *in vacuo*. The compound was purified using size exclusion chromatography (Sephadex LH-20, acetone). After evaporation the product was reprecipitated from acetone (0.5 mL) by the addition of diethyl ether (10 mL). Yield: 19 mg (68%). ¹H NMR (400 MHz, acetone-d₆, 293 K): δ = 10.42 (s, 2H, NH), 8.87 (d, 2H, J = 8.8 Hz, H^{qi-4}), 8.68 (d, 2H, J = 7.6 Hz, H^{qi-7}), 8.64 (d, 2H, J = 6.8 Hz, H^{qi-9}), 8.40 (t, 2H, J = 8.4 Hz, H^{qi-6}), 8.16 (d, 4H, J = 7.6 Hz, H^β and H^γ), 8.02 (t, 2H, J = 7.2 Hz, H^{qi-5}), 7.94 (t, 2H, J = 8.4 Hz, H^{qi-10}), 3.39-3.32 (m, 4H, H^β), 2.10-2.00 (m, 4H, H^γ), 2.10-2.00 (m, 4H, H^γ), 1.53 (s, 6H, H^α). ¹³C NMR (125 MHz, acetone-d₆, 293 K, in ppm): δ = 156.70 (C²), 152.45 (C⁶), 151.62 (C^{qi-2}), 146.11 (C^{qi-9}), 139.01 (C^{qi-6}), 137.23 (C^{qi-8}), 133.42 (C^{*}), 130.09 (C^{qi-5}), 128.77 (C⁵), 123.75 (C⁴), 120.90 (C^{qi-3}), 120.84 (C^{qi-7}), 120.35 (C^{qi-10}), 118.26 (C³), 59.28 (C^β), 38.78 (C^γ), 16.85 (C^α). High resolution ES MS m/z (calc): 725.1301 (725.1309, [M - 2PF₆ - H]⁺). Elem. anal. calcd. for C₃₄H₃₆F₁₂N₆O₂P₂RuS₂ + ½ Acetone: C, 40.81; H, 3.76; N, 8.04. Found: C, 40.53; H, 4.11; N, 8.37.

Single crystals of [3](PF₆)₂ were obtained by crystallization via liquid-vapor diffusion using acetone as solvent and diethylether as counter-solvent. In short, 1.0 mg of [3](PF₆)₂ was dissolved in 0.4 mL of acetone and placed in a small GC vial. This vial was placed in a larger vial containing 2.8 mL diethyl ether. The large vial was closed and vapor diffusion occurred within a few days to afford X-ray quality crystals.

5.4.3 Synthesis of [Ru(H₂bapbpy)(Hmte)₂](PF₆)₂ ([4](PF₆)₂)

In a 2-necked round-bottom flask [2]Cl (50 mg, 0.085 mmol) and Hmte (1.47 mL, 16 mmol) were added in degassed demineralized water (15 mL). The reaction mixture was stirred overnight at 80 °C, resulting in a red solution. After full conversion was ensured by TLC (eluent: acetone/water/aqueous KPF₆ (sat.), 5:2:2), the reaction mixture was cooled down to room temperature and KPF₆ (0.5 g, 2.7 mmol) was added. Then, the aqueous layer was extracted with ethyl acetate (3 × 15 mL), and the organic layer was evaporated *in vacuo*. The compound was purified using size exclusion chromatography (Sephadex LH-20, acetone). After evaporation the product was precipitated from acetone (0.5 mL) by the addition of diethyl ether (10 mL). Yield: 45 mg (58%). ¹H NMR (400 MHz, acetone-d₆, 293 K, in ppm): δ =

10.56 (s, 2H, N-H), 8.80 (d, 2H, $J = 6.0$ Hz py-6), 8.51 (d, 2H, $J = 7.6$ Hz, H⁵), 8.27 (d, 2H, $J = 8.4$ Hz, H⁴), 8.07 (dd, 2H, $J = 8.8$ Hz, py-4), 7.62 (d, 2H, $J = 8.4$ Hz, H⁵), 7.50 (d, 2H, $J = 8.4$ Hz, py-3), 7.36 (dd, 2H, $J = 7.2$ Hz, py-5), 3.42 (t, 4H, $J = 5.6$ Hz, H^γ), 2.01 (t, 4H, $J = 5.6$ Hz, H^β), 1.56 (s, 6H, H^α). ¹³C NMR (100 MHz, acetone-d₆, 293 K, in ppm): δ = 162.1 (C²), 154.3 (C^{py-6}), 139.9 (C^{py-4}), 139.2 (C⁴), 133.9 (C⁶), 130.5 (C^{py-2}), 120.3 (C^{py-5}), 119.2 (C⁵), 117.7 (C^{py-3}), 116.6 (C^{py-3}), 116.1 (C³), 59.5 (C^γ), 38.9 (C^β), 17.0 (C^α). High resolution ES MS m/z (calc): 574.0961 (574.0963, [M – PF₆ – H – Hmte + CH₃CN]⁺). Elem. anal. calcd. for C₂₆H₃₂F₁₂N₆O₂P₂RuS₂ + ½ acetone + ½ H₂O: C, 34.63; H, 3.80; N, 8.81. Found: C, 34.44; H, 4.33; N, 9.01.

Single crystals of [4](PF₆)₂ were obtained by crystallization through liquid-vapor diffusion using acetone as solvent and diethyl ether as counter-solvent. In short, 1.0 mg of [4](PF₆)₂ was dissolved in 0.4 mL of acetone and placed in a small vial. This vial was placed in a larger vial containing 2.8 mL diethyl ether. The large vial was closed and vapor diffusion occurred within a few days to afford X-ray quality crystals.

5.4.4 Crystal data for [2]Cl

All reflection intensities were measured at 110(2) K using a KM4/Xcalibur (detector: Sapphire3) with enhance graphite-monochromated Mo $K\alpha$ radiation ($\lambda = 0.71073$ Å) under the program CrysAlisPro (Version 1.171.35.11 Oxford Diffraction Ltd., 2011). The program CrysAlisPro was used to refine the cell dimensions. Data reduction was done using the program CrysAlisPro. The structure was solved with the program SHELXS-2014/7 and was refined on F^2 with SHELXL-2014/7.⁵² Analytical numeric absorption corrections based on a multifaceted crystal model were applied using CrysAlisPro. The temperature of the data collection was controlled using the system Cryojet (manufactured by Oxford Instruments). The H atoms (except when specified) were placed at calculated positions using the instructions AFIX 43 or AFIX 137 with isotropic displacement parameters having values 1.2 or 1.5 times U_{eq} of the attached C atoms. The H atoms attached to N2 n and N5 n ($n = A, B$) were located from difference Fourier maps; their atomic coordinates were refined freely using some restraints (DFIX instructions).

The structure is ordered. The crystal was found to be twinned non-merohedrally, and the twin relationship is a twofold axis found along the direct-space vector 0.0044 0.0086 1.0000. The batch scale factor of the minor component refines to 0.3188(11). The final structure refinement was performed using the HKL5 instruction (true hkl files including reflection sets for the twinned component 1 and the associated overlapped reflections from component 2).

Fw = 590.48, small orange block, 0.22 × 0.17 × 0.14 mm³, triclinic, $P-1$ (no. 2), $a = 12.6164(2)$, $b = 13.6053(3)$, $c = 14.3404(3)$ Å, $\alpha = 100.1729(17)$, $\beta = 92.9120(16)$, $\gamma = 106.0391(17)^\circ$, $V = 2315.57(8)$ Å³, $Z = 4$, $D_x = 1.694$ g cm⁻³, $\mu = 1.027$ mm⁻¹, T_{min} - T_{max} : 0.831–0.900. 36503

Reflections were measured up to a resolution of $(\sin \theta/\lambda)_{\max} = 0.59 \text{ \AA}^{-1}$. 9478 Reflections were unique ($R_{\text{int}} = 0.031$, including overlapped reflections from twin component 2), of which 7962 were observed [$I > 2\sigma(I)$]. 616 Parameters were refined using 4 restraints. $R1/wR2$ [$I > 2\sigma(I)$]: 0.0410/0.1012. $R1/wR2$ [all refl.]: 0.0536/0.1091. $S = 1.096$. Residual electron density found between -0.75 and 0.87 e.\AA^{-3} .

5.4.5 Crystal data for [3](PF₆)₂

All reflection intensities were measured at 110(2) K using a SuperNova diffractometer (equipped with Atlas detector) with Cu $K\alpha$ radiation ($\lambda = 1.54178 \text{ \AA}$) under the program CrysAlisPro (Version 1.171.37.35 Agilent Technologies, 2014). The same program was used to refine the cell dimensions and for data reduction. The structure was solved with the program SHELXS-2014/7 and was refined on F^2 with SHELXL-2014/7.⁵² Analytical numeric absorption correction based on a multifaceted crystal model was applied using CrysAlisPro. The temperature of the data collection was controlled using the system Cryojet (manufactured by Oxford Instruments). The H atoms were placed at calculated positions (unless otherwise specified) using the instructions AFIX 23, AFIX 43, AFIX 137 or AFIX 147 (for the disordered O-H group) with isotropic displacement parameters having values 1.2 or 1.5 U_{eq} of the attached C or O atoms. The H atoms attached to N2, N5 and O1 were found from difference Fourier maps, and their coordinates were refined freely using the DFIX restraints.

The structure is partly disordered. One of the two counter-ions, and O2/O2' (OH group) are disordered over two orientations. The occupancy factors of the major components of the disorder refine to 0.624(13) and 0.77(5), respectively. The crystal that was mounted on the diffractometer was non-merohedrally twinned, and the twin relationship corresponds to a twofold axis along the $0.0009\mathbf{a}^* + 0.9998\mathbf{b}^* + 0.0201\mathbf{c}^*$ vector. The BASF scale factor refines to 0.2115(9).

$F_w = 1015.82$, red block, $0.21 \times 0.19 \times 0.14 \text{ mm}^3$, monoclinic, $P2_1/n$ (no. 14), $a = 9.54745$ (18), $b = 21.8432$ (4), $c = 18.4565$ (3) \AA , $\beta = 98.2773$ (17) $^\circ$, $V = 3808.95$ (12) \AA^3 , $Z = 4$, $\mu = 6.08 \text{ mm}^{-1}$, $T_{\text{min}}-T_{\text{max}}$: 0.401-0.563. 27773 reflections were measured up to a resolution of $(\sin \theta/\lambda)_{\max} = 0.616 \text{ \AA}^{-1}$. 10943 reflections were unique ($R_{\text{int}} = 0.022$), of which 9630 were observed [$I > 2\sigma(I)$]. 620 Parameters were refined using 256 restraints. $R1/wR2$ [$I > 2\sigma(I)$]: 0.029/0.0943. $R1/wR2$ [all refl.]: 0.0333/0.0963. $S = 0.99$. Residual electron density found between -0.66 and 0.64 e.\AA^{-3} .

5.4.6 Crystal data for [4](PF₆)₂

All reflection intensities were measured at 110(2) K using a SuperNova diffractometer (equipped with Atlas detector) with Cu $K\alpha$ radiation ($\lambda = 1.54178 \text{ \AA}$) under the program CrysAlisPro (Version 1.171.36.32 Agilent Technologies, 2013). The same program was used to refine the cell dimensions and for data reduction. The structure was solved with the

program SHELXS-2014/7 and was refined on F^2 with SHELXL-2014/7.⁵² Analytical numeric absorption correction based on a multifaceted crystal model was applied using CrysAlisPro. The temperature of the data collection was controlled using the system Cryojet (manufactured by Oxford Instruments). The H atoms were placed at calculated positions (unless otherwise specified) using the instructions AFIX 23, AFIX 43 or AFIX 137 with isotropic displacement parameters having values 1.2 or 1.5 U_{eq} of the attached C atoms. The H atoms attached to N2 and O1 were found from difference Fourier maps, and their coordinates were refined freely using the DFIX instruction.

The structure is ordered. The ruthenium complex is found at sites of twofold axial symmetry, and only one half of the molecule is found to be crystallographically independent.

$F_w = 915.70$, orange-red needle, $0.25 \times 0.05 \times 0.02 \text{ mm}^3$, monoclinic, $I2/a$, $a = 18.9321(3)$, $b = 11.23471(18)$, $c = 15.6066(2) \text{ \AA}$, $\beta = 96.7047(15)^\circ$, $V = 3296.77(9) \text{ \AA}^3$, $Z = 4$, $\mu = 6.94 \text{ mm}^{-1}$, $T_{\text{min}}-T_{\text{max}}: 0.391-0.881$. 10972 reflections were measured up to a resolution of $(\sin \theta/\lambda)_{\text{max}} = 0.616 \text{ \AA}^{-1}$. 3243 reflections were unique ($R_{\text{int}} = 0.024$), of which 3045 were observed [$I > 2\sigma(I)$]. 239 Parameters were refined using 2 restraints. $R1/wR2$ [$I > 2\sigma(I)$]: 0.0378/ 0.1016. $R1/wR2$ [all refl.]: 0.0399/0.1034. $S = 1.06$. Residual electron density found between -0.74 and $2.11 \text{ e}^- \text{ \AA}^{-3}$.

Additional notes:

(i) The residual electron density peak of $2.11 \text{ e}^- \text{ \AA}^{-3}$ found at 0.75 \AA from Ru1 is chemically meaningless. All remaining residual electron density peaks are lower than $1 \text{ e}^- \text{ \AA}^{-3}$.

(ii) The occupancy factor of Ru1 was refined freely (its value was $1.034(3) \times 0.5 = 0.517(2)$) before being constrained to 0.5 in the final refinement.

5.4.7 UV-vis spectroscopy absorbance studies

Photoreactivity and stability studies were monitored using a UV-vis spectrometer equipped with temperature control set to 298 K and a magnetic stirrer. The measurements were performed in a quartz cuvette, containing 3 mL of solution (0.010-0.050 mM). The stirred sample was irradiated perpendicularly to the axis of the spectrometer with a blue LED ($\lambda = 445 \text{ nm}$, $\Delta\lambda_{1/2} = 22 \text{ nm}$, photon flux $\Phi = 1.8 \times 10^{-8} \text{ mol} \cdot \text{s}^{-1}$, $t_{\text{irr}} = 10 \text{ minutes}$) fitted to the top of the cuvette, and an absorption spectrum was measured at regular time intervals and analyzed using Microsoft Excel. Mass spectrometry was performed at the beginning and at the end of the irradiation to confirm the nature of the reagent and products.

5.4.8 Gel studies

HPLC purified ODN1 was ordered from Sigma-Aldrich and received as a solid (fixed amount), and LC-MS water was added in such amounts that a 1 mM solution was obtained.

[1]Cl and [2]Cl were dissolved in methanol, [3](PF₆)₂ and [4](PF₆)₂ were dissolved in acetone to obtain 1 mM solutions. Then, 5 μL of ODN solution, 15 μL Ru solution, and 5 μL MilliQ water were transferred to a 1 mL quartz cuvette, and irradiated for 10 minutes by blue LED ($\lambda_{\text{irr}} = 445 \text{ nm}$, $\Delta\lambda_{1/2} = 22 \text{ nm}$, photon flux $\Phi = 2.2 \times 10^{-7} \text{ mol}\cdot\text{s}^{-1}$, $t_{\text{irr}} = 10 \text{ minutes}$). Following irradiation, the sample was transferred to a 1.5 mL Eppendorf microtube and incubated in the dark for 6 hours at 298 K. Then, 1-2 μL of the mixture (containing 400 pmol of ODN1 per lane) was added to 3 μL formamide/dye solution (formamide 0.01% (w/v), bromophenol blue and 0.01% (w/v), Xylenecyanol 0.01% (w/v)) and loaded (without heating) on a 20% polyacrylamide gel containing 8 M Urea in 1x Tris/Borate/EDTA buffer. After electrophoresis (22 mA/gel) the gel was stained for 5 min in 0.01% w/v Toluidine Blue O ((7-amino-8-methyl-phenothiazin-3-ylidene)-dimethyl-ammonium) in water on a rotary shaker. The background staining was removed by washing the gel multiple times with tap water. The procedure was adapted from Popa and Bosch.⁴²

5.4.9 HRMS ODN experiments

HPLC purified ODN1 ((s⁵CTACGGTTTCAC³)) was ordered from Sigma-Aldrich and received as a solid (fixed amount). LC-MS water was added in such amounts that a 1 mM solution was obtained. [1]Cl and [2]Cl were dissolved in methanol, [3](PF₆)₂ and [4](PF₆)₂ were dissolved in acetone to obtain 1 mM solutions. Then, 15 μL of ODN1 aqueous solution, 45 μL Ru solution, and 450 μL LC-MS grade water, were transferred to a 1 mL quartz cuvette, and irradiated for 10 minutes by blue a LED ($\lambda_{\text{irr}} = 445 \text{ nm}$, $\Delta\lambda_{1/2} = 22 \text{ nm}$, photon flux $\Phi = 2.2 \times 10^{-7} \text{ mol}\cdot\text{s}^{-1}$, $t_{\text{irr}} = 10 \text{ minutes}$). Following irradiation, the sample was transferred to a 1.5 mL Eppendorf microtube and incubated in the dark for 6 hours at 298 K. For every sample a control sample shielded from light in a parallel experiment was performed. Then, the solutions were directly injected (flowrate = 5 μL min⁻¹, 1:1 water/methanol) in an Orbitrap high-resolution mass spectrometer (Thermo, San Jose, CA, USA), equipped with a conventional ESI source. The mass spectra have been recorded in the range 300-2000 m/z values. The following standardized working conditions were applied: spray voltage 2.7 kV, tube lens voltage -113 V, capillary voltage -20 V and capillary temperature 280 °C. Sheath and auxiliary gases were set at 23 a.u. and 4 a.u., respectively. The mass spectra were deconvoluted using ProMass for Xcalibur (ThermoQuest, Finnigan).

5.5 References

1. L. Kelland, *Nat. Rev. Cancer*, 2007, **7**, 573-584.
2. J. Reedijk, *Proc. Natl. Acad. Sci. USA*, 2003, **100**, 3611-3616.
3. S. E. Sherman and S. J. Lippard, *Chem. Rev.*, 1987, **87**, 1153-1181.
4. F. Wang, A. Habtemariam, E. P. L. van der Geer, R. Fernández, M. Melchart, R. J. Deeth, R. Aird, S. Guichard, F. P. A. Fabbiani, P. Lozano-Casal, I. D. H. Oswald, D. I. Jodrell, S. Parsons and P. J. Sadler, *Proc. Natl. Acad. Sci. USA*, 2005, **102**, 18269-18274.
5. A.-M. Florea and D. Büsselberg, *Cancers*, 2011, **3**, 1351.
6. Z. H. Siddik, *Oncogene*, 2003, **22**, 7265-7279.
7. E. Wachter, A. Zamora, D. K. Heidary, J. Ruiz and E. C. Glazer, *Chem. Commun.*, 2016, **52**, 10121-10124.
8. A. G. Quiroga, *J. Inorg. Biochem.*, 2012, **114**, 106-112.
9. L. Messori, L. Cubo, C. Gabbiani, A. Álvarez-Valdés, E. Michelucci, G. Pieraccini, C. Ríos-Luci, L. G. León, J. M. Padrón, C. Navarro-Ranninger, A. Casini and A. G. Quiroga, *Inorg. Chem.*, 2012, **51**, 1717-1726.
10. F. J. Ramos-Lima, A. G. Quiroga, B. García-Serrelde, F. Blanco, A. Carnero and C. Navarro-Ranninger, *J. Med. Chem.*, 2007, **50**, 2194-2199.
11. B. S. Howerton, D. K. Heidary and E. C. Glazer, *J. Am. Chem. Soc.*, 2012, **134**, 8324-8327.
12. N. J. Farrer, J. A. Woods, L. Salassa, Y. Zhao, K. S. Robinson, G. Clarkson, F. S. Mackay and P. J. Sadler, *Angew. Chem., Int. Ed.*, 2010, **49**, 8905-8908.
13. R. E. Mahnken, M. Bina, R. M. Deibel, K. Luebke and H. Morrison, *Photochem. Photobiol.*, 1989, **49**, 519-522.
14. R. E. Mahnken, M. A. Billadeau, E. P. Nikonowicz and H. Morrison, *J. Am. Chem. Soc.*, 1992, **114**, 9253-9265.
15. D. A. Lutterman, P. K. L. Fu and C. Turro, *J. Am. Chem. Soc.*, 2006, **128**, 738-739.
16. Z. Li, S. J. Burya, C. Turro and K. R. Dunbar, *Phil. Trans. R. Soc. A*, 2013, **371**, 20120128.
17. M. A. Sgambellone, A. David, R. N. Garner, K. R. Dunbar and C. Turro, *J. Am. Chem. Soc.*, 2013, **135**, 11274-11282.
18. T. Joshi, V. Pierroz, C. Mari, L. Gemperle, S. Ferrari and G. Gasser, *Angew. Chem., Int. Ed.*, 2014, **53**, 2960-2963.
19. Z. Li, A. David, B. A. Albani, J.-P. Pellois, C. Turro and K. R. Dunbar, *J. Am. Chem. Soc.*, 2014, **136**, 17058-17070.
20. F. S. Mackay, J. A. Woods, P. Heringová, J. Kašpárková, A. M. Pizarro, S. A. Moggach, S. Parsons, V. Brabec and P. J. Sadler, *Proc. Natl. Acad. Sci. USA*, 2007, **104**, 20743-20748.
21. F. Navas, S. Perfahl, C. Garino, L. Salassa, O. Novakova, C. Navarro-Ranninger, P. J. Bednarski, J. Malina and A. G. Quiroga, *J. Inorg. Biochem.*, 2015, **153**, 211-218.
22. P. Heringová, J. Woods, F. S. Mackay, J. Kasparkova, P. J. Sadler and V. Brabec, *J. Med. Chem.*, 2006, **49**, 7792-7798.
23. N. J. Farrer, J. A. Woods, V. P. Munk, F. S. Mackay and P. J. Sadler, *Chem. Res. Toxicol.*, 2010, **23**, 413-421.
24. C. Moucheron, *New J. Chem.*, 2009, **33**, 235-245.
25. C. Mari, V. Pierroz, S. Ferrari and G. Gasser, *Chem. Sci.*, 2015, **6**, 2660-2686.
26. A. N. Hidayatullah, E. Wachter, D. K. Heidary, S. Parkin and E. C. Glazer, *Inorg. Chem.*, 2014, **53**, 10030-10032.
27. S. J. Burya, A. M. Palmer, J. C. Gallucci and C. Turro, *Inorg. Chem.*, 2012, **51**, 11882-11890.
28. O. Filevich and R. Etchenique, *Photochem. Photobiol. Sci.*, 2013, **12**, 1565-1570.
29. L. Cubo, A. M. Pizarro, A. G. Quiroga, L. Salassa, C. Navarro-Ranninger and P. J. Sadler, *J. Inorg. Biochem.*, 2010, **104**, 909-918.
30. P. M. Takahara, A. C. Rosenzweig, C. A. Frederick and S. J. Lippard, *Nature*, 1995, **377**, 649-652.
31. V. H. S. van Rixel, B. Siewert, S. L. Hopkins, S. H. C. Askes, A. Busemann, M. A. Siegler and S. Bonnet, *Chem. Sci.*, 2016, **7**, 4922-4929.
32. J. L. Beck, M. L. Colgrave, S. F. Ralph and M. M. Sheil, *Mass Spectrom. Rev.*, 2001, **20**, 61-87.
33. M. Groessl and P. J. Dyson, *Curr. Top. Med. Chem.*, 2011, **11**, 2632-2646.
34. E. R. Jamieson and S. J. Lippard, *Chem. Rev.*, 1999, **99**, 2467-2498.
35. J.-M. Teuben and J. Reedijk, *J. Biol. Inorg. Chem.*, 2000, **5**, 463-468.
36. J. Rodríguez, J. Mosquera, J. R. Couceiro, M. E. Vázquez and J. L. Mascareñas, *Angew. Chem., Int. Ed.*, 2016, **55**, 15615-15618.

37. R. E. Goldbach, I. Rodriguez-Garcia, J. H. van Lenthe, M. A. Siegler and S. Bonnet, *Chem. Eur. J.*, 2011, **17**, 9924-9929.
38. S. Bonnet, G. Molnár, J. Sanchez Costa, M. A. Siegler, A. L. Spek, A. Bousseksou, W.-T. Fu, P. Gamez and J. Reedijk, *Chem. Mater.*, 2009, **21**, 1123-1136.
39. Z. Arcis-Castillo, S. Zheng, M. A. Siegler, O. Roubeau, S. Bedoui and S. Bonnet, *Chem. Eur. J.*, 2011, **17**, 14826-14836.
40. D. Musumeci, C. Platella, C. Riccardi, A. Merlino, T. Marzo, L. Massai, L. Messori and D. Montesarchio, *Dalton Trans.*, 2016, **45**, 8587-8600.
41. D. Musumeci, L. Rozza, A. Merlino, L. Paduano, T. Marzo, L. Massai, L. Messori and D. Montesarchio, *Dalton Trans.*, 2015, **44**, 13914-13925.
42. L. M. Popa and L. Bosch, *FEBS Lett.*, 1969, **4**, 143-146.
43. A. Casini, C. Gabbiani, E. Michelucci, G. Pieraccini, G. Moneti, P. J. Dyson and L. Messori, *J. Biol. Inorg. Chem.*, 2009, **14**, 761-770.
44. A. Casini, A. Guerri, C. Gabbiani and L. Messori, *J. Inorg. Biochem.*, 2008, **102**, 995-1006.
45. A. Casini, G. Mastrobuoni, C. Temperini, C. Gabbiani, S. Francese, G. Moneti, C. T. Supuran, A. Scozzafava and L. Messori, *Chem. Commun.*, 2007, **2**, 156-158.
46. Y. Mantri, S. J. Lippard and M.-H. Baik, *J. Am. Chem. Soc.*, 2007, **129**, 5023-5030.
47. J. Grau, R. F. Brissos, J. Salinas-Uber, A. B. Caballero, A. Caubet, O. Roubeau, L. Korrodi-Gregorio, R. Perez-Tomas and P. Gamez, *Dalton Trans.*, 2015, **44**, 16061-16072.
48. H. Song, J. T. Kaiser and J. K. Barton, *Nat Chem*, 2012, **4**, 615-620.
49. Y.-H. Hsiang, L. F. Liu, M. E. Wall, M. C. Wani, A. W. Nicholas, G. Manikumar, S. Kirschenbaum, R. Silber and M. Potmesil, *Cancer Res.*, 1989, **49**, 4385-4389.
50. M. R. Gill, S. N. Harun, S. Halder, R. A. Boghazian, K. Ramadan, H. Ahmad and K. A. Vallis, *Sci. Rep.*, 2016, **6**, 31973.
51. C. R. Martinez and B. L. Iverson, *Chem. Sci.*, 2012, **3**, 2191-2201.
52. G. Sheldrick, *Acta Crystallogr. Sect. C*, 2015, **71**, 3-8.

CHAPTER 6

The metal matters:
Tetrapyridyl nickel, palladium, and platinum
anticancer compounds with spectacularly
different activity and mechanism of action

This chapter is to be submitted as a full paper: Vincent H.S. van Rixel, Anja Busemann, Bianka Siewert, Mathijs F. Wissingh, Marc Falandt, Gijs Ruigrok, Maxime A. Siegler, Samantha L. Hopkins, Walter Berger, Sylvestre Bonnet, *manuscript in preparation.*

6.1 Introduction

The anticancer drug cisplatin is one of the landmarks in medicinal inorganic chemistry.¹ Cisplatin has an over 95% cure rate for patient diagnosed with testicular, bladder, or ovarian cancer.² However, undesired side effects associated with cisplatin are severe (e.g., nephrotoxicity, neurotoxicity, ototoxicity, or nausea), and tumors sometimes exhibit or acquire cisplatin resistance.³

To counter resistances and minimize side effects associated with cisplatin, much research effort has been invested in determining the mechanism of action (MoA). The usually accepted MoA is that after cisplatin is administered intravenously the high extracellular chloride concentration (> 100 mM) ensures that the chloride ligands remain coordinated. Cisplatin then enters the cell either through passive diffusion or via copper(II) transporters.⁴ In the cell the chloride concentration is much lower (3-20 mM) resulting in hydrolysis of cisplatin first to form $[\text{Pt}(\text{NH}_3)_2(\text{OH}_2)\text{Cl}]^+$.⁵ Once inside the nucleus this species can form coordination bonds with nucleobases, mainly guanines. In this process the DNA is structurally altered, shielded from DNA excision repair by HMG-proteins, and consequentially the cell is sensitized for apoptosis.⁶⁻⁸ DNA therefore is one of the important intracellular targets for metal based anticancer compounds, including second and third generation cisplatin derivatives. Alternatively, the so-called intercalating agents do not rely on 2-electron bonding to DNA, but their flat and aromatic nature enables π - π stacking interactions with the DNA base pairs.^{9, 10}

The biochemical effects of metallodrugs are not limited to DNA-damage induced apoptosis. Coordination of the biologically available thiol glutathione to the platinum center is associated with detoxification.^{11, 12} Cisplatin can also disturb cellular homeostasis and cell redox balance, and increases the presence of reactive oxygen species (ROS).^{13, 14} In this context metallodrugs specifically designed to disturb the intracellular redox balance have been developed as anticancer compounds.¹⁵ As cancer cells already exhibit high metabolic activity and low level of antioxidants they have an increased sensitivity toward such perturbations.¹⁶

In this chapter three novel and analogous complexes based on the same tetradentate ligand H₂bapbpy (6,6'-bis[N-(pyridyl)-1-amino]-2,2'-bipyridine) are presented, but coordinated to Ni²⁺, Pd²⁺, or Pt²⁺ that all in column 10 of the periodic table. Palladium complexes as analogues of platinum complexes are often

discarded as anticancer drugs due to their unfavorably fast ligand exchange kinetics,¹⁷ which is a feature crucial for its success as a homogenous catalysts for many coupling reactions. Nickel compounds suffer from the same problem, and also have a wider range of coordination geometries compared to palladium and platinum. In this work the structurally related complexes $[\text{Ni}(\text{H}_2\text{bapbpy})(\text{OH}_2)_2]\text{Cl}_2$ (**[1]** Cl_2), $[\text{Pd}(\text{H}_2\text{bapbpy})](\text{PF}_6)_2$ (**[2]** $(\text{PF}_6)_2$), and $[\text{Pt}(\text{H}_2\text{bapbpy})](\text{PF}_6)_2$ (**[3]** $(\text{PF}_6)_2$) show strikingly different biological activities: whereas **[1]** Cl_2 harbors only moderate biological activity, **[3]** $(\text{PF}_6)_2$ exhibits high cytotoxicity comparable to cisplatin, while **[2]** $(\text{PF}_6)_2$ shows activities against a wide range of human cancer cell lines in the nanomolar range. Remarkably, the palladium compound **[2]** $(\text{PF}_6)_2$ is not only much more cytotoxic than its platinum analogue; it exerts a distinctively different mechanism of action. It represents the first palladium anticancer drug that causes a complete collapse of the cell redox balance and shows promising *in vivo* anticancer activity.

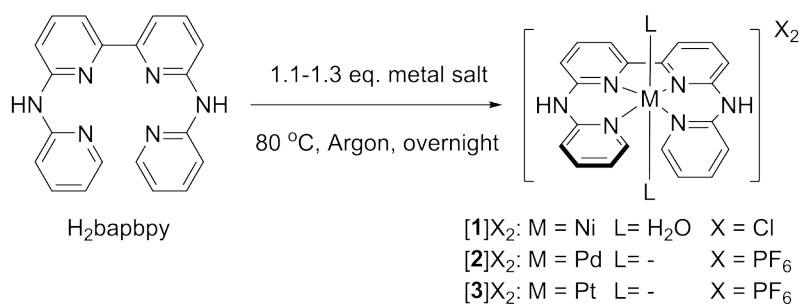
6.2 Results

6.2.1 Synthesis and crystal structures

The nickel complex **[1]** Cl_2 was synthesized by reacting H_2bapbpy with 1.1 equivalent of $\text{NiCl}_2 \cdot 6\text{H}_2\text{O}$ in ethanol overnight at 80 °C (Scheme 6.1). After filtration **[1]** Cl_2 was obtained as a light brown powder. Mass spectrometry of an acetonitrile solution showed clear signals corresponding to $[\mathbf{1} - 2 \times \text{H}_2\text{O} + 2 \times \text{CH}_3\text{CN}]^{2+}$ ($m/z = 240.2$, calc. $m/z = 240.1$) indicating that the axial water ligands are labile and are easily replaced by CH_3CN , whereas virtually no signals for $[\mathbf{1}]^{2+}$ are observed (Figure SVI.1.). This result suggests that *in vitro* or *in vivo* water can easily be substituted in the presence of competing biological ligands. The palladium and platinum complexes **[2]** $(\text{PF}_6)_2$ and **[3]** $(\text{PF}_6)_2$ were synthesized by reacting H_2bapbpy with 1.3 equivalents of $\text{K}_2[\text{PdCl}_4]$ or $\text{K}_2[\text{PtCl}_4]$, respectively, in an ethanol-water mixture overnight at 80 °C (Scheme 6.1). After filtration the filtrate was treated with KPF_6 yielding yellow precipitates.

Slow vapor diffusion of diethyl ether into a solution of **[1]** Cl_2 in methanol gave brown-colored crystals suited for X-ray diffraction (Figure 6.1A). The nickel(II) center is in an octahedral geometry with the ligand H_2bapbpy in the basal plane and two water ligand in the apical positions. Vapor diffusion of an acetonitrile solution containing **[2]** $(\text{PF}_6)_2$ or **[3]** $(\text{PF}_6)_2$ yielded ruby-colored crystals suited for X-

ray diffraction (Figure 6.1BC). Both complexes were found to have a square-planar geometry, and interestingly the crystals obtained from the $[3](PF_6)_2$ solution resulted in the structure of $[Pt(H_2bapbpy)]PF_6$. The pK_a of the amines in the $H_2bapbpy$ ligand when coordinated will be further discussed in Chapter 7. In all three structures the tetradentate $H_2bapbpy$ or $Hbapbpy$ ligand coordinates to the metal in a non-planar fashion. Selected bond distances and angles are reported in Table SVI.1 and Table SVI.2. The distance between the palladium(II) or platinum(II) center and their coordinating nitrogen atoms are all around 2.0 Å. Overall, whereas the nickel(II) complex stands out due to its octahedral geometry, the palladium(II) and platinum(II) are highly similar.



Scheme 6.1 Synthesis of $[1]Cl_2$, $[2](PF_6)_2$, and $[3](PF_6)_2$.

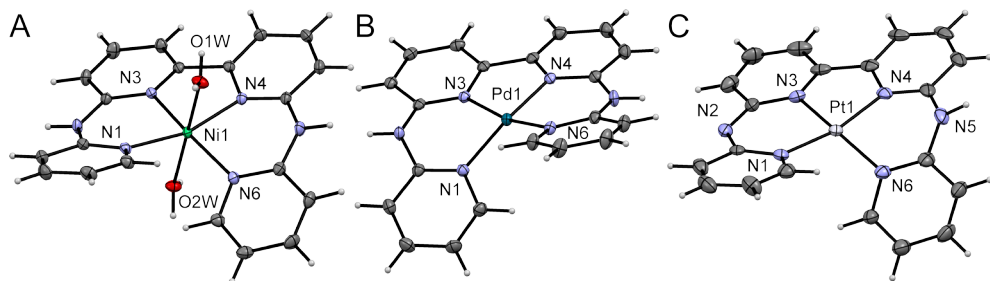


Figure 6.1 Displacement ellipsoid of cationic parts of $[1]^{2+}$ (A), $[2]^{2+}$ (B), and $[Pt(H_2bapbpy)]^+$ (C) (50% probability level) as observed in the crystal structure of respectively $[1]Cl_2$, $[2](PF_6)_2 \cdot 2 \times CH_3CN$, and $[Pt(H_2bapbpy)]PF_6$. Counter anions and lattice solvent molecules have been omitted for clarity. Selected bond distances and angles are reported in Table SVI.1 and Table SVI.2.

6.2.2 Cytotoxic properties

The cytotoxicity of the three complexes was tested against five different cancer cell lines (A375, A431, A549, MCF-7, MDA-MB231) and one non-malignant lung cell

line (MRC-5). The cell testing protocol was adapted from Hopkins et al.¹⁸ as follows: 24 h after seeding, the cells were incubated for 24 h with the drug, then the drug-containing medium was removed, and finally the cells were incubated with drug-free medium for another 48 h. An SRB cell-counting assay was performed at 96 h, and effective concentrations (EC₅₀) were determined by comparison with drug-free control cells. The cytotoxicity results are summarized in Table 6.1. EC₅₀ values for [1]Cl₂ range between 35 μM for A375 cells and 74 μM for A549 cells, i.e. the nickel complex is mildly cytotoxic. For [3](PF₆)₂ EC₅₀ values between 0.80 μM for MCF-7 cells and 1.4 μM for MRC-5 cells were found, which makes the platinum complex [3](PF₆)₂ slightly more cytotoxic than cisplatin and much more cytotoxic than [1]Cl₂. For [2](PF₆)₂ the EC₅₀ values ranged between 0.058 μM for A375 cells and 0.19 μM for A549 cells, which is remarkably low. It is 5-20 times more toxic than its platinum analogue [3](PF₆)₂ or cisplatin over the full panel of tested cell lines in spite of the almost identical structural features.^{17, 19, 20} This makes compound [2](PF₆)₂ one of the most cytotoxic palladium compounds known to date.

Table 6.1 Cytotoxicity expressed as effective concentrations (EC₅₀ with 95% confidence intervals, in μM) of [1]Cl₂, [2](PF₆)₂, [3](PF₆)₂, and cisplatin on skin (A375, A431), lung (A549), and breast (MCF-7, MDA-MB231) cancer cell lines, and on non-cancerous lung fetal cell line (MRC-5).

Cell Line	[1]Cl ₂	[2](PF ₆) ₂	[3](PF ₆) ₂	cisplatin
A375	35 -4.8 +5.6	0.058 -0.005 +0.006	0.95 -0.12 +0.14	1.6 -0.52 +0.77
A431	58 -11 +14	0.087 -0.012 +0.014	1.2 -0.13 +0.14	3.9 -0.91 1.18
A549	74 -6.0 +6.5	0.19 -0.018 +0.020	0.91 -0.11 +0.12	3.1 -0.98 +1.4
MCF-7	74 -19 +26	0.095 -0.021 +0.027	0.80 -0.12 +0.14	4.0 -1.5 +2.4
MDA-MB231	40 -16 +28	0.12 -0.026 +0.033	1.3 -0.48 +0.75	> 25 -
MRC-5	64 -14 +18	0.11 -0.011 +0.012	1.4 -0.43 +0.63	12 -3.9 +5.9

6.2.3 Cell Imaging

The distinctly differing cytotoxic properties of [2](PF₆)₂ and [3](PF₆)₂ suggest different mechanisms of action for the two analogues, and thus prompted further investigations performed by Dr. Bianka Siewert. A549 cells were first treated with 0.5 μM [2](PF₆)₂ or 1.0 μM [3](PF₆)₂ for 26 h and then inspected by bright field microscopy (Figure 6.2). Compared to the untreated controls (Figure 6.2A) the cells treated with [2](PF₆)₂ displayed cell shrinkage, loss of cell-cell contact, and membrane blebbing as depicted in Figure 6.2B, suggesting apoptosis. Nevertheless, the formation of ‘balloon cells’ (big bubbles, highlighted with white arrows in Figure 6.2B) indicated on the one hand that membrane modulation may cause disturbances of the osmotic balance, and on the other hand that also necrotic cell death might occur. For cells treated with [3](PF₆)₂ these effects were clearly not observed. Despite the structural similarity of the two compounds, only treatment with the platinum compound leads to contraction patterns and appearance of enlarged, flat cells typically associated with DNA-damage in p53 wild-type cells like A549.^{21, 22}

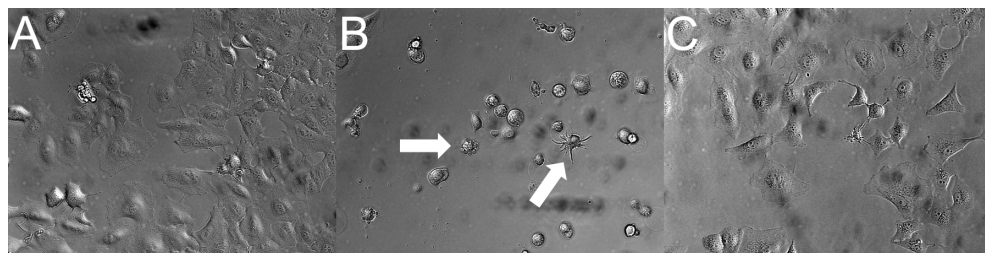


Figure 6.2 Bright field microscopy images (20 × magnification) of A549 cells without treatment (A) or after 26 h treatment with 0.5 μM [2](PF₆)₂ (B) or with 1.0 μM [3](PF₆)₂ (C).

6.2.4 Uptake and subcellular fractionation studies with A549 cells

To determine uptake and localization of the non-emissive compounds [1]Cl₂, [2](PF₆)₂, and [3](PF₆)₂, A549 lung cancer cells were treated for 24 hours close to the EC₅₀ concentration, trypsinized, and fractionated by Anja Busemann into the following four fractions: the cytosol, the membranes, the nuclei, and the cytoskeleton. The metal content of each fraction was measured by ICP-MS and is reported in Table 6.2, Figure SVI.2 and Figure SVI.3. Total uptake for [1]Cl₂, [2](PF₆)₂, and [3](PF₆)₂ was 720, 132, and 1586 pmol/10⁶ cells, respectively, which corresponded to an uptake efficiency with respect to the total dose added to each

well of 0.3, 20, and 47%, respectively. Thus, [1]Cl₂ was poorly taken up, [2](PF₆)₂ had a moderate uptake efficiency, and [3](PF₆)₂ had a very high uptake efficiency. Compared to cisplatin that showed an uptake of 22.9 pmol/10⁶ cells (< 0.1%), all three complexes are taken up well. To conclude, the amount of palladium complex necessary to kill half of the cells is extraordinary low compared to the amount of nickel or platinum complex necessary to induce a comparable effect.

Table 6.2 Uptake in the different fractions of A549 cells for compounds [1]Cl₂, [2](PF₆)₂, [3](PF₆)₂, and cisplatin.

Compound	Treatment (μM)	Metal uptake (pmol/10 ⁶ cells)	Metal uptake efficiency (%)	Fractions	Relative Metal Distribution (%)	Metal Distribution (pmol/10 ⁶ cells)
[1]Cl ₂	70	720 ± 251	0.3	Cytosol	9	66.4 ± 12.6
				Membrane	74	533 ± 197
				Nucleus	13	96.5 ± 43.4
				Cytoskeleton	3	23.6 ± 7.7
[2](PF ₆) ₂	0.20	132 ± 37.4	20	Cytosol	5	6.1 ± 1.4
				Membrane	86	113 ± 34.8
				Nucleus	6	7.55 ± 2.0
				Cytoskeleton	4	5.07 ± 3.0
[3](PF ₆) ₂	1.0	1586 ± 667	47	Cytosol	2	28.8 ± 8.5
				Membrane	35	555 ± 180
				Nucleus	15	236 ± 140
				Cytoskeleton	48	766 ± 350
Cisplatin	3.3	22.9 ± 6.1	< 0.1	Cytosol	8	1.89 ± 0.7
				Membrane	64	14.6 ± 3.1
				Nucleus	14	3.13 ± 1.1
				Cytoskeleton	14	3.28 ± 1.3

Concerning the subcellular compartmentalization of the complexes, 74% of [1]Cl₂ and 86% of [2](PF₆)₂ were localized in the membrane fraction (533 pmol/10⁶ cells

and 113 pmol/10⁶ cells respectively). Uptake in the membrane fraction for [3](PF₆)₂ was 555 pmol/10⁶ cells (35% of total) and comparable to [1]Cl₂, but much higher than [2](PF₆)₂. [3](PF₆)₂ is also highly abundant in the other fractions: in the nucleus at 236 pmol/10⁶ cells (15%), and in the cytoskeleton at 766 pmol/10⁶ cells (48%) unlike [1]Cl₂ and [2](PF₆)₂. Due to the high general uptake of all complexes, the compounds are quite abundant in all cell fractions. However, the highest fraction preference was witnessed for [2](PF₆)₂ for the membrane fraction (86%) while this highly cytotoxic compound exhibited the lowest nuclear localization making it questionable whether DNA represents the major target of this palladium complex.

Since all complexes were substantially present in the membrane fraction that includes mitochondria, mitochondria in A549 cells were isolated, digested, and the metal concentration was measured by ICP-MS. No substantial metal uptake was found in the mitochondria (Table SVI.4). Thus, treatment around the EC₅₀ concentration [3](PF₆)₂ has the highest uptake efficiency (47%) and is abundantly present in the membrane, nucleus, and cytoskeleton fractions. Treatment with [2](PF₆)₂ also resulted in a high uptake efficiency (20%), and the metal was mainly localized in the membrane fraction (86%), relatively minor in the nucleus (6%) but absent in the mitochondria. [1]Cl₂ has the poorest uptake efficiency (0.3%) of the complexes, but due to a much higher treatment concentration still 720 pmol/10⁶ cells was taken up, which represents a five-fold higher uptake than complex [2](PF₆)₂. Clearly, the differences in absolute metal uptake cannot explain the remarkable difference in cytotoxicity between the three compounds. [2](PF₆)₂ is despite its low intracellular presence of the three presented H₂bapbpy complexes by far the most cytotoxic. These results confirmed the initial indications that [2](PF₆)₂ and [3](PF₆)₂ are cytotoxic via different mechanisms.

6.2.5 Thermal binding with pUC19 plasmid DNA

Photomicrographs of A549 cells treated with [3](PF₆)₂ suggested that – similar to cisplatin – cell death or cell cycle arrest might occurred due to DNA damage. As all three H₂bapbpy complexes were significantly present in the nucleus, DNA-binding studies were performed by Dr. Samantha L. Hopkins using gel electrophoresis to determine the affinity of [1]Cl₂, [2](PF₆)₂, and [3](PF₆)₂ for DNA. The pUC19 plasmid used for this study (2686 BP) exists in three forms: supercoiled (SC, most condensed form, migrates the fastest), single-nicked open circular (OC, relaxed form of the SC, migrates in between the SC and LD), and linear dimer (LD, largest

form at 5372 bp, migrates the slowest). Complex [1]Cl₂, [2](PF₆)₂, and [3](PF₆)₂ were incubated at varied DNA base pair (BP) to metal complex (MC) ratios for 24 h (Figure 6.3). Each gel included a cisplatin control in lane 3 that only showed a band that migrated slightly less compared to the untreated SC DNA. For [1]Cl₂ at all tested BP:MC ratios (Figure 6.3A, lane 4-9) identical migration through the gel of SC, OC, and LD compared to the untreated control (lane 2 and lane 10) was observed. [1]Cl₂ has thus no affinity for pUC19 plasmid DNA. Complexes [2](PF₆)₂ and [3](PF₆)₂ showed no binding to DNA at 200:1 BP:MC ratio (Figure 6.3B and C, lane 4), but at a 75:1 or lower BP:MC ratio migration of the SC-plasmid was severely retarded (Figure 6.3B and C, lane 5-9). At the highest concentrations in metal (10:1-5:1 BP:MC, Figure 6.3B, lane 8-9), the binding of [2](PF₆)₂ strongly deviated from that of [3](PF₆)₂ at the same concentrations (Figure 6.3C, lane 8-9). However, both square-planar complexes [2](PF₆)₂ and [3](PF₆)₂ interacted strongly with pUC19 plasmid DNA. As expected from the tetradentate nature of the H₂bapbpy ligand that coordinates around the metal ion without leaving any space for the coordination of a base pair, their interaction with DNA differ strongly from cisplatin at higher concentrations of the metal.

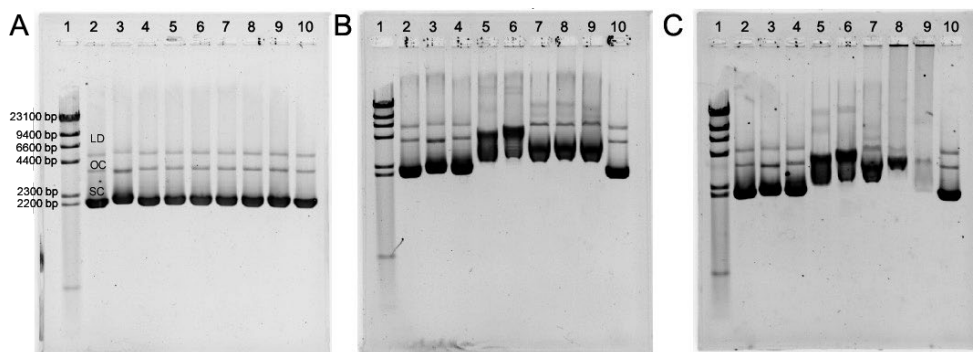


Figure 6.3 Agarose gel of pUC19 plasmid DNA incubated with [1]Cl₂ (A), [2](PF₆)₂ (B), or [3](PF₆)₂ (C). The lanes correspond to (1) λ DNA MW marker, (2 and 10) DNA control, (3) 5:1 BP:MC cisplatin control, (4-9) 200:1, 75:1, 50:1, 25:1, 10:1, 5:1 BP:MC ratio. The bands of the λ MW marker correlate to 23, 9.4, 6.6, 4.4, 2.3, and 2.0 kpb. The DNA control bands are labelled according to the form the linear dimer (LD), open circular (OC), and supercoiled (SC) DNA. $t_{\text{incubation}} = 24 \text{ h}$, $T_{\text{incubation}} = 37 \text{ }^{\circ}\text{C}$.

6.2.6 Oxidative stress

Disturbance of the cellular redox balance as a result of oxidative stress is often one of the main drivers of cytotoxicity induced by metal complexes.²³ To determine

whether the MoA of [2](PF₆)₂ and [3](PF₆)₂ involves infliction of oxidative stress by for example generation of reactive oxygen species (ROS), A549, CH1 (ovarian cancer), and MG63 (osteosarcoma) cells were treated with [2](PF₆)₂ and [3](PF₆)₂ at various concentrations by Prof. dr. Walter Berger. These cancer cell lines represent high (A549), low (CH1), and intermediate (MG63) resistance towards oxidative stress. Furthermore, co-treatment of the palladium or platinum complex with non-toxic doses of N-acetyl-L-cysteine (NAC, 2.0 mM) or L-buthylsulfoximine (BSO, 1.0 μM) was performed to evaluate the role of oxidative stress on cell death. In cells glutathione (GSH) mediates homeostasis imbalance and oxidative stress. As a precursor of GSH, co-treatment with NAC increases the capacity of cells to control oxidative stress. Co-treatment with BSO on the other hand reduces GSH levels by inhibiting GSH synthesis, and consequently sensitizes cells toward oxidative stress. The results of the co-treatment assay are summed up in Table 6.3. Co-treatment of [2](PF₆)₂ with NAC resulted in an EC₅₀ value of > 1 μM for A549 and CH1 cells, and of 0.441 μM for MG63 cells, whereas without co-treatment [2](PF₆)₂ showed much higher cytotoxicity (EC₅₀ = 0.055, < 0.01, and < 0.01 μM, respectively). Thus, co-treatment with NAC strongly inhibited the cytotoxicity of [2](PF₆)₂. When co-treated with BSO the measured EC₅₀ values of [2](PF₆)₂ were 0.007, < 0.01, and < 0.01 μM for A549, CH1, and MG63 cells. Thus, only for A549 cells an increase in cytotoxicity was observable in the presence of BSO. For [3](PF₆)₂ the measured EC₅₀ values for A549 cells with and without co-treatment of NAC or BSO were always > 1 μM. For CH1 and MG63 cells treated only with [3](PF₆)₂, EC₅₀ values were 0.028 and 0.128 μM, with NAC 0.097 and 0.151 μM, and with BSO 0.009 and 0.120 μM, respectively, indicating minor cytotoxicity decrease by NAC and statistically insignificant effects of BSO. Overall, NAC does have a strongly inhibiting effect on the cytotoxicity of [2](PF₆)₂, whereas for [3](PF₆)₂ this effect is much weaker. Co-treatment with BSO increased the activity in case of A549 cells treated with [2](PF₆)₂ and CH1 cells treated with [3](PF₆)₂. Additionally, both compounds were much more active against CH1 cells compared to A549 cells. The data demonstrates that the presence of GSH in the cells plays a crucial role in the MoA of both compounds, but that this effect is by far more significant for [2](PF₆)₂ than for [3](PF₆)₂. The complete protective effect of NAC against the toxicity of [2](PF₆)₂ suggests a MoA depending highly on the induction of oxidative stress, whereas this effect is much less important for the toxicity of [3](PF₆)₂.

Table 6.3 Cell growth inhibition effective concentrations (EC₅₀ with 95% confidence intervals, in μM) of [2](PF₆)₂ and [3](PF₆)₂ when co-treated with NAC (2.0 mM) or BSO (1.0 μM) on cancer cells with high (A549), low (CH1), or intermediate (MG63) resistance toward oxidative stress.

Cell Line	[2](PF ₆) ₂		[2](PF ₆) ₂ + NAC		[2](PF ₆) ₂ + BSO		[3](PF ₆) ₂		[3](PF ₆) ₂ + NAC		[3](PF ₆) ₂ + BSO	
	EC ₅₀	95% CI	EC ₅₀	95% CI	EC ₅₀	95% CI	EC ₅₀	95% CI	EC ₅₀	95% CI	EC ₅₀	95% CI
A549	0.055	-0.012 +0.016	> 1	-	0.007	-0.001 +0.001	> 1	-	> 1	-	> 1	-
CH1	< 0.01	-	0.441	-0.087 +0.109	< 0.01	-	0.028	-0.012 +0.023	0.097	-0.035 +0.055	0.009	-0.005 +0.005
MG63	< 0.01	-	> 1	-	< 0.01	-	0.128	-0.018 +0.021	0.151	-0.024 +0.028	0.120	-0.018 +0.021

6.2.7 Impact of the p53 mutation status on cytotoxicity

Expression of tumor suppressor protein p53 is often crucial for the anticancer activity of DNA damaging agents like cisplatin.²⁴ Thus, testing the cytotoxic activity of the palladium and platinum compounds against RKO (colon carcinoma) cells with different p53 statuses can provide clues on DNA-damage dependence of the MoAs. Therefore, RKO cells with wild-type (low protein expression in unstressed cells), mutated (high expression due to lack of protein degradation), and knock-out (no protein expression) p53-status were treated by Prof. dr. Walter Berger with [2](PF₆)₂ or [3](PF₆)₂, and co-treated with NAC (0, 1, or 2 mM). The results of this assay are summarized in Table 6.4. For [2](PF₆)₂ the measured EC₅₀ values were 0.016, 0.028, and 0.016 μM for wild-type, mutated, and knock-out RKO cells, respectively. When co-treated with NAC, no EC₅₀ value could be determined, due to the absence of cytotoxicity under those conditions, which indicates a minimal 6-fold loss in cytotoxicity. Absence of p53 in RKO cells did not change the cytotoxicity of [2](PF₆)₂, but with mutated p53 the cytotoxic activity decreased almost 2-fold. For [3](PF₆)₂ the measured EC₅₀ values were 0.258, 0.298, and 0.088 μM for wild-type, mutated, and knock-out RKO cells, respectively. Thus, mutation of p53 did again induce a minor decrease of the cytotoxicity compared to the wild-type, and almost a 3-fold increased cytotoxic activity compared to knock-out cells. The stronger activity in the knock-out cells suggests, that wild-type p53-mediated DNA damage response and cell cycle arrest (supported by the

appearance of large flat cells indicative for cell cycle arrest at G2 phase) might protect cells from [3](PF₆)₂-mediated cell death. These observations point toward a MoA based on DNA damage for [3](PF₆)₂. Co-treatment with 1 or 2 mM NAC induced no significant change in cytotoxicity for [3](PF₆)₂ in wild-type, mutated, and knock-out RKO cells. Together the data confirms that the MoA of [2](PF₆)₂ probably relies on raising oxidative stress levels in cells. In contrast, according to this p53 expression assay the MoA of [3](PF₆)₂ might involve DNA-damage and seems to be highly independent from infliction of oxidative stress.

Table 6.4 Cell growth inhibition effective concentrations (EC₅₀ values with 95% confidence interval, in μM) of [2](PF₆)₂ and [3](PF₆)₂ alone or co-treated with NAC (1 or 2 mM) on RKO cancer cells with regular (wt), high (mut), and knock-out (ko) expression of tumor suppressor p53.

Cell Line	[2](PF ₆) ₂		[2](PF ₆) ₂ + NAC 1 mM		[2](PF ₆) ₂ + NAC 2 mM		[3](PF ₆) ₂		[3](PF ₆) ₂ + NAC 1 mM		[3](PF ₆) ₂ + NAC 2 mM	
	RKO p53 wt	0.016	- +0.003	> 0.1	- -	> 0.1	- -	0.258	-0.033 +0.37	0.291	-0.031 +0.034	0.336
RKO p53 mut	0.028	-0.005 +0.007	> 0.1	- -	> 0.1	- -	0.298	-0.024 +0.026	0.340	-0.029 +0.032	0.510	-0.056 +0.066
RKO p53 ko	0.016	- +0.003	> 0.1	- -	> 0.1	- -	0.088	-0.004 +0.004	0.094	-0.004 +0.004	0.107	-0.007 +0.007

6.2.8 *In vivo* experiments

The *in vivo* anticancer activity of [2](PF₆)₂ and [3](PF₆)₂ was evaluated in CT-26 colon cancer-bearing mice by Prof. dr. Walter Berger using methods as recently published.²⁵ Treatment consisted of equimolar dosages [2](PF₆)₂ (2.5 mg/kg) or [3](PF₆)₂ (2.8 mg/kg), which was found to be the maximum-tolerated dose for [2](PF₆)₂. The complexes were administered by intraperitoneal injections for 5 times (on day 3, 5, 7, 10, and 12) and mice were sacrificed 24 h after the last application. The impact of the metal complexes on tumor growth was determined by measuring the tumor volume (mm³) and the results are shown in Figure 6.4. Compared to untreated control BALB/c mice, [3](PF₆)₂ treatment had no effect on tumor growth, indicating that in this treatment regime [3](PF₆)₂ is inactive at the doses used. In contrast, [2](PF₆)₂ induced from the first day a significant delay in

tumor growth and on day 12 a 37% reduction compared to the control group. Thus, as previously witnessed in *in vitro* experiments, treatment with [2](PF₆)₂ or [3](PF₆)₂ leads to different activity, despite structural similarities, also under *in vivo* conditions.

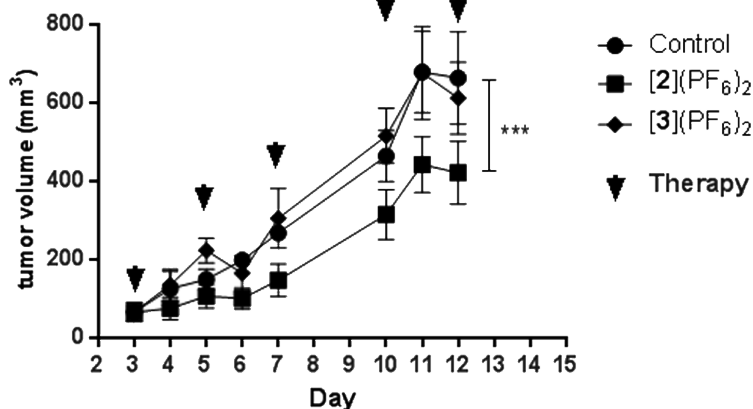


Figure 6.4 Tumor volume of Balb/c mice treated with [2](PF₆)₂ and [3](PF₆)₂. CT-26 cells were injected subcutaneously into the right flank of Balb/c mice. Mice were treated on day 3, 5, 7, 10, and 12 (indicated by black triangles) with either compound [2](PF₆)₂ at concentrations of 2.5 mg/kg (i.p.) or [3](PF₆)₂ at concentrations of 2.8 mg/kg (i.p.). ***, $p < 0.001$, two-way ANOVA, Bonferroni post-test.

6.3 Conclusion

H₂bapbpy complexes [1]Cl₂, [2](PF₆)₂, and [3](PF₆)₂ demonstrate very diverse cytotoxicity patterns. Exposure of various cancer cell lines to the drugs results in EC₅₀ values for [2](PF₆)₂ in the nanomolar range, for [3](PF₆)₂ in the submicromolar to low micromolar range, and for [1]Cl₂ in high micromolar range. Whereas the distinct differences in cytotoxicity and uptake of [1]Cl₂ can be explained by the coordination geometry, the differences in cytotoxicity and uptake between the square-planar complexes palladium [2](PF₆)₂ and platinum [3](PF₆)₂ is unexpected and enigmatic.

Palladium complexes are regularly dismissed as potential (anticancer) drugs due to the much higher ligand exchange rates compared to their platinum analogues. As a result monodentate (chloride) ligands are already extracellularly substituted

(hydrolyzed), and make a cisplatin-like prodrug approach that requires intracellular activation unlikely. However, coordination of a tetradentate ligand to ensure compound stability potentially prevents this problem. With the ligand H₂bapbpy a remarkably high uptake (also for the platinum analogue) is observed. Furthermore, the results in this chapter have demonstrated that the MoA of the palladium complex [2](PF₆)₂ might involve the disturbance of the cellular redox balance without intracellular activation. The unchanged activity of the geometrically identical [3](PF₆)₂ when co-treated with oxidative stress regulators NAC or BSO indicate that interference with the redox balance in cancer cells does not seem to be a major player in the MoA of [3](PF₆)₂.

In vivo experiments further confirmed that different activity of the structurally similar complexes [2](PF₆)₂ and [3](PF₆)₂ is not limited to cell culturing experiments. In CT-26-bearing mice models [2](PF₆)₂ is superior in reducing tumor volume compared to [3](PF₆)₂ in an equimolar low-dosage treatment regime. However, as this regime was a consequence of dose-limiting toxicities of [2](PF₆)₂, treatment with higher dosages of [3](PF₆)₂ are necessary to clarify whether also the platinum complex is a viable anticancer drug. Experiments to investigate whether [3](PF₆)₂ is able to reduce tumor volume in a higher dosage treatment regime are currently planned.

6.4 Experimental

6.4.1 Materials and methods

All NMR spectra were recorded on a Bruker DPX-300 or AV-500 spectrometer. Chemical shifts are indicated in ppm relative to tetramethylsilane. Mass spectra were recorded by using a positive ionization mode. The elemental ultra-trace analyses were performed with an FAST (Elemental Scientific, Omaha, Nebraska, USA), i-CAP-Q ICP-MS (Thermo Scientific, Waltham, Massachusetts, USA) MP2 peristaltic pump controlled flow 110 µl/min standardized setup.

The ligand 6,6'-bis[N-(pyridyl)-1-amino]-2,2'-bipyridine (H₂bapbpy), was synthesized according to literature procedures.²⁶ NiCl₂ • 6H₂O was purchased from J.T. Baker. K₂[PdCl₄] was purchased from Acros. K₂[PtCl₄] and cisplatin were purchased from Sigma-Aldrich.

6.4.2 Synthesis of [Ni(H₂bapbpy)(OH)₂](PF₆)₂ ([1](PF₆)₂)

In a 2-necked round-bottom flask [NiCl₂ • 6H₂O] (42 mg, 0.18 mmol), H₂bapbpy (60 mg, 0.18 mmol), and degassed ethanol (15 mL) were added. The brown suspension was stirred

overnight at 80 °C under argon resulting in a brown suspension. A brown powder was collected by filtration, washed with 10 mL EtOH, 10 mL Et₂O, and 10 mL hexanes. The complex was dried overnight *in vacuo*. Yield: 56 mg (63%). ¹H NMR (500 MHz, D₂O, 293 K, *in ppm*): δ = 136.6 (s), 65.8 (s), 58.9 (s), 51.8 (s), 36.1 (s), 17.0 (s), 13.7 (s). Due to the paramagnetic properties of this compound, no ¹H NMR assignment or ¹³C NMR measurement could be performed. *High resolution ES MS m/z (calc)*: 397.0700 (397.0706, [M – 2×H₂O – 2×Cl – H]⁺). *Elem. Anal. Calcd. For C₂₀H₂₀Cl₂N₆NiO₂ + C₂₀H₁₈N₆NiO₂*: C, 51.16; H, 4.08; N, 17.90. *Found*: C, 51.30; H, 4.31; N, 17.40.

6.4.3 Synthesis of [Pd(H₂bapbpy)](PF₆)₂ ([2](PF₆)₂)

In a 2-necked round-bottom flask K₂[PdCl₄] (48 mg, 0.15 mmol), H₂bapbpy (40 mg, 0.11 mmol) and degassed ethanol-water mixture (7 : 3; 10 mL) were added. The brown suspension was stirred overnight at 80 °C under argon resulting in a red suspension. A precipitate was filtered off and the filtrate was concentrated *in vacuo*. Then, a saturated aqueous solution of KPF₆ (5 mL) was added to the filtrate inducing the precipitation of a yellow solid. The suspension was filtered over a membrane filter and the complex was obtained as a yellow powder and dried *in vacuo*. Yield: 45 mg (51%). ¹H NMR (300 MHz, DMSO-*d*₆, 293 K, *in ppm*): δ = 12.25 (s, 2H, NH), 8.37 (dd, *J* = 7.8 Hz, 2H, H⁴), 8.29 (d, *J* = 6.9 Hz, 2H, H³), 8.19 (dd, *J* = 7.8 Hz, 2H, py-4), 8.14 (d, *J* = 6.3 Hz, 2H, py-6), 7.63 (d, *J* = 8.1 Hz, 2H, H⁵), 7.58 (d, *J* = 8.4 Hz, 2H, py-3), 7.29 (dd, *J* = 6 Hz, 2H, py-5). ¹³C NMR (75 MHz, DMSO-*d*₆, 293 K, *in ppm*): δ = 149.47 (C^{py-6}), 141.84 (C⁴), 141.37 (C^{py-4}), 119.84 (C^{py-5}), 117.44 (C³), 116.01 (C⁵), 115.79 (C^{py-3}). *High resolution ES MS m/z (calc.)*: 445.0393 (445.0395, [M – 2×PF₆ – H]⁺). *Elem. Anal. Calcd. for C₂₀H₁₆F₁₂N₆P₂Pd*: C, 32.61; H, 2.19; N, 11.41. *Found*: C, 32.74; H, 2.23; N, 11.68.

6.4.4 Synthesis of [Pt(H₂bapbpy)](PF₆)₂ ([3](PF₆)₂)

In a 2-necked round bottom flask K₂PtCl₄ (305 mg, 0.73 mmol) H₂bapbpy, (200 mg, 0.59 mmol), and degassed ethanol-water mixture (3 : 2; 30 mL) were added. The brown suspension was stirred overnight at 80 °C under argon resulting in a red suspension. Then, the suspension was cooled to room temperature, and subsequently cooled on ice. The precipitate was filtered off and the filtrate was concentrated *in vacuo*. Then, a saturated aqueous solution of KPF₆ (3.5 mL) was added to the filtrate inducing a yellow solid to precipitate. The suspension was filtered over a membrane filter, and washed with 10 mL water, 10 mL Et₂O, and 10 mL hexanes. The complex was obtained as a yellow powder and dried *in vacuo*. Yield: 150 mg (75%). ¹H NMR (500 MHz, DMSO-*d*₆, 293 K, *in ppm*): δ = 12.32 (s, 2H, NH), 8.48 (dd, *J* = 8 Hz, 2H, H⁴), 8.41 (d, *J* = 7.6 Hz, 2H, H³), 8.36 (d, *J* = 6.4 Hz, 2H, H^{py-6}), 8.27 (dd, *J* = 8.8 Hz, 2H, H^{py-4}), 7.69 (d, *J* = 8 Hz, 2H, H⁵), 7.62 (d, *J* = 8.4 Hz, 2H, H^{py-3}), 7.28 (dd, *J* = 6.8 Hz, 2H, H^{py-5}). ¹³C NMR (126 MHz, DMSO-*d*₆, 293 K, *in ppm*): δ = 152.42, 149.25, 147.19, 146.10, 141.05, 119.85, 117.76, 116.43, 116.01. *High resolution ES MS m/z (calc.)*:

534.0998 (534.1001, $[M - 2 \times PF_6 - H]^+$). *Elem. Anal. Calcd.* For $C_{20}H_{16}F_{12}N_6P_2Pt + \frac{1}{2} EtOH + \frac{1}{2} H_2O$: C, 30.71; H, 2.45; N, 10.23. *Found*: C, 30.62; H, 2.31; N, 10.09.

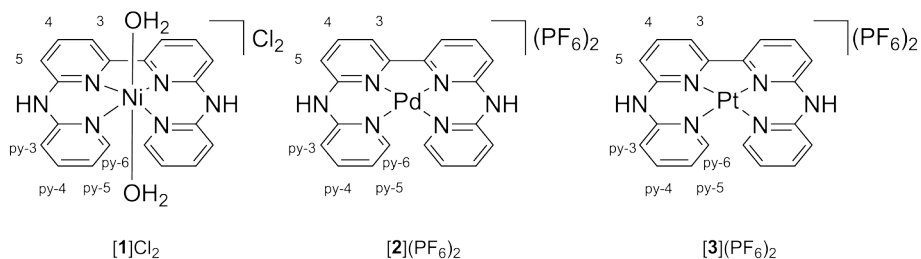


Figure 6.5 Schematic representation of $[1]Cl_2$, $[2](PF_6)_2$, and $[3](PF_6)_2$ with atom numbering used in NMR attribution.

6.4.5 Crystallography

Single crystals were obtained by the vapor diffusion method. In short, $[1]Cl_2$ was dissolved MeOH (1 mg/mL) or $[2](PF_6)_2$ and $[3](PF_6)_2$ in acetonitrile (0.5 mg/mL) and put in a small vial. This vial was placed in a larger vial containing 2.8 mL Et₂O (for $[1]Cl_2$ and $[2](PF_6)_2$) or toluene (for $[3](PF_6)_2$). The large vial was closed and vapor diffusion occurred within a few days to afford X-ray quality crystals.

All reflection intensities were measured at 110(2) K using a SuperNova diffractometer (equipped with Atlas detector) with Mo K α radiation ($\lambda = 0.71073 \text{ \AA}$) for $[1]Cl_2$ and $[2](PF_6)_2$ and with Cu K α radiation ($\lambda = 1.54178 \text{ \AA}$) for $[3](PF_6)_2$ under the program CrysAlisPro (Version 1.171.36.32 Agilent Technologies, 2013). The temperature of the data collection was controlled using the system Cryojet (manufactured by Oxford Instruments). CrysAlisPro program was used to refine the cell dimensions and for data reduction. The structure was solved by direct methods with SHELXS-2014/7 (Sheldrick, 2015) and was refined on F2 with SHELXL-2014/7 (Sheldrick, 2015). Analytical numeric absorption correction based on a multifaceted crystal model was applied using CrysAlisPro. The H atoms were placed at calculated positions (unless otherwise specified) using the instructions AFIX 43 with isotropic displacement parameters having values 1.2 Ueq of the attached C atoms. The structure is ordered

Additional notes for $[1]Cl_2$: The asymmetric unit contains 1.5 molecules of $[1]^{2+}$, three Cl⁻ counteranions. One of the two complex molecules is found at sites of twofold axial symmetry, and only one half of the molecule is crystallographically independent. Cl3 and Cl4 have occupancies of 0.5 as both are located at sites of twofold axial symmetry.

Additional notes for [2](PF₆)₂: One of the two PF₆⁻ counteranions is disordered over three orientations. The occupancy factors of the three components of the disorder refine to 0.491(3), 0.292(3) and 0.217(3)

Additional notes for [Pt(Hbapbpy)]PF₆: The PF₆⁻ counteranion is disordered over two orientations. The occupancy factors of the major component of the disorder refines to 0.661(10). Checks for H atoms attached to N2 and N5 were performed looking at difference Fourier maps. The H atom on N5 could be found, and there are intermolecular N–H...F interactions. On the other hand, there is no H atom attached to N2. The N2–C distances (C5–N2 = 1.354(7), C6–N2 = 1.336(7)) are significantly shorter than the N5–C distances (C15–N5 = 1.373(8), C16–N5 = 1.398(8)).

6.4.6 Cell culturing and EC₅₀ cytotoxicity assay

See Appendix I for extensive description of the assay.

6.4.7 Cell fractionation and isolation of mitochondria

Cell fractionation for intracellular distribution studies for complexes [1]Cl₂, [2](PF₆)₂, [3](PF₆)₂, and cisplatin were conducted on A549 lung cancer cells. 3 × 10⁶ cells were seeded at t = 0 h in Opti-MEM complete in 175 cm² flasks. At t = 24 h cells were treated with complexes to give final concentrations of 70, 0.2, 1.0, and 3.3 μM for respectively [1]Cl₂, [2](PF₆)₂, [3](PF₆)₂, and cisplatin in a total volume of 24 mL. After 24 h of drug incubation at 37 °C, the medium was removed, the cells were washed with PBS-buffer, trypsinized, counted and pelleted by centrifugation (700 × g, 5 min, at room temperature). Then, the pellets were fractionated using the FractionPREP cell fractionation kit from BioVision or Mitochondria Isolation Kit for Cultured Cells from ThermoFisher according to the instruction of the supplier. Samples were digested overnight in concentrated nitric acid (> 65%) and diluted with MilliQ water to obtain a final concentration of 5% HNO₃. For ICP-MS measurements, the system was optimized with a palladium-platinum solution. The calibration range was from 0 to 25 μg/l, and obtained detection limit for all isotopes was 0.01 μg/l. Silver and indium were used for internal standard, to correct for sample dependent matrix effects. The recoveries of the spiked concentrations were all within a 10% deviation. The data from three independent biological replications was used to obtain the values shown in Table 6.2.

6.4.8 DNA binding studies

The pUC19 plasmid used for this study (2686 bp) exists in three forms: supercoiled (SC), single-nicked open circular (OC) and linear dimer (LD). Of particular interest are the SC and OC forms. Although these two forms have the same number of bp, the SC form migrates faster through the agarose gel than the OC form due to the condensed SC form. However, as positively charged metal complexes associate with the SC form, the shape may become larger and it will be less negatively charged, ultimately resulting in slower migration.

Alternatively, if metal complexes coordinatively modify the OC form, it may induce coiling or a condensed structure causing an increase in migration and thus coalescence of the SC and OC form on increasing metal complex concentration. However, if there is no condensation of the OC plasmid structure, but the positively charged metal complexes associate with the OC form then the observed migration would be retarded.

Agarose gel electrophoresis was used to assay the binding of [1]Cl₂, [2](PF₆)₂, and [3](PF₆)₂ to pUC19 plasmid DNA. Two buffers were used for the experiments: 5X tris-boric acid buffer (TBA) and phosphate buffer (PB). TBA (45 mM tris(hydroxymethyl)amino methane and 45 mM boric acid, pH = 7.4) was used in the gel and running buffer. PB (100 mM NaH₂PO₄, pH = 7.0) was used for DNA-MC interactions. The agarose gels were 0.8% w/w agarose gel (0.24 g agarose, 24 g DI H₂O, and 6 mL TBA) and were cast in the OWL B1A Easycast system.

The molar concentration of the pUC19 plasmid DNA base pairs (BP) was determined using its extinction coefficient ($\epsilon_{260\text{ nm}} = 13,200\text{ M}^{-1}\text{cm}^{-1}$).²⁷ All aliquots were prepared with a final volume of 20 μL and prior to loading 4 μL of 6X loading dye was added. The λ DNA-HindIII digest molecular weight (MW) marker was prepared by adding 2 μL (1 μg) of the DNA MW marker, 18 μL PB, and 4 μL 6X loading dye. The MW marker was heated for 3 min at 60 °C prior to loading. In each well, 12 μL (1 μg of pUC19 DNA or 0.5 μg of MW marker) of each sample was loaded.

For each gel, the electrophoresis chamber was filled with 50 mL TBA and 210 mL demineralized H₂O. Each gel was run at a constant voltage of 105 V for 90 min. All gels were stained using 10 μL (10 mg/mL) ethidium bromide in 200 mL demineralized H₂O for 30 min with slight shaking and then destained in 200 mL demineralized H₂O for 20 min. Immediately following destaining, the gel was imaged using a BioRad ChemiDoc imaging system (ethidium bromide setting). Image Lab software was used to process the images.

The samples for thermal binding were prepared under ambient light in amber centrifuge tubes. For each sample 2 μL of pUC19 plasmid (2 μg , [BP]_i = 1.95 $\times 10^{-3}$ M) was used and the amount of metal complex and PB were adjusted to a final volume of 20 μL . Several ratios of base pairs of the plasmid (BP) to metal complex (MC) (200:1, 75:1, 50:1, 25:1, 10:1, and 5:1 BP:MC) were incubated at 37 °C for 24 h. Additionally, the negative control (DNA without metal complex) and a positive control (cisplatin, 5:1 BP:MC ratio) were incubated under the same conditions. Lanes were loaded as follows: (1) λ MW marker, (2) DNA only control, (3) cisplatin (5:1 BP:MC, [cisplatin]_i = 390 μM) control, (4) M complex ([1]Cl₂, [2](PF₆)₂, or [3](PF₆)₂) (200:1 BP:MC, [M]_i = 10 μM), (5) M complex (75:1 BP:MC, [M]_i = 26 μM), (6) M complex (50:1 BP:MC, [M]_i = 39 μM), (7) M complex (25:1 BP:MC, [M]_i = 78 μM), (8) M complex (10:1 BP:MC, [M]_i = 195 μM), (9) M complex (5:1 BP:MC, [M]_i = 391 μM), and (10) DNA only control. The gels were run, stained, and processed as described above.

6.4.9 Impact of alterations in cellular glutathione (GSH) levels on metal drug activity

The cytotoxic impact of the investigated metal compounds alone or in combination with the GSH precursor N-acetyl-L-cysteine (NAC) and the GSH-depleting agent buthionine sulfoximine (BSO) was investigated based on 3-(4,5-dimethylthiazol-2-yl)-2,5-diphenyltetrazolium (MTT)-based viability assay (EZ4U, Biomedica) as published.²⁸ In short, cells were seeded in 96-well plates (2×10^3 /well) and after a 24 h recovery period, pretreated with NAC (1 or 2 mM) or BSO (1 μ M) for 1 h. Then solutions of the metal complexes were added to the preincubated cells for a 72 h continuous exposure alone or in presence of NAC or BSO and viability was determined by MTT assay.

6.4.10 Impact of the genomic p53 status on metal drug sensitivity of colon cancer RKO cells

Evaluation of the anticancer activity of [2](PF₆)₂ and [3](PF₆)₂ was performed for isogenic RKO cell sublines harboring wild-type, mutant, and knock-out status of the tumor suppressor gene p53. Cells were seeded and processed as indicated under section 6.4.9.

6.4.11 Animal experiments

All animal experiments were approved by the local ethics committee and carried out according to the Austrian and FELASA guidelines for animal care and protection and performed under supervision of prof. dr. Walter Berger of the Institute of Cancer Research, Vienna. 6- to 8-week-old Balb/c mice (weighing 25–30 g) were purchased from Harlan Laboratories, San Pietro al Natisone, Italy. The animals were kept in a pathogen-free environment and every procedure was done in a laminar airflow cabinet.

6.4.12 Anticancer activity against CT-26 cells

Murine CT-26 cells (5×10^5) were injected subcutaneously into the right flank of female Balb/c mice. At the day of measurable tumor appearance, treatment was started. Mice were treated with the drug intraperitoneally (solutions freshly prepared in water with 10% v/v DMSO) at indicated drug concentrations on days 3, 5, 7, 10, and 12. Animals were controlled for distress development every day and tumor size was assessed regularly by caliper measurement. Tumor volume was calculated using the formula: length \times width²/2. Differences in tumor growth dynamics were determined by two-way ANOVA with Bonferroni post-test.

6.5 References

1. L. Kelland, *Nat. Rev. Cancer*, 2007, **7**, 573-584.
2. E. H. Einhorn, *Clin. Canc. Res.*, 1997, **3**, 2630-2632.
3. A.-M. Florea and D. Büsselberg, *Cancers*, 2011, **3**, 1351.
4. S. Ishida, J. Lee, D. J. Thiele and I. Herskowitz, *Proc. Natl. Acad. Sci. USA*, 2002, **99**, 14298-14302.
5. M. S. Davies, S. J. Berners-Price and T. W. Hambley, *Inorg. Chem.*, 2000, **39**, 5603-5613.
6. S. E. Sherman and S. J. Lippard, *Chem. Rev.*, 1987, **87**, 1153-1181.
7. U.-M. Ohndorf, M. A. Rould, Q. He, C. O. Pabo and S. J. Lippard, *Nature*, 1999, **399**, 708-712.
8. D. B. Zamble, D. Mu, J. T. Reardon, A. Sancar and S. J. Lippard, *Biochemistry*, 1996, **35**, 10004-10013.
9. S. Patanè, *Int. J. Cardiol.*, 2014, **176**, 1326-1328.
10. M. F. Brana, M. Cacho, A. Gradillas, B. Pascual-Teresa and A. Ramos, *Curr. Pharm. Des.*, 2001, **7**, 1745-1780.
11. X. Wang and Z. Guo, *Anti-Cancer Agents Med. Chem.*, 2007, **7**, 19-34.
12. G. K. Balendiran, R. Dabur and D. Fraser, *Cell Biochem. Funct.*, 2004, **22**, 343-352.
13. Y. Kawai, T. Nakao, N. Kunimura, Y. Kohda and M. Gemba, *J. Pharmacol. Sci.*, 2006, **100**, 65-72.
14. L. P. Rybak, C. A. Whitworth, D. Mukherjea and V. Ramkumar, *Hear. Res.*, 2007, **226**, 157-167.
15. A. L. Noffke, A. Habtemariam, A. M. Pizarro and P. J. Sadler, *Chem. Commun.*, 2012, **48**, 5219-5246.
16. A. Gupte and R. J. Mumper, *Canc. Treat. Rev.*, 2009, **35**, 32-46.
17. A. R. Kapdi and I. J. S. Fairlamb, *Chem. Soc. Rev.*, 2014, **43**, 4751-4777.
18. S. L. Hopkins, B. Siewert, S. H. C. Askes, P. Veldhuizen, R. Zwier, M. Heger and S. Bonnet, *Photochem. Photobiol. Sci.*, 2016, **15**, 644-653.
19. M. N. Alam and F. Huq, *Coord. Chem. Rev.*, 2016, **316**, 36-67.
20. M. Fanelli, M. Formica, V. Fusi, L. Giorgi, M. Micheloni and P. Paoli, *Coord. Chem. Rev.*, 2016, **310**, 41-79.
21. M. Hollstein, D. Sidransky, B. Vogelstein and C. C. Harris, *Science*, 1991, **253**, 49.
22. A. A. Sablina, A. V. Budanov, G. V. Ilyinskaya, L. S. Agapova, J. E. Kravchenko and P. M. Chumakov, *Nat Med*, 2005, **11**, 1306-1313.
23. U. Jungwirth, C. R. Kowol, B. K. Keppler, C. G. Hartinger, W. Berger and P. Heffeter, *Antioxid. Redox Signaling*, 2011, **15**, 1085-1127.
24. S. Fan, M. L. Smith, D. J. Rivert, D. Duba, Q. Zhan, K. W. Kohn, A. J. Fornace and P. M. O'Connor, *Cancer Res.*, 1995, **55**, 1649-1654.
25. J. Mayr, P. Heffeter, D. Groza, L. Galvez, G. Koellensperger, A. Roller, B. Alte, M. Haider, W. Berger, C. R. Kowol and B. K. Keppler, *Chem. Sci.*, 2017, **8**, 2241-2250.
26. S. Bonnet, G. Molnár, J. Sanchez Costa, M. A. Siegler, A. L. Spek, A. Bousseksou, W.-T. Fu, P. Gamez and J. Reedijk, *Chem. Mater.*, 2009, **21**, 1123-1136.
27. S. M. Zeman and D. M. Crothers, *Methods Enzymol.*, 2001, **340**, 51-68.
28. S. Seršen, J. Kljun, K. Kryeziu, R. Panchuk, B. Alte, W. Körner, P. Heffeter, W. Berger and I. Turel, *J. Med. Chem.*, 2015, **58**, 3984-3996.

CHAPTER 7

The metal matters II: Protonation and deprotonation of the non-coordinating amines of $[M(H_2bapbpy)]^{2+}$ complexes

This chapter is to be submitted as a full paper: Vincent H.S. van Rixel, Mathijs F. Wissingh, Maxime A. Siegler, Sylvestre Bonnet, *manuscript in preparation*.

7.1 Introduction

Metal complexes containing the tetrapyrindyl ligand 2,2':6',2'':6'',2''':6''',2''''-quaterpyridine (qtpy, Figure 7.1) were first reported in the 1970s, and were based on iron(III).¹ Since then qtpy has been coordinated to various metal centers (Fe^{II}, Co^{II}, Ni^{II}, Zn^{II}, Ru^{II}, Pd^{II}, and Ag^I),²⁻⁶ and for example [Pt(qtpy)]²⁺ was found to be the best DNA intercalator of a series of platinum complexes with mono-, bi-, tri-, and tetradentate pyridyl ligands.⁷ The absence of reports on the cytotoxicity of these complexes, as well as the absence of further development of [M(qtpy)]²⁺ square-planar complexes as anticancer compounds, may imply that they exhibit poor anticancer activity. According to the cisplatin paradigm, a saturated coordination sphere such as that of square-planar qtpy metal complexes does not allow the metal to coordinate DNA, which may have discouraged the development of this type of complexes.^{8,9} It was recently suggested that octahedral qtpy complexes such as *trans*-[Ru(qtpy)Cl₂] may alleviate this issue, as the two axial positions do allow for binding to biomolecules.⁶

Unlike qtpy complexes of column 10 transition metals, those based on the H₂bapbpy ligand (N,N'-di(pyrid-2-yl)-2,2'-bipyridine-6,6'-diamine, Figure 7.1) have shown high to extremely high cytotoxic activity *in vitro* and promising tumor-reducing activity *in vivo* as shown in Chapter 6. As they share with qtpy metal complexes a fully saturated coordination sphere, the introduction of the two non-coordinating amine bridges thus has a remarkable effect on their interaction with biological systems (see Chapter 6). Meanwhile, Ni²⁺, Cu²⁺, Ru²⁺, Pt⁴⁺, or Os²⁺ metal complexes based on the bidentate ligand 2,2'-dipyridylamine (Hdpa, Figure 7.1), also containing a non-coordinating secondary amine, (and) have recently been reported to exhibit interesting *in vitro* anticancer activity.¹⁰⁻¹⁶ Thus, non-coordinating amine bridges may play a specific role in tuning the biological and anticancer activity of metal compounds.

The research described in this chapter is dedicated to unraveling the reactivity of non-coordinated amine bridges in Pd²⁺ and Pt²⁺ complexes of the H₂bapbpy ligand. More specifically, the overall depletion of electron density of H₂bapbpy upon metal binding leads to enhanced acidity of the amine bridge. As deprotonation of the [M(H₂bapbpy)]²⁺ complex lowers the overall charge of the complex and thus may contribute to modifying cellular uptake, the pK_a of [Pd(H₂bapbpy)]²⁺ ([1]²⁺) and

[Pt(H₂bapbpy)]²⁺ ([2]²⁺) was determined, and the influence of amine deprotonation forming [Pd(Hbapbpy)]⁺ ([3]⁺) and [Pt(Hbapbpy)]⁺ ([4]⁺), on their spectroscopic properties was studied. We were notably able to isolate the two neutral complexes [Pd(bapbpy)] ([5]) and [Pt(bapbpy)] ([6]), in which both amine bridges of the H₂bapbpy ligand are deprotonated, and monitored the equilibria between [5] or [6], their monoprotonated monocationic forms [3]⁺ or [4]⁺, and their bis-protonated, dicationic forms [1]²⁺ or [2]²⁺, respectively.

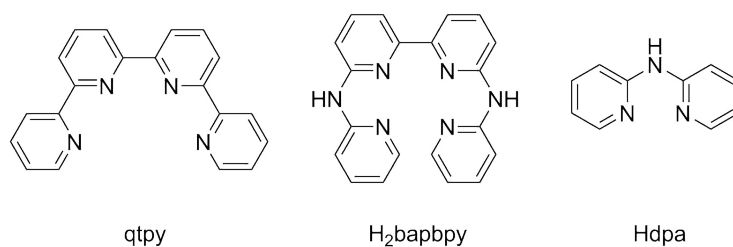


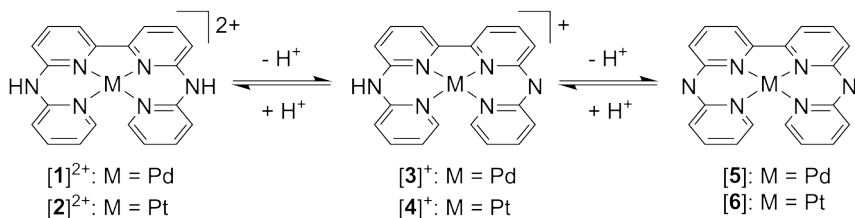
Figure 7.1 Chemical structures of the polypyridyl qtpy, H₂bapbpy, and Hdpa ligands.

7.2 Results

7.2.1 pK_a determination

Addition of a base such as NaOH to aqueous solutions of [1]Cl₂ or [2]Cl₂ was accompanied by instantaneous color changes, which was spectroscopically characterized by the rise of a wide absorption band between 420 and 550 nm. For both complexes this color change was reversed by addition of an excess acid. Such instantaneous and reversible change of the absorbance spectra upon pH variation suggested that an acid-base reaction was taking place, as supramolecular stacking interactions and ligand exchange reactions on transition metal complexes typically occur over longer time scales.¹⁷ The pK_a of the deprotonation equilibrium of [1]²⁺ or [2]²⁺ to form [3]⁺ or [4]⁺, respectively (Scheme 7.1), was determined by controlled titration of aqueous solution of [1]Cl₂ or [2]Cl₂ (67 μM) in hydrochloric acid (33 mM) using aliquots of aqueous sodium hydroxide. The evolution of the UV-vis spectra of both solutions as a function of pH is plotted in Figure 7.2. Next to the new bands appearing in the visible region, the absorption of both complexes in the UV domain diminished in intensity and shifted slightly hypsochromically. The pK_a values for the first deprotonation of [1]²⁺ and [2]²⁺ were found to be 7.8 and 8.3, respectively. Thus, at physiological pH (7.4) the palladium complex [1]²⁺ is partially

deprotonated, while its platinum analogue $[2]^{2+}$ is mostly in the dicationic form. For both complexes increasing the pH above 9.5 led to precipitation. These precipitates were hypothesized to be the neutral forms of the complexes: $[5]$ and $[6]$.



Scheme 7.1 General scheme of different protonation states of palladium and platinum H₂bapbpy complexes.

To confirm this hypothesis, both solids were prepared by first reacting H₂bapbpy with K₂[PdCl₄] or K₂[PtCl₄] in a hot ethanol-water mixture, filtering the reaction mixture, and treating the filtrate with an excess NaOH (5.0 M). The resulting precipitate was washed and dried. Double deprotonation was confirmed by NMR spectroscopy and X-ray crystallography (see section 7.2.4). Of all solvents tried, THF was the only one which would dissolve $[5]$ or $[6]$. Thus, a reverse titration was repeated in a 1:1 THF-water mixture, starting from the isolated solids $[5]$ or $[6]$ by adding hydrochloric acid. Under these conditions, all species stayed in solution while the secondary amine bridges were gradually protonated. Figure 7.3A shows the UV-vis spectrum of $[5]$, which is characterized by absorbance maxima in the visible region at 463 and 490 nm. Addition of six equivalents of HCl, resulted in the spectrum of the monocationic complex $[3]^+$ (dotted curve in Figure 7.3A) via isosbestic points at 345 and 383 nm (Figure SVII.3A). Addition of two more equivalents of HCl was accompanied by well-defined isosbestic points at 318, 345, and 416 nm (Figure SVII.3B), to yield the characteristic UV-vis spectrum of $[1]^{2+}$ (Figure 7.3A, dashed curve). Further acidification did not induce any extra change, indicating that the protonation was completed and that the complex is stable in acidic medium. The presence of two series of well-defined isosbestic points during acid addition allowed for clear distinction of conversion from $[5]$ to $[3]^+$ from that from $[3]^+$ to $[1]^{2+}$ (Scheme 7.1). Identical experiments with the platinum complex demonstrated that protonation from $[6]$ to $[4]^+$ and from $[4]^+$ to $[2]^{2+}$ also occurred

via similar isosbestic points, to re-form the platinum complex $[2]^{2+}$ (Figure 7.3B, Figure SVII.4).

Compounds $[1]^{2+}$ and $[2]^{2+}$ both show only low absorbance in the visible area (395-580 nm). Upon deprotonation of one amine bridge the absorbance in this area increases, and the complexes in their monocationic forms have absorption maxima at 412 and 458 nm, respectively. Upon deprotonation of the second amine bridge, $[5]$ and $[6]$ are obtained and are characterized by new maxima at respectively 463 and 490 nm, and 476 and 506 nm extending their absorbance tail up to 545 and 556 nm. Experiments in 10 mM aqueous solutions of the sodium salts of either NO_2^- , NO_3^- , SO_4^- , Cl^- , or I^- resulted in no change in the UV-vis spectra indicating that these changes in absorbance are exclusively based on acid-base reactions and are not induced by coordination reaction or changes in ionic strength. Although the absorbance of the platinum species are bathochromatically shifted by 10-20 nm compared to the palladium species, the overall trends in acid-base evolutions of absorbance maxima are highly similar.

7.2.2 Temperature effects on electronic absorption spectra

Since $[1]^{2+}$ and $[2]^{2+}$ have been reported as potential anticancer drugs in a system at 37 °C, the temperature dependence of their electronic absorbance spectra was studied. The complexes were dissolved in a 0.1 M phosphate buffer (10% v/v DMSO, pH = 7.4) and their UV-vis spectra were recorded at different temperatures. At 20 °C (blue curve, Figure 7.4) both complexes exhibited significant absorbance in the visible domain, indicating that a mixture between $[1]^{2+}$ and $[3]^+$ or $[2]^{2+}$ and $[4]^+$ was present. Heating $[1]^{2+}$ and $[2]^{2+}$ in the phosphate buffer up to 80 °C (red curve) showed an increase in absorbance between 420 and 580 nm for both compounds in a fashion very similar to the transition from $[1]^{2+}$ to $[3]^+$ (Figure 7.4A), and from $[2]^{2+}$ to $[4]^+$ (Figure 7.4B). The same experiment was performed in demineralized water yielding the same trends, though less pronounced (Figure SVII.5). As the pH of phosphate buffers does not deviate much (i.e., less than 0.05 pH unit in the experimental range),¹⁸ these changes in the UV-vis spectra upon increasing the temperature can be attributed to temperature-induced deprotonation of the amine bridges. Thus, the conversion of $[1]^{2+}$ to $[3]^+$ or $[2]^{2+}$ to $[4]^+$ must be endothermic.

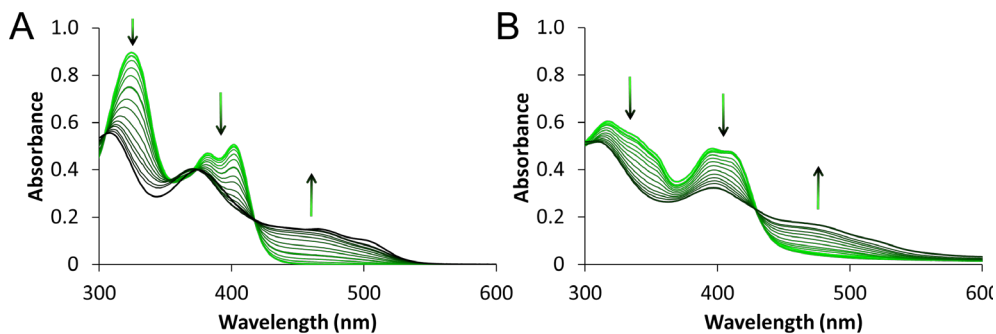


Figure 7.2 UV-vis absorbance spectra of a solution of [1]Cl₂ (A) and [2]Cl₂ (B) upon increasing pH using NaOH. Solvent: H₂O. T = 293 K, [Pd] = [Pt] = 67 μM.

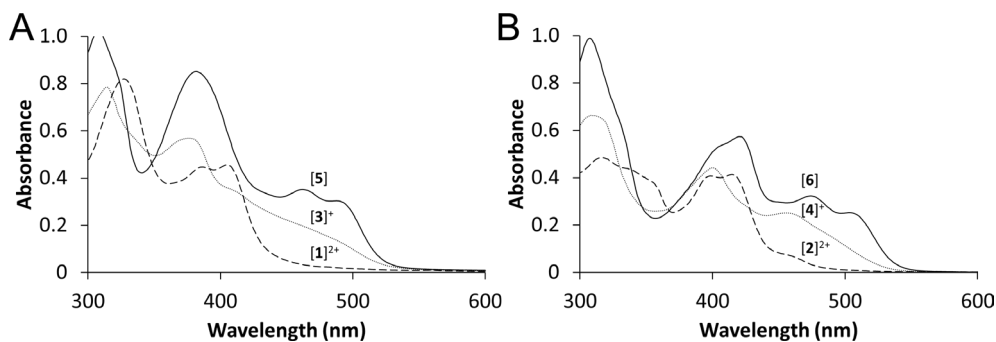


Figure 7.3. UV-vis absorbance spectra of the different protonated states of the palladium (A) and platinum complexes (B). Neutral, monocationic, and dicationic species represented respectively as continuous, dotted, and dashed curve. Solvent: THF-water (1:1). T = 293 K, [Pd] = [Pt] = 67 μM.

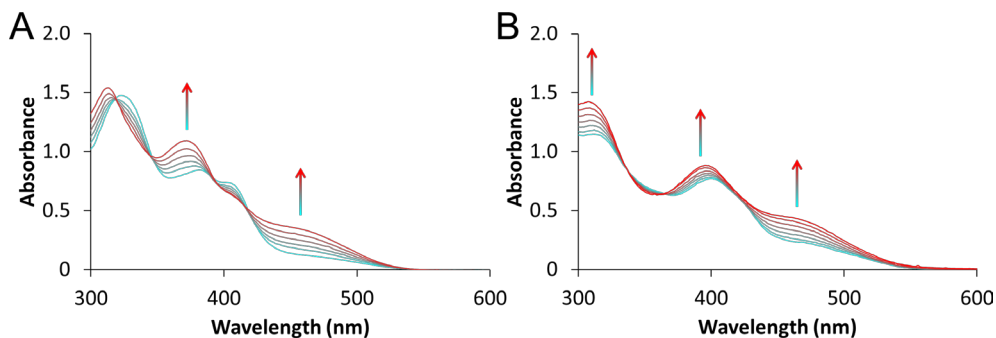


Figure 7.4 Evolution of UV-vis absorbance spectra of [1](PF₆)₂ (A) and [2](PF₆)₂ (B) in phosphate buffer at different temperatures (20 (blue) to 80 °C (red)). [Pd] = [Pt] = 0.1 mM, pH = 7.4.

7.2.3 Excited state calculations for [1]²⁺, [3]⁺, and [5]

The color changes upon temperature and pH variation triggered us to perform TDDFT (Time-dependent density functional theory) calculations to characterize the singlet transitions of [1]²⁺, [3]⁺, and [5].^{19, 20} The theoretical electronic absorbance spectra were obtained by Dr. Sylvestre Bonnet by calculating the first 50 transitions (Figure SVII.6), which provided the basis for the spectra shown in Figure 7.5. The calculated electronic absorbance spectrum of [5] (black curve) shows clear absorbance in the visible region up to 485 nm. The calculated spectrum of [3]⁺ also shows absorbance in the visible region to a similar wavelength as [5] (490 nm) but much less intense. Finally, the calculated electronic absorption spectrum of [1]²⁺ only absorbs visible light up to 431 nm, but also at very low oscillator strength, and its absorbance spectrum is dominated by strong bands in the UV. These calculated spectra fit well the experimentally observed spectra (Figure 7.3A), and confirm that absorbance of the compounds indeed depends on the protonation state of the H₂bapbpy ligand coordinated to palladium.

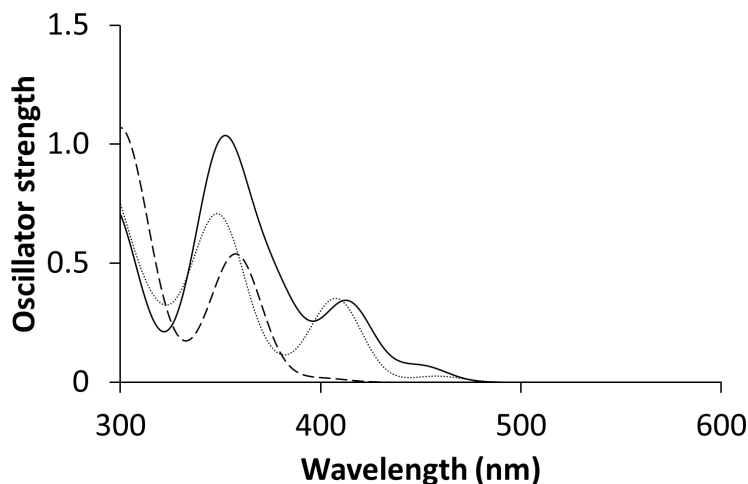


Figure 7.5 TDDFT-calculated spectra for [1]²⁺ (dashed), [3]⁺ (dotted), and [5] (continuous) at the CAM-B3LYP/TZP/COSMO level in water. The theoretical curves were calculated and plotted in ADF with Gaussian Fixed Oscillator strengths. Scaling factor = 1.0, peak width = 30 nm.

The excited states (Figure SVII.6) responsible for the main changes in the visible part of the absorbance spectra of [1]²⁺, [3]⁺, and [5] were visualized using ADF. All excited states relevant for absorbance in the visible domain have major contributions of HOMO → LUMO and HOMO → LUMO+1 transitions (Figure

SVII.7, Figure SVII.8, and Figure SVII.9). In all protonation states the HOMO is localized on the non-coordinating amine bridge, whereas the LUMO is mainly on the bpy part of the ligand, and LUMO+1 mainly on the palladium center involving the $d_{x^2-y^2}$ orbital. Because of steric repulsion between the two terminal pyridyl groups, these rings hardly provide any stabilization. Their orientation out of the bpy conjugation plane, strongly enhances the sp^3 character of the amine bridge. To conclude, Intra-Ligand-Charge-Transfer HOMO \rightarrow LUMO and Ligand-to-Metal-Charge-Transfer HOMO \rightarrow LUMO+1 transitions are responsible for the increased absorbance in the visible domain when [1]²⁺ is deprotonated once or twice.

7.2.4 X-ray structures of [1]²⁺, [3]⁺, and [5]

Single crystals suitable for X-ray diffraction were obtained for all protonation states of the palladium compound. Vapor diffusion of diethyl ether into a solution of [1](PF₆)₂ in acetonitrile yielded single crystals of [1](PF₆)₂ (see also Chapter 6); apart from the complex cation and the hexafluorophosphate anions the asymmetric unit contains two molecules of acetonitrile. Surprisingly, diffusion of diethyl ether vapors into an acetone solution of [1](PF₆)₂ resulted in ruby-colored crystals of [3]₂(HCOO)(PF₆); the presence of the formate anion could be explained by CO₂ capture from the atmosphere. Diffusion of pentane vapors into a THF solution containing [5] yielded amber-colored, needle-shaped crystals suitable for X-ray diffraction; apart from the neutral complex the asymmetric unit contains three molecules of water. Projections of the complexes are provided in Figure 7.6; relevant bond distances and angles of the three complexes are reported in Table 7.1 and Table 7.2, respectively.

In all three compounds the palladium(II) ion is coordinated by the tetradentate ligand in a distorted square-planar geometry, with highly similar bond lengths and angles (Table 7.1 and Table 7.2). The bond length of Pd1-N1 and Pd1-N6 falls between 2.025(2)-2.047(6) Å and for Pd1-N3 and Pd1-N4 between 1.975(6)-1.994(3) Å. The coordination angles N1-Pd1-N4 and N3-Pd1-N6 were used to calculate τ_4 (Table 7.2). This value is indicative for the geometry of four-coordinate complexes.²¹ On a scale from 0 to 1, 0 represents a perfect square-planar geometry and 1 represents a perfect tetrahedral geometry. The compounds [1]²⁺, [3]⁺, and [5] have τ_4 values of 0.193, 0.177, and 0.187, respectively, confirming that protonation or deprotonation of the complex barely affects the square-planar geometry. In addition, the torsion angles of the coordinating N1-N3-N4-N6 atoms, which are

17.3, 15.5, and 16.8° for [1]²⁺, [3]⁺, and [5], respectively, indicate the flatness of the coordination plane.²² As the total content of the unit cell must be charge neutral, the charges of the cationic complexes and counter anions should be balanced. The two PF₆⁻ counter anions in the structure of [1](PF₆)₂ suggest that the palladium complex is dicationic, with both amine nitrogen atoms protonated. Surprisingly, in [3]₂(HCOO)(PF₆) two counter anions were found per two palladium molecules, suggesting a monocationic form for each metal complex, thus with one of the two amine nitrogen atoms deprotonated. However, it may not be excluded that this structure contains one dicationic complex [1]²⁺ and one neutral complex [5]. Finally, for the third structure no counter anions were found, confirming that the palladium complex [5] is neutral.

Table 7.1 Selected distances (Å) of [1]²⁺, [3]⁺, and [5], for atom-labelling see Figure 7.6.

Bond	[1] ²⁺	[3] ⁺	[5]
Pd1-N1	2.0251(16)	2.047(3)	2.047(6)
Pd1-N2	3.207(2)	3.235(3)	3.283(6)
Pd1-N3	1.9846(16)	1.994(3)	1.974(7)
Pd1-N4	1.9802(16)	1.978(3)	1.997(7)
Pd1-N5	3.214(2)	3.305(3)	3.288(6)
Pd1-N6	2.0312(16)	2.027(3)	2.032(7)
N2-C5	1.390(3)	1.381(5)	1.335(10)
N2-C6	1.372(3)	1.373(5)	1.359(10)
N5-C15	1.363(3)	1.338(5)	1.338(10)
N5-C16	1.372(3)	1.354(5)	1.345(10)

As X-ray spectroscopy cannot always unequivocally confirm the presence of single protons, the deprotonation state of the amine bridges in the three structures was further checked by taking a closer look at the bond distances around the secondary amine nitrogen atoms. The distances between the amine nitrogen atoms and the connected pyridine carbon atoms clearly reflect the protonation state of the amines: whereas the C-N distances in [1]²⁺ range between 1.390(3) and 1.363(3) Å, these bond distances are significantly shorter in [5] (ranging from 1.335(10) to 1.359(10) Å, Table 7.1). These shorter distances are indicative of a higher double-bond character in the C-N bonds in [5], as would be expected upon deprotonation. In the structure of [3]₂(HCOO)(PF₆) two sets of C-N bond distances are observed within each complex molecule, with two long and two short distances, indicating one

protonated and one deprotonated amine nitrogen. Deprotonation of the amine bridges should also influence C-N-C angles. Indeed, these angles appear to be slightly smaller for the deprotonated amines (126.1(3)-127.5(7)°) than for the protonated amine nitrogens (129.5(2)-132.2(2)°).

Table 7.2 Selected angles and structural parameters of [1]²⁺, [3]⁺, and [5], for atom-labelling see Figure 7.6.

Angle	[1] ²⁺	[3] ⁺	[5]
N1-Pd1-N3	91.43(7)	91.00(12)	90.9(3)
N3-Pd1-N4	82.19(7)	82.43(12)	83.0(3)
N4-Pd1-N6	92.33(7)	91.81(12)	91.7(3)
N6-Pd1-N1	96.38(7)	96.62(12)	96.5(3)
N1-Pd1-N4	165.35(7)	167.06(12)	166.9(3)
N3-Pd1-N6	167.38(7)	167.85(12)	166.7(3)
C5-N2-C6	129.52(17)	130.0(3)	126.7(7)
C15-N5-C16	132.22(18)	126.1(3)	127.5(7)
N1-N3-N4-N6	17.3	15.5	16.8
τ_4^*	0.193	0.177	0.187

$$*\tau_4 = \frac{360^\circ - (\alpha + \beta)}{141^\circ}$$

Overall, these structural observations clearly confirm that the palladium compound must be formulated as dicationic [1]²⁺, monocationic [3]⁺, and neutral [5], but protonation of the amine does not significantly influence the coordination mode of the ligand and geometry of the central metal ion. Finally, the solvent molecules and anions that are present in the crystal lattices of the compounds demonstrate specific H-bonding interactions that are in agreement with the protonation states of the compounds discussed above. In [1](PF₆)₂ the two lattice acetonitrile molecules form hydrogen bonds with the two amine nitrogens with N-H...N distances of 2.171 and 2.026 Å. By contrast, in the structure of [5] two of the lattice water molecules act as hydrogen bond donors to the amine nitrogens with N...H-O distances of 1.985 and 2.055 Å. The formate ion in [3]⁺ forms two hydrogen bonds to the protonated amine nitrogens of two independent molecules, with N-H...O distances of 1.940 and 1.897 Å.

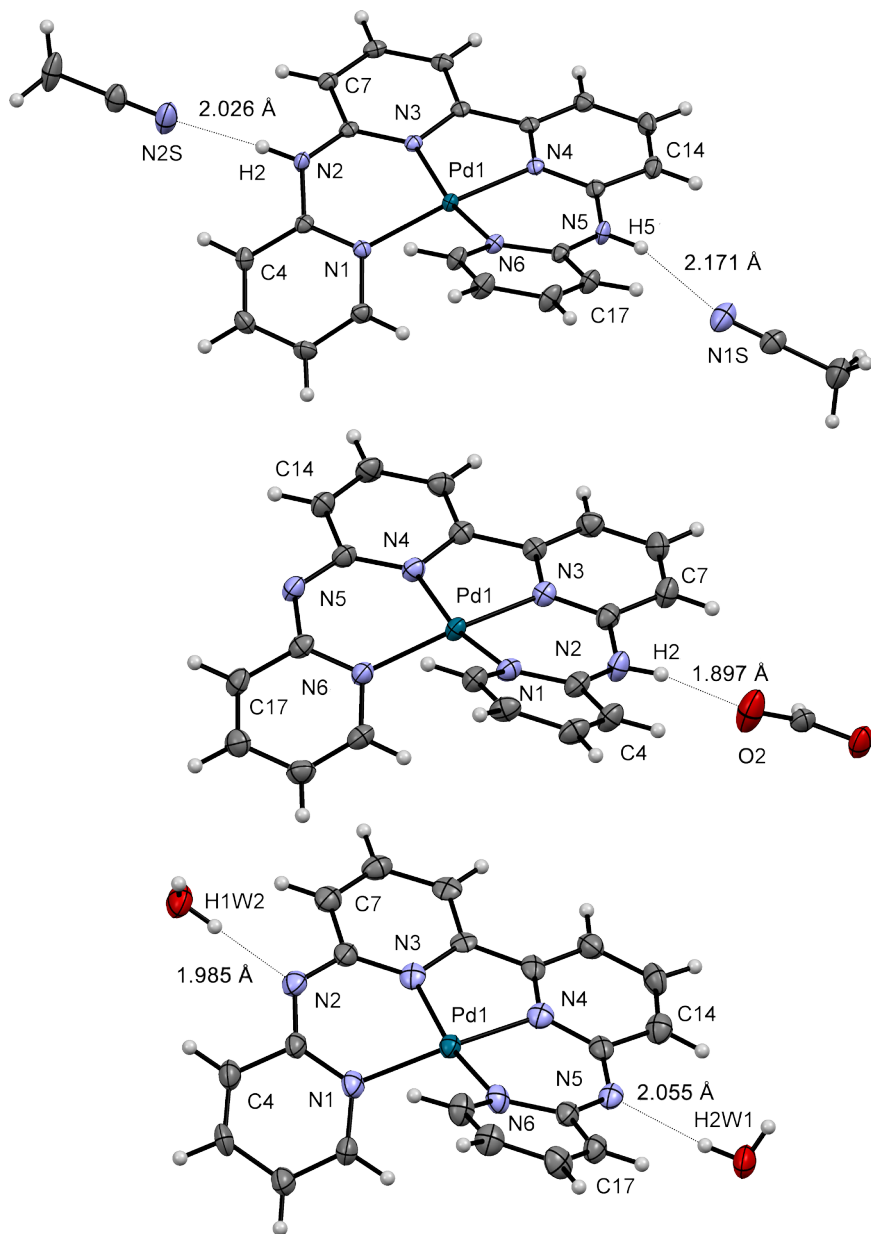


Figure 7.6 Displacement ellipsoid of [1]²⁺ (top), [3]⁺ (middle), and [5] (bottom) (all 50% probability level) as observed in the crystal structure of {[1](PF₆)₂ · 2×CH₃CN}, {[3]₂(PF₆)(HCOO)}, and {[5] · 3×H₂O}, respectively.

7.3 Discussion & Conclusion

We have demonstrated in this chapter that the potential anticancer complexes [1]²⁺ and [2]²⁺ containing the H₂bapbpy ligand have three distinct protonation states with increasing absorption in the visible region of the spectrum when the ligand is deprotonated. In water the pK_a of the first deprotonation takes place close to physiological conditions (at 7.8 and 8.3 respectively for [1]²⁺ and [2]²⁺, Scheme 7.1). Such pH dependence of absorption has been reported in the literature for both organic and inorganic compounds, in which for instance protonation results in a positively charged amine that disturbs conjugation.^{23, 24} The difference in acidity between the palladium and platinum complexes may be of paramount importance for the different *in vitro* and *in vivo* activities of these complexes (see Chapter 6).

Intracellular variation of the charge of these complexes, driven by local variations of the pH and of the polarity of the cellular medium (i.e. membranes vs. cytosol), may result in different compound configuration, uptake mechanisms, and biological activities in different cells and different parts of the cells. The ability to obtain a neutral, monocationic, or dicationic state, and thus the possibility to be taken up via passive diffusion, monocation transporters, or dication transporters, the absence of steric hindrances and the relatively flat geometry of these complexes, could explain the high uptake efficiency reported in Chapter 6. Furthermore, the crystal structures of [1]²⁺, [3]⁺, and [5] show that hydrogen bonding with the secondary bridging amines can occur either as donor or as acceptor or as both, which opens many routes to interact for example with nuclear DNA, contrary to the qtpy complexes that lack the possibility to engage in hydrogen bonding interactions. For a metal complex with a saturated coordination sphere that does not allow for the formation of coordination bonds with biomolecules, the ability to establish H-bonding interactions could strongly influence for instance binding to the phosphate backbone or DNA bases,^{25, 26} which may could play a role in the mechanism of action of this new family of compounds.

7.4 Experimental

7.4.1 Synthesis of [Pd(H₂bapbpy)]Cl₂ ([1]Cl₂) and [Pd(H₂bapbpy)]Cl₂ ([2]Cl₂)

[1]Cl₂ and [2]Cl₂ were synthesized as described in Chapter 6. After isolation as PF₆-salt in a flask the complexes were fully dissolved in CH₃CN. Then, upon addition of aqueous HCl (10 M) precipitation occurred and a powder was filtered off which turned out to be [1]Cl₂ or [2]Cl₂

7.4.2 Synthesis and crystallization of [Pd(bapbpy)] ([5])

K₂[PdCl₄] (163 mg, 0.15 mmol) and H₂bapbpy (127 mg, 0.11 mmol) were added into a 2-neck 25 ml round bottom flask containing a degassed ethanol-water mixture (3:2, 10 mL). The brown suspension was stirred overnight at 80 °C under argon resulting in a red suspension that was filtered. Then, aqueous NaOH (5.0 M) was added to the filtrate upon which a red solid precipitated. The suspension was filtered, washed with water, and redissolved in THF. After rotary evaporation the compound was dried *in vacuo* and obtained as a yellow powder. Yield: 45 mg (51%). Amber yellow needle-shaped crystals suitable for X-ray diffraction were obtained by dissolving 2.0 mg of [5] in 0.8 mL of THF in a small GC vial. This vial was placed in a larger vial containing 2.8 mL pentane. The large vial was closed and vapor diffusion occurred within a few days to afford X-ray quality crystals. ¹H NMR (500 MHz, THF-*d*₈, 293 K, in ppm): δ = 7.75 (dd, *J* = 6.5, 1.5 Hz, 2H, H^{py-6}), 7.55 (dd, *J* = 8.5, 1.5 Hz, 2H, H⁴), 7.41 (ddd, *J* = 8.5, 2.0, 1.0 Hz, 2H, H^{py-4}), 7.27 (dd, *J* = 7.0, 1.0 Hz, 2H, H³), 6.99 (m, 4H, H⁵/H^{py-3}), (ddd, *J* = 6.5, 6.5, 1.5 Hz, H^{py-5}). ¹³C NMR (126 MHz, THF-*d*₈, 293 K, in ppm): δ = 148.74 (C^{py-6}), 136.76 (C⁴), 136.71 (C^{py-4}), 124.56 (C^{py-3}), 124.03 (C⁵), 113.16 (C^{py-5}), 110.60 (C³).

7.4.3 Crystallization of [Pd(Hbapbpy)]₂(HCOO)(PF₆) ([3]₂(HCOO)(PF₆))

Ruby red crystals suitable for X-ray diffraction were obtained by diffusion of diethyl ether into an acetone solution of [1](PF₆)₂. 0.3 mg of [1](PF₆)₂ was dissolved in 0.4 mL of acetone and placed in a small GC vial. This vial was placed in a larger vial containing 2.8 mL diethyl ether. The large vial was closed and vapor diffusion occurred after 7 days to afford X-ray quality crystals of [3]₂(HCOO)(PF₆)

7.4.4 Synthesis of [Pt(bapbpy)] ([6])

K₂[PtCl₄] (48 mg, 0.15 mmol) and H₂bapbpy (40 mg, 0.11 mmol) were added into a 2-neck 25 ml round bottom flask containing a degassed ethanol-water mixture (7:3, 10 mL). The brown suspension was stirred overnight at 80 °C under argon resulting in a red suspension that was filtered. Then, aqueous NaOH (5.0 M) was added upon which a red solid to precipitated. The suspension was filtered, washed with water, and dissolved in THF. After rotary evaporation the compound was dried *in vacuo* and obtained as a yellow powder. Yield: 42 mg (46%). ¹H NMR (500 MHz, 293 K, THF-*d*₈, in ppm): δ = 7.91 (d, 6.5 Hz, 2H, H^{py-6}), 7.68 (t, 8.0, 8.0 Hz, 2H, H⁴), 7.49 (dd, 7.5, 1.0 Hz, 2H, H^{py-4}), 7.36 (d, 2H, 7.0 Hz, H³), 7.03 (d,

8.5 Hz, 2H, H⁵), 6.35 (dd, 6.5, 6.5 Hz, 2H, H^{py-5}). ¹³C NMR (126 MHz, THF-d₈, in ppm): δ = 148.52 (C^{py-6}), 135.63 (C⁴), 125.94 (C^{py-4}), 124.81 (C^{py-3}), 124.40 (C⁵), 112.99 (C^{py-5}), 111.51 (C³).

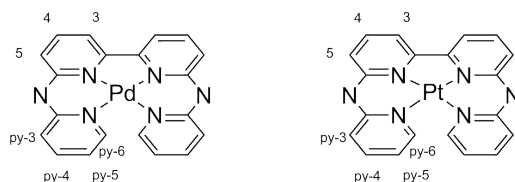


Figure 7.7 Schematic representation of [5] and [6] with atom numbering for NMR attribution.

7.4.5 Absorbance measurements

UV-vis experiments were performed on a Cary 50 Varian spectrometer equipped with a Cary Single Cell Peltier for temperature control. All spectra were recorded with Cary WinUV software from Cary and further processed with Microsoft Office Excel 2010.

7.4.6 pKa determination for [1]²⁺ to [3]⁺ and [2]²⁺ to [4]⁺

pH titration: 6 mL of a 67 μM solution of [1]Cl₂ or [2]Cl₂ in hydrochloric acid (0.033 M) was put in a 15 mL vial. A pH measurement electrode was added and when stable the pH was logged, aliquots (0.5-10 μL) of aqueous NaOH (0.05 – 5M) were added to give a range of pH values while stirring. After each stable pH a UV-vis absorbance spectrum was measured. The relative concentration of [Pd(H₂bapbpy)]²⁺ or [Pt(H₂bapbpy)]²⁺ was determined using the Lambert-Beer Law, and then plotted as a function of the pH. The pKa was determined by modelling the curve using a simplified two-parameter Hill-slope equation:

$$\frac{100}{(1+10^{((\log_{10}pka-X) \cdot Hill\ Slope)})}$$

7.4.7 Absorbance spectroscopy for [5] and [6]

2.5 mL of a 67 μM solution of [5] or [6] in a 1:1 THF-water mixture was prepared. 2 μL aliquots of NaOH (0.05 M) were added to the solutions until no more changes in the spectra were observed to ensure full deprotonation of the metal complex. Then, 2 μL aliquots of aqueous HCl (33 mM) were added, after each addition a UV-vis absorption spectrum was recorded.

7.4.8 Absorbance spectroscopy for [1](PF₆)₂ and [2](PF₆)₂ at different temperatures

Typically, 2.5 mL of a 100 μM solution of [1](PF₆)₂ or [2](PF₆)₂ was prepared, and subsequently an absorbance spectrum was recorded at 20, 40, 60, 80, and again 20 °C in demineralized water or phosphate buffer (pH = 7.4). Upon cooling back down to 20 °C without exception the original spectrum was obtained.

7.4.9 (TD)-DFT

ADF was used to minimize the structures of [1]²⁺, [3]⁺, and [5] using PBEO as functional, TZP as basis set, and COSMO to simulate the water solvent.^{19, 20, 27, 28} TDDFT was then used at the CAM-B3LYP/TZP/COSMO level to calculate the first 50 singlet transition of the three ground state geometries.

7.5 References

1. M. Branca, M. E. Marini and B. Pispisa, *Biopolymers*, 1976, **15**, 2219-2226.
2. D. Belli Dell' Amico, F. Calderazzo, M. Curiardi, L. Labella and F. Marchetti, *Inorg. Chem.*, 2004, **43**, 5459-5465.
3. D. Belli Dell'Amico, F. Calderazzo, M. Curiardi, L. Labella and F. Marchetti, *Inorg. Chem. Commun.*, 2005, **8**, 673-675.
4. K.-M. Lam, K.-Y. Wong, S.-M. Yang and C.-M. Che, *J. Chem. Soc., Dalton Trans.*, 1995, **7**, 1103-1107.
5. E. C. Constable, S. M. Elder, J. Healy, M. D. Ward and D. A. Tocher, *J. Am. Chem. Soc.*, 1990, **112**, 4590-4592.
6. E. Wachter, A. Zamora, D. K. Heidary, J. Ruiz and E. C. Glazer, *Chem. Commun.*, 2016, **52**, 10121-10124.
7. M. Cusumano, M. L. Di Pietro and A. Giannetto, *Inorg. Chem.*, 1999, **38**, 1754-1758.
8. P. M. Takahara, A. C. Rosenzweig, C. A. Frederick and S. J. Lippard, *Nature*, 1995, **377**, 649-652.
9. U.-M. Ohndorf, M. A. Rould, Q. He, C. O. Pabo and S. J. Lippard, *Nature*, 1999, **399**, 708-712.
10. C. Shobha Devi, P. Nagababu, S. Natarajan, N. Deepika, P. Venkat Reddy, N. Veerababu, S. S. Singh and S. Satyanarayana, *Eur. J. Med. Chem.*, 2014, **72**, 160-169.
11. C. Icsel, V. T. Yilmaz, Y. Kaya, H. Samli, W. T. A. Harrison and O. Buyukgungor, *Dalton Trans.*, 2015, **44**, 6880-6895.
12. F. Shahsavari, M. Bozorgmehr, E. Mirzadegan, A. Abedi, Z. Mehri Lighvan, F. Mohammadi, N. Safari, V. Amani and A.-H. Zarnani, *Anti-Cancer Agents Med. Chem.*, 2016, **16**, 393-403.
13. L. He, X. Chen, Z. Meng, J. Wang, K. Tian, T. Li and F. Shao, *Chem. Commun.*, 2016, **52**, 8095-8098.
14. A. Zianna, G. Psomas, A. Hatzidimitriou and M. Lalia-Kantouri, *J. Inorg. Biochem.*, 2016, **163**, 131-142.
15. J. M. Gichumbi, B. Omondi and H. B. Friedrich, *Eur. J. Inorg. Chem.*, 2017, **2017**, 915-924.
16. S. Kathiresan, S. Muges, J. Annaraj and M. Murugan, *New J. Chem.*, 2017, **41**, 1267-1283.
17. A. Masuya, N. Iki, C. Kabuto, Y. Ohba, S. Yamauchi and H. Hoshino, *Eur. J. Inorg. Chem.*, 2010, **2010**, 3458-3465.
18. B. Raghuraman, G. Gustavson, O. C. Mullins and P. Rabbito, *AIChE J.*, 2006, **52**, 3257-3265.
19. G. te Velde, F. M. Bickelhaupt, E. J. Baerends, C. Fonseca Guerra, S. J. A. van Gisbergen, J. G. Snijders and T. Ziegler, *J. Comput. Chem.*, 2001, **22**, 931-967.
20. C. Fonseca Guerra, J. G. Snijders, G. te Velde and E. J. Baerends, *Theor. Chem. Acc.*, 1998, **99**, 391-403.
21. M. H. Reineke, M. D. Sampson, A. L. Rheingold and C. P. Kubiak, *Inorg. Chem.*, 2015, **54**, 3211-3217.
22. S. Zheng, N. R. M. Reintjens, M. A. Siegler, O. Roubeau, E. Bouwman, A. Rudavskiy, R. W. A. Havenith and S. Bonnet, *Chem. Eur. J.*, 2016, **22**, 331-339.
23. M. R. Mazières, C. Duprat, J. G. Wolf and A. D. Roshal, *Dyes Pigm.*, 2009, **80**, 355-360.
24. S. R. Kennedy, M. N. Kozar, H. P. Yennawar and B. J. Lear, *Inorg. Chem.*, 2016, **55**, 8459-8467.
25. Y. Mantri, S. J. Lippard and M.-H. Baik, *J. Am. Chem. Soc.*, 2007, **129**, 5023-5030.
26. J. Reedijk, *Proc. Natl. Acad. Sci. USA*, 2003, **100**, 3611-3616.
27. C. C. Pye and T. Ziegler, *Theor. Chem. Acc.*, 1999, **101**, 396-408.
28. S. J. A. van Gisbergen, J. G. Snijders and E. J. Baerends, *Comput. Phys. Commun.*, 1999, **118**, 119-138.

CHAPTER 8

The ligand matters: Pd and Pt anticancer drugs based on a tetrapyridyl ligand containing a single amine bridge

This chapter is to be submitted as a full paper: Vincent H.S. van Rixel, Lucas J.S. Marinelli, Maxime A. Siegler, Sylvestre Bonnet, *manuscript in preparation*.

8.1 Introduction

Inorganic anticancer compounds typically interact with biomolecules following two different modes. The first mode is direct binding of biomolecules such as DNA or proteins to the metal center to form a metal-ligand coordination bond.¹ The formation of these coordination bonds is commonly preceded by the release of a ligand present in the original or intermediate complex. The anticancer drug cisplatin and most of its derivatives rely on this mechanism of action.² Chloride ligands initially bound to the metal center in cisplatin are first substituted by water molecules, before the main target in the nucleus, specifically the N7 atom of guanine DNA base pairs, coordinates to the metal ion.^{3,4}

The second type of interaction is an indirect binding mode of the complex with its biomolecular target. Typically, one of the ligands of a metal complex intercalates via π - π or hydrophobic interactions to DNA or proteins. Typical intercalators consist of planar polyaromatic and extended polypyridyl ligands.^{5, 6} Whereas organic intercalators such as daunorubicin are widely used in the clinics as cancer-treatment, no inorganic intercalators have made it to the clinic yet.⁷⁻⁹

In this chapter the use of coordinatively saturated tetrapyridyl palladium(II) and platinum(II) complexes as potentially intercalating anticancer drugs is described. In Chapter 6 and Chapter 7 it was demonstrated that for complexes based on the ligand H₂bapbpy (N,N'-di(pyrid-2-yl)-2,2'-bipyridine-6,6'-diamine, Figure 8.1) the choice of the metal center had a strong influence on the biological activity of the complex *in vitro* and *in vivo*, on its cellular uptake, and on its pK_a. H₂bapbpy is characterized by the presence of two non-coordinating amine bridges that can be deprotonated easily in water upon metal coordination. The influence of the deprotonation of these bridging amines on the physico-chemical and biological properties of these complexes has been extensively discussed in Chapter 7. In this chapter the palladium(II) and platinum(II) complexes of Hbbpya (N,N-bis(2,2'-bipyrid-6-yl)amine), Figure 8.1) are presented,^{10, 11} a tetrapyridyl ligand similar to H₂bapbpy except for its single unique non-coordinated amine bridge.

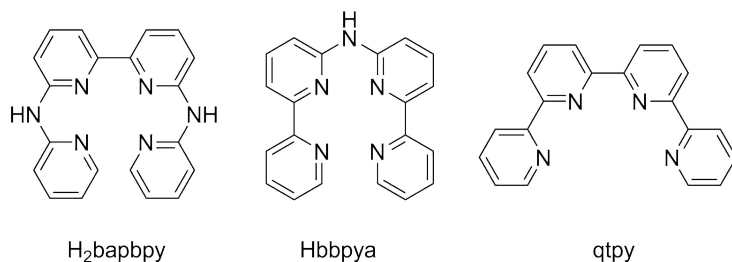
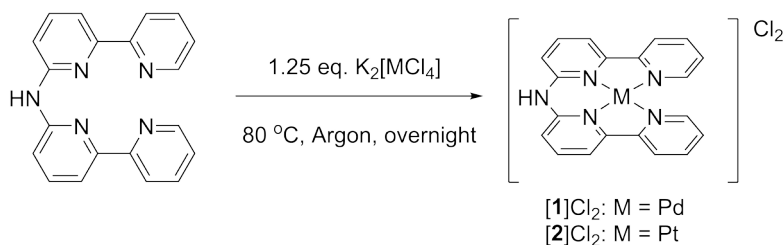


Figure 8.1 Chemical structures of the three tetrapyrrolyl ligands H₂bapbpy, Hbbpya, and qtpy.

8.2 Results

8.2.1 Synthesis and crystal structure

The square-planar complexes [Pd(Hbbpya)]Cl₂ ([1]Cl₂) and [Pt(Hbbpya)]Cl₂ ([2]Cl₂) were synthesized by reacting the ligand Hbbpya with K₂[PdCl₄] and K₂[PtCl₄], respectively, in an ethanol-water mixture (Scheme 8.1). After purification using size exclusion chromatography, analysis with NMR spectroscopy, elemental analysis, and high resolution mass spectrometry confirmed that the compounds were analytically pure. Vapor diffusion of acetone into a solution of [1]Cl₂ in methanol yielded yellow-colored crystals suitable for X-ray diffraction studies (Figure 8.2).



Scheme 8.1 Synthesis of [1]Cl₂ and [2]Cl₂.

The compound [1]Cl₂ crystallizes with one molecule of MeOH. Pd1-N1 and Pd1-N5 bond distances of the terminal pyridyl groups are 2.0600(18) and 2.0680(18) Å, respectively (Table 8.1), whereas the Pd1-N2 and Pd1-N4 bond distances of the internal pyridines are 1.9887(10) and 1.9933(18) Å, respectively, thus much shorter. These trends are similar to those in [Pd(H₂bapbpy)](PF₆)₂ ([3](PF₆)₂), but are even

more pronounced in the analogue palladium(II) complex without any amine bridge, i.e. $[\text{Pd}(\text{qtpy})](\text{PF}_6)_2$.¹²

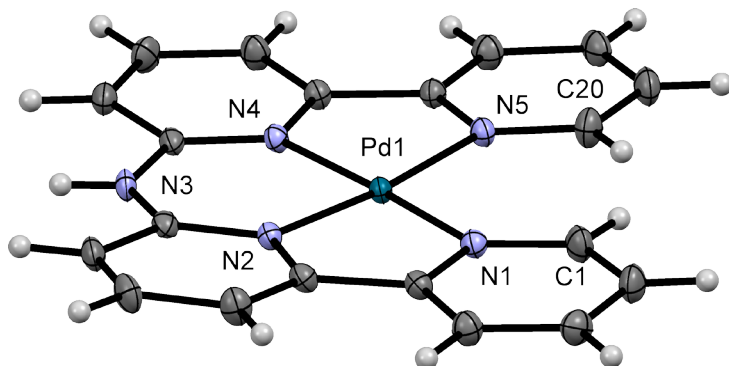


Figure 8.2 Displacement ellipsoid of the cationic part of $[\mathbf{1}]\text{Cl}_2$ (50% probability level). Counter anions, and the lattice solvent molecule have been omitted for clarity.

Table 8.1 Selected bond lengths (Å) in the crystal structures of $[\mathbf{1}]\text{Cl}_2$, of the H_2bapbpy analogue $[\mathbf{3}](\text{PF}_6)_2$, and of $[\text{Pd}(\text{qtpy})](\text{PF}_6)_2$.

Bond	$[\mathbf{1}]\text{Cl}_2$	Bond	$[\mathbf{3}](\text{PF}_6)_2^{\text{a}}$	Bond	$[\text{Pd}(\text{qtpy})](\text{PF}_6)_2^{\text{b}}$
Pd1-N1	2.0600(18)	Pd1-N1	2.0251(16)	Pd1-N2	2.056
Pd1-N2	1.9887(18)	Pd1-N3	1.9846(16)	Pd1-N1	1.928
Pd1-N4	1.9933(18)	Pd1-N4	1.9802(16)	Pd1-N1B	1.928
Pd1-N5	2.0680(18)	Pd1-N6	2.0312(16)	Pd1-N2B	2.056
Pd1-N _{ave} ^c	2.028	Pd1-N _{ave}	2.005	Pd1-N _{ave}	1.992

a: Values taken from Chapter 6

b: Values taken from Constable et al.¹²

c: Average value of the four coordinating Pd-N bonds in each complex.

The differences between the open and closed side of the tetrapyrrolyl ligands are also apparent when comparing the bond angles. For $[\mathbf{1}]\text{Cl}_2$ the N1-Pd1-N5 angle on the open side is $108.84(7)^\circ$, while the angle N2-Pd1-N4 on the closed side is $93.22(7)^\circ$, thus more than 15° smaller. In $[\mathbf{3}](\text{PF}_6)_2$ and $[\text{Pd}(\text{qtpy})](\text{PF}_6)_2$ bond internal angles N3-Pd1-N4 and N1-Pd1-N5 are $82.19(7)$ and 81.2° , respectively. These differences can be explained by the formation of one 6-membered ring and two 5-membered rings with Hbbpypa , while coordination of H_2bapbpy generates

one 5-membered ring and two 6-membered rings, and qtpy generates only 5-membered rings. Such differences increase the opening of the ligands as follows: H₂bapbpy < Hbbpya < qtpy: in [3](PF₆)₂ N6-Pd1-N1 is 96.38(7)°, in [1]Cl₂ N1-Pd1-N5 is 105.84(7)°, and in [Pd(qtpy)](PF₆)₂ N2-Pd1-N2B is 117.8°.

Table 8.2 Selected bond angles, torsion angles (°), and τ_4 values for [1]Cl₂, [3](PF₆)₂, and [Pd(qtpy)](PF₆)₂.

Angle	[1]Cl ₂	Angle	[3](PF ₆) ₂ ^a	Angle	[Pd(qtpy)](PF ₆) ₂ ^b
N1-Pd1-N2	80.38(7)	N1-Pd1-N3	91.43(7)	N2-Pd1-N1	80.5
N2-Pd1-N4	93.22(7)	N3-Pd1-N4	82.19(7)	N1-Pd1-N1B	81.2
N4-Pd1-N5	80.48(7)	N4-Pd1-N6	92.34(7)	N1B-Pd1-N2B	80.8
N5-Pd1-N1	105.84(7)	N6-Pd1-N1	96.38(7)	N2B-Pd1-N2	117.8
N1-Pd1-N4	173.35(7)	N1-Pd1-N4	165.35(6)	N2-Pd1-N1B	161.7
N2-Pd1-N5	173.37(7)	N3-Pd1-N6	167.38(6)	N1-Pd1-N2B	161.7
N1-N2-N4-N5	0.20	N1-N3-N4-N6	17.30	N2-N1-N1B-N2B	0.54
τ_4^*	0.090	τ_4^*	0.193	τ_4^*	0.260

* τ_4 is obtained using the equation $\frac{360^\circ - (\alpha + \beta)}{141^\circ}$; a value of 0 corresponds to a square-planar coordination geometry and a value of 1 to a tetrahedral coordination geometry.

a Values taken from Chapter 6

b Values taken from Constable et al.¹²

As a result of the different chelating rings generated by the three ligands the distortions of the square-planar coordination sphere also greatly vary. A perfect square-planar coordination geometry can be defined as a four-coordinate complex with ligands that coordinate in a single plane, and it should contain bond angles of only 90 and 180°. The τ_4 value introduced by Houser and co-workers quantifies the square-planarity of tetracoordinated metal complexes by distinguishing complexes with a τ_4 value of 0 that are perfectly square-planar, and complexes with a τ_4 value of 1 that have a perfect tetrahedral geometry. Using the crystal structures of [1]Cl₂, [3](PF₆)₂, and [Pd(qtpy)](PF₆)₂ τ_4 values of respectively 0.090, 0.193, and 0.260 (Table 8.2) were calculated indicating that [1]Cl₂ is by far the most square-planar geometry, while [3](PF₆)₂ and [Pd(qtpy)](PF₆)₂ have both severely distorted geometries. The torsion angle of the coordinating nitrogen atoms is a measure of the degree of flatness of the coordination plane of square-planar complexes. For [1]Cl₂, [3](PF₆)₂, and [Pd(qtpy)](PF₆)₂ these torsion angles are 0.20, 17.30, and 0.54°, respectively. Thus, whereas in [1]²⁺ and [Pd(qtpy)]²⁺ the tetrapyrrolyl ligands are coordinated almost in one single plane, in [3]²⁺ the ligand assumes a more helical

geometry. To conclude, [1]Cl₂ is highly square-planar and very flat. The distance between the hydrogen atoms of C1 and C20 is 1.905 Å, which is apparently long enough to prevent distortion of the coordinated Hbbpya ligand. Previously, Hbbpya has already demonstrated a high degree of planarity in octahedral iron(II) complexes, and preliminary data shows that it is also highly planar in nickel(II) and ruthenium(II) complexes (Figure SVIII.3).¹³ This planar geometry significantly differs from the H₂bapbpy ligand that coordinates to metal ions in a distorted fashion. Although a crystal structure of [2]Cl₂ was not obtained, similar geometric features are expected as palladium(II) and platinum(II) complexes with identical ligands are usually very similar (Chapter 6). Overall, the removal of an amine bridge in H₂bapbpy, results in the ligand Hbbpya that can coordinate to palladium(II) or platinum(II) with a highly square-planar geometry.

8.2.2 Cytotoxic properties of [1]Cl₂ and [2]Cl₂

The similar coordination mode of Hbbpya and H₂bapbpy to palladium(II) and platinum(II) ions may predict similar activities for these metal complexes *in vitro*. To check this hypothesis, the cytotoxicity of the two new Hbbpya metal complexes [1]Cl₂ and [2]Cl₂ was tested against three different cancer cell lines (A375 skin, A549 lung, and MDA-MB231 breast cancer) and one non-malignant lung cell line (MRC-5). The cell-testing protocol was adapted from Hopkins et al.¹⁴: 24 h after seeding, the cells were incubated for 24 h with the drug, the media was refreshed, and the cells were further incubated with drug-free medium for 48 h. A sulforhodamine B (SRB) cell-counting assay was performed at 96 h, and effective concentrations (EC₅₀) were determined by comparing cell viability of treated wells with drug-free control wells. The EC₅₀ values are summarized in Table 8.3. EC₅₀ values for A375 and A549 cancer cell lines for [1]Cl₂ and [2]Cl₂ were similar and ranged between 1.6-1.9 μM. For MDA-MB231 and MRC-5 cancer cells both compounds showed lower cytotoxicity in the 4.7-6.8 μM range. Overall, the cytotoxicity of [1]Cl₂ and [2]Cl₂ was found comparable with that of cisplatin, i.e. in the low micromolar range. The cytotoxicity of [2]Cl₂ is comparable with that of [Pt(H₂bapbpy)](PF₆)₂ ([4](PF₆)₂), but the cytotoxicity of [1]Cl₂ was nowhere near the exceptional activity of [3](PF₆)₂, that showed EC₅₀ values below 0.2 μM for all the cell lines tested in this panel. Although the ligands are highly similar, once coordinated to palladium they have highly different biological properties as their palladium(II) complexes.

Table 8.3 Cytotoxicity expressed as cell growing inhibition effective concentrations (EC₅₀ with 95% confidence intervals, in μM) for [1]Cl₂, [2]Cl₂, and cisplatin on skin (A375), lung (A549), and breast (MDA-MB231) cancer cell lines, and on non-cancerous lung fetal cell line (MRC-5).

Cell Line	[1]Cl ₂		[2]Cl ₂		cisplatin	
A375	1.9	-0.26 +0.30	1.8	-0.39 +0.50	1.6	-0.52 +0.77
A549	1.9	-0.34 +0.42	1.6	-0.47 +0.67	3.1	-0.98 +1.4
MDA-MB231	6.6	-1.43 +1.8	4.7	-1.2 +1.5	> 25	-
MRC-5	6.8	-1.5 +1.9	5.6	-2.0 +3.0	12	-3.9 +5.9

8.2.3 Cellular Uptake

Considering the different *in vitro* activity of [1]Cl₂ and [3](PF₆)₂ uptake studies were performed to determine whether the differences in cytotoxicity are caused by different intracellular concentrations of both palladium compounds. A375 or A549 cells were seeded, and treated with [1]Cl₂, [2]Cl₂, [3](PF₆)₂, [4](PF₆)₂, or cisplatin at their EC₅₀ concentrations. After 24 h drug incubation, cells were washed, trypsinized, counted, digested and the amount of metal content was measured using ICP-MS (see Experimental section for the full procedure). [1]Cl₂ and [2]Cl₂ showed similar uptake by A375 or A549 cells (7.2 and 9.4 nmol/10⁶ cells) with an uptake efficiency of 8 and 16%. [3](PF₆)₂ showed an uptake of 1.2 (54%) and 5.3 nmol/10⁶ cells (39%) for A375 and A549 cells, respectively. For [4](PF₆)₂ a similar trend was observed with 19 and 22 nmol/10⁶ cells for A375 and A549 cells, respectively, corresponding to an uptake efficiency of 58% in both cell lines. Cisplatin, by comparison, showed very low metal uptake (0.06 and 0.07 nmol/10⁶ cells for A375 and A549 cells, respectively), which demonstrates that once in the cell cisplatin is much more harmful than the tetrapyrridyl complexes. The lower cytotoxicity of the Hbbpya complexes compared to the H₂bapbpy complexes does not seem to be related to a lower metal uptake: treatment at the EC₅₀ the uptake values were overall similar. Compound [4](PF₆)₂ may owe its higher cytotoxicity

compared to [1]Cl₂ and [2]Cl₂ due to a higher uptake, but [3](PF₆)₂ clearly has a much lower metal uptake and much higher cytotoxicity. These uptake results emphasize the remarkable cytotoxicity of [3](PF₆)₂ as its cellular concentrations in this experiment are the lowest by far, while it exhibited the highest cytotoxicity.

Table 8.4 Cellular uptake for A375 and A549 for compounds [1]Cl₂, [2]Cl₂, [3](PF₆)₂, [4](PF₆)₂, and cisplatin.

Cell line	Compound	Treatment Concentration (μM)	Metal Uptake (nmol/10 ⁶ cells)	Rel. Uptake Efficiency (%)
A375	[1]Cl ₂	1.9	9.4 ± 2.8	16
	[2]Cl ₂	1.7	7.9 ± 1.8	12
	[3](PF ₆) ₂	0.05	1.2 ± 0.2	54
	[4](PF ₆) ₂	1.0	19 ± 4.4	58
	cisplatin	1.6	< 0.01	< 1
A549	[1]Cl ₂	1.9	8.6 ± 2.1	13
	[2]Cl ₂	1.7	7.2 ± 0.8	8
	[3](PF ₆) ₂	0.2	5.3 ± 0.5	39
	[4](PF ₆) ₂	1.0	22 ± 2.1	58
	cisplatin	3.3	< 0.01	< 1

8.2.4 Lipophilicity and pKa

In medicinal chemistry higher uptake and improved cytotoxicity are often associated with higher lipophilicity. The octanol-water partition coefficient (logP value) is widely used as an indicator of lipophilicity (positive logP value) or hydrophilicity (negative logP value). The PF₆ salts of the H₂bapbpy complexes were first converted to [3]Cl₂ and [4]Cl₂, respectively, as DMSO would be required for initial solubilization of the PF₆ salts. Full details regarding the counter ion exchange procedure are provided in the Experimental section. The logP values for complexes [1]Cl₂ to [4]Cl₂ are shown in Table 8.5. The logP value for [4]Cl₂ (-0.45) was the highest of all the complexes, and also corresponded with the highest cellular uptake of [4](PF₆)₂. [3]Cl₂ with a logP value of -1.63 is the most hydrophilic of the compounds, and as the PF₆⁻ salt was taken up second highest. The logP values of [1]Cl₂ and [2]Cl₂ were found to be -0.96 and -1.59, respectively. In conclusion, all four tested complexes are rather hydrophilic, and no obvious

relationship between metal uptake and $\log P$ could be observed for this series of complexes.

Each amine bridge in the tetrapyrridyl ligands H**2**bapbpy and Hbbpya bears an acidic proton. Consecutive deprotonation of the two amine bridges in H**2**bapbpy can result in dicationic, monocationic, or neutral complexes, whereas the single amine bridge in Hbbpya complexes can only lead to dicationic or monocationic species. Of course, the acid-base equilibrium may influence both the $\log P$ values and the uptake of these complexes *in vitro*. In Chapter 7 the pK_a for the first deprotonation of [3]²⁺ and [4]²⁺ was found to be 7.8 and 8.3 in water. For [1]²⁺ and [2]²⁺ the pK_a in water was also determined by monitoring with UV-vis spectroscopy the titration of [1]Cl₂ and [2]Cl₂ in HCl (33 mM) with NaOH. Under acidic conditions the UV-vis spectra of [1]²⁺ and [2]²⁺ only show absorption in the visible region with a tail up to 423 nm and 425 nm, respectively (green curves in Figure 8.3). Upon base addition a significant increase in absorbance was observed, characterized by a new absorption maximum at 416 nm for [1]²⁺ and 430 nm for [2]²⁺. Simultaneously, a major decrease in absorbance was found at 261 and 362 nm for [1]²⁺ and at 239 and 372 nm for [2]²⁺. The evolution of the absorbance spectra for both complexes occurred with isosbestic points at 316 and 397 nm for [1]²⁺, and at 312 and 405 nm for [2]²⁺, indicating that only one reaction takes place. Further basification did not lead to any further change in the absorbance. The pH-dependence of the absorbance spectra of [1]²⁺ and [2]²⁺ in water can be explained by the deprotonation of [1]²⁺ or [2]²⁺ to form [Pd(bbpya)]⁺ or [Pt(bbpya)]⁺, respectively. The corresponding pK_a was determined to be 5.5 and 4.6 for [1]²⁺ and [2]²⁺, respectively. Thus, [1]²⁺ and [2]²⁺ have much lower pK_a 's compared to [3]²⁺ and [4]²⁺. Such higher acidity can be explained by a difference in steric repulsion: Hbbpya complexes have an almost perfect square-planar geometry ($\tau = 0.090$), whereas complexes of H**2**bapbpy are much more distorted ($\tau = 0.193$, Figure 8.2 and Figure 7.2). As a result the negative charge located on the deprotonated bbpya⁻ ligand in [Pd(bbpya)]⁺ and [Pt(bbpya)]⁺ is much better delocalized than the negative charge located on Hbapbpy⁻ in [Pd(Hbapbpy)]⁺ and [Pt(Hbapbpy)]⁺. Another reason for the lower pK_a of [1]²⁺ and [2]²⁺ compared to [3]²⁺ and [4]²⁺ is that the negative charge of the [Pd(bbpya)]⁺ and [Pt(bbpya)]⁺ complexes may be delocalized over two bpy moieties, whereas that of the [Pd(Hbapbpy)]⁺ and [Pt(Hbapbpy)]⁺ complexes is delocalized over only one bpy moiety and two pyridyl fragments. Overall, at physiological pH (7.4) the Hbbpya complexes will be

fully deprotonated, thus monocationic, whereas the H₂bapbpy complexes will be mixtures of dicationic and monocationic species.

Table 8.5 LogP and pKa values for [1]Cl₂, [2]Cl₂, [3]Cl₂, and [4]Cl₂.

Compound	logP	pKa
[1]Cl ₂	-0.96	5.5
[2]Cl ₂	-1.59	4.6
[3]Cl ₂	-1.63	7.8
[4]Cl ₂	-0.45	8.3

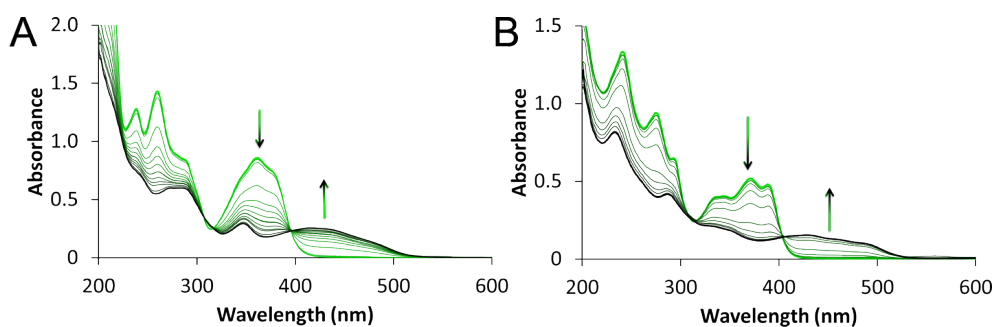


Figure 8.3 Evolution of the UV-vis spectrum of [1]²⁺ (left) and [2]²⁺ (right) upon increasing the pH of an HCl aqueous solution (33 mM) of the metal complex using NaOH. [Pd] = [Pt] = 67 μM.

8.2.5 Excited stated calculations for [1]²⁺ and [Pd(bbpya)]⁺

Although the differences in pKa between Hbbpya and H₂bapbpy complexes are large, their deprotonation was accompanied by similar changes of the absorption spectra in the visible domain. DFT and TDDFT calculations were performed by Dr. Sylvestre Bonnet to characterize the singlet excited states of [Pd(Hbbpya)]²⁺ and [Pd(bbpya)]⁺ and to confirm the hypothesis presented in the previous section.^{15, 16}

After structure minimization of both molecules in water at the PBE0/TZP/COSMO level the first singlet excited states were calculated by TDDFT and visualized using ADF (Figure 8.4 and Figure 8.5). All excited states absorbing in the visible domain have major contributions of HOMO → LUMO and HOMO → LUMO+1 transitions (Table SVIII.1, Table SVIII.2). In both the protonated and the deprotonated states the HOMO is localized on the non-coordinated amine bridge and its adjacent pyridyl rings. The LUMO and LUMO+1 are conjugated across the full (H)bbpya

ligand in contrast to H₂bapbpy that only does so on half of the atoms (essentially the bpy part). Excited states at 402 and 429 nm calculated for the deprotonated palladium complex are absent in the protonated complex (Figure SVIII.4, Table SVIII.1, and Table SVIII.2). In fact, not any excited states in the visible domain were found for [1]²⁺, and confirm the experimental finding of low absorption in the visible part in Figure 8.3. Thus, Intra-Ligand-Charge-Transfers HOMO → LUMO and HOMO → LUMO+1 transitions are responsible for the increased absorbance of [1]²⁺ upon deprotonation. The flatness of the coordinating Hbbpya is responsible for increased stabilization of the deprotonated species, which explains the lower pK_a measured for Hbbpya complex [1]²⁺, compared to its H₂bapbpy analogue.

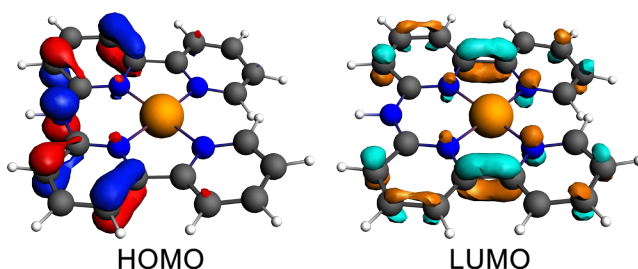


Figure 8.4 Selected orbital isodensity surfaces calculated by ADF for [1]²⁺.

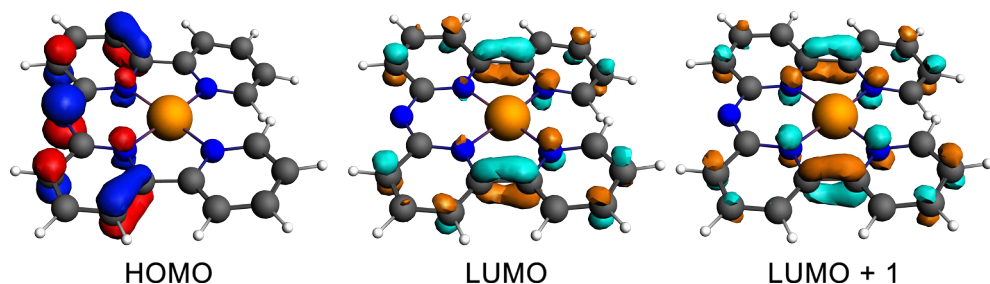


Figure 8.5 Selected orbital isodensity surfaces calculated by ADF for [Pd(bbpya)]⁺.

8.3 Discussion and Conclusion

Although the tetrapyrridyl ligands Hbbpya and H₂bapbpy structurally are highly similar, the coordination to palladium(II) or platinum(II) centers results in complexes with significant differences in coordination geometry, acidity, cellular uptake, and cytotoxicity. The crystal structures of the palladium(II) complexes with qtpy, Hbbpya, or H₂bapbpy show that the palladium Hbbpya complex is the most square-planar as well as the flattest of the three complexes. In the H₂bapbpy

complexes electronic conjugation in the distorted ligand is less possible, making deprotonation less favorable compared to Hbbpya complexes. As a result [1]²⁺ and [2]²⁺ will not be present as dicationic species *in vitro* whereas [3]²⁺ and [4]²⁺ are present in both dicationic and monocationic forms. Under the hypothesis that the complexes described in this chapter are taken up via passive diffusion, both the charge state and the lipophilicity may play a key role.¹⁷⁻¹⁹ Specifically in case of the H**2**bapby complexes, their pK_a values close to physiological conditions makes the complexes flexible regarding charge-dependent biochemical interactions with for instance negatively charged DNA.

The observed differences in cytotoxicity can be explained by differences in uptake for [1]Cl₂, [2]Cl₂, and [4](PF₆)₂ assuming that these complexes have similar mechanism of actions (MoAs). However, the cytotoxicity and uptake of [3](PF₆)₂ demonstrate that [3](PF₆)₂ is orders of magnitude more efficient in killing the cell once taken up, and that it has a distinct MoA compared to the other complexes. [1]Cl₂ and [2]Cl₂, albeit less cytotoxic than [3](PF₆)₂, also show that the class of non-cyclic tetrapyridyl complexes is promising as anticancer agents when the ligand is functionalized with a single non-coordinating amine bridge. These complexes also show that non-coordinated chloride counter-anions, combined with the amine bridges, result in much more water-soluble complexes compared to cisplatin. Future work to extend, functionalize, and improve on this class of complexes may involve: (i) variation of the metal center, to iridium(III),²⁰ rhenium(I),²¹ osmium(II),^{22, 23} or gold(III);^{24, 25} (ii) the use of palladium(IV) or platinum(IV) centers to facilitate a prodrug (photo)reduction strategy,²⁶⁻³³ (iii) or the use of cyclometallated versions of the H**2**bapby and Hbbpya ligands, to determine whether subsequent changes of the charge of these complexes results in higher or lower uptake and cytotoxicity.

8.4 Experimental

8.4.1 General procedures

Chemicals were bought from Alfa Aesar (K₂PtCl₄), Acros organics (K₂PdCl₄), and Sigma-Aldrich. Reactions were performed under a nitrogen atmosphere using standard Schlenk techniques. NMR spectra were recorded on a Bruker DPX-500 spectrometer. Chemical shifts are indicated in ppm relative to TMS. Mass spectra were recorded by using a Thermoquest Finnagen AQA Spectrometer. UV-vis experiments were performed on a Cary Varian

spectrometer. pH measurements were performed using a PHM220 lab pH meter. Metal concentrations for logP determination were measured on a Vista MPX ICP-OES.

8.4.2 Synthesis of [Pd(Hbbpya)]Cl₂ ([1]Cl₂)

In a 2-necked round bottom flask K₂PdCl₄ (304 mg, 0.72 mmol) and Hbbpya (171 mg, 0.53 mmol) were added into a degassed ethanol-water mixture (7:3, 100 mL) preheated at 80 °C. The resulting yellow suspension was stirred overnight at 80 °C in a nitrogen atmosphere resulting in a dark green/black suspension. The solution was cooled down to room temperature, filtered, and from the filtrate all solvents were rotary evaporated. The solids were dissolved in MeOH (5 mL) and purified by size exclusion chromatography (Sephadex L-20) using MeOH as eluent. The yellow band was collected and MeOH was removed by rotary evaporation, which resulted in [1]Cl₂ as a yellow powder. Yield: 42% (111 mg). ¹H NMR (500 MHz, D₂O, 293 K, in ppm): δ = 8.55 (d, J = 5.5 Hz, 2H, H⁵), 8.36 (m, 2H, H³, H⁶), 8.19 (t, J = 8.0 Hz, 2H, H⁴), 8.00 (d, J = 7.5 Hz, 2H, H³), 7.71 (m, 2H, H⁴), 7.44 (d, J = 8.5 Hz, 2H, H⁵). ¹³C NMR (126 MHz, D₂O, 293 K, in ppm): δ = 155.5 (C⁶), 152.0 (C²), 148.7 (C⁵), 145.1 (C²), 143.0 (C³), 142.4 (C⁴), 128.4 (C⁴), 124.6 (C⁶), 118.3 (C³), 118.2 (C⁵). High resolution ES MS m/z (calc): 430.0286 (430.0284 = [M - H - 2×Cl]⁺). Elem. Anal. Calcd. For C₂₀Cl₂H₁₅N₅Pd + MeOH + H₂O: C, 45.63; H, 3.83; N, 12.67. Found: C, 45.11; H, 3.94; N, 12.86.

8.4.3 Synthesis of [Pt(Hbbpya)]Cl₂ ([2]Cl₂)

In a 2-necked round bottom flask K₂PtCl₄ (300 mg, 0.730 mmol) and Hbbpya (200 mg, 0.590 mmol) were added into a degassed ethanol-water mixture (3:2, 100 mL) preheated at 80 °C. The resulting yellow suspension was stirred overnight at 80 °C in a nitrogen atmosphere resulting in a dark red suspension. The suspension was cooled to room temperature, subsequently cooled on ice, and then filtered. From the filtrate all solvents were rotary evaporated. The solids were dissolved in MeOH (5 mL) and purified by size exclusion chromatography (Sephadex L-20) using MeOH as eluent. The yellow band was collected and MeOH was removed by rotary evaporation, which resulted in [2]Cl₂ as a red/orange powder. Yield 42% (155 mg), ¹H NMR (500 MHz, CD₃OD and DCl, 293 K, in ppm): δ = 8.99 (d, J = 5.5 Hz, 2H, H⁶), 8.58 (d, J = 7.5 Hz, 2H, H³), 8.50 (t, J = 7.5 Hz, 2H, H⁴), 8.39 (t, J = 8.0 Hz, 2H, H⁴), 8.23 (d, J = 6.5 Hz, 2H, H⁴), 7.99 (m, 2H, H⁵), 7.77 (d, J = 8.5 Hz, 2H, H⁵). ¹³C NMR (126 MHz, 293 K, CD₃OD and DCl): δ = 156.4 (C⁶), 152.4 (C²), 150.4 (C⁵), 144.4 (C²), 143.7 (C³), 142.4 (C⁴), 129.6 (C⁴), 125.6 (C⁶), 119.9 (C³), 118.8 (C⁵) ppm. High resolution ES MS (H₂O) m/z (calc.): 519.0893 (519.0897 = [M - H - 2×Cl]⁺). Elem. Anal. Calcd. For C₂₀ClH₁₄N₅Pt + ½ H₂O: C, 41.93; H, 2.82; N, 12.22. Found: C, 41.78; H, 3.12; N, 13.51.

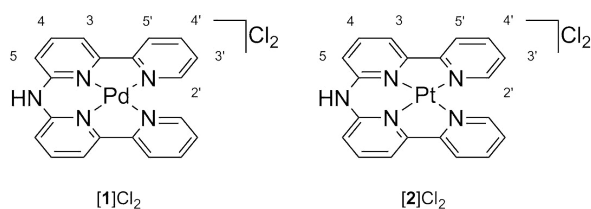


Figure 8.6 Schematic representation of [1]Cl₂ and [2]Cl₂ with atom numbering for NMR attribution.

8.4.4 pKa determination

pH titration: 6 mL of a 67 μM solution of [1]Cl₂ or [2]Cl₂ in hydrochloric acid (0.033 M) was put in a 15 mL vial. A pH measurement electrode was added and when stable the pH was logged, aliquots of aqueous NaOH (0.05 – 5M) were added to give a range of pH values while stirring. After each stable pH a UV-vis absorbance spectrum was recorded. The relative concentration of [M(Hbbpya)]²⁺ was calculated using the Lambert-Beer law and then plotted vs. pH. The pKa was determined by modelling the curve using a simplified two-parameter Hill-slope equation: $\frac{100}{(1+10^{((\log_{10}pka-x) \cdot Hill\ Slope)})}$.

8.4.5 Log P value determination

1.00 mM stock solutions of [1]Cl₂ and [2]Cl₂ in octanol-saturated water were prepared. 0.2 mL aliquots were transferred to 15 mL corning centrifugation tubes and diluted with octanol-saturated water to 1.0 mL, to give 0.2 mM solutions (in threefold). Then, 1.0 mL water-saturated octanol was added to each solution (not for the control samples, which remained at a volume of 1 mL). The solutions were shaken for 60 minutes on a GFL 3016 shaker at maximum speed and centrifuged for 10 minutes at RCF = 2800 g at T = 293 K. Then, 100 μL of the aqueous phase (in threefold) was transferred into a vial, and 1.0 ml 65% nitric acid was added to degrade the compounds overnight. 0.8 mL of the resulting solution was then diluted with 11 mL MilliQ water in corning tubes. Then the metal concentration of each sample was measured using ICP-JOS, and the initial equilibrium metal concentration in the water and octanol phases was calculated from the dilution factors. Finally, the logP value was calculated using the following equation: $\log P_{oct/aq} = \log \frac{[M]_{total} - [M]_{aq}}{[M]_{aq}}$.

8.4.6 Cell culturing and EC₅₀ cytotoxicity assay

See Appendix I for extensive description of the assay

8.4.7 Cellular uptake of [1]Cl₂, [2]Cl₂, [3](PF₆)₂, and [4](PF₆)₂

Uptake studies for complexes [1]Cl₂, [2]Cl₂, [3](PF₆)₂, and [4](PF₆)₂ were conducted on A375 and A549 lung cancer cells. 10 × 10³ A375 cells and 17 × 10³ A549 cells were seeded at t = 0 h in Opti-MEM complete in each well of a 6-well plate. At t = 48 h cells were treated with

complexes to give a final concentration close to the EC₅₀ values (1.9, 1.7, 0.05 or 0.2, and 1.0 μM for respectively [1]Cl₂, [2]Cl₂, [3](PF₆)₂, and [4](PF₆)₂ in the dark after 24 h in a total volume of 4 mL. After 24 h of drug incubation at 37 °C, the medium was aspirated, the cells were washed with PBS-buffer, trypsinized, counted using BioRad Cell Counting Slides on a BioRad TC10 automated cell counter, and pelleted by centrifugation (700 × g, 5 min). The supernatant was removed, and each sample was digested overnight in concentrated nitric acid at room temperature (> 65%). MilliQ water was added to each sample to obtain a final concentration of 5% HNO₃. For ICP-MS measurements, the system was optimized with a palladium-platinum solution. The calibration range was from 0 to 25 μg/l, and obtained detection limit for all isotopes was 0.01 μg/l. Silver and indium were used for internal standard, to correct for sample-dependent matrix effects. No reference sample was available; therefore several samples were spiked with a known concentration. The recoveries of the spiked concentrations were all within a 10% deviation.

8.5 References

1. P. C. A. Bruijninx and P. J. Sadler, in *Adv. Inorg. Chem.*, eds. E. Rudi van and D. H. Colin, Academic Press, 2009, vol. Volume 61, pp. 1-62.
2. B. Rosenberg, L. Vancamp, J. E. Trosko and V. H. Mansour, *Nature*, 1969, **222**, 385-386.
3. P. M. Takahara, A. C. Rosenzweig, C. A. Frederick and S. J. Lippard, *Nature*, 1995, **377**, 649-652.
4. E. R. Jamieson and S. J. Lippard, *Chem. Rev.*, 1999, **99**, 2467-2498.
5. S. Satyanarayana, J. C. Dabrowiak and J. B. Chaires, *Biochemistry*, 1993, **32**, 2573-2584.
6. Z. Xu, W. Cheng, K. Guo, J. Yu, J. Shen, J. Tang, W. Yang and M. Yin, *ACS Appl. Mater. Interfaces*, 2015, **7**, 9784-9791.
7. M. F. Brana, M. Cacho, A. Gradillas, B. Pascual-Teresa and A. Ramos, *Curr. Pharm. Des.*, 2001, **7**, 1745-1780.
8. R. Martinez and L. Chacon-Garcia, *Curr. Med. Chem.*, 2005, **12**, 127-151.
9. S. Patanè, *Int. J. Cardiol.*, 2014, **176**, 1326-1328.
10. A. G. Quiroga, J. M. Pérez, E. I. Montero, D. X. West, C. Alonso and C. Navarro-Ranninger, *J. Inorg. Biochem.*, 1999, **75**, 293-301.
11. R. Arancibia, C. Quintana, C. Biot, M. E. Medina, S. Carrère-Kremer, L. Kremer and A. H. Klahn, *Inorg. Chem. Commun.*, 2015, **55**, 139-142.
12. E. C. Constable, S. M. Elder, J. Healy, M. D. Ward and D. A. Tocher, *J. Am. Chem. Soc.*, 1990, **112**, 4590-4592.
13. S. Zheng, N. R. M. Reintjens, M. A. Siegler, O. Roubeau, E. Bouwman, A. Rudavskiy, R. W. A. Havenith and S. Bonnet, *Chem. Eur. J.*, 2016, **22**, 331-339.
14. S. L. Hopkins, B. Siewert, S. H. C. Askes, P. Veldhuizen, R. Zwier, M. Heger and S. Bonnet, *Photochem. Photobiol. Sci.*, 2016, **15**, 644-653.
15. G. te Velde, F. M. Bickelhaupt, E. J. Baerends, C. Fonseca Guerra, S. J. A. van Gisbergen, J. G. Snijders and T. Ziegler, *J. Comput. Chem.*, 2001, **22**, 931-967.
16. C. Fonseca Guerra, J. G. Snijders, G. te Velde and E. J. Baerends, *Theor. Chem. Acc.*, 1998, **99**, 391-403.
17. C. A. Puckett and J. K. Barton, *Biochemistry*, 2008, **47**, 11711-11716.
18. M. Dickerson, Y. Sun, B. Howerton and E. C. Glazer, *Inorg. Chem.*, 2014, **53**, 10370-10377.
19. C. A. Puckett and J. K. Barton, *J. Am. Chem. Soc.*, 2007, **129**, 46-47.
20. H. Ahmad, A. Wragg, W. Cullen, C. Wombwell, A. J. H. M. Meijer and J. A. Thomas, *Chem. Eur. J.*, 2014, **20**, 3089-3096.
21. A. Leonidova, V. Pierroz, R. Rubbiani, Y. Lan, A. G. Schmitz, A. Kaeck, R. K. O. Sigel, S. Ferrari and G. Gasser, *Chem. Sci.*, 2014, **5**, 4044-4056.
22. Y. Sun, L. E. Joyce, N. M. Dickson and C. Turro, *Chem. Commun.*, 2010, **46**, 6759-6761.

23. G. Marcon, S. Carotti, M. Coronello, L. Messori, E. Mini, P. Orioli, T. Mazzei, M. A. Cinellu and G. Minghetti, *J. Med. Chem.*, 2002, **45**, 1672-1677.
24. A. Bindoli, M. P. Rigobello, G. Scutari, C. Gabbiani, A. Casini and L. Messori, *Coord. Chem. Rev.*, 2009, **253**, 1692-1707.
25. S. Nobili, E. Mini, I. Landini, C. Gabbiani, A. Casini and L. Messori, *Med. Res. Rev.*, 2010, **30**, 550-580.
26. F. S. Mackay, J. A. Woods, P. Heringová, J. Kašpárková, A. M. Pizarro, S. A. Moggach, S. Parsons, V. Brabec and P. J. Sadler, *Proc. Natl. Acad. Sci. USA*, 2007, **104**, 20743-20748.
27. J. Mayr, P. Heffeter, D. Groza, L. Galvez, G. Koellensperger, A. Roller, B. Alte, M. Haider, W. Berger, C. R. Kowol and B. K. Keppler, *Chem. Sci.*, 2017, **8**, 2241-2250.
28. V. Pichler, J. Mayr, P. Heffeter, O. Domotor, E. A. Enyedy, G. Hermann, D. Groza, G. Kollensperger, M. Galanksi, W. Berger, B. K. Keppler and C. R. Kowol, *Chem. Commun.*, 2013, **49**, 2249-2251.
29. K. Mitra, *Dalton Trans.*, 2016, **45**, 19157-19171.
30. M. A. Medrano, M. Morais, V. F. C. Ferreira, J. D. G. Correia, A. Paulo, I. Santos, C. Navarro-Ranninger, A. A. Valdes, A. Casini, F. Mendes and A. G. Quiroga, *Eur. J. Inorg. Chem.*, 2017, **2017**, 1835-1840.
31. N. Kratochwil, P. Bednarski, H. Mrozek, A. Vogler and J. Nagle, *Anti-cancer Drug Des.*, 1996, **11**, 155-171.
32. P. J. Bednarski, R. Grünert, M. Zielzki, A. Wellner, F. S. Mackay and P. J. Sadler, *Chem. Biol.*, 2006, **13**, 61-67.
33. S. Alonso-de Castro, E. Ruggiero, A. Ruiz-de-Angulo, E. Rezabal, J. C. Mareque-Rivas, X. Lopez, F. Lopez-Gallego and L. Salassa, *Chem. Sci.*, 2017, **8**, 4619-4625.

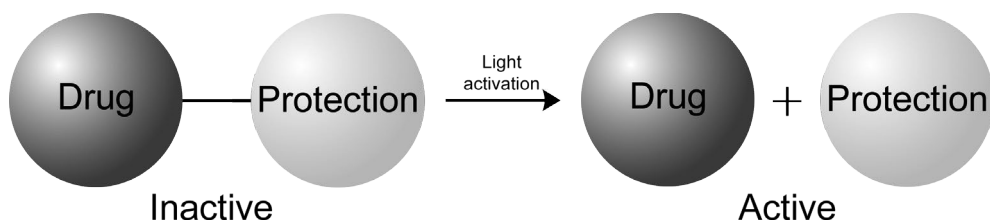
CHAPTER 9

Summary, Discussion, Conclusion, and Outlook

9.1 Summary

9.1.1 Ruthenium polypyridyl complexes as photoactivated chemotherapeutic agents

In this thesis several approaches are described to develop ruthenium polypyridyl complexes for photoactivated chemotherapy (PACT). In PACT a non-toxic drug is activated upon light irradiation to become cytotoxic, enabling local activation of a cytotoxic compound in the body, and hence more control over side effects and dosage (Scheme 9.1). In the case of photoactivated metal-based anticancer complexes this strategy commonly relies on a photosubstitution reaction, during which a ligand is photosubstituted by a solvent molecule. In PACT both the metal product and the released ligand may act as the chemotherapeutic agent. When the metal-based photoproduct bears the toxicity load, photoactivation releases a protecting non-toxic organic ligand, allowing the coordination of other biomolecules to the metal center. When the photoreleased organic ligand bears the toxicity load, coordination of the metal to the toxic ligand inhibits, or 'cages', its biological activity by sterically preventing interaction with the protein target.



Scheme 9.1 Mechanism of PACT: A chemical bond between a drug and a protecting group renders the conjugate inactive, while light activation induces bond breaking and enables the drug to exert its biological activity.

In the research described in this thesis we first set out functionalizing ruthenium polypyridyl complexes of the $[\text{Ru}(\text{tpy})(\text{bpy})(\text{L})]^{2+}$ family (Figure 9.1), where L is a monodentate ligand. First, as described in Chapter 2, thiol ligands L were investigated as potential protecting ligands for the $[\text{Ru}(\text{tpy})(\text{bpy})(\text{OH}_2)]^{2+}$ species, but these proved not to be suitable for that purpose. Once coordinated, the thiolate ligand oxidized easily into sulfenyl and sulfinyl derivatives, rendering the complex thermally unstable. Furthermore, photosubstitution of the thiol ligand proved to be much less effective than that of thioether ligands.¹

In the course of this research *in vitro* cytotoxicity data confirmed that $[\text{Ru}(\text{tpy})(\text{bpy})(\text{OH}_2)]^{2+}$ is essentially non-toxic, despite its ability to interact with DNA.^{2,4} Therefore, this complex was used as a photocaging agent for a cytotoxic microtubule-inhibiting (MTI) anticancer agent developed by the group of Dr. Alexander Kornienko from Texas State University, USA. This inhibitor contains a thioether functional group (SRR') that can be used to coordinate to $[\text{Ru}(\text{tpy})(\text{bpy})(\text{OH}_2)]^{2+}$. The resulting complex, $[\text{Ru}(\text{tpy})(\text{bpy})(\text{MTI-SRR}')](\text{PF}_6)_2$, proved to be 40-60 times less toxic in the dark than the free organic ligand, while green light irradiation of the caged complex recovered the high toxicity of the uncaged ligand. EC_{50} values for cell viability in the low nanomolar range were measured after light activation. Microtubule polymerization assays confirmed that upon photorelease of the ligand microtubule polymerization was inhibited, while in the dark microtubules were polymerizing normally. These results confirm that the photocytotoxicity observed in cells is indeed induced by the photochemical release of a microtubule polymerization inhibitor.

Besides the $[\text{Ru}(\text{tpy})(\text{bpy})(\text{L})]^{2+}$ scaffold, $[\text{Ru}(\text{bpy})_2(\text{LL})]^{2+}$ complexes have also been the subject of intense research for potential use in PACT (Figure 9.1). Substitution of on (sterically demanding) bidentate ligand LL or two monodentate ligands by water molecules to form *cis*- $[\text{Ru}(\text{bpy})_2(\text{OH}_2)_2]^{2+}$ has resulted in many light-activatable complexes with toxic metal complexes and/or toxic ligands as photoproducts. The photoproduct *cis*- $[\text{Ru}(\text{bpy})_2(\text{OH}_2)_2]^{2+}$ also allows for a binding mode to DNA similar to that of cisplatin. By contrast, polypyridyl ruthenium compounds with two labile ligands in mutual *trans* positions have been rarely investigated in anticancer research, although this configuration is commonly used in ruthenium chemistry, for example as water oxidation catalysts (with salen as a tetradentate ligand).⁵ In fact, one of the first ruthenium complexes that was proposed as anticancer compound, KP1019, also contains two indazole ligands in mutual *trans* positions.⁶ However, due to intracellular reduction into ruthenium(II), and to the monodentate character of the ligands bound to ruthenium, its coordination sphere was not very stable.⁷

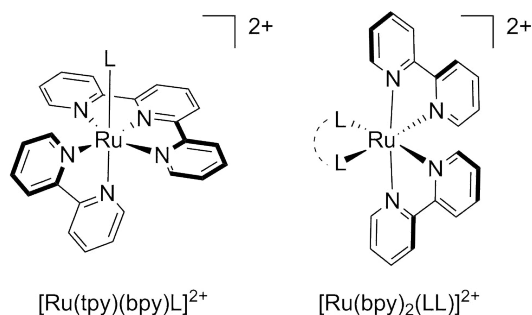


Figure 9.1 Chemical structures of $[Ru(tpy)(bpy)L]^{2+}$ and $[Ru(bpy)_2(LL)]^{2+}$.

In Chapter 4, anticancer complexes are presented based on the H₂biqbpy ligand (Figure 9.2), a tetrapyridyl ligand that coordinates in the basal plane to ruthenium(II). Not only did coordination of H₂biqbpy to ruthenium(II) lead to the cytotoxic and light-activatable complex $[Ru(H_2biqbpy)(dmsO)(Cl)]Cl$, but coordination of two axial monodentate thioether ligands resulted in $[Ru(H_2biqbpy)(HAMet)(Amet)]PF_6$. The $[Ru(H_2biqbpy)(HAMet)(Amet)]PF_6$ protected complex exhibited significant reduced toxicity compared to $[Ru(H_2biqbpy)(dmsO)(Cl)]Cl$. Green light irradiation of various cancer cell lines treated with $[Ru(H_2biqbpy)(dmsO)(Cl)]Cl$ resulted in an up to 20-fold increase of cytotoxicity compared to the dark control. It was further demonstrated that this type of complexes are poor singlet oxygen generators. Photodynamic therapy (PDT), which relies on the generation of singlet oxygen, may fall short in treating certain tumors characterized by low oxygen concentrations. In this scenario, PACT compounds based on the $[Ru(H_2biqbpy)(L)(L')]^{2+}$ structure provide an interesting alternative for PDT, as their mechanism of activation does not rely on the presence of dioxygen. Furthermore, the H₂biqbpy ruthenium complexes induced cell death upon light irradiation by apoptosis, which may be interesting for solving some of the clinical problems of PDT. PDT treatment induces significant side effects due to the mode of cell death on the irradiation site, which is often non-programmed cell death or necrosis. These types of cell death are characterized by a loss in cell membrane integrity and lead to the release of cells contents in the extracellular environment, which usually triggers a painful inflammation reaction. Treatment with ruthenium complexes based on H₂biqbpy induce programmed cell death or apoptosis and may prevent such undesired inflammation reactions and thus lower pain for the patient.

Cellular uptake and cell fractionation assays described in Chapter 4 have demonstrated that 7.5-16 ng Ru/10⁶ cells of these ruthenium complexes were taken up by A549 cancer cells, and that the complex predominantly accumulated in the membrane fraction that includes organelles, lysosomes, and membranes. Significant amounts were also present in the nucleus (1.7-3.2 ng Ru/10⁶ cells), which justified DNA interaction experiments. Gel electrophoresis measurements demonstrated that the interaction between [Ru(H₂biqbpy)(dmsO)Cl]Cl or [Ru(H₂biqbpy)(HAMet)(Amet)]PF₆ and pUC19 plasmid DNA is controlled by light irradiation, which confirmed the protecting role of the sulfur-based ligands. Increasing light dosages corresponded to increasing activation of the compounds, which confirmed that the fully activated complex showed the highest degree of interaction with pUC10 plasmid DNA. However, the adducts between the complexes and the plasmid DNA could not be characterized. Further studies using HRMS and a well-defined single strand oligonucleotide (ODN) confirmed, in collaboration with Prof. Luigi Messori from Florence University, Italy, that it was possible to characterize these adducts by mass spectrometry. As expected the inactivated complex shows negligible interaction with the ODN, while blue light activation resulted in oligonucleotides containing either one or two bound ruthenium complexes, without the sulfur ligand.

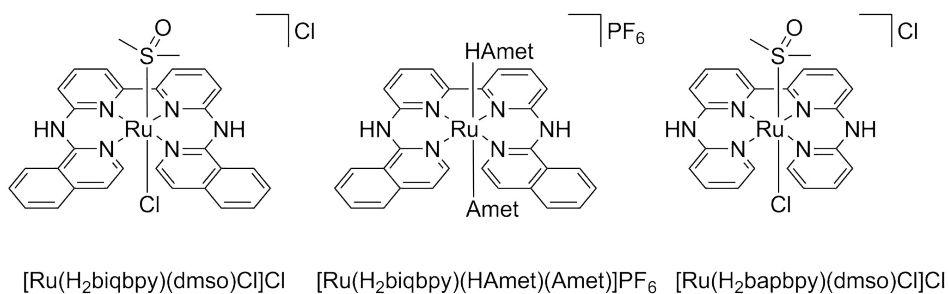


Figure 9.2 Chemical structures of [Ru(H₂biqbpy)(dmsO)Cl]Cl, [Ru(H₂biqbpy)(HAMet)(Amet)]PF₆, and [Ru(H₂bapbpy)(dmsO)Cl]Cl.

Overall, the results described in Chapters 2-5 demonstrate that ruthenium polypyridyl complexes containing sulfur-based monodentate ligands have great potential as photoactivatable compounds for chemotherapy. The photosubstitution of thioether or sulfoxide ligands can be used to control cytotoxicity, the type of cell death, and the interaction of ruthenium complexes with biological molecules.

These features provide an excellent basis for the further development of PACT compounds in the treatment of hypoxic tumors.

9.1.2 Square-planar tetrapyridyl complexes as anticancer compounds

By far most research on anticancer metallodrugs is devoted to platinum compounds largely inspired by the success story of cisplatin. This enthusiasm for platinum has resulted in nine cisplatin analogues that are currently used in the clinics (see Chapter 1). Platinum complexes that are structurally very different from cisplatin, as well as non-platinum transition-metal based complexes, have the disadvantage in terms of clinical development that their mechanism of action must strongly differ from that of cisplatin to allow for treating platinum-resistant tumors. Furthermore, metal-based medicines also have to deal with the often aversive response of the general public toward heavy metals.

Notwithstanding these trends, we investigated the coordination of the ligand H₂bapbpy to palladium(II) and platinum(II), which resulted in the metal complexes [Pd(H₂bapbpy)]²⁺ and [Pt(H₂bapbpy)]²⁺ (Chapter 6) that are structurally similar to the light-activatable ruthenium complex [Ru(H₂bapbpy)(dmsO)Cl]Cl for example, except for the missing axial monodentate ligands. These column 10 complexes showed very interesting and very distinct *in vitro* cytotoxicity patterns. [Pd(H₂bapbpy)](PF₆)₂, tested over a wide panel of cancer cell lines, exhibited exceptional cytotoxic activity, with EC₅₀ values ranging from 200 nM to even 50 nM. The EC₅₀ values of [Pt(H₂bapbpy)](PF₆)₂ were found to be 4-16 times higher, making the platinum complex significantly less active, but still as active as cisplatin. When co-treated with N-Acetyl-L-cysteine (NAC), a reactive oxygen species (ROS) scavenger, the activity of the palladium complex was quenched, whereas for the platinum complex this effect was much smaller. When co-treated with ROS sensitizer L-buthionine sulfoximine (BSO) the palladium complex showed spectacularly enhanced cytotoxicity, whereas this effect was much less pronounced for its platinum analogue. The platinum complex on the other hand, showed more enhancement on p53-gene deficient cancer cells than the palladium compound. Spectacularly high uptake was observed for both complexes, but [Pd(H₂bapbpy)]²⁺ mostly accumulated in the membranes, whereas [Pt(H₂bapbpy)]²⁺ was more evenly distributed among cytosol, membranes, nucleus, and cytoskeleton. *In vivo* equimolar dosages of [Pd(H₂bapbpy)](PF₆)₂ or [Pt(H₂bapbpy)](PF₆)₂ in CT-26 colon cancer Balb/c mice (in collaboration with Prof.

Walter Berger from the Medical University of Vienna, Austria) resulted in significant tumor reduction for the palladium complex, while for the platinum complex no such effect was observed. Overall, *in vitro* cytotoxicity, NAC, BSO, p53, uptake experiments, and *in vivo* experiments, all suggest that the structurally similar complexes act via different mechanisms of action.

The excellent coordination properties of the tetradentate H₂bapbpy ligand enforces a tetradentate coordination mode to square-planar metal centers such as Pd²⁺ or Pt²⁺. Thus neither the palladium nor the platinum complex are expected to operate in cancer cells via ligand substitution reactions. This stability of the coordination sphere was observed when for instance an aqueous solution of [M(H₂bapbpy)]Cl₂ (0.10 mM, M = Pd or Pt) containing 100 eq. of NaCl was heated to 80 °C: no significant spectroscopic changes could be attributed to ligand substitution (Figure 9.3). Thus, *in vitro*, *in vivo*, and in physiological conditions, these complexes are expected to be stable, without the occurrence of any ligand exchange.

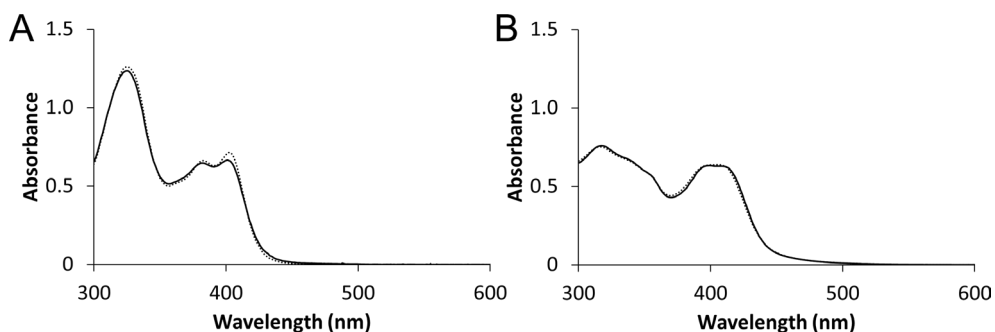


Figure 9.3 UV-vis absorbance spectra of [Pd(H₂bapbpy)]Cl₂ (A) and [Pt(H₂bapbpy)]Cl₂ (B) in a NaCl (aq, 10 mM) solution at 20 (continuous) and 80 °C (dotted). [Pd] = [Pt] = 0.10 mM.

In vitro studies were also performed with platinum and palladium complexes containing a tetrapyrrolyl ligand with one amine bridge (Hbbp_ya) instead of the two amine bridges in H₂bapbpy: cytotoxicity was comparable to that of cisplatin, but nowhere near the cytotoxicity of [Pd(H₂bapbpy)](PF₆)₂ (Chapter 8). Coordination of Hbbp_ya to a palladium(II) center resulted in a less distorted square-planar geometry than its H₂bapbpy analogue (Figure 9.4). For square-planar Hbbp_ya complexes the presence of a single amine bridge limits the number

of charged states of the molecule: either dicationic ($[M(\text{Hbbpya})]^{2+}$) or monocationic ($[M(\text{bbpya})]^+$) upon deprotonation of the amine. For H_2bapbpy metal complexes a third, neutral state can also be obtained. The pK_a of the first deprotonation is at 5.5 and 4.6 for $[\text{Pd}(\text{Hbbpya})]^{2+}$ and $[\text{Pt}(\text{Hbbpya})]^{2+}$, respectively, whereas for $[\text{Pd}(\text{H}_2\text{bapbpy})]^{2+}$ and $[\text{Pt}(\text{H}_2\text{bapbpy})]^{2+}$ this pK_a is much higher (7.8 and 8.3, respectively) and close to physiological conditions (Chapter 7). Thus, under physiological conditions the Hbbpya complexes are expected to be in the deprotonated, monocationic forms, whereas the H_2bapbpy complexes are mixtures of the dicationic and monocationic forms.

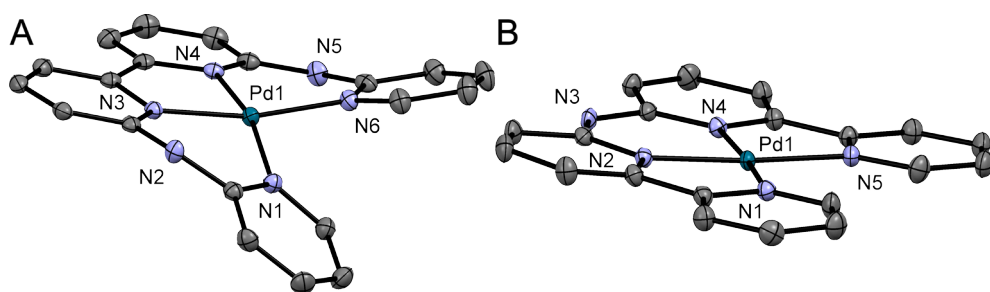


Figure 9.4 Displacement ellipsoid of $[\text{Pd}(\text{H}_2\text{bapbpy})]^{2+}$ (A) and $[\text{Pd}(\text{Hbbpya})]^{2+}$ (B) (50% probability level) as observed in the crystal structure of respectively $[\text{Pd}(\text{H}_2\text{bapbpy})](\text{PF}_6)_2$ and $[\text{Pd}(\text{Hbbpya})]\text{Cl}_2$. H atoms, counter anions, and lattice solvent molecules have been omitted for clarity.

9.2 Discussion

9.2.1 *Trans* influence and of sulfur-based monodentate ligands in $[\text{Ru}(\text{tpy})(\text{bpy})(\text{L})]^{n+}$

The *trans* effect and *trans* influence has been extensively discussed for square-planar complexes such as cisplatin,⁸ but less for octahedral geometries. First, it is important to distinguish between the *trans* influence and the *trans* effect. The *trans* influence of a given ligand is defined as the weakening of the coordination bond of a second ligand positioned in *trans* position compared to this ligand in the ground state of the metal complex. This thermodynamic effect results in longer bond lengths for ligands that are coordinated *trans* to ligands having a stronger *trans* influence.⁹ The *trans* effect of a ligand is defined as the effect of this ligand on the relative stability of the transition state for the substitution of the ligand positioned in *trans* position. This kinetic effect can change ligand substitution rates by several

orders of magnitude, depending on the strength of the *trans* effect. σ -Donating and π -accepting properties of ligands play a crucial role in both phenomena. A σ -donating ligand will bind more strongly to the metal center and can stabilize the transition state of the metal complex during substitution. On the other hand, a π -accepting ligand can accept electron density from the metal center also stabilizing the transition state.

In the $[\text{Ru}(\text{tpy})(\text{bpy})(\text{L})]^{n+}$ scaffold the monodentate ligand L is positioned *trans* to one of the coordinating N-atoms of the bidentate bpy ligand (Figure 9.1). In Table 9.1, the Ru-N bond distances and the Ru-L distances are listed in which L can have different σ -donating as well as π -accepting properties. As the ligand L in these examples is expected to have little steric effects and all complexes have the same structure $[\text{Ru}(\text{tpy})(\text{bpy})(\text{L})]^{n+}$, Table 9.1 fairly describes the *trans* influence of ligand L on the Ru-N bond distances. In $[\text{Ru}(\text{tpy})(\text{bpy})(\text{OH}_2)]^{2+}$, the Ru-N length is 2.017 Å, which is the shortest of the selected compounds, thus the aqua ligand has the lowest *trans* influence. This can be explained by the poor σ -donating properties of the aqua ligand. The longest Ru-N bond distance, thus with the highest *trans* influence of the L ligand, is observed in $[\text{Ru}(\text{tpy})(\text{bpy})(\kappa\text{S-dmso})]^{2+}$ (2.085 Å), which can be explained by the stronger π -accepting properties of the dmso ligand. The Ru-N bond in $[\text{Ru}(\text{tpy})(\text{bpy})(\text{Hmte})]^{2+}$ with 2.064 Å falls between the pyridine and sulfoxide complexes, and confirms properties of a thioether as a (poorly) σ -donating and (poorly) π -accepting ligand.¹⁰ No entries in the Cambridge Structural Database of $[\text{Ru}(\text{tpy})(\text{bpy})(\text{L})]^{n+}$ with a amine or thiol were found, which would have been relevant in the physiological context.

Table 9.1 Selected bond lengths (Å) in complexes of the $[\text{Ru}(\text{tpy})(\text{bpy})(\text{L})]^{n+}$ scaffold.

Compound	Ru-N	Ru-L
$[\text{Ru}(\text{tpy})(\text{bpy})(\text{OH}_2)](\text{BF}_4)_2$	2.017	L = O = 2.143
$[\text{Ru}(\text{tpy})(\text{bpy})\text{Cl}]\text{Cl}^{11}$	2.031	L = Cl = 2.397
$[\text{Ru}(\text{tpy})(\text{bpy})(\text{py})]\text{Cl}_2^{12}$	2.047	L = N = 2.100
$[\text{Ru}(\text{tpy})(\text{bpy})(\kappa\text{S-Hmte})](\text{PF}_6)_2^{13}$	2.064	L = S = 2.369
$[\text{Ru}(\text{tpy})(\text{bpy})(\kappa\text{S-dmso})](\text{PF}_6)_2^{14}$	2.085	L = S = 2.282

9.2.2 *Trans* influence in [Ru(N'NNN')(L)(L')]²⁺ scaffold

The tetrapyridyl ligands H₂bapbpy or H₂biqbpy that coordinate in the basal plane in octahedral ruthenium(II) compounds, force the ruthenium complex to assume a configuration with *trans* axial monodentate ligands. As the *trans* effect and influence have mainly been described for square-planar complexes, and ruthenium complexes are most commonly synthesized with *cis* configurations, the structural and kinetic *trans* effects for *trans* ruthenium complexes have hardly been analyzed. In Table 9.2 the bond distances of the *trans* axial monodentate ligands of selected metal complexes are listed.

On the one hand, compared to the [Ru(tpy)(bpy)(L)]ⁿ⁺ scaffold the [Ru(H₂bapbpy)(L)₂]ⁿ⁺ scaffold has more variations of the *trans* influence due to the presence of two potentially different *trans* ligands. On the other hand, both types of structures allow for comparing the stability and lability of sulfur-based ligands L, depending on the nature of the *trans* ligand. For example, the *trans* influence of thioether vs. pyridine ligands are similar: the Ru-S bond distances in [Ru(H₂bapbpy)(Hmte)₂]²⁺ and [Ru(H₂bapbpy)(HAMet)₂]²⁺ (Figure SIX.1) are all about 2.38 Å, close to the 2.369 Å of [Ru(tpy)(bpy)(Hmte)]²⁺, where the ligand *trans* to the thioether ligand is pyridine. However, a significant *trans* effect was observed for bis-thioether complexes that was absent in mono-thioether complexes. In [Ru(tpy)(bpy)(SRR')]²⁺, where the *trans* ligand is pyridine, the Ru-S bond is thermally very stable in demineralized water¹ or in chloride containing media²; no ligand substitution of the thioether is observed after 3 days. The [Ru(H₂bapbpy)(Hmte)₂]²⁺ complex is only stable in demineralized water, but in presence of chloride containing media one thioether is substituted over longer periods of time. It would thus be interesting to study the reactivity of asymmetric [Ru(H₂bapbpy)(SRR')(py)]²⁺ complexes, and to study whether the Ru-S bond is thermally more stable than in [Ru(H₂bapbpy)(Hmte)₂]²⁺ or [Ru(H₂bapbpy)(HAMet)₂]²⁺ complexes.

Table 9.2 Selected bond lengths (Å) for various complexes containing two monodentate axial ligands.

Compound	Ru-S	Ru-L
[Ru(H ₂ bapbpy)(κS-dmso)Cl]Cl	2.227	L = Cl = 2.451
[Ru(H ₂ bapbpy)(κS-Hmte) ₂](PF ₆) ₂	2.382	L = S = 2.382
[Ru(H ₂ bapbpy)(κS-HAmet) ₂](PF ₆) ₂	2.377	L = S = 2.377
<i>cis</i> -[Ru(κS-dmso) ₃ (κO-dmso)Cl ₂] ¹⁰	2.245	L = O = 2.136
	2.274	L = Cl = 2.421
	2.264	L = Cl = 2.243
<i>trans</i> -[Ru(κS-dmso) ₄ Cl ₂] ¹⁰	2.352	L = Cl = 2.402

Sulfur-bound sulfoxides show a qualitatively similar but quantitatively stronger effect due to the stronger π -accepting properties of dmso compared to thioethers: κ S-dmso induces a strong *trans* influence. In [Ru(tpy)(bpy)Cl]⁺ the Ru-Cl bond is significantly shorter (2.397 Å) than in [Ru(H₂bapbpy)(dmso)Cl]⁺ (2.451 Å), and in [Ru(H₂bapbpy)(κS-dmso)Cl]Cl the Ru-S bond is also shorter (2.227 Å) than that in *trans*-[Ru(κS-dmso)₄Cl₂] (2.352 Å). The better σ -donating and π -donating properties of the chloride ligand result in more electron density at the metal center for the π -accepting dmso. In addition, κ S-dmso also has a strong *trans* effect and increases the lability of the *trans* ligand. For example, it was impossible to obtain a H₂bapbpy ruthenium complex with two *trans* dmso ligands. In fact, the synthesis of [Ru(H₂biqbpy)(dmso)₂]Cl₂ was attempted but was not successful. ¹H NMR analysis showed that once DMSO-d₆ was added to a solution of [Ru(H₂biqbpy)(dmso)(OD₂)]Cl₂ a singlet peak at 2.71 ppm corresponding to free dmso (●) appeared next to the multiplet at 2.67 ppm corresponding to residual dmso-d₅ (◆, Figure 9.5). The integral of the peak of the coordinated dmso (■) at 2.44 ppm decreased from 6 to 4 protons, whereas the new singlet integrated for 2 protons. Overall, these changes are clear signatures that the initially coordinated dmso ligand is removed. Furthermore, the unchanged aromatic spectrum upon dmso-d₆ addition indicates that only coordination of a chemically identical ligand occurred. Thus, the coordinated dmso was replaced by DMSO-d₆ and under these conditions [Ru(H₂biqbpy)(dmso)₂]Cl₂ is unstable because competition for the metal π electrons between two π -accepting dmso ligands does not allow for simultaneous *trans* coordination of two κ S-dmso ligands. Overall, both thioether

and sulfoxide ligands are suitable monodentate ligands for protecting anticancer complexes based on ruthenium(II) provided the *trans* ligand is not itself another thioether or sulfoxide ligands.

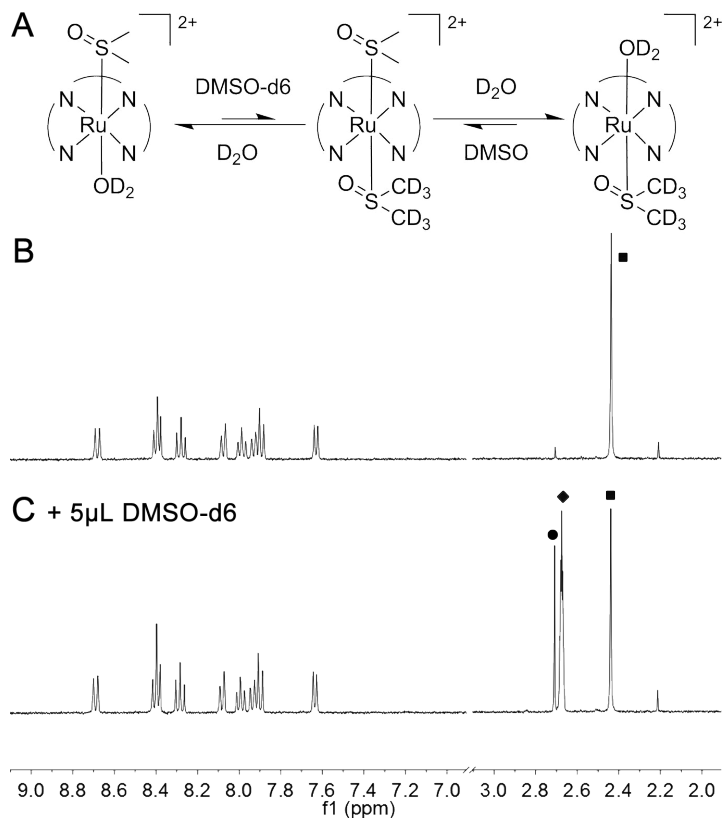


Figure 9.5 Reaction between $[\text{Ru}(\text{H}_2\text{biqbpy})(\text{dmsO})(\text{OD}_2)]\text{Cl}_2$ and DMSO-d_6 (A). ^1H NMR spectra (9.0-7.0, and 3.0-2.0 ppm) of $[\text{Ru}(\text{H}_2\text{biqbpy})(\text{dmsO})(\text{OD}_2)]\text{Cl}_2$ (0.15 mM) in D_2O (B) and upon addition of 5 μL DMSO-d_6 (C). T = 293 K, Solvent: D_2O . Notations: ■ = coordinated dmsO, ● = free dmsO; ◆ = residual dmsO-d5.

9.2.3 Minor changes, major effects

The research described in this thesis reveal that minor changes in a chemical structure, such as having one or two non-coordinating amine bridge(s) in the ligand, or substituting one metal center by another, may induce major changes in the biological effects of metal-based drugs. First, changing the tetrapyridyl ligand from H_2biqbpy to H_2bapbpy in $[\text{Ru}(\text{N}'\text{NNN}')(\text{dmsO})\text{Cl}]\text{Cl}$ resulted in similar photoreactivity with oligonucleotides, but a major decrease in dark cytotoxicity. The two additional phenyl rings in H_2biqbpy is a significant difference that causes

the ruthenium complex to have a higher lipophilic and intercalating character. Second, when the ruthenium(II) center was replaced for nickel(II), the octahedral geometry was preserved, but the complex lost its absorption in the visible domain, and it did not exhibit significant dark cytotoxicity. Third, when the ruthenium center was replaced by a palladium(II) or platinum(II) center, the geometry of the metal complex changed from octahedral to square-planar, and the complexes became very (Pt^{2+}) to extremely (Pd^{2+}) cytotoxic. Finally, variation in the tetrapyridyl ligand from two amine bridges to one resulted in palladium(II) and platinum(II) complexes in which especially the cytotoxicity of the palladium(II) was reduced (Chapter 8).

The remarkable differences in cytotoxicity between the H_2bapby and $Hbbpya$ palladium complexes can partially be explained by differences in cellular uptake. Without exception, the synthesized square-planar complexes are taken up very well (8-58%, Chapter 6 and 8), whereas for the octahedral complexes uptake efficiency was inferior to 0.3 % for $[Ni(H_2bapby)(OH)_2]Cl_2$ (Chapter 6) and even lower for the ruthenium(II) H_2biqby complexes (Chapter 4). In comparison, the positive control cisplatin also showed similarly low uptake efficiency (< 0.1%), thus differences in cellular uptake cannot be attributed to coordination geometry alone. Although uptake assays were different across Chapter 4, 6, and 8, and notably as different cell numbers, metal complex concentrations, and relative volumes of the medium compared to the seeding area, were used, one interesting observation could be drawn: the square-planar tetrapyridyl complexes exhibit a (far) higher general cytotoxicity, but once inside the cell, octahedral (ruthenium) complexes (and cisplatin) were found much more efficient in cell killing, as they killed 50% of the cells at much lower intracellular concentrations (Table 9.3). A proposed explanation for the differences in cellular uptake is the possibility that deprotonation of the amine bridges can modulate the overall charge of the complex, and its ability to pass through the cellular membrane. In Chapter 7 and 8, it is shown that this deprotonation is notably relevant for the square-planar palladium and platinum complexes.

Table 9.3 A549 cellular uptake for [Ru(H₂biqbpv)(dmsO)Cl]Cl, [Pd(H₂bapbpy)](PF₆)₂, [Pt(H₂bapbpy)](PF₆)₂, and cisplatin with treatment concentrations is close to the corresponding EC₅₀ values.

Compound	Treatment Concentration (μM)	t _{inc} (h)	Metal uptake (pmol/10 ⁶ cells)
[Ru(H ₂ biqbpv)(dmsO)Cl]Cl	9.3	6	11
[Pd(H ₂ bapbpy)](PF ₆) ₂	0.2	24	132
[Pt(H ₂ bapbpy)](PF ₆) ₂	1.0	24	1586
cisplatin	3.3	24	23

9.3 Conclusion and Outlook

The success of cisplatin and all its clinically used derivatives have set the working standards in the field of anticancer metallodrugs. New metal-based anticancer drugs should either perform well against cancers with cisplatin-resistance, or have no side effects without loss of anticancer activity compared to cisplatin. In the first part of this thesis, a strategy has been presented that relies on light activation to increase selectivity; in the dark compounds are non-toxic and upon irradiation a ligand photosubstitution reaction takes place. Although [Ru(tpy)(bpy)(OH₂)]²⁺ turned out to be a poorly cytotoxic agent, it appeared to be an excellent photocaging agent for a thioether-bearing anticancer microtubule inhibitor. Tetrapyrrolyl ruthenium complexes with *trans* axial monodentate ligands have proven to be cytotoxic and phototoxic. Recurring themes in photopharmacology are the question of the activation wavelength – red light penetrates human tissue deeper than blue light – and the difference in light activation strategies, which are based either on bond-breaking photoreactions or photochemical generation of reactive oxygen species. Lead compounds [Ru(tpy)(bpy)(MTI-SRR')](PF₆)₂ and [Ru(H₂biqbpv)(dmsO)Cl]Cl are activatable by irradiating green light (520 nm), which offers decisive advantages over systems that require UV or blue light to be activated. Currently, experiments are performed to assess whether the phototoxicity can be translated to *in vivo* cancer models.

Another consequence of the cisplatin doctrine is the widespread vision that anticancer metallodrugs should target DNA by means of coordination bonds. New directions where metal complexes target proteins, mitochondria, or non-DNA targets, are currently explored, although they still remain limited.¹⁵⁻²⁰ A common

approach in inorganic chemistry research is to develop compounds that form coordination bonds with biomolecules. When cytotoxic responses are found *in vitro* against chemotherapy-resistant cancer cells in the low micromolar range, chemical biology approaches, ICP-MS, or imaging techniques, can be employed for target determination. However, such approaches possibly lead to targets that are not necessarily relevant for cancer therapy, contrary to medicinal organic chemistry in which drug design starts with selecting a target relevant for cancer therapy.²¹⁻²⁵ On the other hand, in the second part of this thesis palladium(II) and platinum(II) complexes were presented with extraordinary cytotoxic properties that come from purely inorganic chemistry design principles. These complexes are a perfect example of drug design without pre-conceived biological targeting, but also deviate from the cisplatin doctrine as no ligand substitution reactions are expected to occur due to the tetradentate nature of the ligand and the square-planar metal centers. Perhaps as a consequence, a strong cytotoxic activity *in vitro* observed against several platinum-resistant cancer cell lines was discovered, which is both lucky and a problem for the clinical development of such compounds, as finding a biological target is often a tedious and time-consuming effort. At that stage, a structure-activity relationship will be required, as well as extensive biological studies to unravel possible mechanisms of action. In the end, drug discovery also comes down to a little bit of luck...

9.4 References

1. R. E. Goldbach, I. Rodriguez-Garcia, J. H. van Lenthe, M. A. Siegler and S. Bonnet, *Chem. Eur. J.*, 2011, **17**, 9924-9929.
2. B. Siewert, V. H. S. van Rixel, E. J. van Rooden, S. L. Hopkins, M. J. B. Moester, F. Ariese, M. A. Siegler and S. Bonnet, *Chem. Eur. J.*, 2016, **22**, 10960-10968.
3. O. Novakova, J. Kasparkova, O. Vrana, P. M. van Vliet, J. Reedijk and V. Brabec, *Biochemistry*, 1995, **34**, 12369-12378.
4. J. Rodríguez, J. Mosquera, J. R. Couceiro, M. E. Vázquez and J. L. Mascareñas, *Angew. Chem., Int. Ed.*, 2016, **55**, 15615-15618.
5. K. Nakanishi, T. Koshiyama, S. Iba and M. Ohba, *Dalton Trans.*, 2015, **44**, 14200-14203.
6. B. K. Keppler, M. Henn, U. M. Juhl, M. R. Berger, R. Niebl and F. E. Wagner, in *Ruthenium and Other Non-Platinum Metal Complexes in Cancer Chemotherapy*, eds. E. Baulieu, D. T. Forman, M. Ingelman-Sundberg, L. Jaenicke, J. A. Kellen, Y. Nagai, G. F. Springer, L. Träger, L. Will-Shahab and J. L. Wittliff, Springer Berlin Heidelberg, Berlin, Heidelberg, 1989, pp. 41-69.
7. M. A. Jakupec, E. Reisner, A. Eichinger, M. Pongratz, V. B. Arion, M. Galanski, C. G. Hartinger and B. K. Keppler, *J. Med. Chem.*, 2005, **48**, 2831-2837.
8. B. J. Coe and S. J. Glenwright, *Coord. Chem. Rev.*, 2000, **203**, 5-80.
9. J. Ribas Gispert, *Coordination Chemistry*, Wiley-VCH, Weinheim, 2008.
10. E. Alessio, G. Mestroni, G. Nardin, W. M. Attia, M. Calligaris, G. Sava and S. Zorzet, *Inorg. Chem.*, 1988, **27**, 4099-4106.
11. A. Taketoshi, T. Koizumi and T. Kanbara, *Tetrahedron Lett.*, 2010, **51**, 6457-6459.
12. C. R. Hecker, P. E. Fanwick and D. R. McMillin, *Inorg. Chem.*, 1991, **30**, 659-666.
13. A. Bahreman, B. Limburg, M. A. Siegler, E. Bouwman and S. Bonnet, *Inorg. Chem.*, 2013, **52** 9456-9469.
14. J. J. Rack, J. R. Winkler and H. B. Gray, *J. Am. Chem. Soc.*, 2001, **123**, 2432-2433.
15. A. Casini and J. Reedijk, *Chem. Sci.*, 2012, **3**, 3135-3144.
16. A. Casini, C. Gabbiani, F. Sorrentino, M. P. Rigobello, A. Bindoli, T. J. Geldbach, A. Marrone, N. Re, C. G. Hartinger, P. J. Dyson and L. Messori, *J. Med. Chem.*, 2008, **51**, 6773-6781.
17. A. Bindoli, M. P. Rigobello, G. Scutari, C. Gabbiani, A. Casini and L. Messori, *Coord. Chem. Rev.*, 2009, **253**, 1692-1707.
18. J. D. White, M. F. Osborn, A. D. Moghaddam, L. E. Guzman, M. M. Haley and V. J. DeRose, *J. Am. Chem. Soc.*, 2013, **135**, 11680-11683.
19. J. D. White, M. M. Haley and V. J. DeRose, *Acc. Chem. Res.*, 2016, **49**, 56-66.
20. L. N. Lameijer, S. L. Hopkins, T. G. Brevé, S. H. C. Askes and S. Bonnet, *Chem. Eur. J.*, 2016, **22**, 18484-18491.
21. H. Han and L. H. Hurley, *Trends Pharmacol. Sci.*, 2000, **21**, 136-142.
22. D. Morgensztern and H. L. McLeod, *Anti Canc. Drugs*, 2005, **16**, 797-803.
23. A. Belfiore, *Curr. Pharm. Des.*, 2007, **13**, 671-686.
24. G. Alvisi, I. K. H. Poon and D. A. Jans, *Drug Resist. Update*, 2006, **9**, 40-50.
25. C.-F. Cheng, J. Fan, Z. Zhao, D. T. Woodley and W. Li, *Curr. Signal Transduction Ther.*, 2010, **5**, 121-127.

APPENDIX I: GENERAL BIOCHEMICAL METHODS

Cell Culturing

Cells were thawed and at least passaged twice before starting (photo)cytotoxicity experiments. Each cell line was cultured in Dulbecco's Modified Eagle Medium with phenol red, supplemented with 8.0% v/v fetal calf serum (FCS), 0.2% v/v penicillin/streptomycin (P/S), and 0.9% v/v Glutamine-S (GM). Cells were cultured in either 25 cm² or 75 cm² flasks and split at 70-80% confluence (three times per week for 25 cm² flasks, once per week for 75 cm² flasks). The flasks were incubated at 37 °C at 7.0% CO₂. The medium was refreshed three times a week. Cells used in all biological experiments were cultured for a maximum of eight weeks.

Cell irradiation setup

The cell irradiation system consists of a Ditabis thermostat (980923001) fitted with two flat-bottom microplate thermoblocks (800010600) and a 96-LED array fitted to a standard 96-well plate. The 520 nm LED (OVL-3324), fans (40 mm, 24 V DC, 9714839), and power supply (EA-PS 2042-06B) were ordered from Farnell. Full description of the cell irradiation setup is given in Hopkins et al.¹ Human cancer cell lines (A375, human malignant melanoma; A431, human epidermoid carcinoma; A549, human lung carcinoma; MCF-7, human mammary gland adenocarcinoma; MDA-MB-231, human mammary gland adenocarcinoma, MRC-5, fetal lung fibroblasts) were distributed by the European Collection of Cell Cultures (ECACC), and purchased through Sigma Aldrich. Dulbecco's Minimal Essential Medium (DMEM, with and without phenol red, without glutamine), 200 mM GM, trichloroacetic acid (TCA), glacial acetic acid, sulforhodamine B (SRB), tris(hydroxymethyl)aminomethane (tris base), 4,5,6,7-tetrachloro-2',4',5',7'-tetraiodofluorescein disodium salt (rose bengal), and *cis*-diamineplatinum(II) dichloride (cisplatin), were purchased from Sigma Aldrich. (2*R*,3*R*,4*R*,5*R*)-hexan-1,2,3,4,5,6-hexol (D-mannitol) was purchased from Santa Cruz Biotechnology via Bio-Connect. FCS was purchased from Hyclone. Penicillin and streptomycin were purchased from Duchefa and were diluted to a 100 mg/mL solution. Trypsin and Opti-MEM® (without phenol red) were purchased from Gibco® Life Technologies. Trypan blue (0.4% in 0.81% sodium chloride and 0.06% potassium phosphate

dibasic solution) was purchased from BioRad. Plastic disposable flasks and 96-well plates were from Sarstedt. Cells were counted using a BioRad TC10 automated cell counter with BioRad Cell Counting Slides. UV-vis measurements for analysis of 96-well plates were performed on a M1000 Tecan Reader. Cells were inspected with an Olympus IX81 microscope. Cells were stained for fluorescence-assisted-cell-sorting (FACS) using Annexin V-FITC purchased from Bioconnect and propidium iodide purchased from Sigma Aldrich and analyzed by a Cell Lab Quanta SC flow cytometer from Beckman Coulter.

Optimized assay for the determination of (photo)cytotoxicity

The (photo)cytotoxicity of cancer cell lines (A375, A431, A549, MCF-7, MDA-MB231) or one non-cancerous lung cell line (MRC-5) was assessed using an assay adapted from Hopkins et al.¹ Cell cultures with a maximum confluence of 70-80% were trypsinized and centrifuged (1.5 min, 1.2 relative centrifugal force), trypsin and DMEM complete were removed, and the cells were re-suspended using Opti-MEM supplemented with 2.4% v/v FCS, 0.2% v/v P/S, and 1.0% v/v GM, (hereafter called Opti-MEM complete). 10 μ L of cell suspension and 10 μ L of trypan blue were mixed and pipetted into a cell counting slide, and cells were counted. The cell suspension was diluted to the appropriate seeding density (A375, 5×10^3 ; A431, 8×10^3 ; A549, 5×10^3 ; MCF-7, 8×10^3 ; MDA-MB231, 12×10^3 ; MRC-5, 6×10^3 cells/well) and seeded in the wells of a 96-well plate. Cisplatin positive control solution was prepared from a stock solution based on clinical formulation (3.3 mM cisplatin, 55 mM mannitol, 154 mM NaCl).² In case of poor water solubility, sterilized dimethylsulfoxide (DMSO) was used to dissolve the complexes in such amounts that the maximum v/v% of DMSO per well did not exceed 0.5% v/v.

A complete (photo)cytotoxicity experiment lasted 96 h: cells were seeded at $t = 0$ h, treated at $t = 24$ h, irradiated at $t = 30$ h, or irradiated and $t = 48$ h, the medium was refreshed at $t = 48$ h, and fixed at $t = 96$ h. For every irradiated plate a parallel control plate was prepared and treated identically to the irradiated plate, but without irradiation. To prevent border effects, cells were only seeded in the inner 60 wells as shown in Figure SI.1 (unseeded wells indicated by blue). Border wells B12-F12 (Figure S18, grey, pink) were seeded with cells for qualitative positive controls such as cisplatin or Rose Bengal. In the remaining outer wells 200 μ L of Opti-MEM complete was pipetted.

The cells were incubated in the dark for 24 h at 37 °C at 7.0% CO₂. At t = 24 h the cells were treated with freshly prepared solutions of the compounds and dissolved in Opti-MEM complete. Different concentrations were prepared and of each concentration 100 µL was added to three wells (B3:G11, Figure SI.1, red). In case of the cytotoxicity assay, the medium was refreshed at t = 24 h. In case of the photocytotoxicity assay, at t = 30 h or t = 48 h the 96-well plates were taken out of the incubator and were irradiated using the 96-well LED 520 nm array system. During irradiation the temperature of the wells was controlled at 35-37 °C by the thermoblock preheated to 39 °C coupled to LED cooling with a fan.¹ After refreshing or irradiation, all 96-well plates were placed back into a standard (dark) incubator for the remainder of the experiment, until the cells were fixated by addition of 100 µL TCA (10% w/v).

The plates were stored at 4 °C for at least 4 h as part of the SRB assay that was adapted from Vichai et al.³ In short, after fixation the TCA medium mixture was removed, rinsed with demineralized water three times, and air dried. Then, each well was stained with 100 µL SRB solution (0.6% w/v SRB in 1% v/v acetic acid) for 30 min, the SRB solution was removed, and washed with acetic acid (1% v/v) until no SRB came off, normally requiring 3-5 times. Once air dry, 200 µL of tris base (tromethamine, 10 mM) was pipetted to each well. To determine the cell viability the absorbance at 510 nm was measured using a M1000 Tecan Reader. To make sure all the SRB was dissolved, this measurement was performed at least 30 minutes after addition of tris base. The SRB absorbance data per compound per concentration was averaged over three identical wells (technical replicates, n_t = 3) in Excel and made suitable for use in GraphPad Prism. Relative cell populations were derived from the average of the untreated controls (n_c = 6). In any case, it was checked that the cell viability of the control cells of the samples irradiated without compound were similar (maximum difference of 10%) to the unirradiated samples without ruthenium compound to make sure no harm was done by the light. The data from three independent biological replications was used to obtain the dose-response curves and EC₅₀ values using non-linear regression of hills-slope equation with a fixed Y maximum (100%) and minimum (0%) relative cell population values.¹

96-well plate layout used in (photo)cytotoxicity assay

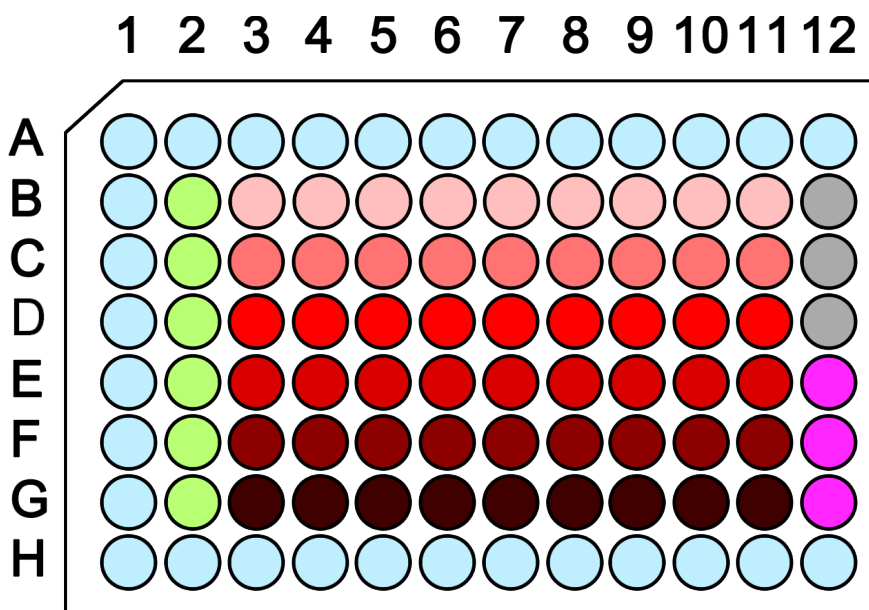


Figure SI.1 Layout of a 96-well plate used in the photocytotoxicity assay. All the wells are seeded with cells apart from the outer 36 blue wells that are filled with 200 μL Opti-MEM complete. The wells in green (B2:G2) are the untreated control cells, the wells colored by a different intensity of red (B3:B11), are cells treated with various concentration of the compound. The grey wells (B12:D12) are wells treated with the positive dark control cisplatin (3.3 μM). The pink wells (E12:G12) are wells treated with the positive light control Rose Bengal (5.0 μM).

References

1. S. L. Hopkins, B. Siewert, S. H. C. Askes, P. Veldhuizen, R. Zwier, M. Heger and S. Bonnet, *Photochem. Photobiol. Sci.*, 2016, **15**, 644-653.
2. M. D. Hall, K. A. Telma, K.-E. Chang, T. D. Lee, J. P. Madigan, J. R. Lloyd, I. S. Goldlust, J. D. Hoeschele and M. M. Gottesman, *Cancer Res.*, 2014, **74**, 3913-3922.
3. V. Vichai and K. Kirtikara, *Nat. Protoc.*, 2006, **1**, 1112-1116.

APPENDIX II: SUPPORTING INFORMATION FOR CHAPTER 2

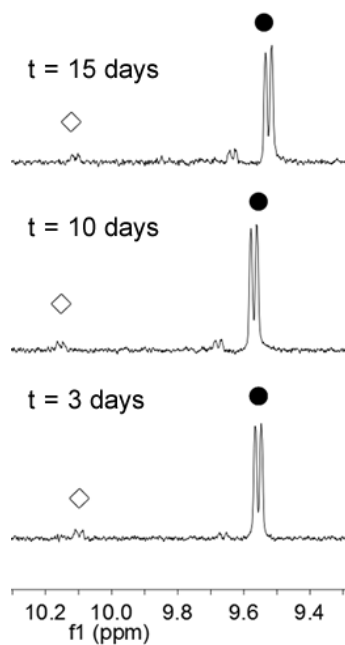


Figure SII.1 Evolution of the ¹H NMR spectra (region 10.3-9.3 ppm) of the reaction between [1]²⁺ and H₂Cys at 298 K in phosphate buffer (pD = 7.8). The peaks around 10.00 (◊) and 9.54 (●) correspond to the A6 proton for complex [2]⁺ and [1]²⁺, respectively. Conditions: [Ru]₀ = 7.7 mM, [H₂Cys] = 7.7 mM.

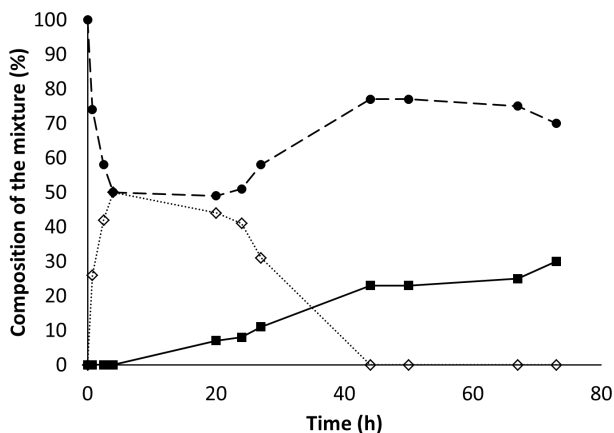


Figure SII.2 Composition of the reaction mixture during the reaction of $[\text{Ru}(\text{tpy})(\text{bpy})(\text{OH}_2)]^{2+}$ ($[1]^{2+}$) and H_2Acys at 353 K under an argon atmosphere. Relative integration of ^1H NMR peaks at 10.12, 10.00, and 9.54 ppm for the unknown side product (\blacksquare), $[3]^+$ (\diamond), and $[1]^{2+}$ (\bullet), respectively. The ^1H NMR peaks in this region correspond to the A6 proton for each complex. Conditions: phosphate buffer pD = 7.8, $[\text{Ru}]_0 = 5.0$ mM, $[\text{H}_2\text{Acys}] = 5.0$ mM.

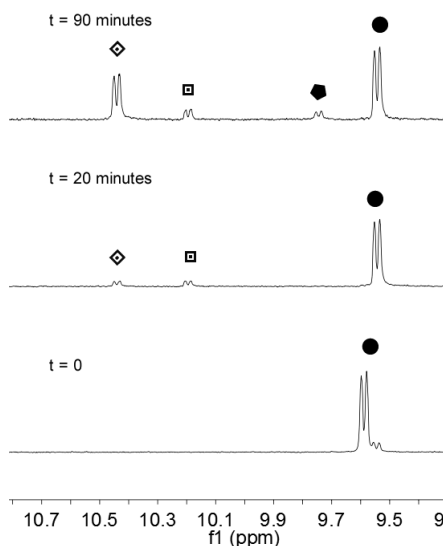


Figure SII.3 Evolution of the ^1H NMR spectra (region 10.8-9.0 ppm) of the reaction between $[1](\text{PF}_6)_2$ and commercial HACysMe after different time intervals at 353 K in CD_3OD under an argon atmosphere. Notations: (\diamond) $[4]^+$, (\square) unknown side product, (\blacklozenge) $[\text{Ru}(\text{tpy})(\text{bpy})\text{Cl}]^+$, (\bullet) $[1]^{2+}$. ^1H NMR peaks in this region correspond to the A6 proton for each complex. Conditions: $[\text{Ru}]_0 = 6.5$ mM, $[\text{HACysMe}] = 49.5$ mM.

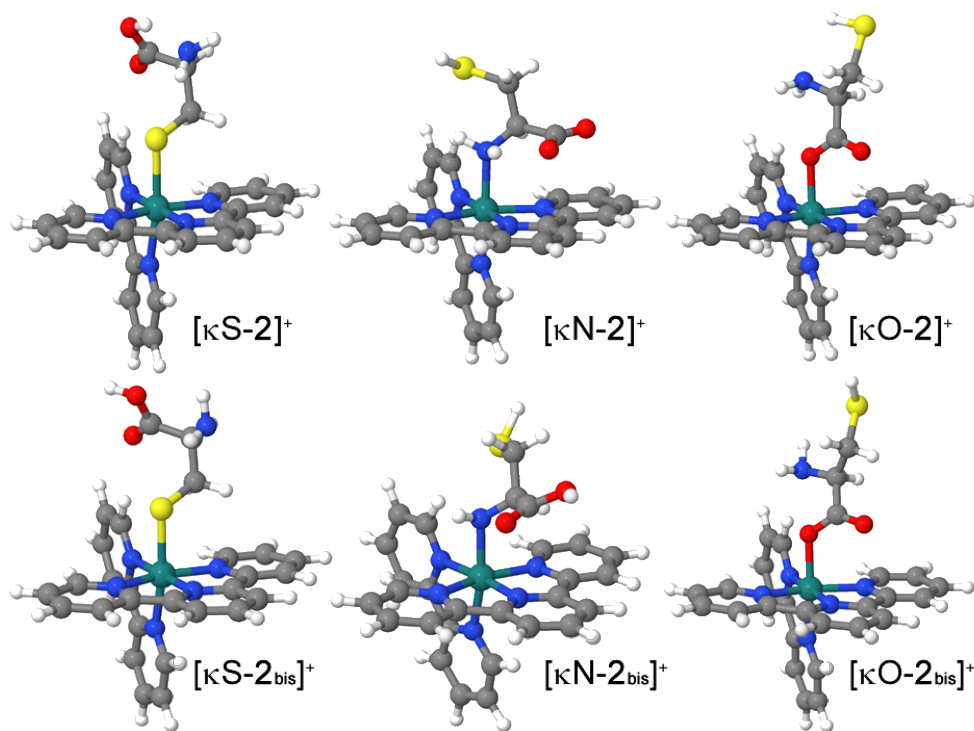


Figure SII.4 Structures of the κS , κN , and κO isomers of $[\text{Ru}(\text{tpy})(\text{bpy})(\text{Hcys})]^+$ optimized in water (COSMO) by DFT. Top: most stable conformers in water. Bottom: second least stable conformer in water. See energies in Table SII.1.

Table SII.1 Absolute and relative energies in vacuum and in water (COSMO) of the isomers of [2]⁺ optimized by DFT.

	E (vacuum) (Hartree)	E (water) (Hartree)	ΔE (vacuum) (kcal.mol ⁻¹)	ΔE (water) (kcal.mol ⁻¹)
[κS-2] ⁺	-2052.114793	-2052.197445	0.0	0.0
[κS-2bis] ⁺	-2052.108926	-2052.189717	3.7	4.8
[κN-2] ⁺	-2052.089841	-2052.187013	15.7	6.5
[κN-2bis] ⁺	-2052.076531	-2052.147804	24.0	31.2
[κO-2] ⁺	-2052.093757	-2052.176934	13.2	12.9
[κO-2bis] ⁺	-2052.095173	-2052.172660	12.3	15.6

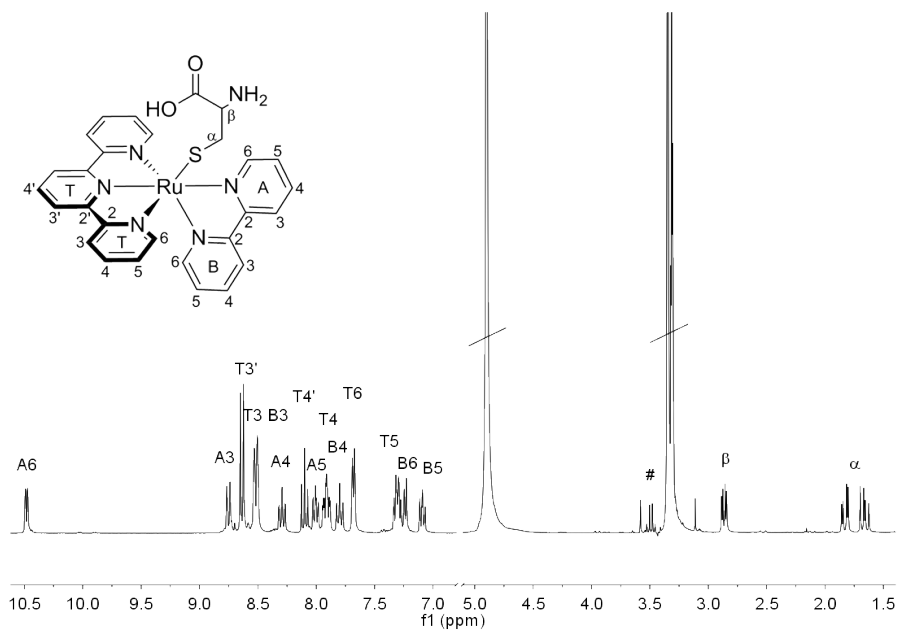


Figure SII.5 ¹H NMR spectrum (region 10.6-6.9 and 5.1-1.4 ppm) of a solution of [2]PF₆ in CD₃OD. Notation: # = EtOH.

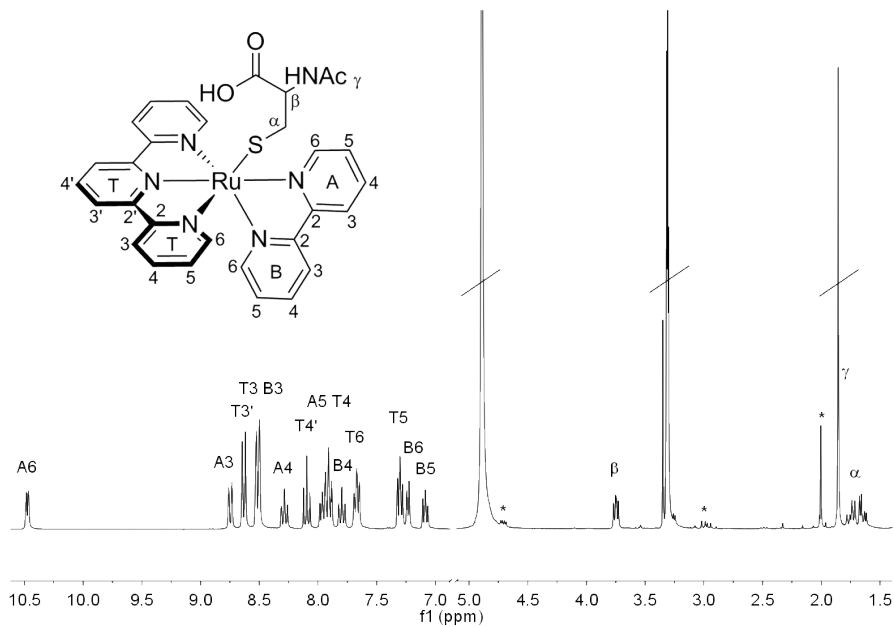


Figure SII.6 ¹H NMR spectrum (region 10.6-6.9 and 5.1-1.4 ppm) of a solution of [3]PF₆ in CD₃OD. Notations: * = H₂Ac₂

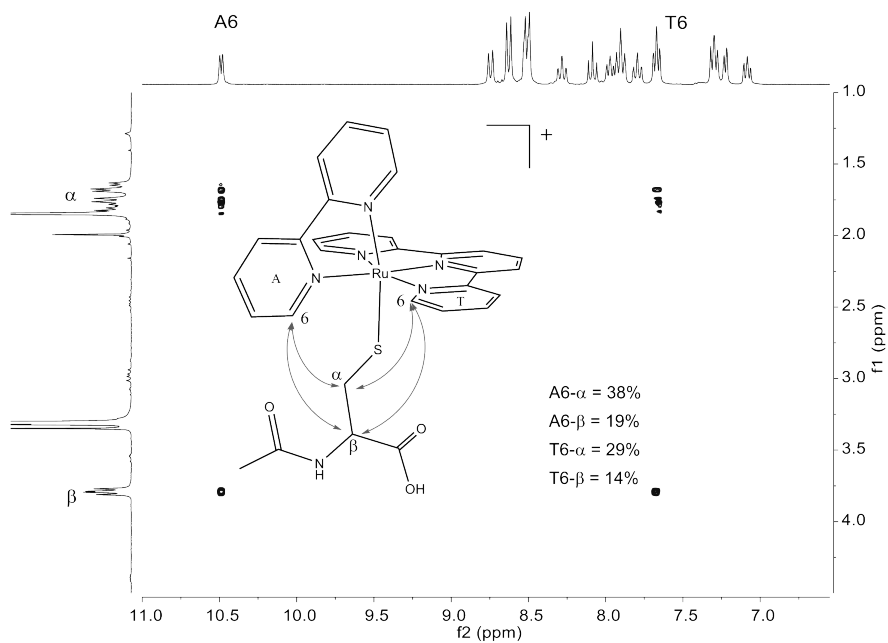


Figure SII.7 NOESY spectrum of $[3]PF_6$ in CD_3OD showing coupling between the α and β protons of cysteine (region 1.0-4.5 ppm, f_1) and the bpy (A6) and tpy (T6) protons (region 11.0-6.0 ppm, f_2). Integrals of the off-diagonal NOESY peaks are indicated as percentage of the sum of the four peaks, and show that α is closer to Ru than β , thus that $HAcs^-$ is bound to Ru via S.

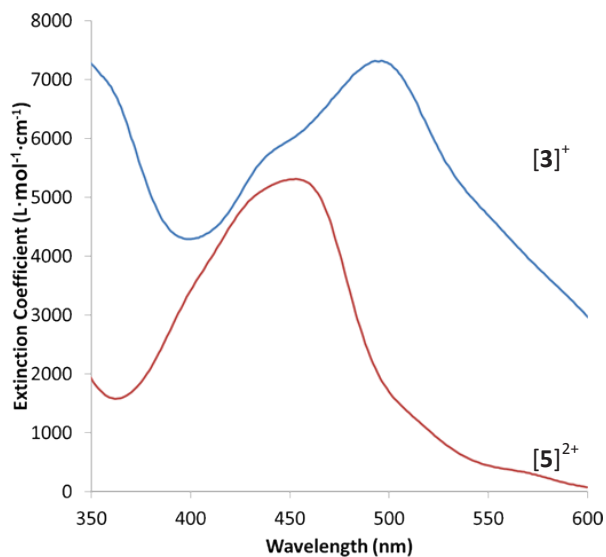


Figure SII.8 UV-vis spectra of the thiolato complex $[\text{Ru}(\text{tpy})(\text{bpy})(\text{HAcys})]\text{PF}_6$ (blue) and of the thioether analogue $[\text{Ru}(\text{tpy})(\text{bpy})(\text{HAMet})]\text{Cl}_2$ (red) in water. pH~7, 298 K.

Table SII.2 Conversion of compound $[3]^+$ into the aqua complex $[1]^{2+}$ and into unknown side products as a function of time, under air and argon.^{[a], [b]}

time	Side product (■) (%)	argon			air			Side product (+) (%)
		$[3]^+$ (%)	$[1]^{2+}$ (%)	Side product (+) (%)	Side product (■) (%)	$[3]^+$ (%)	$[1]^{2+}$ (%)	
0 hours	12	88	0	0	18	82	0	0
4 hours	10	85	5	0	13	79	8	0
1 day	9	84	7	0	19	67	14	0
4 days	9	82	9	0	17	52	31	0
3 weeks	9	77	14	0	26	0	55	19

^[a] Conditions: $[\text{Ru}]_0 = 6.4 \text{ mM}$, in D_2O , in the dark, at 298 K.

^[b] Relative integration of the peak at 10.12, 10.00, 9.71, or 9.54 ppm for the side product, $[3]^+$, the second side product, or $[1]^{2+}$, respectively, versus the sum of all four peaks at 10.12, 10.00, 9.71, and 9.54 ppm.

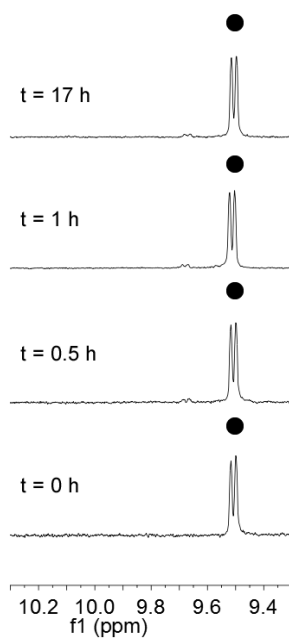


Figure SII.9 ^1H NMR spectra (region 10.3-9.3 ppm) of the reaction between $[1](\text{PF}_6)_2$ and the disulfide H_2Acys_2 (6) at different time intervals at 353 K in D_2O . Notations: ● = $[1]^{2+}$. ^1H NMR peaks in this region correspond to the A6 proton for each complex. Conditions: $[\text{Ru}]_0 = 6.0\text{ mM}$, $[\text{H}_2\text{Acys}_2] = 6.0\text{ mM}$.

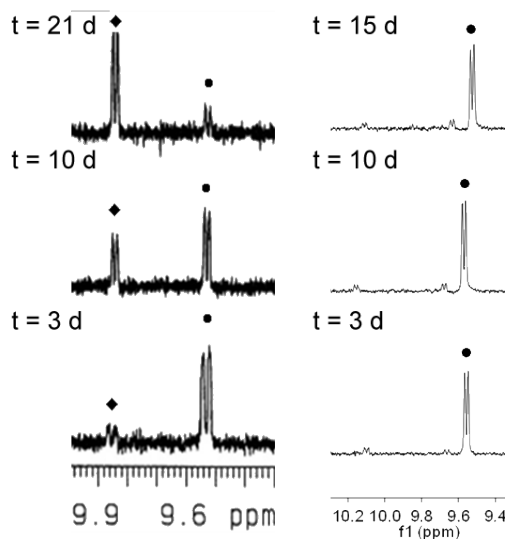


Figure SII.10 Evolution of the ^1H NMR spectra (region 10.2-9.4 ppm) of the reaction between $[1]^{2+}$ and H_2Cys in D_2O . a) reaction according to Bugarčić et al.¹ b) reaction in our hands; peaks at 10.00 and 9.54 ppm are expected as the A6 proton for complex $[2]^+$ (◆) and $[1]^{2+}$ (●), respectively (see main text). Conditions: a) $[\text{Ru}]_0 = 4.0 \text{ mM}$, $[\text{H}_2\text{Cys}] = 4.0 \text{ mM}$, $\text{pH} = 7.4$, $T = 295 \text{ K}$. b) $[\text{Ru}]_0 = 7.7 \text{ mM}$, $[\text{H}_2\text{Cys}] = 7.7 \text{ mM}$, $\text{pH} = 7.4$, $T = 298 \text{ K}$.

References

1. A. Mijatović, B. Šmit, A. Rilak, B. Petrović, D. Čanović and Ž. D. Bugarčić, *Inorg. Chim. Acta*, 2013, **394**, 552-557.

APPENDIX III: SUPPORTING INFORMATION FOR CHAPTER 3

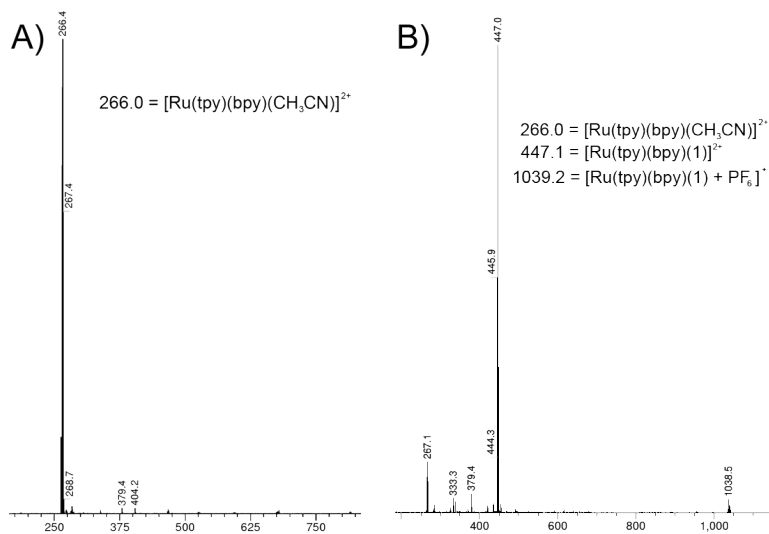


Figure SIII.1 ESI mass spectrum of $[\text{2}](\text{PF}_6)_2$ after light activation (A) and the dark control (B) in acetonitrile with peak attribution.

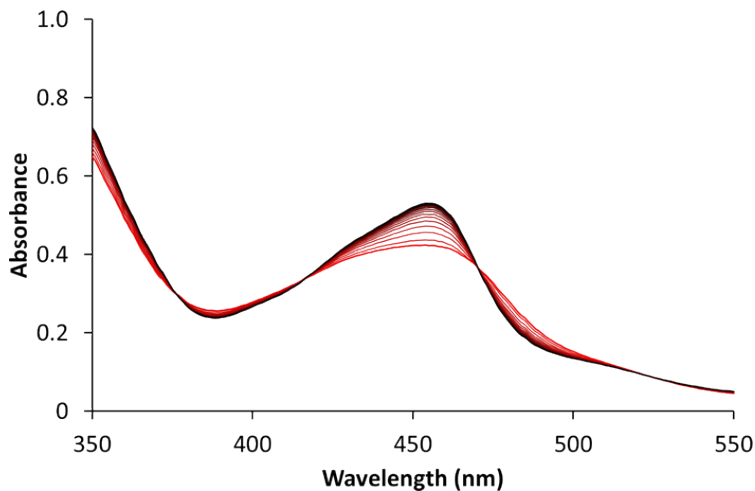


Figure SIII.2 Evolution of the electronic absorption spectra of a solution of $[2](PF_6)_2$ in acetonitrile upon blue light irradiation under nitrogen ($\lambda = 445 \text{ nm}$, $\Delta\lambda_{1/2} = 11 \text{ nm}$, 10.5 mW , $1.27 \times 10^{-7} \text{ mol}\cdot\text{s}^{-1}$). Time: 0 min (red curve) to 30 min (black curve). Conditions: $[Ru]_0 = 50 \text{ }\mu\text{M}$, irradiated volume was 3.0 mL at 293 K.

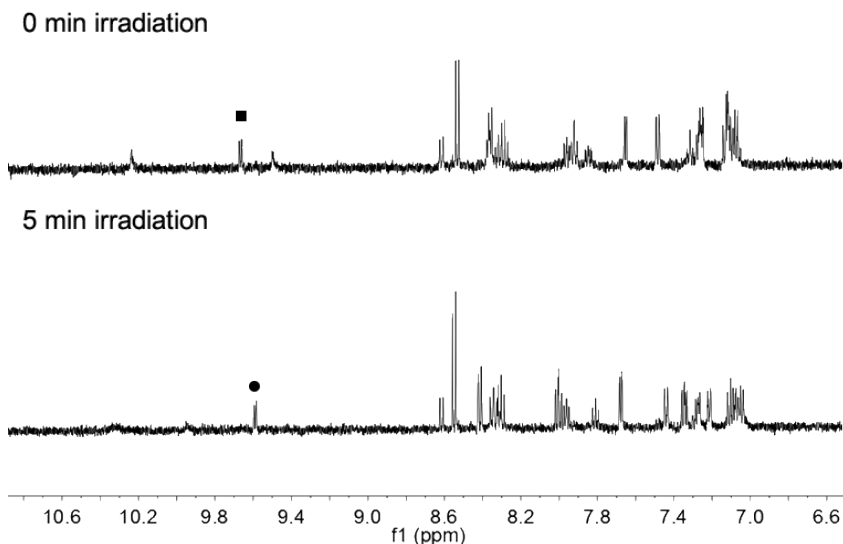


Figure SIII.3 ^1H NMR spectra (500 MHz, CD_3CN , region 10.7-6.5 ppm) of a solution of $[2](PF_6)_2$ before (top) and after (bottom) having been irradiated by white light. Notations: (■) A6 proton of $[2](PF_6)_2$, (●) A6 proton of $[\text{Ru}(\text{tpy})(\text{bpy})(\text{CH}_3\text{CN})](PF_6)_2$. Conditions: $T = 298 \text{ K}$, $[Ru]_0 = 200 \text{ }\mu\text{M}$.

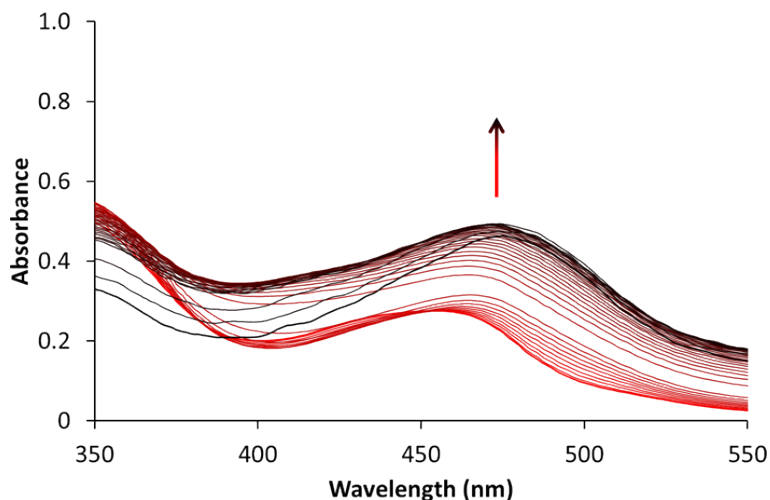


Figure SIII.4 Evolution of the electronic absorption spectra of a solution of $[2](PF_6)_2$ in water upon blue light irradiation under nitrogen ($\lambda = 445$ nm, $\Delta\lambda_{1/2} = 11$ nm, 10.5 mW, photon flux 1.27×10^{-7} mol.s $^{-1}$). Time: 0 min (red curve) to 30 min (black curve). Conditions: $[Ru]_0 = 34$ μ M, irradiated volume was 3.0 mL at 293 K.

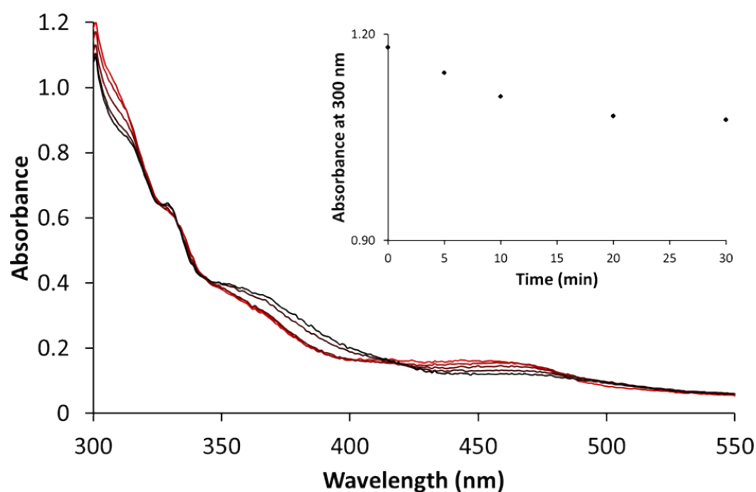


Figure SIII.5 Evolution of the UV-vis spectrum of a well of a 96-well plate containing compound $[2](PF_6)_2$ ($[Ru] = 60$ μ M) in the cell-culturing medium Opti-MEM complete, under green light irradiation (37 °C) between 0 min (red) and 30 min (black).

APPENDIX IV: SUPPORTING INFORMATION FOR CHAPTER 4

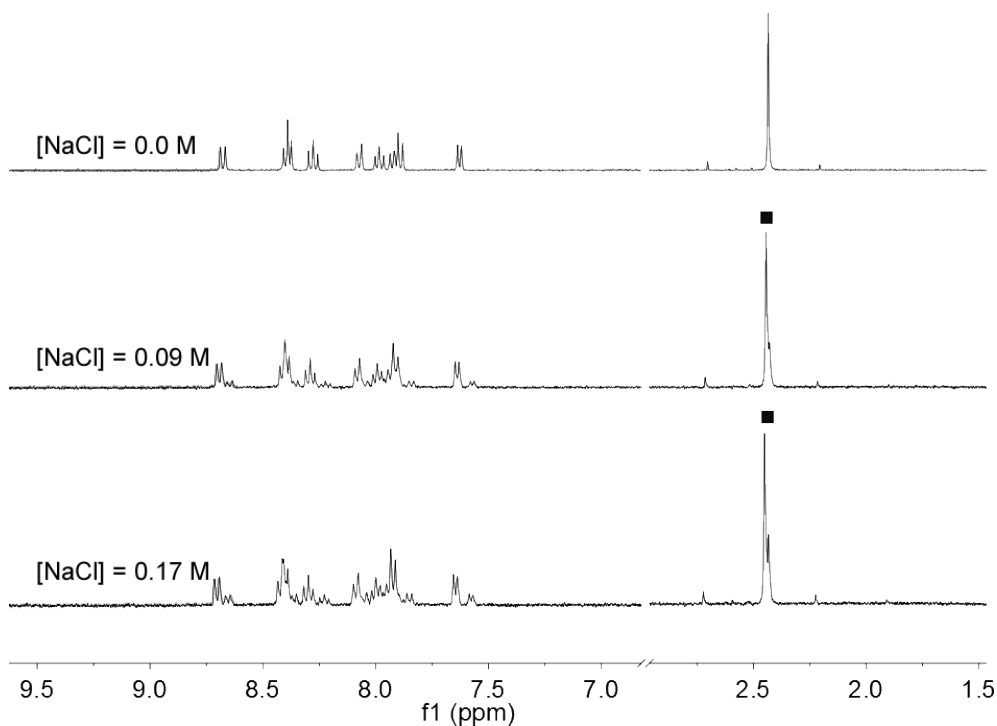


Figure SIV.1 Evolution of the ^1H NMR spectra (400 MHz, D_2O , region 9.5-7.0 and 3.5-1.5 ppm) of $[1a]^{2+}$ under addition of NaCl at 298 K in D_2O . The initial spectrum (at $[\text{NaCl}] = 0$ M) is that of $[1a]^{2+}$, the spectrum at $[\text{NaCl}] = 0.08$ M and $[\text{NaCl}] = 0.17$ M a mixture of $[1a]^{2+}$ and $[1]^+$. Notations: ■ = methyl group of dmsoligated species, splitting of ■ indicates partial formation of $[\text{Ru}(\text{H}_2\text{biqbpy})(\text{dmsoligated})\text{Cl}]^+$. $[\text{Ru}]_0 = 0.5$ mM.

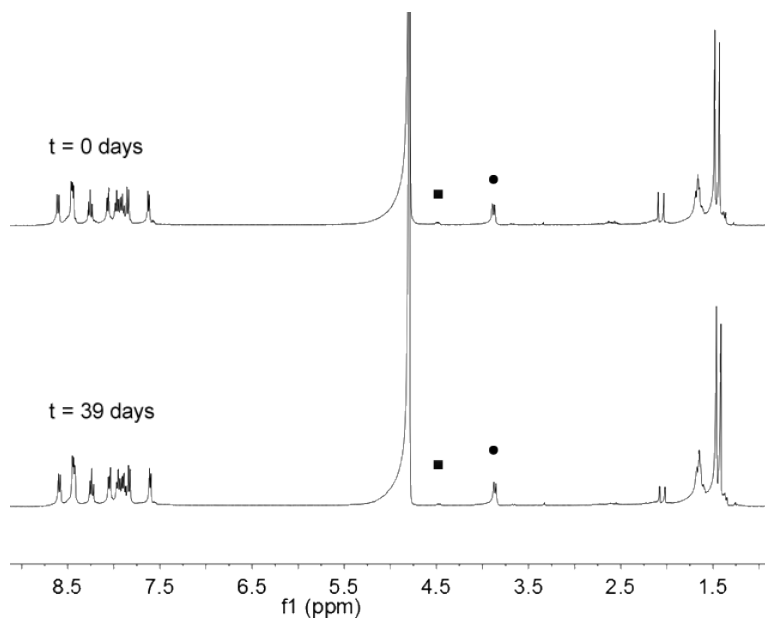


Figure SIV.2 Evolution of the ^1H NMR spectra (400 MHz, D_2O , region 9.0-1.0 ppm) of a solution of $[\mathbf{2}]\text{PF}_6$ in D_2O under argon. Notations: ■ = characteristic chiral proton (δ) of free Amet; ● = characteristic chiral proton (δ) of ruthenium-coordinated Amet in $[\mathbf{2a}]$ (see Scheme 4.2). $[\text{Ru}]_0 = 0.38 \text{ mM}$

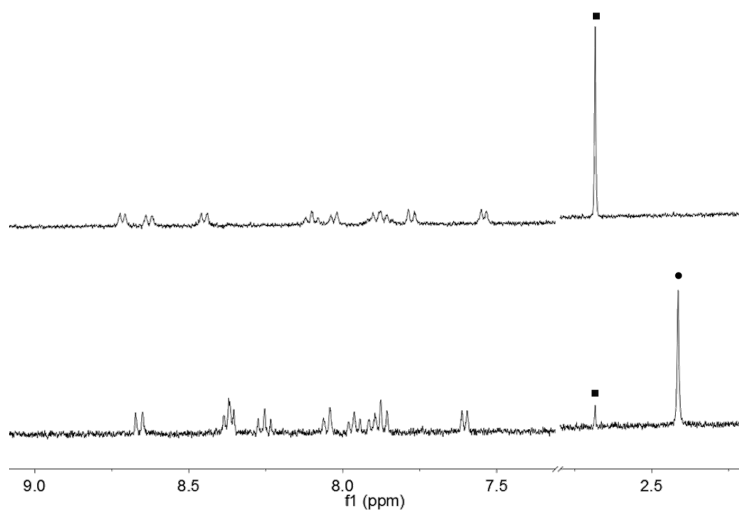


Figure SIV.3 ^1H NMR spectra (400 MHz, region 9.0-7.5 and 3.0-2.0 ppm) of a solution of $[\mathbf{1}]\text{Cl}$ in D_2O that has been irradiated by green light (top) and stored in the dark (bottom) at 310 K in a 96-well plate. Notations: ■ = free dmsu (CH_3), ● = sulfur-coordinated dmsu (CH_3) in $[\mathbf{1}]\text{Cl}$. $[\text{Ru}]_0 = 0.038 \text{ mM}$. Light source: green LED array, 520 nm, $75 \text{ J}\cdot\text{cm}^{-2}$.

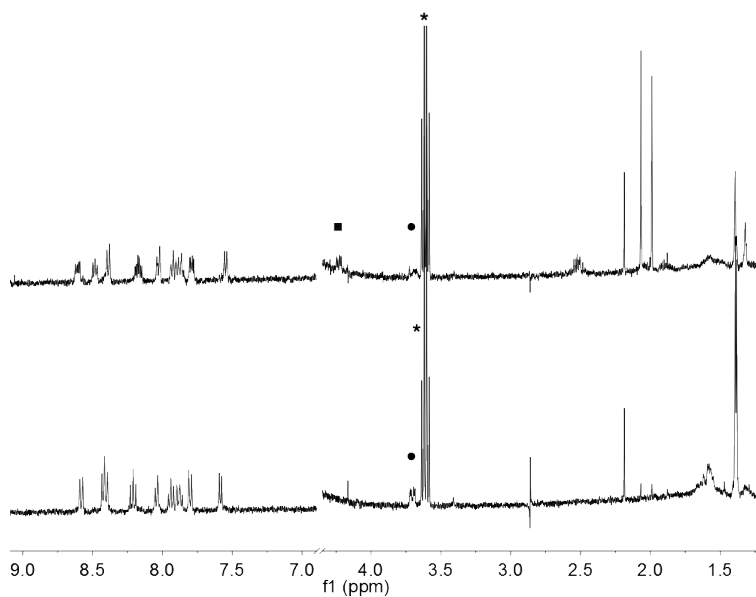


Figure SIV.4 ^1H NMR spectra (400 MHz, D_2O , region 9.0-7.0 and 4.5-1.0 ppm) of a solution of $[\text{2}]\text{PF}_6$ in D_2O that has been irradiated by green light (top) or stored in the dark (bottom) at 310 K in a 96-well plate. $[\text{Ru}]_0 = 0.087$ mM. Light source: green LED array, 520 nm, $75 \text{ J}\cdot\text{cm}^{-2}$.

Notations: ■ = characteristic chiral proton (δ) of free Amet; ● = characteristic chiral proton (δ) of ruthenium-coordinated Amet; * = ethanol originating from working in ethanol sterilized environment for cell experiments.

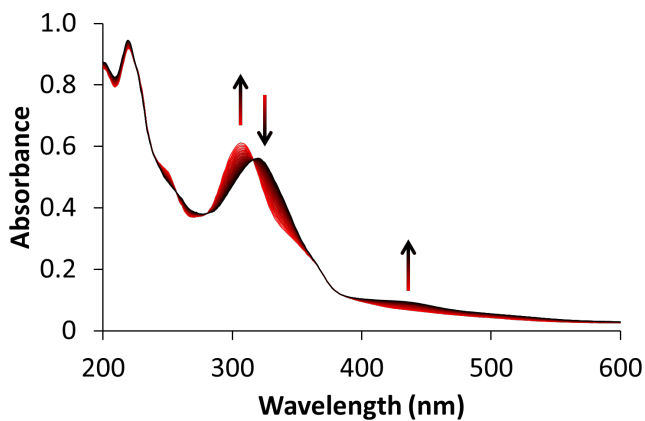


Figure SIV.5 Evolution of the UV-vis spectrum of a solution of [1]Cl in demineralized water, thus of [1a]⁺, upon blue light irradiation under argon. Conditions [Ru]₀ = 0.025 mM irradiated volume 3.00 mL, 298 K. Light source: $\lambda = 450$ nm, $\Delta\lambda_{1/2} = 25$ nm, 0.65 mW, 8.53×10^{-9} mol.s⁻¹.

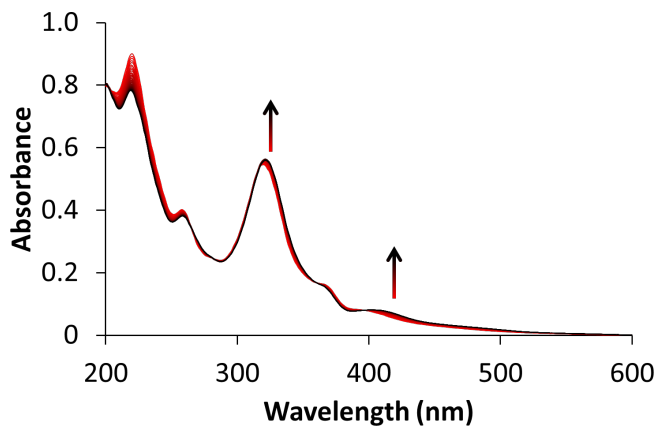


Figure SIV.6 Evolution of the UV-vis spectrum of a solution of [2]PF₆ in demineralized water upon blue irradiation under argon. Conditions [Ru]₀ = 0.025 mM, irradiated volume 3.00 mL, 298 K. Light source: $\lambda = 450$ nm, $\Delta\lambda_{1/2} = 25$ nm, 0.65 mW, 8.53×10^{-9} mol.s⁻¹.

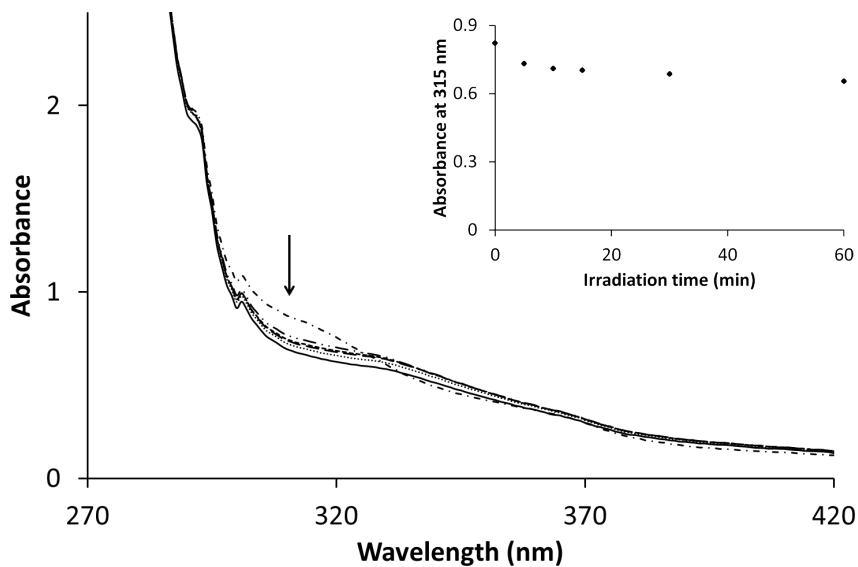


Figure SIV.7 Evolution of the UV-vis spectra of [1]Cl (38 μ M) in the medium Opti-MEM complete under green light irradiation (37 $^{\circ}$ C) in a well in a 96-well plate at 0 min (---), 5 min (---), 10 min (— —), 15 min (- - -), 30 min (···), and 60 min (—).

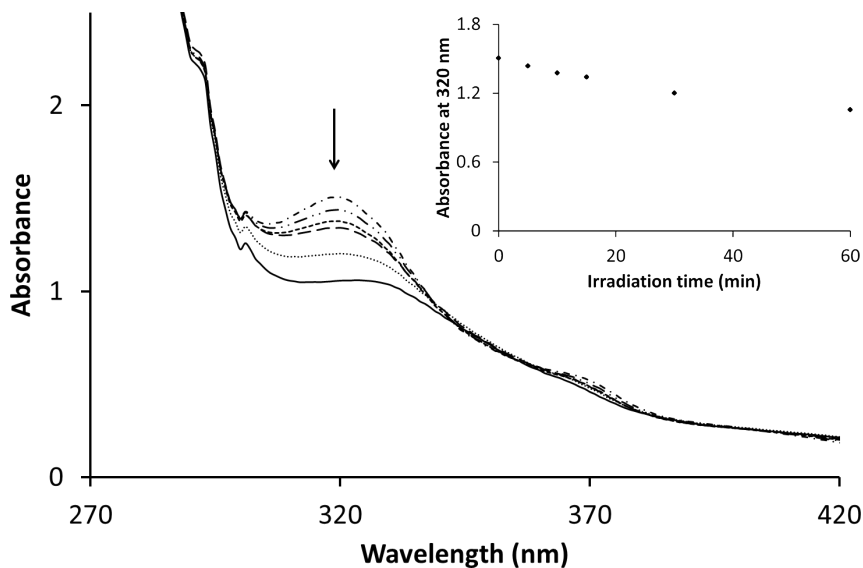


Figure SIV.8 Evolution of the UV-vis spectra of [2]PF₆ (88 μ M) in the medium Opti-MEM complete under green light irradiation (37 $^{\circ}$ C) in a well of a 96-well plate at 0 min (---), 5 min (---), 10 min (— —), 15 min (- - -), 30 min (···), and 60 min (—).

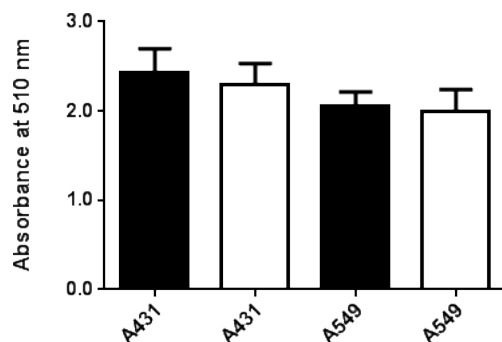


Figure SIV.9 Average absorbance at 510 nm (with standard deviation) of control cells used in photocytotoxicity assay for A431 and A549 cells kept in the dark (black bar) or irradiated with green light (520 nm, 60 min, 75 J.cm⁻²) indicated with a white bar. Phototoxicity assay outline: cells seeded at 8×10^3 (A431) or 5×10^3 (A549) cells/well at $t = 0$ h, treated with Opti-MEM complete at $t = 24$ h, irradiated at $t = 30$ h or 48 h, and SRB assay performed at $t = 96$ h. Incubation conditions: 37 °C and 7% CO₂.

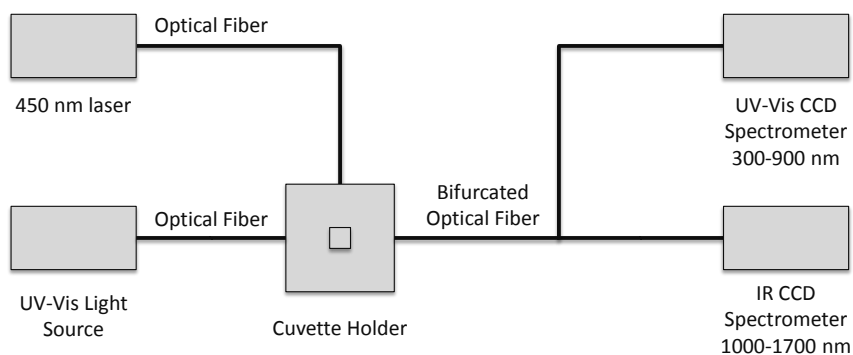


Figure SIV.10 Schematic overview of the custom-built setup to determine singlet oxygen quantum yield.

The quantum yield of singlet oxygen production was calculated using the relative method with $[\text{Ru}(\text{bpy})_3]\text{Cl}_2$ as the standard ($\Phi_{std}^\Delta = 0.73$ in CD_3OD), according to:

$$\Phi_{sam}^\Delta = \Phi_{std}^\Delta \times \frac{A_{std}^{450}}{A_{sam}^{450}} \times \frac{E_{sam}}{E_{std}}$$

where Φ^Δ is the quantum yield of singlet oxygen generation, A^{450} is the absorbance at 450 nm (always kept below 0.1 for a 1 cm path length cuvette), E is the integrated emission peak of singlet oxygen at 1273 nm, and *sam* and *std* indexes denote the 'sample' and 'standard' respectively.

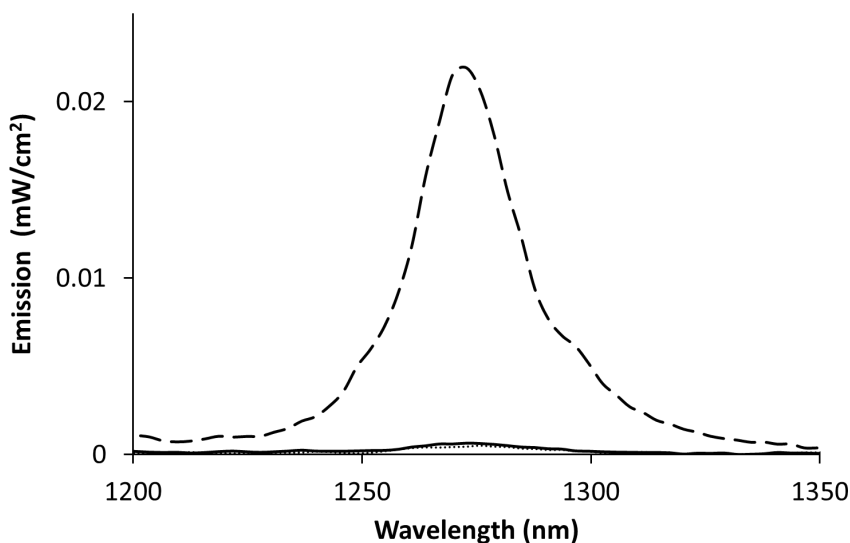


Figure SIV.11 Time-integrated emission spectra of $[\text{Ru}(\text{bpy})_3]\text{Cl}_2$ (— —), $[\text{1}]\text{Cl}$ (⋯), $[\text{2}]\text{PF}_6$ (—) irradiated with blue light (450 nm, 101 mW, photon flux = $0.53 \mu\text{mol}\cdot\text{s}^{-1}$), stirred under air in CD_3OD at 298 K. Emission was measured and averaged over 4×40 s.

Table SIV.1 Time-integrated emission data for $[\text{Ru}(\text{bpy})_3]\text{Cl}_2$, $[\text{1}]\text{Cl}$, and $[\text{2}]\text{PF}_6$ measured in CD_3OD stirred under air at 298 K. Emission was averaged 4×40 s.

Compound	Concentration (μM)	Absorbance at 450 nm	Integrated Emission ($\text{mW}\cdot\text{cm}^{-2}$) at 1273 nm	Quantum yield (%)
$[\text{Ru}(\text{bpy})_3]\text{Cl}_2$	5.3	0.11	0.02192	73 ^a
$[\text{1}]\text{Cl}$	23	0.14	0.00045	1.3
$[\text{2}]\text{PF}_6$	8.9	0.084	0.00065	2.3

^a Value taken from De Rosa et al. ¹.

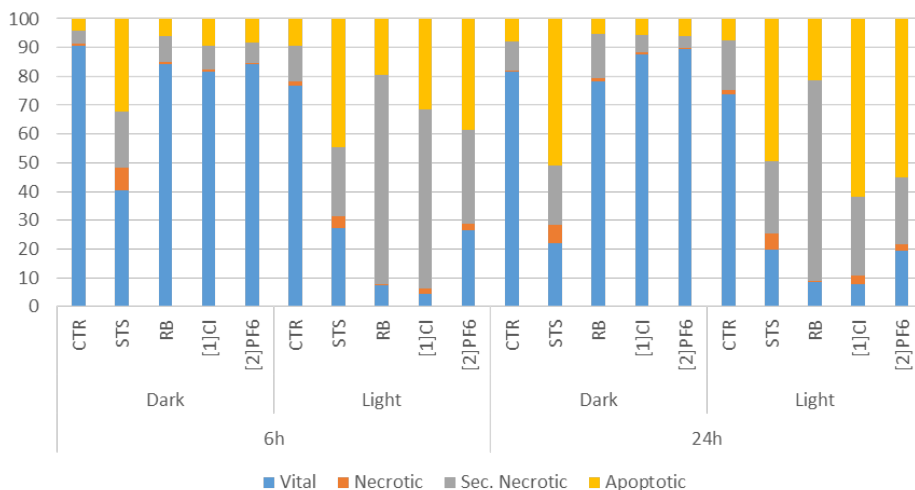


Figure SIV.12 Annexin V FITC/propidium iodide FACS analysis of cells treated with Staurosporine (STS, 0.3 μM), Rose Bengal (10 μM), [1]Cl (1.5 μM), or [2]PF₆ (10 μM). Cells were seeded at $t = 0$, grown for 24 h, treated with the appropriate compound for 6 h or 24 h, then irradiated with green light (520 nm, 60 min, 75 $\text{J}\cdot\text{cm}^{-2}$, 'Light'), then incubated for a further 24 h before flow cytometric analysis. In parallel, a second set of cells were treated with the same protocol, except that they were kept in the dark instead of irradiated ('Dark'). The diagram shows the relative distribution (cell count) of vital, necrotic, apoptotic, and secondary apoptotic cells in the different samples.

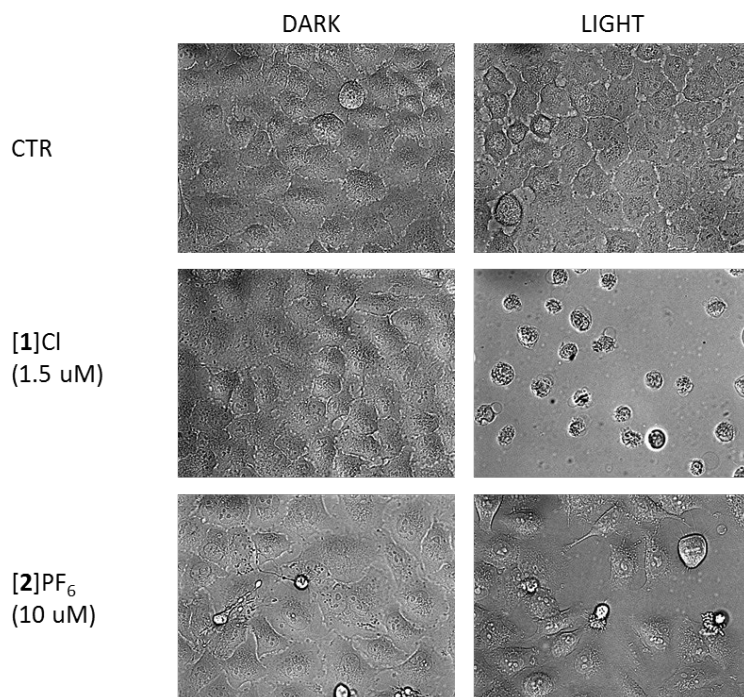


Figure SIV.13 Micrographs (40 \times) of A549 cells 24 h after green light irradiation (520 nm, 60 min, 75 J.cm⁻²). Cells seeded at t = 0 (200,000 cells per 35 mm petri dish), incubated in the dark for 24 h (7% CO₂, 37 °C), treated with [1]Cl or [2]PF₆ or with no drug (CTR) at t = 24 h, either irradiated at t = 6 h (LIGHT) or left in the dark (DARK), further incubated for 24 h in the dark, and then imaged.

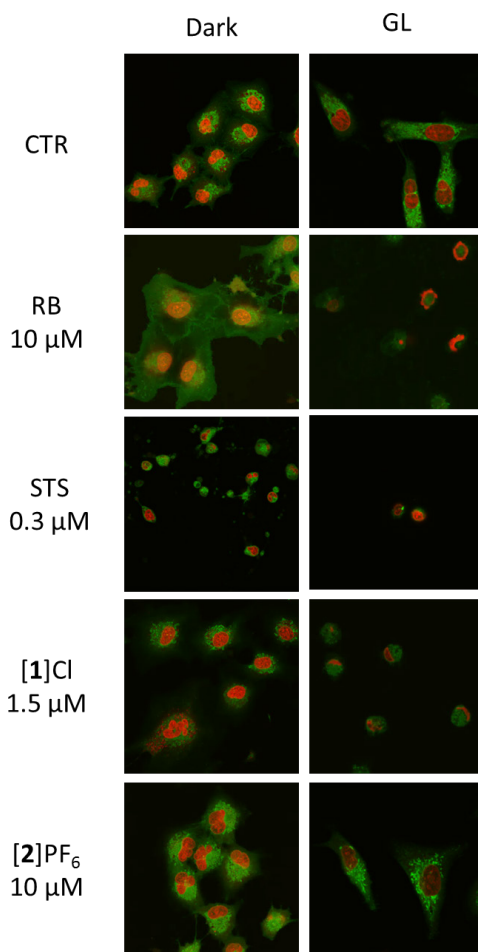


Figure SIV.14 Confocal micrographs of the emission of the mitochondrial dye tetramethylrhodamine ethyl ester ($\lambda_{\text{ex}} = 551 \text{ nm}$, $\lambda_{\text{em}} = 593 \text{ nm}$) and the emission of the DNA intercalator Draq5 ($\lambda_{\text{ex}} = 646 \text{ nm}$, $\lambda_{\text{em}} = 681 \text{ nm}$) in A549 cells treated with Rose Bengal ($10 \mu\text{M}$) Staurosporine (STS, $0.3 \mu\text{M}$), [1]Cl ($1.5 \mu\text{M}$), or [2]PF₆ ($10 \mu\text{M}$) left in the dark (left column) or irradiated with green light 24 h after treatment (right column). Analysis was performed 24 h after light irradiation. Irradiation conditions: 520 nm , 60 min , $75 \text{ J}\cdot\text{cm}^{-2}$.

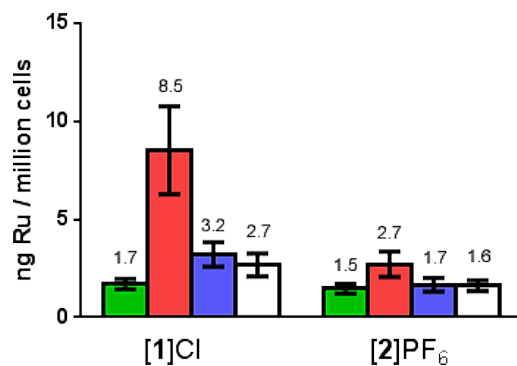
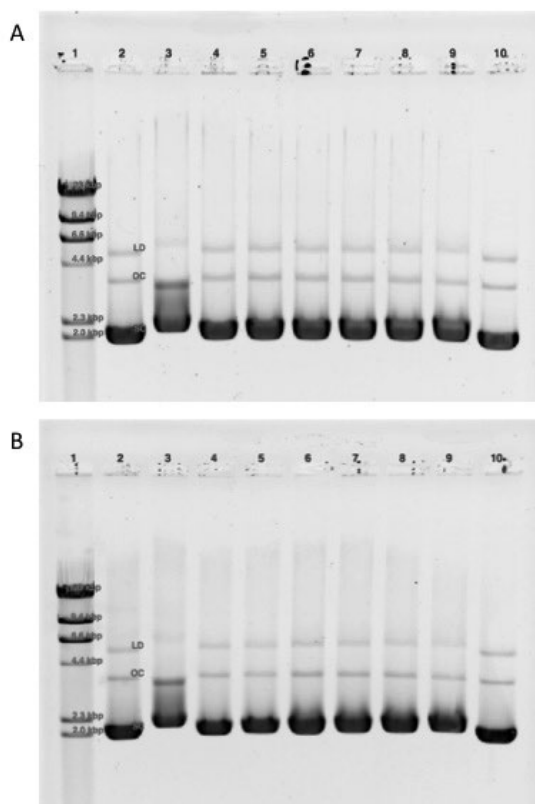
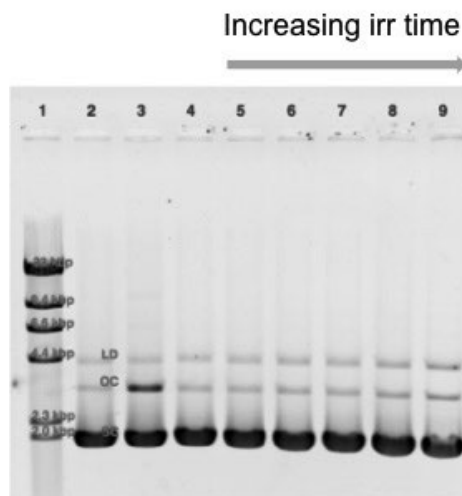


Figure SIV.15 Relative distribution of ruthenium in cytosol, membranes, nucleus, and cytoskeleton indicated by the green, red, blue, and white bar, respectively, of A549 cells (expressed in ng Ru/10⁶ cells) after 6 h treatment with EC₅₀ concentration of [1]Cl or [2]PF₆.



Lane	BP:MC	[DNA BP] _f (M)	[MC] _f (M)
1	λ MW marker	1.95×10^{-3}	
2	37 °C control	1.95×10^{-3}	0
3	Cisplatin 5:1 BP:MC	1.95×10^{-3}	1.95×10^{-5}
4	100:1 BP:MC	1.95×10^{-3}	3.91×10^{-4}
5	50:1 BP:MC	1.95×10^{-3}	1.95×10^{-4}
6	25:1 BP:MC	1.95×10^{-3}	1.30×10^{-4}
7	15:1 BP:MC	1.95×10^{-3}	7.82×10^{-4}
8	10:1 BP:MC	1.95×10^{-3}	3.91×10^{-5}
9	5:1 BP:MC	1.95×10^{-3}	1.95×10^{-5}
10	λ MW marker	1.95×10^{-3}	

Figure SIV.16 Agarose gels showing the thermal binding of metal complexes [1a]²⁺ (A) and [2a]⁰ (B) to pUC19 plasmid DNA. The table below shows the lane assignment, description (DNA base pair (BP) to metal complex (MC) ratios), and the final concentrations. The λ MW marker bands correlate to 23, 9.4, 6.6, 4.4, 2.3, and 2.0 kbp. The control DNA band consists of three bands correlating to linear dimer (LD), open circular (OC), and supercoiled (SC) forms.



Lane	BP:MC	Time or irradiation (min)	J.cm ⁻²
1	λ MW marker		
2	Dark DNA control		
3	Irr DNA control	60	75
4	100:1 BP:MC	0	0
5	50:1 BP:MC	5	6
6	25:1 BP:MC	15	19
7	15:1 BP:MC	30	38
8	10:1 BP:MC	45	56
9	5:1 BP:MC	60	75

Figure SIV.17 Agarose gels showing the photoinduced binding of cisplatin to pUC19 plasmid DNA. The table below shows the lane assignment, description (DNA base pair (BP) to metal complex (MC) ratios), time of irradiation (min), and calculated light doses (J.cm⁻²). The λ MW marker bands correlate to 23, 9.4, 6.6, 4.4, 2.3, and 2.0 kbp. The control DNA band consists of three bands correlating to linear dimer (LD), open circular (OC), and supercoiled (SC) forms.

References

1. M. C. DeRosa and R. J. Crutchley, *Coord. Chem. Rev.*, 2002, **233-234**, 351-371.

APPENDIX V: SUPPORTING INFORMATION FOR CHAPTER 5

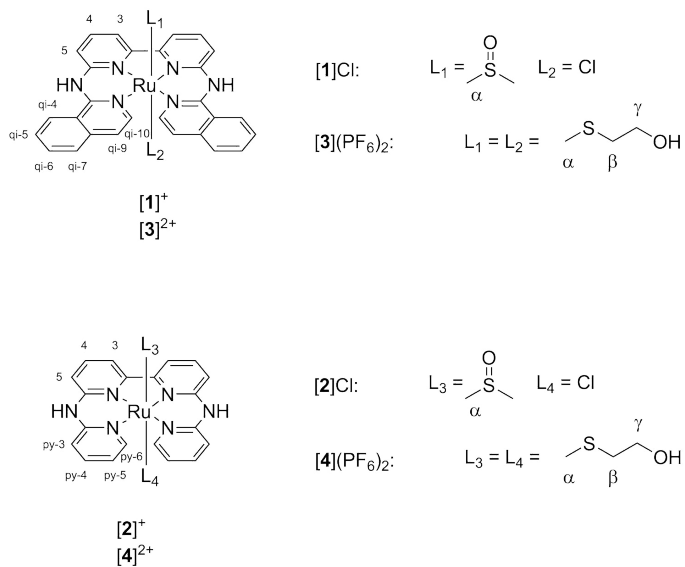


Figure SV.1 Chemical structure of [Ru(H₂biqbpy)L₂]⁺ and of [Ru(H₂bapbpy)L₂]⁺ and atom numbering used in NMR attribution.

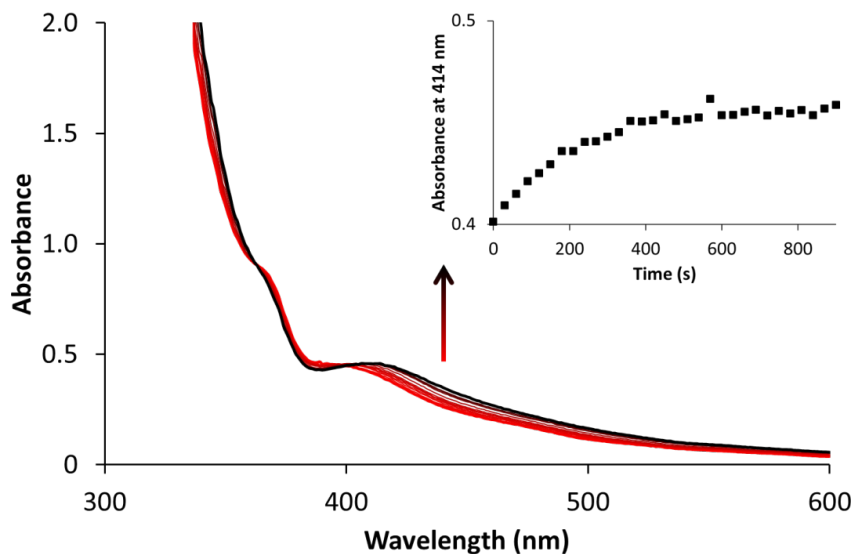


Figure SV.2 Evolution of the electronic absorption spectra of a solution of [4](PF₆)₂ in demineralized water (5 v/v% acetone-d₆) upon blue light irradiation ($\lambda_{\text{irr}} = 445 \text{ nm}$, $\Delta\lambda_{1/2} = 22 \text{ nm}$, photon flux $\Phi = 1.81 \times 10^{-7} \text{ mol}\cdot\text{s}^{-1}$, $t_{\text{irr}} = 15 \text{ min}$). Time: 0 min (red curve) to 15 min (black curve). Conditions $[\text{Ru}]_0 = 0.05 \text{ mM}$, irradiated volume was 3.0 mL at 298 K. Inset: Plot of the absorbance at 414 nm as a function of irradiation time.

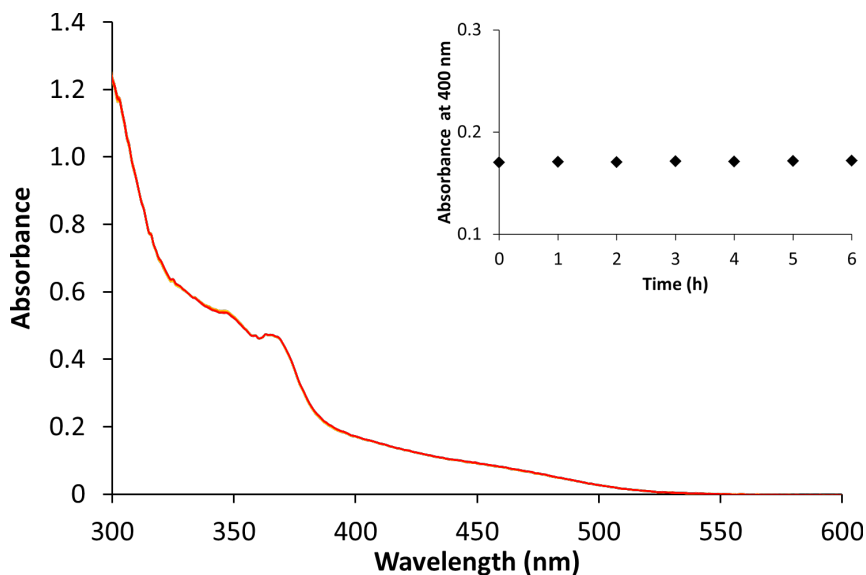


Figure SV.3 Stability of the UV-vis absorption spectrum of a solution of [2]Cl in demineralized water over 6 hours in the dark. Inset: Evolution of absorbance at 400 nm. Conditions: $[\text{Ru}] = 0.05 \text{ mM}$, $T = 298 \text{ K}$.

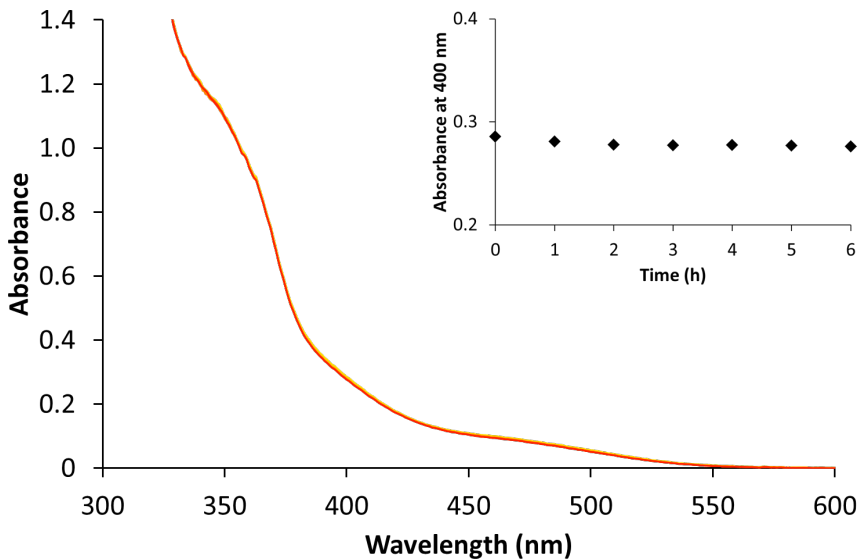


Figure SV.4 Stability of the UV-vis absorption spectrum of a solution of [1]Cl in demineralized water over 6 hours in the dark. Inset: evolution of absorbance at 400 nm. Conditions: [Ru] = 0.05 mM, T = 298 K.

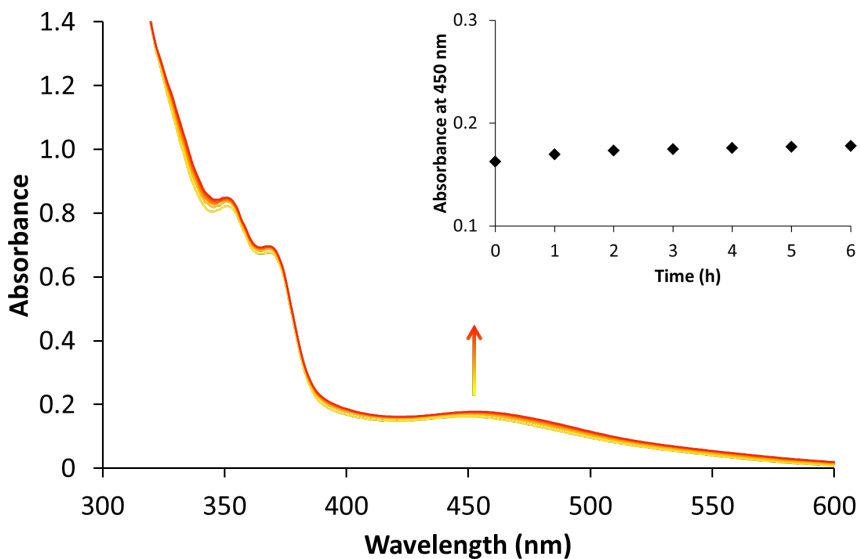


Figure SV.5 Evolution of UV-vis spectrum of [3](PF₆)₂ over 6 hours in demineralized water in the dark. Inset: evolution of absorbance at 450 nm. Conditions: [Ru] = 0.05 mM, T = 298 K.

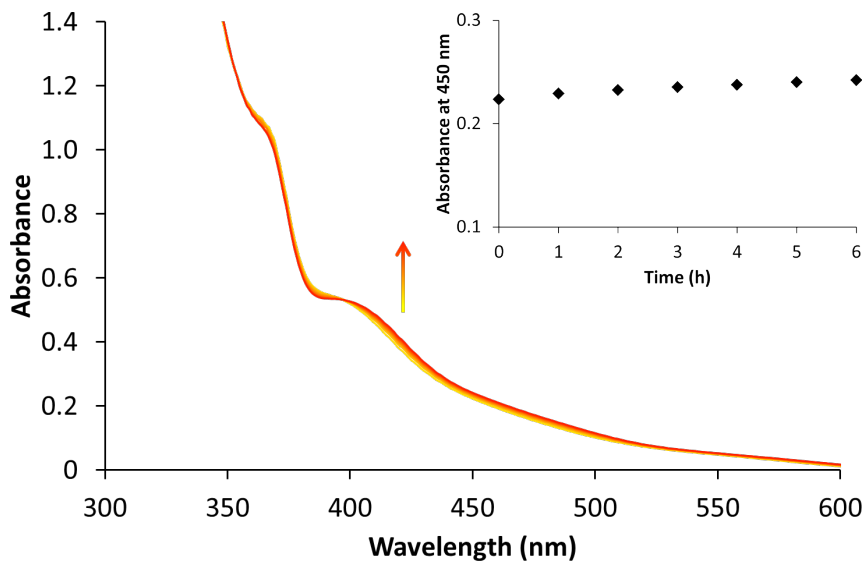


Figure SV.6 Evolution of UV-vis spectrum of [4](PF₆)₂ over 6 hours in demineralized water in the dark. Inset: evolution of absorbance at 450 nm. Conditions: [Ru] = 0.05 mM, T = 298 K

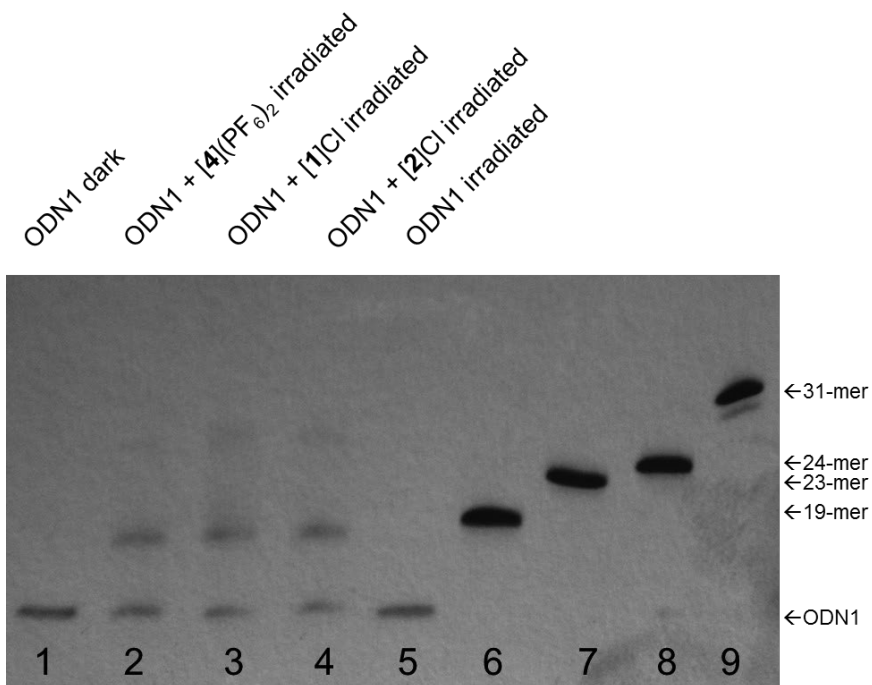


Figure SV.7 Gel electrophoresis of light-induced binding of [1]Cl, [2]Cl, or [4](PF₆)₂ (lane 2, 3, and 4) analyzed by polyacrylamide gel including ODN1 (dark, lane 1), ODN1 (irradiated, lane 5), 19, 23, 24, 31-mer control. Conditions: T = 25 °C, [Ru] = 0.75 mM, [ODN] = 0.25 mM, Staining agent: Toluidine blue, λ_{irr} = 445 nm, Δλ_{1/2} = 22 nm, photon flux Φ = 2.2 × 10⁻⁷ mol.s⁻¹, t_{irr} = 10 min.

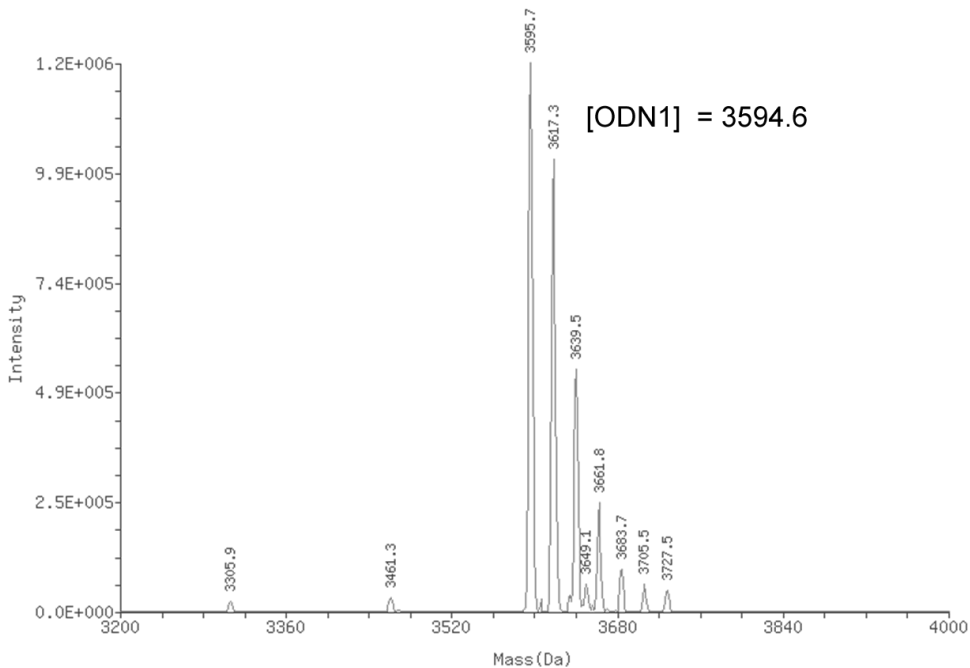


Figure SV.8 Deconvoluted mass spectrometry data of ODN1 ($s(5^{\prime}\text{CTACGGTTTCAC}^3)$) or $\text{C}_{116}\text{H}_{149}\text{N}_{40}\text{O}_{72}\text{P}_{11}$. Conditions: $[\text{ODN}] = 0.03 \text{ mM}$, $T = 298 \text{ K}$.

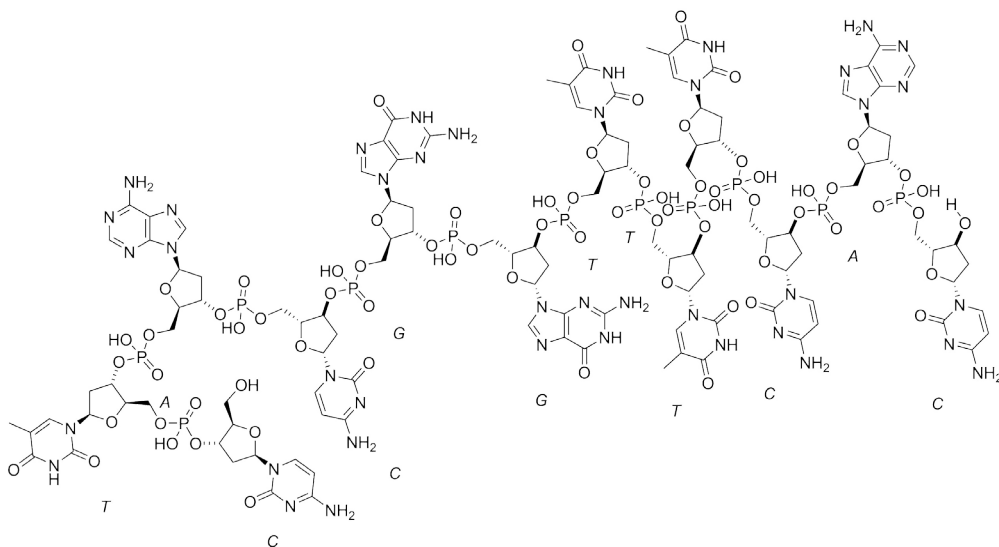


Figure SV.9 Chemical structure of ODN1 $s(5^{\prime}\text{CTACGGTTTCAC}^3)$.

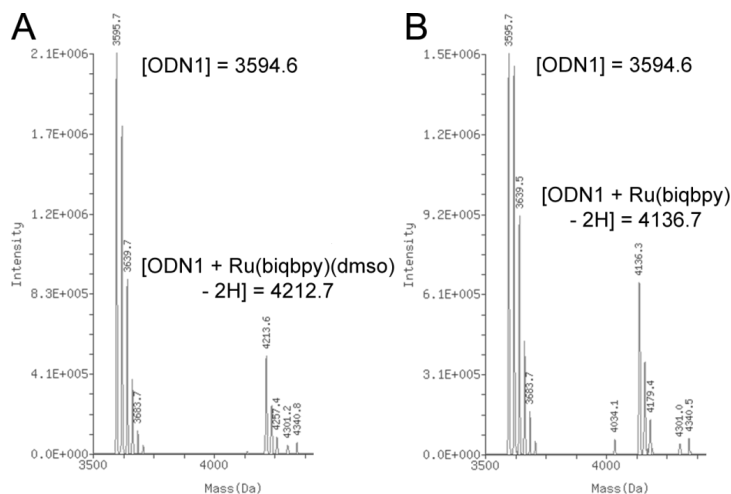


Figure SV.10 Deconvoluted mass spectrometry data of ODN1 and [1]Cl incubated in the dark (A) or after light activation (B). Conditions: [ODN] = 0.03 mM, [Ru] = 0.09 mM, $t_{\text{incubation}} = 6$ h, $T = 298$ K, $\lambda_{\text{irr}} = 445$ nm, $\Delta\lambda_{1/2} = 22$ nm, photon flux $\Phi = 2.17 \times 10^{-7}$ mol.s $^{-1}$.

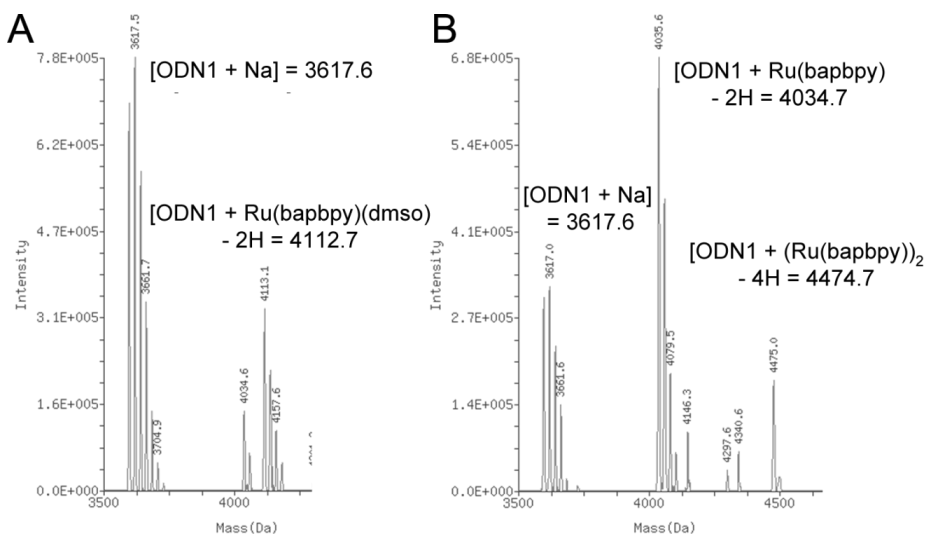


Figure SV.11 Deconvoluted mass spectrometry data of ODN1 and [2]Cl incubated in the dark (A) or after light activation (B). Conditions: [ODN] = 0.03 mM, [Ru] = 0.09 mM, $t_{\text{incubation}} = 6$ h, $T = 298$ K, $\lambda_{\text{irr}} = 445$ nm, $\Delta\lambda_{1/2} = 22$ nm, photon flux $\Phi = 2.17 \times 10^{-7}$ mol.s $^{-1}$.

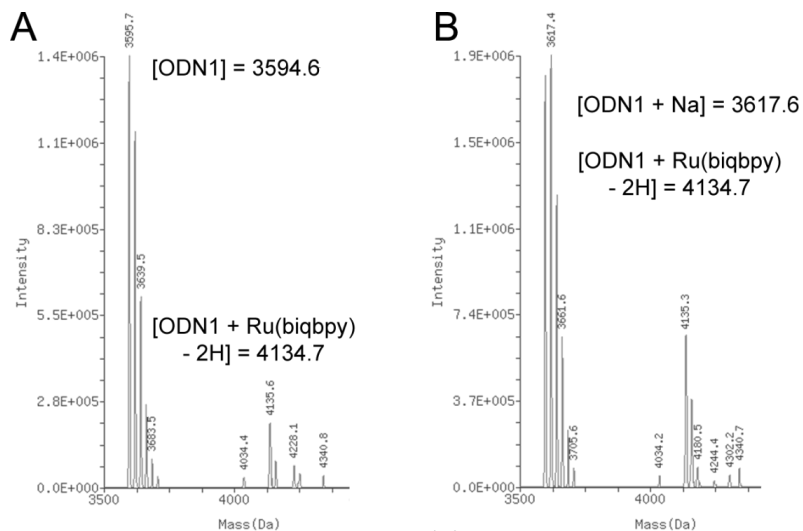


Figure SV.12 Deconvoluted mass spectrometry data of ODN1 and [3](PF₆)₂ incubated in the dark (A) or after light activation (B). Conditions: [ODN] = 0.03 mM, [Ru] = 0.09 mM, $t_{\text{incubation}} = 6 \text{ h}$, $T = 298 \text{ K}$, $\lambda_{\text{irr}} = 445 \text{ nm}$, $\Delta\lambda_{1/2} = 22 \text{ nm}$, photon flux $\Phi = 2.17 \times 10^{-7} \text{ mol.s}^{-1}$.

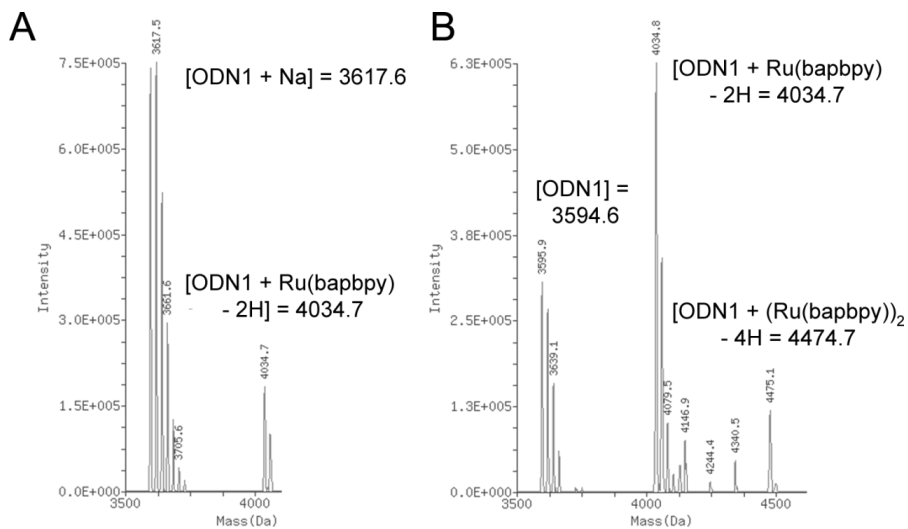


Figure SV.13 Deconvoluted mass spectrometry data of ODN1 and [4](PF₆)₂ incubated in the dark (A) or after light activation (B). Conditions: [ODN] = 0.03 mM, [Ru] = 0.09 mM, $t_{\text{incubation}} = 6 \text{ h}$, $T = 298 \text{ K}$, $\lambda_{\text{irr}} = 445 \text{ nm}$, $\Delta\lambda_{1/2} = 22 \text{ nm}$, photon flux $\Phi = 2.17 \times 10^{-7} \text{ mol.s}^{-1}$.

APPENDIX VI: SUPPORTING INFORMATION FOR CHAPTER 6

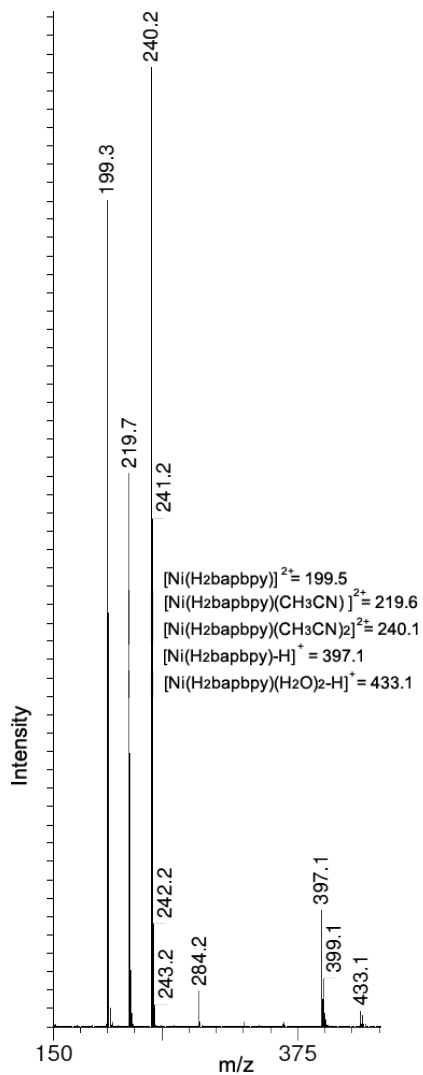


Figure SVI.1. m/z spectrum of [1]Cl₂ in acetonitrile. [Ni] = 0.01 mM.

Table SVI.1 Selected bond lengths (Å) for [1]Cl₂, [2](PF₆)₂, and [Pt(Hbapbpy)](PF₆)

Bond	[1]Cl ₂	[2](PF ₆) ₂	[Pt(Hbapbpy)](PF ₆)
M-N1	2.0630(16)	2.0251(16)	2.013(4)
M-N3	2.0348(16)	1.9846(16)	1.981(4)
M-N4	2.0325(16)	1.9802(16)	1.990(4)
M-N6	2.0579(16)	2.0312(16)	2.035(4)
N2-C5	1.381(3)	1.390(3)	1.354(7)
N2-C6	1.383(2)	1.372(3)	1.336(7)
N5-C15	1.381(3)	1.363(3)	1.373(8)
N5-C16	1.384(3)	1.372(3)	1.398(8)
Ni-O1W	2.1225(15)	-	-
Ni-O2W	2.1131(15)	-	-

Table SVI.2 Selected angles (°) for [1]Cl₂, [2](PF₆)₂, and [Pt(Hbapbpy)](PF₆)

Angle	[1]Cl ₂	[2](PF ₆) ₂	[Pt(Hbapbpy)](PF ₆)
N1-M-N3	90.06(6)	91.43(7)	92.50(18)
N3-M-N4	80.42(6)	82.19(7)	81.77(19)
N4-M-N6	90.03(6)	92.34(7)	91.53(19)
N6-M-N1	101.75(7)	96.38(7)	96.42(18)
N1-M-N4	164.36(6)	165.35(6)	167.67(17)
N3-M-N6	164.37(7)	167.38(6)	165.28(18)
C5-N2-C6	132.09(17)	129.52(17)	127.0(5)
C15-N5-C16	132.23(18)	132.22(18)	128.5(4)
N1-N3-N4-N6	17.70	17.30	16.86

Table SVI.3 Cytotoxicity (EC₅₀ with 95% confidence interval, in μM) of H₂bapbpy and cisplatin on skin (A375, A431), lung (A549), breast (MCF-7, MDA-MB231), and brain cancer cell lines, and non-cancerous lung fetal cell line (MRC-5).

Cell Line	H ₂ bapbpy	CI	cisplatin	CI
A375	5.66	-1.00 +1.22	1.60	-0.52 +0.77
A431	26.94	-9.00 +13.51	3.92	-0.91 1.18
A549	4.66	-2.07 +3.72	3.14	-0.98 +1.42
MCF-7	5.52	-3.31 +8.28	4.02	-1.49 +2.35
MDA-MB-231	66.43	-16.36 +21.70	> 25	-
MRC-5	25.97	-10.66 +18.09	11.61	-3.91 +5.89

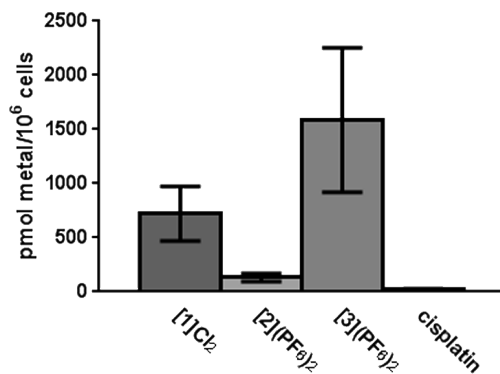


Figure SVI.2 General uptake of [1]Cl₂, [2](PF₆)₂, [3](PF₆)₂, and cisplatin at respectively 70, 0.20, 1.0, and 3.3 μM by A549 cells (expressed in pmol metal/10⁶ cells) after 24 h.

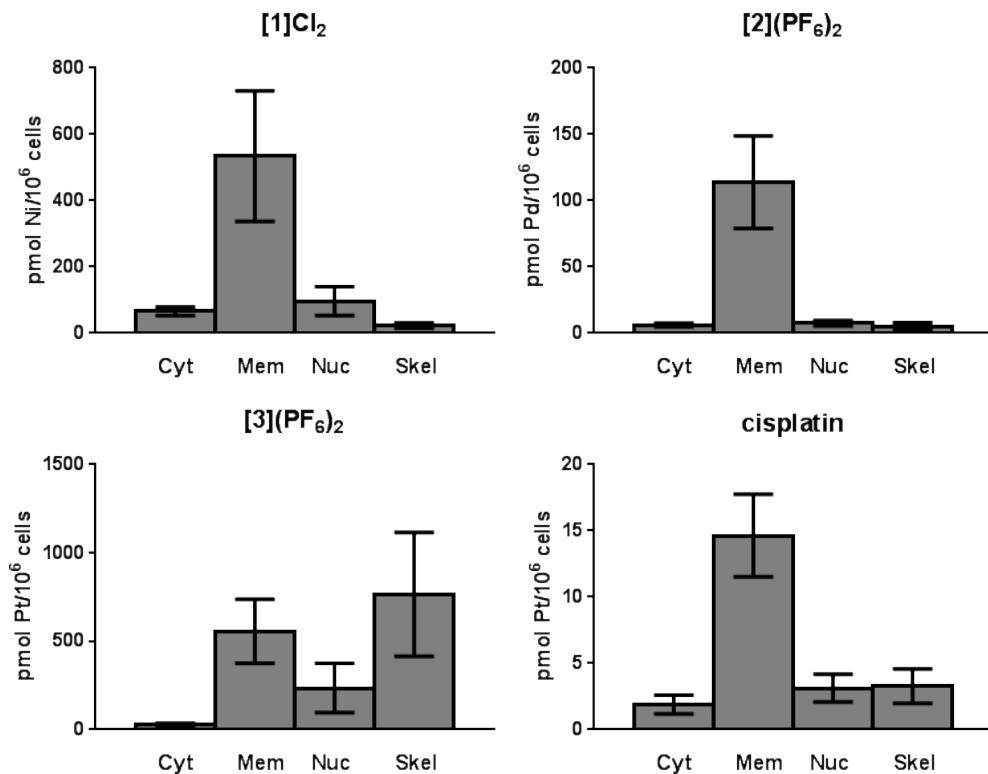


Figure SVI.3 Relative distribution of [1]Cl₂, [2](PF₆)₂, [3](PF₆)₂, and cisplatin at respectively 70, 0.20, 1.0, and 3.3 μM in A549 cells (expressed in pmol metal/10⁶ cells) in cytosol (Cyt), membranes (Mem), nucleus (Nuc), or cytoskeleton (Skel) after 24 h.

Table SVI.4 Uptake in the cytosol, mitochondria, and cytoskeleton fractions of A549 cells for compound [1]Cl₂, [2](PF₆)₂, [3](PF₆)₂, and cisplatin.

Compound	Fraction	Distribution among cytosol, mitochondria, and rest fraction (%)	Distribution among cytosol, mitochondria, and rest fraction (pmol/10 ⁶ cells)
[1]Cl₂	Cytosol	21	338.2 ± 60.2
	Mitochondria	3	47.3 ± 70.6
	Rest	76	1239 ± 546
[2](PF₆)₂	Cytosol	13	30.7 ± 6.24
	Mitochondria	1	1.76 ± 0.63
	Rest	86	196 ± 40.4
[3](PF₆)₂	Cytosol	2	60.4 ± 43.6
	Mitochondria	1	16.1 ± 12.8
	Rest	97	2851 ± 380
cisplatin	Cytosol	25	13.8 ± 0.45
	Mitochondria	5	2.87 ± 0.44
	Rest	69	37.6 ± 19.3

APPENDIX VII: SUPPORTING INFORMATION FOR CHAPTER 7

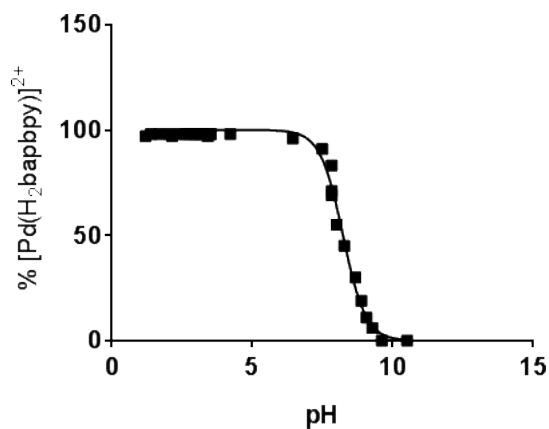


Figure SVII.1 pH dependent presence of [1]²⁺ (%) at different pH in water.

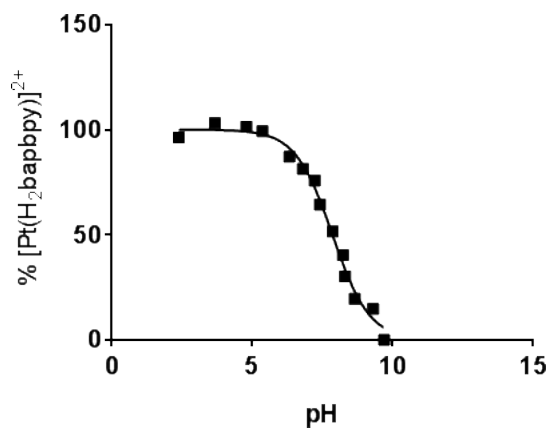


Figure SVII.2 pH dependent presence of [2]²⁺ (%) at different pH in water.

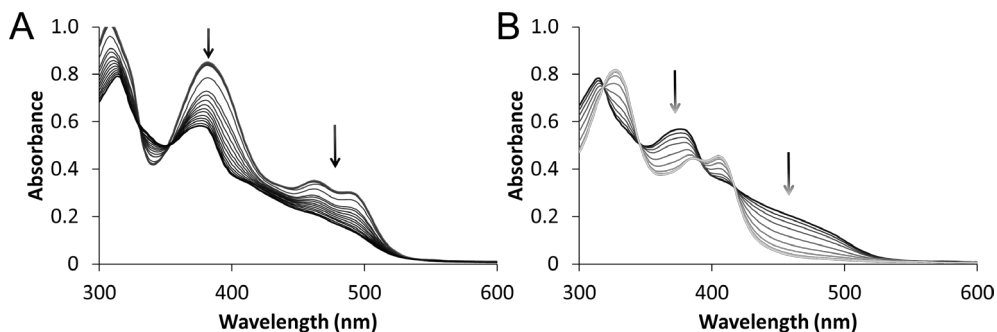


Figure SVII.3 Evolution of the UV-vis spectrum of [5] to [3]⁺ (A) and from [3]⁺ to [1]²⁺ (B) upon decreasing pH using HCl (33 mM, 2 μ L aliquots). Solvent: water-THF mixture (1:1) slightly basified with NaOH to ensure full initial deprotonation. T = 293 K, [Pd] = 67 μ M.

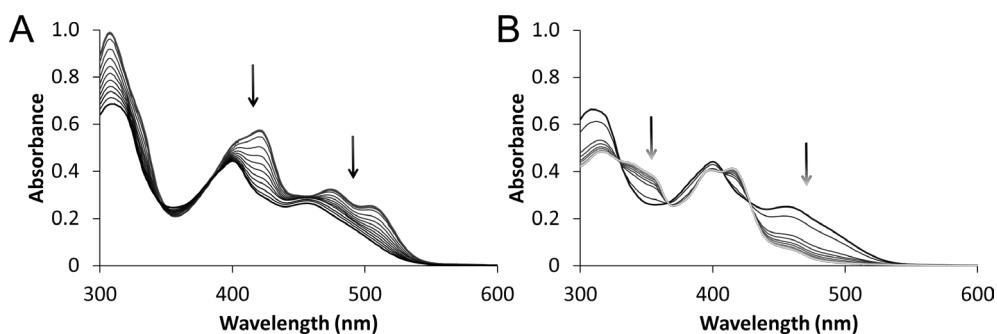


Figure SVII.4 Evolution of the UV-vis spectrum of [6] to [4]⁺ (A) and from [4]⁺ to [2]²⁺ (B) upon decreasing pH using HCl (33 mM, 2 μ L aliquots). Solvent: water-THF mixture (1:1) slightly basified with NaOH to ensure full initial deprotonation. T = 293 K, [Pt] = 67 μ M.

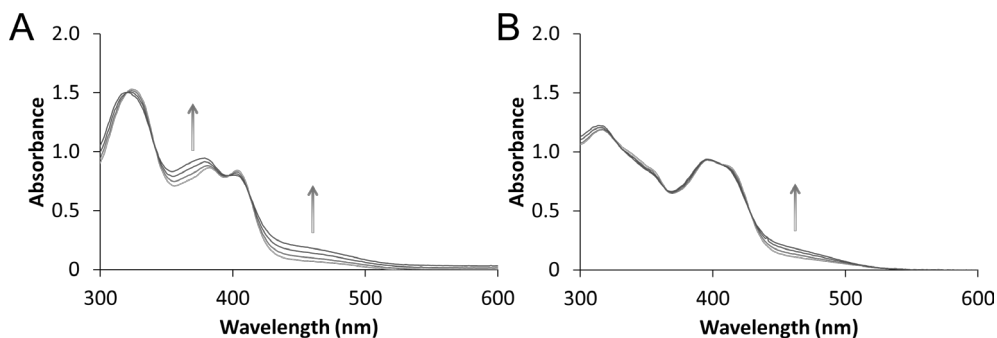


Figure SVII.5 Evolution of UV-vis spectra of [1](PF₆)₂ (A) and [2](PF₆)₂ (B) in demineralized water at different temperature (20 (blue) to 80 °C (red)). [Pd] and [Pt] = 0.10 mM.

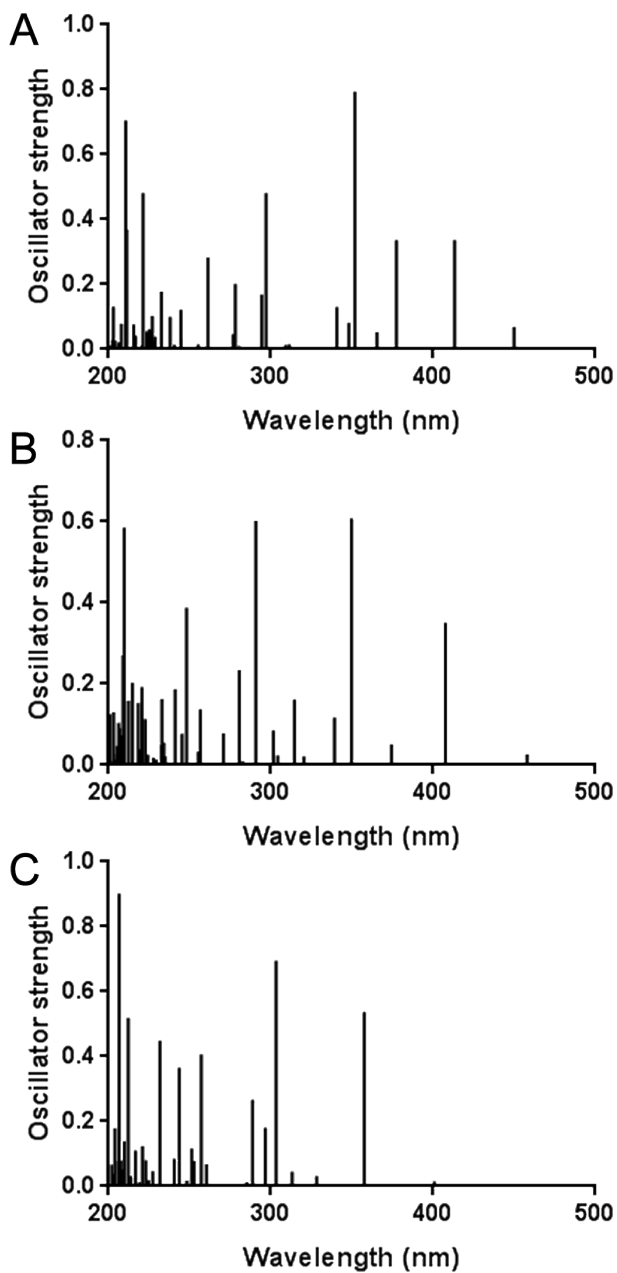


Figure SVII.6 TDDFT calculated excited states for [5] (A), [3]⁺ (B), and [1]²⁺ (C) at the CAM-B3LYP/TZP/COSMO level.

Table SVII.1 Calculated (TDDFT) singlet transitions for [5] from ground singlet state geometry.

Wavelength (nm)	Oscillator strength	Major Contributions
450	0.0685	HOMO → LUMO+1 (56%)
413	0.3367	HOMO → LUMO (30%) HOMO → LUMO (61%) HOMO → LUMO+1 (28%)
377	0.3371	HOMO-1 → LUMO+1 (53%) HOMO-1 → LUMO (22%) HOMO → LUMO+2 (17%)
365	0.0528	HOMO-3 → LUMO+1 (47%) HOMO → LUMO+4 (18%)

Table SVII.2 Calculated (TDDFT) singlet transitions for [3]⁺ from ground singlet state geometry.

Wavelength (nm)	Oscillator strength	Major Contributions
458	0.0261	HOMO → LUMO+1 (72%) HOMO → LUMO (16%)
408	0.3510	HOMO → LUMO (73%) HOMO → LUMO+1 (14%)
374	0.0516	HOMO-3 → LUMO+1 (55%) HOMO-4 → LUMO+1 (12%)

Table SVII.3 Calculated (TDDFT) singlet transitions for [1]²⁺ from ground singlet state geometry.

Wavelength (nm)	Oscillator strength	Major Contributions
401	0.0153	HOMO → LUMO+1 (36%) HOMO → LUMO (31%)
389	0.0038	HOMO-3 → LUMO+1 (52%) HOMO-3 → LUMO (32%)
358	0.5362	HOMO → LUMO (57%) HOMO → LUMO+1 (32%)

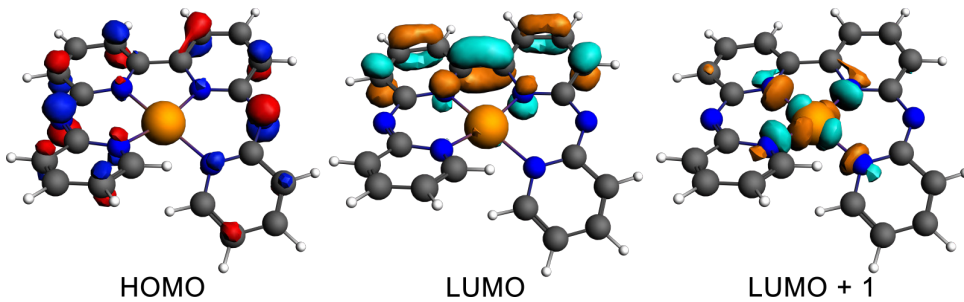


Figure SVII.7 Selected orbital surfaces calculated by ADF of [5].

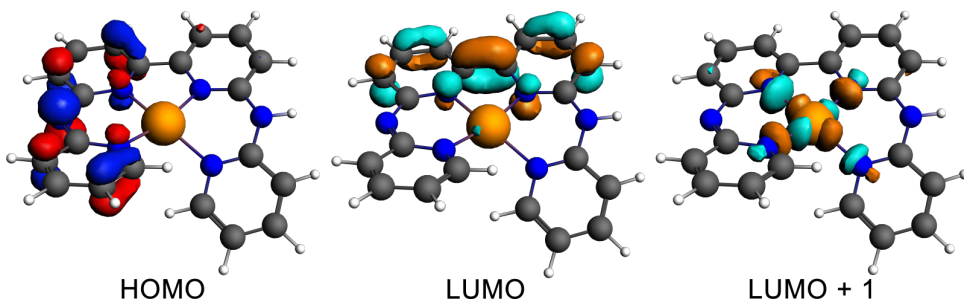


Figure SVII.8 Selected orbital surfaces calculated by ADF of [3]⁺.

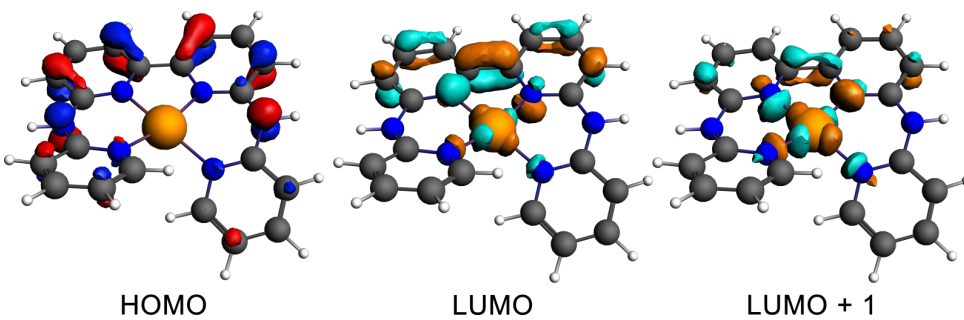


Figure SVII.9 Selected orbital surfaces calculated by ADF of [1]²⁺.

APPENDIX VIII: SUPPORTING INFORMATION FOR CHAPTER 8

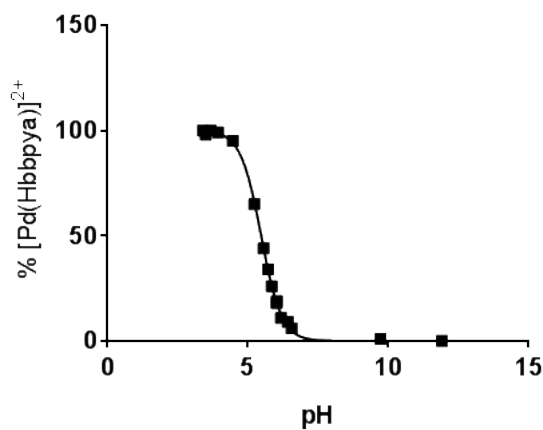


Figure SVIII.1 pH dependent presence of $[1]^{2+}$ (%) at different pH in water.

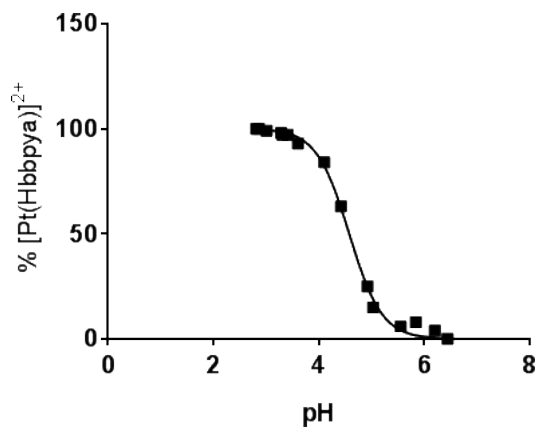


Figure SVIII.2 pH dependent presence of $[2]^{2+}$ (%) at different pH in water.

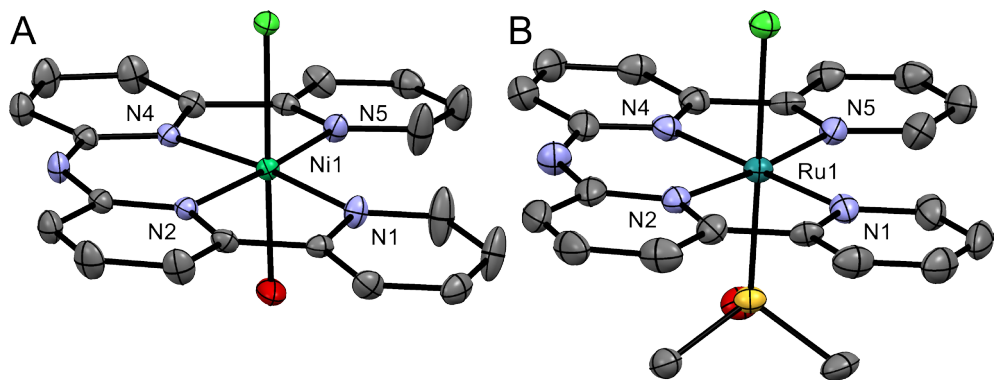


Figure SVIII.3 Displacement ellipsoid of the cationic part of $[\text{Ni}(\text{Hbbpya})(\text{OH}_2)\text{Cl}]^+$ (A) and $[\text{Ru}(\text{Hbbpya})(\text{dmsol})\text{Cl}]^+$ (B) (50% probability level) as observed in the crystal structure of $[\text{Ni}(\text{Hbbpya})(\text{OH}_2)\text{Cl}]\text{Cl}$ and $[\text{Ru}(\text{Hbbpya})(\text{dmsol})\text{Cl}]\text{Cl}$. Chloride counter anions, H atoms, and the lattice solvent molecule, have been omitted for clarity. Torsion angle N1-N2-N4-N5 are 0.00 and 0.73° for the nickel(II) and ruthenium(II) complexes, respectively.

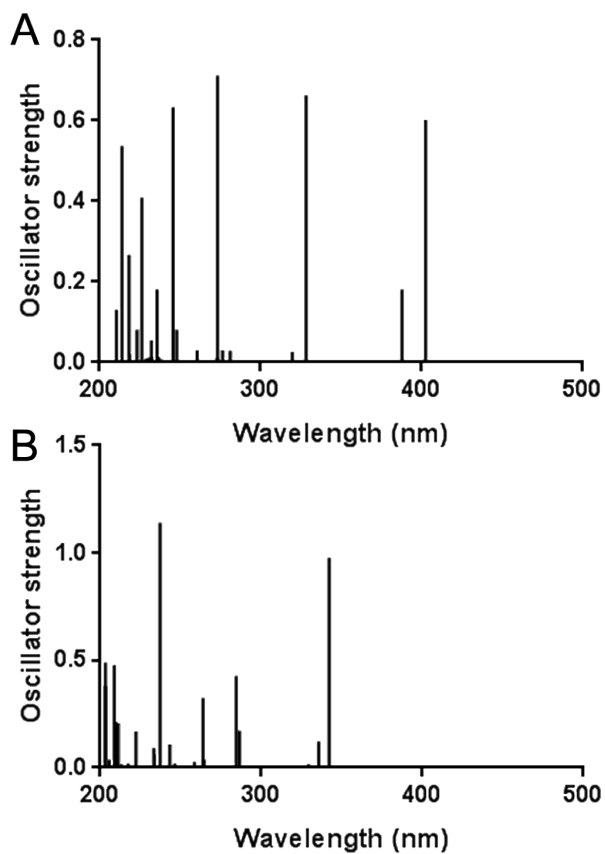


Figure SVIII.4 TDDFT calculated excited states for [Pd(Hbbpya)]²⁺ (A) and [Pd(bbpya)]⁺ (B) at the CAM-B3LYP/TZP/COSMO level.

Table SVIII.1 Calculated (TDDFT) singlet transitions for [Pd(Hbbpya)]²⁺ from ground singlet state geometry.

Wavelength (nm)	Oscillator strength	Major Contributions
388	0.0037	HOMO-4 → LUMO (95%)
368	0.0007	HOMO-1 → LUMO (64%) HOMO-3 → LUMO (24%)
342	0.9778	HOMO → LUMO (90%)

Table SVIII.2 Calculated (TDDFT) singlet transitions for [Pd(bbpya)]⁺ from ground singlet state geometry.

Wavelength (nm)	Oscillator strength	Major Contributions
429	0.0041	HOMO → LUMO (89%)
402	0.6025	HOMO → LUMO (95%)
388	0.1810	HOMO → LUMO+1 (76%)
369	0.0007	HOMO-3 → LUMO+2 (75%)

APPENDIX IX: SUPPORTING INFORMATION FOR CHAPTER 9

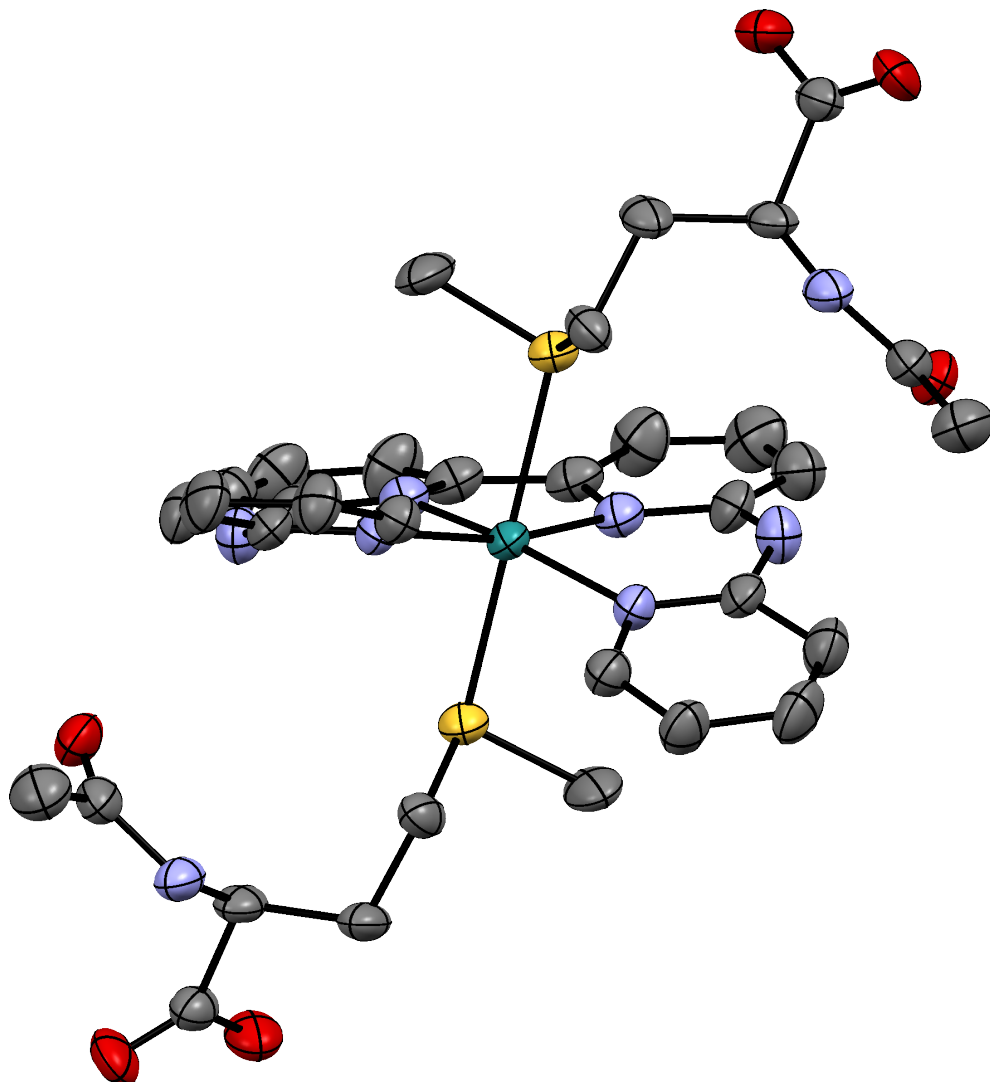
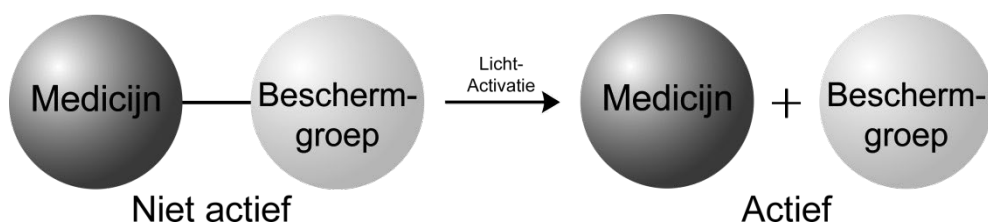


Figure SIX.1 Displacement ellipsoid of the cationic part of $[\text{Ru}(\text{H}_2\text{bapbpy})(\text{HAMet})]^{2+}$ (50% probability level) as observed in the crystal structure of $[\text{Ru}(\text{H}_2\text{bapbpy})(\text{HAMet})_2](\text{PF}_6)_2$. Counter anions, H atoms, and the lattice solvent molecule, have been omitted for clarity.

SAMENVATTING

Ruthenium-polypyridylcomplexen als licht-activeerbare chemotherapeutisch geneesmiddel

Dit proefschrift bevat de beschrijving van verscheidene ruthenium-polypyridylcomplexen die kunnen worden toegepast in licht-activeerbare chemotherapie (PACT). In PACT wordt een niet biologisch-actieve verbinding geactiveerd tot een geneesmiddel door het te bestralen met zichtbaar licht (Schema 1). Door zeer locale bestraling toe te passen kan de cytotoxiciteit van een verbinding worden beperkt tot de tumor, waardoor bijwerkingen worden geminimaliseerd en behandelingsdoses geoptimaliseerd kunnen worden. In het geval van licht-activeerbare metaalcomplexen veroorzaakt de bestraling vaak een uitwisselingsreactie waarbij een van de liganden wordt vervangen door een (labiel) watermolecuul. In PACT kunnen zowel het metaalcomplex als het ligand dienst doen als chemotherapeutisch medicijn. Indien het metaalcomplex de werkzame verbinding is, ontstaat door afsplitsing van het ligand de mogelijkheid tot bijvoorbeeld de vorming van een coördinatiebinding tussen het metaalion en een biomolecuul. Indien het door licht afgesplitste ligand het werkzame medicijn is, leidt een coördinatiebinding met een metaalion in de actieve plaats van een enzym tot belemmering van de biologische activiteit, doordat interactie met het doelwitmolecuul geblokkeerd wordt. De laatstgenoemde strategie staat ook wel bekend als 'photocaging'.



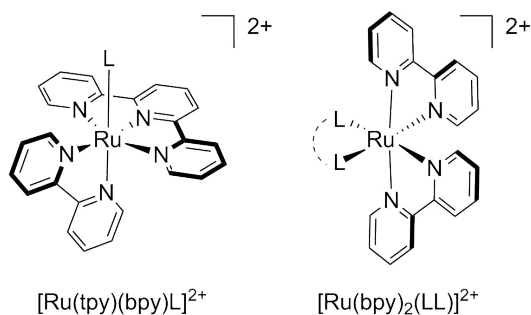
Schema 1. PACT-mechanisme: Een chemische verbinding tussen een medicijn en een beschermgroep deactiveert het medicijn. Bestraling met licht verbreekt de chemische binding waardoor het medicijn zijn biologische werking kan uitoefenen.

In dit proefschrift is eerst beschreven hoe de eigenschappen van ruthenium-polypyridylcomplexen uit de $[\text{Ru}(\text{tpy})(\text{bpy})(\text{L})]^{n+}$ familie gevarieerd kunnen worden door de keuze van monodentaat ligand L (Figuur 1). In Hoofdstuk 2 wordt de studie beschreven naar de mogelijkheid om $[\text{Ru}(\text{tpy})(\text{bpy})(\text{OH}_2)]^{2+}$ te deactiveren door coördinatie met thiolbevattende liganden, maar helaas bleken deze liganden hiervoor ongeschikt. Eenmaal gecoördineerd aan het rutheniumion oxideert het thiolaatligand gemakkelijk tot de sulfenyl- en sulfinylvorm. Daarnaast bleek fotosubstitutie van het thiolaatligand veel minder efficiënt te gebeuren dan de fotosubstitutie van thioetherliganden.¹

Gedurende het onderzoek bleek dat $[\text{Ru}(\text{tpy})(\text{bpy})(\text{OH}_2)]^{2+}$ *in vitro* een geringe cytotoxische activiteit heeft, ook al is dit complex wel in staat interactie met DNA aan te gaan.^{2,4} Daarom lijkt dit complex een zeer geschikt 'photocaging' agens: het is met een coördinatiebinding gebonden aan een microtubuli inhibitor (MTI), ontworpen in de groep van Dr. Alexander Kornienko van Texas State University (USA). Deze inhibitor is gefunctionaliseerd met een thioether donoratoom die gebruikt kan worden om de inhibitor aan $[\text{Ru}(\text{tpy})(\text{bpy})(\text{OH}_2)]^{2+}$ te binden (Hoofdstuk 3). Het hieruit ontstane complex $[\text{Ru}(\text{tpy})(\text{bpy})(\text{MTI-SRR}')](\text{PF}_6)_2$ bleek 40-60 keer minder toxisch dan het vrije MTI-SRR' ligand. Wanneer $[\text{Ru}(\text{tpy})(\text{bpy})(\text{MTI-SRR}')](\text{PF}_6)_2$ wordt geactiveerd door bestraling met groen licht, kan de toxiciteit van het ligand grotendeels worden herwonnen. De EC₅₀ waarden voor cellevensvatbaarheid van het geactiveerde complex en vrij MTI-SRR' bevonden zich in het nanomolair domein. Met behulp van een microtubulipolymerisatieassay kon worden bevestigd dat microtubuli polymerisatie stopte wanneer het toegediende $[\text{Ru}(\text{tpy})(\text{bpy})(\text{MTI-SRR}')](\text{PF}_6)_2$ geactiveerd werd met licht met als gevolg dat het vrijgekomen ligand de polymerisatie van de microtubuli kon blokkeren. In het controle-experiment zonder lichtactivatie vond deze polymerisatie wel plaats. Deze resultaten wijzen erop dat de verkregen cytotoxiciteit na bestraling veroorzaakt wordt door een fotodissociatiereactie van $[\text{Ru}(\text{tpy})(\text{bpy})(\text{MTI-SRR}')](\text{PF}_6)_2$ waarbij het vrijgekomen MTI-SRR' de werkzame verbinding is.

Naast de modelverbinding $[\text{Ru}(\text{tpy})(\text{bpy})(\text{L})]^{2+}$ is ook veel onderzoek gedaan naar de familie van complexen met algemene formule $[\text{Ru}(\text{bpy})_2(\text{LL})]^{2+}$ als potentiële PACT-kandidaten (Figuur 2). Substitutie van een (sterisch gehinderd) bidentaat ligand LL of twee monodentaat liganden in water leidt tot *cis*- $[\text{Ru}(\text{bpy})_2(\text{OH}_2)_2]^{2+}$.

Het fotoproduct $cis-[Ru(bpy)_2(OH_2)_2]^{2+}$ kan net als cisplatina aan DNA binden met twee baseparen gebonden in *cis*-posities. Daarentegen zijn ruthenium-polypyridylcomplexen met twee labiele, monodentaat liganden in wederzijdse *trans*-posities in anti-kankeronderzoek zeldzaam, terwijl deze veel voorkomen bijvoorbeeld in onderzoek naar wateroxidatie-katalysatoren.⁵ Verder heeft KP1019, één van de eerst gerapporteerde op ruthenium gebaseerde anti-kanker complexen, twee indazoolliganden in wederzijdse *trans*-posities.⁶

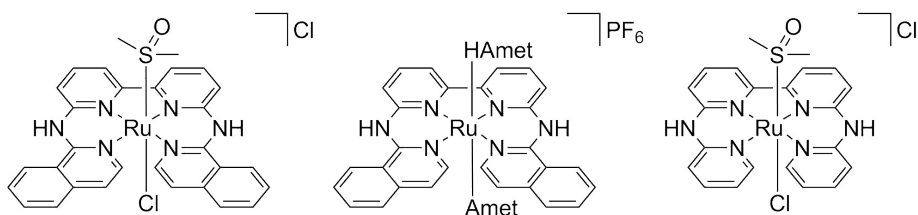


Figuur 1. Chemische structuren van $[Ru(tpy)(bpy)(L)]^{2+}$ en $[Ru(bpy)_2(LL)]^{2+}$.

In Hoofdstuk 4 worden potentiële anti-kanker complexen beschreven die gebaseerd zijn op het $H_2biqbpy$ ligand (Figuur 2), een rigide tetrapyridyl ligand dat alleen met alle donoratomen in een vlak met een metaalion kan binden. Coördinatie van $H_2biqbpy$ aan ruthenium(II) leidde niet alleen tot het cytotoxische en licht-actievebare complex $[Ru(H_2biqbpy)(dmsO)Cl]Cl$, maar coördinatie van twee axiale monodentaat thioetherliganden resulteerde in de verbinding $[Ru(H_2biqbpy)(HAMet)(AMet)]PF_6$, dat een significant lagere cytotoxiciteit heeft dan $[Ru(H_2biqbpy)(dmsO)Cl]Cl$. Activatie van de verbindingen met groen licht zorgde voor een cytotoxiciteit die tot 20 keer hoger is dan hetgeen gevonden is in het controle-experiment zonder licht-activatie. Verder is aangetoond dat deze complexen zeer inefficiënt zijn in het genereren van singletzuurstof. De vorming van singletzuurstof ligt aan de basis van fotodynamische therapie (PDT). PDT is hierdoor echter niet geschikt voor de behandeling van zuurstof-arme tumoren. Daarom kunnen als alternatief voor PDT, PACT-verbindingen gebaseerd op $[Ru(H_2biqbpy)(L)(L')]^{2+}$ gebruikt worden als potentiële anti-kanker geneesmiddelen, omdat hun werking onafhankelijk is van de aanwezigheid van zuurstof. Daarnaast veroorzaken $H_2biqbpy$ -ruthenium complexen die met licht geactiveerd zijn apoptose, een gecontroleerde vorm van celdood. Een PDT-

behandeling heeft daarentegen als nadeel dat behandelde cellen via necrose doodgaan. Deze ongecontroleerde vorm van celdood leidt tot verlies van celmembraanintegriteit waardoor de inhoud van de cel vrijkomt in het extracellulaire milieu, met als mogelijk gevolg een pijnlijke ontstekingsreactie. Behandeling met H₂biqbpy-ruthenium complexen leidt tot apoptose (geprogrammeerde celdood) waardoor zulke ongewenste ontstekingsreacties voorkomen worden. Uiteindelijk zou dit moeten leiden tot minder pijn bij de patiënt.

Opname- en fractioneringsexperimenten zoals beschreven in Hoofdstuk 4 laten zien dat A549 cellen ongeveer 7,5-16 ng ruthenium opnemen per 10⁶ cellen en dat de complexen overwegend accumuleren in de membraanfractie bestaande uit organellen, lysosomen en membranen. In de nucleus werden ook significante hoeveelheden ruthenium aangetroffen (1,7-3,2 ng Ru/10⁶ cellen), wat het uitvoeren van DNA-interactie-experimenten rechtvaardigde. Met behulp van gelelektroforese experimenten is vastgesteld dat de interactie tussen [Ru(H₂biqbpy)(dmsO)Cl]Cl of [Ru(H₂biqbpy)(HAMet)(Amet)]PF₆ met pUC19 plasmide DNA beïnvloed kan worden door bestraling met licht. Deze controle wijst wederom op de beschermende rol van de thioetherliganden. Een toename van lichtdosis leidt tot meer ontscherming van de verbindingen en zorgt voor meer interactie met het pUC19 plasmide DNA. Deze ruthenium-DNA adducten konden helaas niet gekarakteriseerd worden. Studies naar de interactie van een gedefinieerde enkelstrengs oligonucleotide (ODN) met verschillende ruthenium-tetrapyridylcomplexen (Figuur 2) zijn uitgevoerd in samenwerking met Prof. Luigi Messori aan de Universiteit van Florence. Hieruit bleek dat de adducten van de rutheniumverbindingen met de ODN wel goed gekarakteriseerd konden worden met HRMS. Zoals verwacht vertoonde niet-geactiveerde complexen verwaarloosbare interactie met de ODN, terwijl activatie met blauw licht resulteerde in adducten bestaande uit één ODN en één of twee rutheniumcomplexen na verlies van het monodentate zwavelligand.



[Ru(H₂biqbpy)(dmsO)Cl]Cl [Ru(H₂biqbpy)(HAmet)(Amet)]PF₆ [Ru(H₂bapbpy)(dmsO)Cl]Cl

Figuur 2. Chemische structuren van [Ru(H₂biqbpy)(dmsO)Cl]Cl, [Ru(H₂biqbpy)(HAmet)(Amet)]PF₆ en [Ru(H₂bapbpy)(dmsO)Cl]Cl.

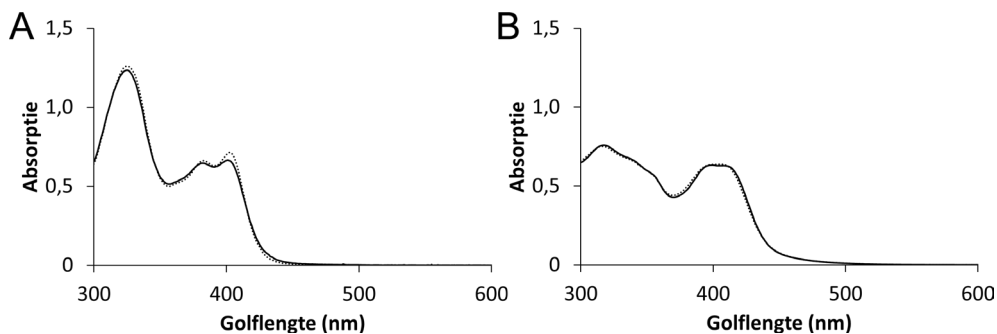
Over het geheel genomen tonen de resultaten uit Hoofdstuk 2-5 aan dat ruthenium-polypyridylcomplexen met zwavel bevattende monodentaat liganden veel potentie hebben als licht-activeerbare verbindingen voor chemotherapie. De fotosubstitutie van een thioether- of sulfoxideligand kan gebruikt worden om cytotoxiciteit, het type celdood en de interactie van rutheniumcomplexen met biologische moleculen te beïnvloeden. Deze kwaliteiten leggen de basis voor verdere ontwikkeling van PACT-verbindingen ter behandeling van hypoxische tumoren.

Vlak-vierkante tetrapyridyl complexen als anti-kanker geneesmiddel

In het onderzoeksveld van anti-kanker metallodrugs wordt veruit het meeste onderzoek gedaan naar verbindingen gebaseerd op platina, veelal geïnspireerd op het succes van cisplatina. Tot zover heeft dit geleid tot negen varianten op cisplatina die op dit moment toegepast worden in de kliniek (zie Hoofdstuk 1). Alternatieven voor cisplatinacomplexen moeten een ander werkingsmechanisme hebben om behandeling van cisplatina-resistente tumoren mogelijk te maken. De coördinatie van het ligand H₂bapbpy met palladium(II) en platina(II) ionen is onderzocht, wat leidde tot de metaalcomplexen [Pd(H₂bapbpy)]²⁺ en [Pt(H₂bapbpy)]²⁺ (Hoofdstuk 6) die qua structuur vergelijkbaar zijn met het licht-activeerbare rutheniumcomplex [Ru(H₂bapbpy)(dmsO)Cl]Cl, maar zonder axiale monodentaat liganden. Deze kolom 10 complexen vertoonden *in vitro* zeer hoge cytotoxiciteit. Over een brede selectie van verschillende kankercellijnen vertoonde [Pd(H₂bapbpy)](PF₆)₂ ongekende cytotoxische activiteit met EC₅₀ waarden van 200 nM tot zelfs 50 nM. De EC₅₀ waarden van [Pt(H₂bapbpy)](PF₆)₂ waren 4-16 keer hoger en vergelijkbaar met de cytotoxische activiteit van cisplatina. Wanneer de kankercellijnen met de palladium(II)- of platinum(II)verbindingen behandeld

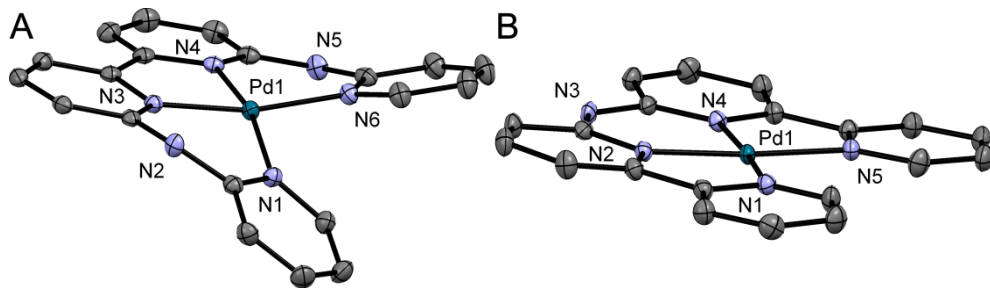
werden en gelijktijdig met N-Acetyl-L-cysteïne (NAC) – een vanger van reactieve zuurstofverbindingen (ROS) – werd de activiteit van het palladiumcomplex geheel teniet gedaan, terwijl de activiteit van het platina complex vrijwel gelijk bleef. Wanneer kankercellijnen met de palladium(II)- of platinum(II)verbindingen behandeld werden en gelijktijdig met L-buthionine sulfoximine (BSO) – een stof die de cellen meer ontvankelijk maakt voor ROS – vertoonde het palladium complex een spectaculair verhoogde activiteit, terwijl dit effect veel minder aanwezig was voor de platinaverbinding. Het platinacomplex vertoonde een hogere cytotoxische activiteit dan het palladiumcomplex in kankercellijnen waarin het p53-gen ontbrak. Beide complexen worden zeer goed opgenomen door de cellen, maar waar $[\text{Pd}(\text{H}_2\text{bapbpy})]^{2+}$ vooral in de membranen accumuleert, is $[\text{Pt}(\text{H}_2\text{bapbpy})]^{2+}$ gelijkmatiger verdeeld over de cytosol-, membraan-, nucleus- en cytoskeletfracties. In samenwerking met Prof. Walter Berger van de Medische Universiteit van Wenen zijn *in vivo* experimenten uitgevoerd. Hierin zijn CT-26 darmkanker Balb/c muizen behandeld met equimolaire doses van $[\text{Pd}(\text{H}_2\text{bapbpy})](\text{PF}_6)_2$ of $[\text{Pt}(\text{H}_2\text{bapbpy})](\text{PF}_6)_2$. Dit resulteerde in een significante reductie in tumorgroei bij behandeling met het palladiumcomplex, terwijl een dergelijk effect voor het platinacomplex niet gevonden werd. Over het geheel genomen suggereren *in vitro* cytotoxiciteit, NAC, BSO, p53, celopname experimenten, als ook *in vivo* experimenten dat de qua structuur vergelijkbare palladium- en platinacomplexen verschillende werkingsmechanismen hebben.

Coördinatie van het tetradentaat ligand H_2bapbpy aan Pd^{2+} of Pt^{2+} resulteert in een vlak-vierkante geometrie. Hierdoor is het onwaarschijnlijk dat het palladium- of platinacomplex in kankercellen werkzaam is via ligandsubstitutiereacties zoals in geval bij cisplatina. De stabiliteit van de coördinatieomgeving blijkt uit experimenten waarin oplossingen van $[\text{M}(\text{H}_2\text{bapbpy})]\text{Cl}_2$ in water (0.10 mM, M = Pd of Pt) met 100 equivalenten NaCl werden verwarmd tot 80 °C. Hierna werden geen significante spectroscopische veranderingen waargenomen die zijn toe te schrijven aan ligandsubstitutie (Figuur 3). Gebaseerd op de waarnemingen mag worden aangenomen dat deze Pd(II)- en Pt(II)-complexen stabiel zijn *in vitro*, *in vivo* en in fysiologische omstandigheden.



Figuur 3. UV-vis absorptiespectra van $[\text{Pd}(\text{H}_2\text{bapbpy})]\text{Cl}_2$ (A) en $[\text{Pt}(\text{H}_2\text{bapbpy})]\text{Cl}_2$ (B) in een waterige NaCl-oplossing (10 mM) bij 20 (doorgetrokken lijn) en 80 °C (stippellijn). $[\text{Pd}] = [\text{Pt}] = 0,10$ mM.

In vitro studies zijn ook uitgevoerd met platina- en palladiumcomplexen van een tetrapyridylligand met één aminebrug (Hbbpya) in plaats van de twee aminebruggen in H2bapbpy. De cytotoxiciteit van deze verbindingen was vergelijkbaar met die van cisplatina, maar was veel lager dan dat van $[\text{Pd}(\text{H}_2\text{bapbpy})](\text{PF}_6)_2$ (Hoofdstuk 7). Coördinatie van Hbbpya aan een palladium(II)-ion resulteerde in een veel minder verstoorde vlak-vierkante geometrie dan in de H2bapbpy-verbinding (Figuur 4). Door de aanwezigheid van slechts één aminebrug in vlak-vierkante Hbbpya complexen is het aantal ladingstoestanden beperkt tot dicationisch ($[\text{M}(\text{Hbbpya})]^{2+}$) of monocationisch wanneer het amine gedeprimeerd is ($[\text{M}(\text{bbpya})]^+$). Voor H2bapbpy complexen is deprotonering van twee amines mogelijk, waardoor een derde, neutrale toestand bereikbaar is ($[\text{M}(\text{bapbpy})]$). De pKa voor de eerste deprotonering is 5,5 en 4,6 voor respectievelijk $[\text{Pd}(\text{Hbbpya})]^{2+}$ en $[\text{Pt}(\text{Hbbpya})]^{2+}$, terwijl voor $[\text{Pd}(\text{H}_2\text{bapbpy})]^{2+}$ en $[\text{Pt}(\text{H}_2\text{bapbpy})]^{2+}$ de eerste pKa veel hoger is (respectievelijk 7,8 en 8,3). Er mag dus worden aangenomen dat de Hbbpya-complexen in fysiologische condities gedeprimeerd en in hun monocationische vorm zijn, terwijl de H2bapbpy-complexen in zowel dicationisch als monocationische vorm aanwezig zijn.



Figuur 4. Projecties van $[\text{Pd}(\text{H}_2\text{bapby})]^{2+}$ (A) en $[\text{Pd}(\text{Hbbpya})]^{2+}$ (B). Ter verduidelijking zijn H-atomen, anionen en oplosmiddelmoleculen weggelaten.

Referenties

1. R. E. Goldbach, I. Rodriguez-Garcia, J. H. van Lenthe, M. A. Siegler and S. Bonnet, *Chem. Eur. J.*, 2011, **17**, 9924-9929.
2. B. Siewert, V. H. S. van Rixel, E. J. van Rooden, S. L. Hopkins, M. J. B. Moester, F. Ariese, M. A. Siegler and S. Bonnet, *Chem. Eur. J.*, 2016, **22**, 10960-10968.
3. O. Novakova, J. Kasparkova, O. Vrana, P. M. van Vliet, J. Reedijk and V. Brabec, *Biochemistry*, 1995, **34**, 12369-12378.
4. J. Rodríguez, J. Mosquera, J. R. Couceiro, M. E. Vázquez and J. L. Mascareñas, *Angew. Chem., Int. Ed.*, 2016, **55**, 15615-15618.
5. K. Nakanishi, T. Koshiyama, S. Iba and M. Ohba, *Dalton Trans.*, 2015, **44**, 14200-14203.
6. B. K. Keppler, M. Henn, U. M. Juhl, M. R. Berger, R. Niebl and F. E. Wagner, in *Ruthenium and Other Non-Platinum Metal Complexes in Cancer Chemotherapy*, eds. E. Baulieu, D. T. Forman, M. Ingelman-Sundberg, L. Jaenicke, J. A. Kellen, Y. Nagai, G. F. Springer, L. Träger, L. Will-Shahab and J. L. Wittliff, Springer Berlin Heidelberg, Berlin, Heidelberg, 1989, pp. 41-69.

CURRICULUM VITAE

Vincent van Rixel was born in Beverwijk, The Netherlands on 28 November 1987. In 2006 he graduated from the Kennemer College High School in Beverwijk at the gymnasium level. In 2010, he received his Bachelor of Science degree in Molecular Science and Technology of Leiden University and Technical University Delft. During the BSc program he visited Sofia University (Tokyo, Japan) in 2007 for a summer school program, and Occidental College (Los Angeles, USA) in 2010 for a summer research program. His bachelor thesis was entitled '*Nickel NHC-Complexes in the Hydrosilylation of Alkynes*'. In 2012, he received a Master of Science degree in Chemistry with a specialization in 'Science Communication and Society' at Leiden University. His chemistry thesis was entitled '*Photo-Active Anticancer Prodrugs based on [Ru(H₂bapbpy)(SRR')₂]²⁺*' and his science communication thesis was entitled '*Online Science and Technology Communication: Interactivity and social media in The Netherlands*'. In 2013, he received a second Master of Science degree in Public Administration with a specialization in 'International Public Administration' at Leiden University. His public administration thesis was entitled '*The Influence of International Focusing Events on Domestic Policy: A Study on the Effect of the Fukushima Nuclear Crisis on Dutch Nuclear Energy Policy*'.

In February 2013 he started his PhD research under the supervision of Dr. S. Bonnet and Prof. Dr. E. Bouwman in the research group 'Metals in Catalysis, Biomimetics and Inorganic Materials' (MCBIM) of the Leiden Institute of Chemistry, Leiden University. During his PhD studies, he collaborated with Dr. T. Marzo, Prof. Dr. C. Bazzicalupi, and Prof. Dr. L. Messori (University of Florence), Dr. A. Kornienko and Dr. T. Betancourt (Texas State University), Prof. Dr. W. Berger (Institute for Cancer Research, Medical University of Vienna), G. Moolenaar and Dr. N. Goosen (Leiden University), Prof. Dr. F. Ariese (VU Amsterdam), Prof. Dr. B. Liagre (University of Limoges), and Dr. N. Pannu (Leiden University). In 2016 he went to Florence to investigate the '*Interaction of Light-activatable Ruthenium Polypyridyl Complexes with ODNs*' which was financially supported by COST Action CM1105 (Ref. 32634). In total, he supervised one MSc and four BSc students and frequently supervised first and second year chemistry lab courses.

He presented parts of the research described in this thesis at the following meetings and conferences:

- Reedijk Symposium 2013, Leiden, The Netherlands (poster).
- Holland Research School of Molecular Chemistry (HRSMC) Symposium, 2013 and 2014 in respectively Leiden and Amsterdam, The Netherlands (poster).
- 17th International Conference on Biological Inorganic Chemistry (ICBIC17), 2015, Beijing, China (poster).
- WG-5 meeting of the COST Action CM1105, 2015, Belgrade, Serbia (oral).
- Chemistry as Innovating Science (CHAINS), 2015, Veldhoven, The Netherlands (oral).
- International Symposium on Functional Metal Complexes that Bind to Biomolecules – 4th Whole Action Meeting of the COST Action CM1105, 2015, Palma de Mallorca, Spain (oral).

During his PhD research, he participated in the following courses:

- HRSMC Physical Methods in Inorganic Chemistry.
- HRSMC Advanced Metal-Organic Chemistry and Catalysis.
- Master Course 'Metals and Life' (Leiden University).
- Master Course 'Spin and Photochemistry' (Leiden University).
- Graduate School courses of Leiden University: Time management, On being a Scientist, Communication in Science, and Effective Communication.

LIST OF PUBLICATIONS

J. Berding, J. A. van Paridon, **V. H. S. van Rixel** and E. Bouwman, '[NiX₂(NHC)₂] Complexes in the Hydrosilylation of Internal Alkynes', *Eur. J. Inorg. Chem.*, 2011, 2450-2458.

V. H. S. van Rixel, A. Busemann, A. J. Göttle and S. Bonnet, 'Preparation, Stability, and Photoreactivity of Thiolato Ruthenium Polypyridyl Complexes: Can Cysteine Derivatives Protect Ruthenium-based Anticancer Complexes?', *J. Inorg. Biochem.*, 2015, **150**, 174-181.

V. H. S. van Rixel, B. Siewert, S. L. Hopkins, S. H. C. Askes, A. Busemann, M. A. Siegler and S. Bonnet, 'Green light-induced Apoptosis in Cancer Cells by a Tetrapyridyl Ruthenium Prodrug Offering Two Trans Coordination Sites', *Chem. Sci.*, 2016, **7**, 4922-4929.

B. Siewert, **V. H. S. van Rixel**, E. J. van Rooden, S. L. Hopkins, M. J. B. Moester, F. Ariese, M. A. Siegler and S. Bonnet, 'Chemical Swarming: Depending on Concentration, an Amphiphilic Ruthenium Polypyridyl Complex Induces Cell Death via Two Different Mechanisms', *Chem. Eur. J.*, 2016, **22**, 10960-10968.

B. Siewert, M. Langerman, Y. Hontani, J. T. M. Kennis, **V. H. S. van Rixel**, B. Limburg, M. A. Siegler, V. Talens Saez, R. E. Kieltyka and S. Bonnet, 'Turning on the Red Phosphorescence of a [Ru(tpy)(bpy)(Cl)]Cl Complex by Amide Substitution: Self-aggregation, Toxicity, and Cellular Localization of an Emissive Ruthenium-based Amphiphile', *Chem. Commun.*, 2017, *in press*.

V. H. S. van Rixel, G. F. Molenaar, M. A. Siegler, L. Messori and S. Bonnet, 'Controlling with Light the Interaction between Trans Tetrapyridyl Ruthenium Complexes and an Oligonucleotide', *manuscript submitted*.

V. H. S. van Rixel, A. Busemann, M. F. Wissingh, M. A. Siegler, T. Marzo, C. Bazzicalupi and S. Bonnet, 'Crystal structure of a four-way DNA junction containing a platinum anticancer complex', *manuscript in preparation*.

V. H. S. van Rixel, A. Busemann, B. Siewert, S. L. Hopkins, M. F. Wissingh, M. Falandt, G. Ruigrok, M. A. Siegler, W. Berger and S. Bonnet, 'The metal matters: Tetrapyridyl nickel, palladium, and platinum complexes with minimal to nanomolar anti-cancer activity', *manuscript in preparation*.

V. H. S. van Rixel, T. Ozel, T. Betancourt, L. N. Lameijer, A. Kornienko and S. Bonnet, 'A microtubule-targeted rigidin analogue caged by a ruthenium polypyridyl complex that can be released with green light', *manuscript in preparation*.

V. H. S. van Rixel, M. A. Siegler and S. Bonnet, 'The metal matters II: Protonation and deprotonation of the non-coordinating amines of $[M(H_2bapbpy)]^{2+}$ complexes', *manuscript in preparation*.

V. H. S. van Rixel, L. J. S. Marinelli, M. A. Siegler and S. Bonnet, 'The ligand matters: Pd and Pt anticancer drugs based on a tetrapyridyl ligand containing a single amine bridge', *manuscript in preparation*.

ACKNOWLEDGEMENTS

COST Action CM1105 (Functional metal complexes that bind to biomolecules) is acknowledged for financial support for a short term scientific mission at the University of Florence. Prof. Dr. Luigi Messori, Dr. Tiziano Marzo, Dr. Lara Massai, and Dr. Federica Scaletti (University of Florence) are kindly acknowledged for their hospitality, help, and collaboration during this short term scientific mission. Dr. Adrien Göttle (Leiden University) is acknowledged for DFT calculations (Chapter 2). Prof. Dr. Alexander Kornienko (Texas State University) is acknowledged for supplying the microtubule inhibiting ligand (Chapter 3). Dr. Tania Betancourt, Tugba Özel, and Taryn Olivas (Texas State University) are acknowledged for performing the tubulin polymerization assay (Chapter 3). Dr. Samantha Hopkins (Leiden University) is acknowledged for gel electrophoresis experiments (Chapter 4 and 6) and designing the (photo)cytotoxicity assay employed throughout this thesis. Dr. Sven Askes (Leiden University) is acknowledged for singlet oxygen emission experiments (Chapter 4). Elena Michelucci (University of Florence) is acknowledged for HRMS measurements and corresponding data work-up (Chapter 5). Geri Moolenaar and Dr. Nora Goosen (Leiden University) are kindly acknowledged for performing gel electrophoresis experiments (Chapter 5) and for collaborations in ongoing projects. Prof. Dr. Walter Berger (University of Vienna) is kindly acknowledged for performing *in vitro* co-treatment, p53 cytotoxicity assays and *in vivo* experiments (Chapter 6) and for collaboration in ongoing projects. Crystallographer Dr. Maxime Siegler (Johns Hopkins University, USA) is gratefully acknowledged for X-ray crystallography. Jos van Brussel (Leiden University) is acknowledged for elemental analyses and ICP-OES measurements (Chapter 4 and 8). Marc Verheul (Deltares) is acknowledged for ICP-MS measurements (Chapter 4, 6, and 8). Hans van den Elst (Leiden University) is acknowledged for HRMS experiments. Dr. Karthick Sai Sankar Gupta and Fons Lefeber are gratefully acknowledged for NMR assistance. John van Dijk and Anne-Geert Volbeda (Leiden University) are acknowledged for ESI-MS measurements. Jordi Amat Cuello-Garibo, Lucien Lameijer, Michael Meijer, and Dr. Sipeng Zheng (Leiden University) are kindly acknowledged for exchange of ideas, results, and support. Dr. Bianka Siewert (Leiden University) is gratefully acknowledged for providing biochemical training, fluorescence-

activated cell sorting and imaging data (Chapter 4 and 6). Anja Busemann is gratefully acknowledged for contributions to Chapter 2 and performing cell fractionation experiments (Chapter 4 and 6). Supervised students, namely Amanda van der Wekken-Schaaf, Jaco Lugthart, Tim Ofman, Joost de Graaff, Mark Falandt and Gijs Ruijgrok (Chapter 6), Iris de Bruin, Rick Spierenburg, and Mathijs Wissingh (Chapter 6 and 7), and Lucas Marinelli (Chapter 8) are all acknowledged for their input and contributions to this thesis.